



DISSERTATION

**Static and dynamic properties of
two-dimensional systems
with competing interactions**

ausgeführt zum Zwecke der Erlangung des akademischen Grades
eines Doktors der technischen Wissenschaften

unter der Anleitung von
Ao.Univ.Prof. Dipl.-Ing. Dr.techn. Gerhard Kahl
am Institut für Theoretische Physik (E136)
der Technischen Universität Wien

eingereicht an der Technischen Universität Wien
Fakultät für Physik von

Dipl.-Ing. Dieter Schwanzer
Matrikelnummer: 9725032
Ratschkygasse 12/15
1120 Wien

Datum

Unterschrift

Kurzfassung

Im Gegensatz zu atomaren Systemen zeigen Systeme der weichen Materie eine Vielzahl von leicht veränderbaren Teilchenwechselwirkungen. Sowohl die Art, als auch der Salzgehalt und der pH-Wert des Lösungsmittels haben einen maßgeblichen Einfluß auf die Wechselwirkung zwischen den Kolloidteilchen, aus denen sich ein System von weicher Materie zusammensetzt. Durch derartige Eingriffe in weiche Systeme ist es möglich, die Teilchenwechselwirkungen so zu verändern, dass eine kurzreichweitige anziehende Kraft einer langreichweitigen abstoßenden Kraft gegenübersteht. Anstatt sich in eine ungeordnete Phase hoher Teilchendichte und eine ungeordnete Phase geringer Teilchendichte zu trennen, bilden Systeme mit derartigen konkurrierenden Kräften bei niedrigen Temperaturen sogenannte Mikrophasen aus: periodische Strukturen hoher Teilchendichte, die von Lösungsmittel umgeben sind.

Die vorliegende Dissertation beschäftigt sich mit einem derartigen Wechselwirkungsmodell mit konkurrierenden Kräften. Mit Hilfe von Flüssigkeitstheorien und Monte Carlo Simulationen können jene Parameter identifiziert werden, die zur Bildung von Mikrophasen führen. Die Untersuchungen dieser Arbeit zeigen, dass die Mikrophasenbildung bei einer ausreichenden starken langreichweitigen abstoßenden Kraft erfolgt. Des Weiteren wird in der vorliegenden Arbeit mittels Monte Carlo Simulationen das dynamische Verhalten einer speziellen Mikrophase, jener der sphärischen Cluster von Teilchen, sowie das dynamische Verhalten der einzelnen Teilchen untersucht. Dabei zeigt sich, dass die Teilchencluster nur oberhalb einer bestimmten Dichte geordnete Strukturen ausbilden. Schließlich behandelt die vorliegende Arbeit den Einfluss einer porösen Matrix auf Teilchen mit konkurrierenden Wechselwirkungskräften. In Abhängigkeit von deren gegenseitiger Wechselwirkung, werden die Teilchen dabei von der Matrix adsorbiert oder halten sich bevorzugt im Zentrum jener Bereiche auf die frei von Matrix sind.

Abstract

In contrast to atomic materials, soft matter systems show a wide range of particle interactions, that can be easily modified, for instance by changing the solvent or its salt concentration and pH value. Using these measures, the particle interactions in soft matter systems can be tuned in such a way that a short range attraction competes with a long ranged repulsion. At low temperatures, systems with this kind of competing interactions are known to self assemble into so-called microphases, i. e. periodic domains of high particle density surrounded by a low particle density fluid, instead of phase separating into one high and one low density liquid phase.

The present work is dedicated to a model that features such competing interactions. We use the framework of liquid state theories based on the Ornstein-Zernike equation and Monte Carlo simulations to explore the parameter space of this model potential to find those potential parameter combinations that favor microphase formation rather than bulk phase separation. We find that a sufficiently strong long ranged repulsion guarantees the formation of microphases at low enough temperatures. Furthermore, we investigate the dynamic behavior of clusters of particles as well as of the individual particles in the cluster-microphase formed at low densities, using extensive Monte Carlo simulations. We find, that the particle clusters only form ordered structures above a certain particle density, while remaining mobile down to the lowest investigated temperatures, at lower densities. Finally, the effect of a disordered porous matrix on the properties of a fluid of particles with competing interactions is studied. We find that in these so-called quenched-annealed systems the cluster forming fluid particles are either adsorbed into the matrix or avoid the matrix particles, depending on the interaction between fluid and matrix.

*Wisdom is not a product of schooling
but the lifelong attempt to acquire it.*

Albert Einstein (1879-1955)

Contents

1	Introduction	1
2	Model	5
3	Theory - Statistical mechanics	9
3.1	General Concepts	9
3.2	Time and Ensemble averages	10
3.2.1	Time averages	11
3.2.2	Ensemble averages	11
3.3	Types of Ensembles	12
3.3.1	Microcanonic ensembles (<i>NVE</i> -ensembles)	12
3.3.2	Canonic ensembles (<i>NVT</i> -ensembles)	12
3.3.3	Grandcanonic ensembles (μVT -ensembles)	15
3.4	Static Structure	20
3.5	Important observables	25
3.5.1	Energy	25
3.5.2	Pressure	26
4	Methods	31
4.1	Monte-Carlo Simulations	31
4.1.1	General	31
4.1.2	Monte Carlo Moves	35
4.1.3	Implementation Details	38
4.1.4	MC Dynamics	44
4.2	Integral Equations	46
4.2.1	Ornstein-Zernike Equation	46
4.2.2	Closure Relations	53
4.2.3	Algorithm for Solving the Ornstein-Zernike Equations	57
4.2.4	Integral Equations in Two Dimensions	62
4.2.5	Chemical potential μ	66
4.3	Cluster Analysis	68
4.3.1	Cluster Identification	68
4.3.2	Cluster Tracking	71
4.3.3	Voronoi tessellation	75
4.3.4	Bond-Order Parameters	77

4.3.5	Radius of gyration	79
5	Results	81
5.1	Static Properties and Phase Diagrams	81
5.1.1	Computation of Phase Diagrams	81
5.1.2	Overview	85
5.1.3	Systems showing microphase formation	90
5.1.4	Systems showing liquid-vapor phase separation	98
5.2	Clusters and Dynamic Properties	103
5.2.1	General Cluster Properties	108
5.2.2	Structural Particle and Cluster Properties	113
5.2.3	Thermal Particle and Cluster Properties	123
5.2.4	Dynamic Particle and Cluster Properties	125
5.3	Quenched Annealed Systems	143
5.3.1	Overview of investigated systems	143
5.3.2	Snapshots and Cluster Properties	146
5.3.3	Structure functions	154
5.3.4	Mean Square Displacement	164
6	Conclusions	167
	Appendices	171
A	2D-FFT Approximations	171
A.1	remarks	176
	Bibliography	179
	Acknowledgments	187
	Curriculum Vitae	191

Chapter 1

Introduction

Soft matter can be characterized as reacting with a strong mechanical deformation to an external force. Examples for such soft matter systems range from blood to surfactant micelles and include milk, mayonnaise, ice cream and protein solutions [1, 2, 3, 4], making soft matter very common and even necessary for every day life. All substances in the examples above are composed of mesoscopic particles of a size ranging from $\sim 1\text{nm}$ to $1\mu\text{m}$ dispersed in a microscopic solvent (e.g. water) [1].

The cause of the large deformations observed in all of these soft matter systems, can be traced back to the elastic constants like the shear modulus [1, 5]

$$G \propto \frac{\epsilon}{a^3}; \quad (1.1)$$

here the interaction energy scale between particles of the substance in question is given by ϵ and the distance between these particles is given by a . At room temperature (i.e. $\sim 293\text{K}$) the interaction energy scale for (hard) atomic systems and soft matter systems equally ranges from $\sim 0.1\text{eV} < \epsilon < 10\text{eV}$ [1]. However as stated above, the size and typical distance of soft matter particles a_{soft} ranges from $1\text{nm} < a_{\text{soft}} < 1\mu\text{m}$, while the distance in atomic systems is in the order of $a_{\text{atomic}} \sim 0.1\text{nm}$. Using equation (1.1) this results in a shear modulus G for soft matter systems that is three to twelve orders of magnitude smaller than that of atomic systems, explaining the huge difference in mechanic properties between atomic and soft matter systems.

In experiments soft matter systems feature several advantages compared to atomic systems. Due to the larger size of the colloidal particles, they can be observed directly using optical methods like confocal microscopy or video microscopy [6, 7]. Moreover, unlike in atomic systems, the interaction between the colloidal particles can be easily tuned by changing the architecture of the colloids or by changing the properties of the solvent (e.g. different solvent, different salt concentration) [1, 8]. The present work focuses on two dimensional colloidal systems, where the mesoscopic colloidal particles interact via spherically symmetric potentials. Aside of permitting the particles to overlap at very small distances, these potentials are characterized by an attraction at small distances and a repulsion at longer distances, which compete with each other (competing interactions). Additionally the potentials used in this work take a microscopic solvent into account in an implicit way, which is done by integrating out the

solvents degrees of freedom (effective interaction, see chapter 2). While the attractive part of these potentials alone favors a bulk phase separation (at an appropriate temperature and density), the additional long range repulsion prevents the building of a single large high density domain and instead forces the system to build multiple, smaller high density domains (microphases) [9, 10, 11, 12]. Depending on the density, the microphases formed by systems with competing interactions have different shapes. In two dimensions the systems forms (i) spherical clusters of colloidal particles at low particle densities, (ii) stripes with alternating high and low colloid density at intermediate average density and (iii) spherical bubbles (inverted clusters) [9, 12, 13, 10, 14]. In three dimensions the sequence of microphases from low to high density is: clusters, cylinders, lammellae, inverse cylinders and bubbles [11, 10].

Systems featuring competing interactions are characterized by a high potential of self assembly into certain target structures, without the need of orientational interactions. These structures could be used for example in the creation of defect tolerant microelectronics [15, 9, 16]. However, the advances in optical lithography during the last decade already allow the production of structures in the order of 20nm and could make such a venture unfeasible.

The colloid interaction used in this work was originally introduced by Sear *et al.* in [9] to explain the behavior of silver nanoparticles at an air-water interface using computer simulations. Imperio and Reatto later computed energy, specific heat, structure functions and the phase diagram for a particular parameter set of this model potential, using Monte Carlo simulations [12]. Additionally they investigated the phase transition of this model from the bulk fluid phase to the microphases [17] as well the behavior of these microphases under the confinement of walls [18] and under shear [19]. Archer later confirmed in [20] that results from density functional theory (DFT) are *generally in good qualitative agreement* with the findings of Imperio and Reatto for bulk and confined systems [12, 18].

In this work the model potential introduced by Sear *et al.* [9] is investigated in two dimensional systems using Monte Carlo simulations as well as Ornstein-Zernike based integral equations. A more general set of potential parameters than the one used in the work of Imperio and Reatto is considered here, in order to distinguish the potential parameter sets of the model that do feature microphase formation, from those that lead to a bulk phase separation into a high and a low density fluid phase. We also study the dynamics of the clusters and of the particles in the cluster phase at low temperatures to find out under which conditions the particles and clusters freeze. Finally the effect of a porous matrix on systems featuring short range attractive, long range repulsive interactions, so-called quenched-annealed (QA) systems, is investigated. Quenched-annealed systems are of scientific relevance not only because they often show a behavior not observed in the bulk [13], but also because they can model a large variety of materials that are of relevance in technology like catalysts, filters and oil shale [13, 21, 22, 23, 24].

The present work is organized as follows:

Chapter 2 introduces the potential of competing interactions used in the present work in more detail and describes the most important features of the systems investigated here.

Chapter 3 gives an overview over those sections of statistical mechanics and thermodynamics that are relevant for this work and introduces the most important observables.

Chapter 4 describes the methods used in this work: Monte Carlo simulations in **section 4.1**, the Ornstein-Zernike based integral equations including the closure relations as well as the associated two dimensional solving algorithm in **section 4.2** and the methods for identification and tracking of particle clusters in **section 4.3**.

Chapter 5 presents the results of this work. Sets of potential parameters featuring microphase formation are identified in **section 5.1**, while **section 5.2** summarizes static and dynamic properties of the clusters (identified via the algorithms of section 4.3). **Section 5.3** presents results of quenched-annealed systems with competing interaction.

Chapter 6 gives a summary of the results of this work as well as concluding remarks and suggestions for future research.

Chapter 2

Model

In this work we investigate colloidal suspensions with competing interactions in two dimensions. The restriction to two spacial dimensions is realized both in nature as well as in experiment by confining the colloidal particles to an interface between two fluids (e.g. an air-water interface). Examples for colloidal suspensions with competing interactions have already been mentioned in chapter 1 and give an overview of the variety of different systems addressed in this work.

Colloidal suspensions consist (at least) of two components: One is given by the small solvent molecules (e.g. water) in which the second component, the bigger molecules of the solute, is embedded in. Usually the colloidal molecules (with diameters of $\approx 1nm - 1\mu m$) are orders of magnitude larger than the molecules of the solvent (with diameters of $\approx 0.1nm$). Because the kinetic energy of the particles is proportional to the thermal energy ($E_{\text{kin}} = mv^2/2 \propto E_{\text{therm}} = k_B T \Rightarrow v \propto \sqrt{2k_B T/m}$), the velocity of the thermal motion of the solvent particles is by orders of magnitude higher than that of the solute (colloidal) particles [25].

In the present work we are not interested in the properties of the solvent but only in the properties of the colloidal solute. Fortunately it is possible to integrate out degrees of freedom that are of no relevance, like the ones of the solvent and also the internal degrees of freedom of the colloids [25]. This so-called coarse-graining procedure results in interactions between the centers of mass of the individual colloids, the presence of the solvent is considered in an implicit form. The interaction between the centers of mass of the colloids obtained in that way are called effective interaction [1, 26]. (The depletive attraction mentioned for some of the systems in chapter 1 stems from the presence of the solvent or, to be more precise, from the absence of solvent molecules between two solute molecules at close distance). In the general case of effective interactions multi-body terms are present so the superposition principle is not valid for them anymore. We assume that the effective interactions between the colloidal particles of our model system can reasonably well be approximated by pair potentials with sufficient accuracy. As a model pair interaction we selected the potential first introduced by R. P. Sear *et al.* [9] and further investigated by A. Imperio and L. Reatto [12, 17, 18, 19]. As a representative of the class systems with competing interactions (e.g. short ranged attractive - long range repulsive potentials) it consists of a hard core [$\Phi_{\text{hc}}(r)$], an attractive well [$\Phi_{\text{a}}(r)$], as well as a repulsive tail [$\Phi_{\text{r}}(r)$] (see equation (2.4)).

The hard core part takes into account that the cores of the colloids do not overlap (see equation (2.1)). The short range attraction as well as the long range repulsion are modeled using exponential functions (Kac-potentials [27]) (see equations (2.2) and (2.3)).

$$\Phi_{\text{hc}}(r) = \begin{cases} \infty & r \leq \sigma \\ 0 & r > \sigma \end{cases} \quad (2.1)$$

$$\Phi_{\text{a}}(r) = -\epsilon_{\text{a}} \frac{\sigma^2}{R_{\text{a}}^2} \exp\left(-\frac{r}{R_{\text{a}}}\right) \quad (2.2)$$

$$\Phi_{\text{r}}(r) = +\epsilon_{\text{r}} \frac{\sigma^2}{R_{\text{r}}^2} \exp\left(-\frac{r}{R_{\text{r}}}\right) \quad (2.3)$$

In view of the pioneering work on this system by A. Imperio and L. Reatto we will refer to this specific potential as "Imperio-Reatto potential" (Φ_{IR}) henceforth:

$$\Phi_{\text{IR}}(r) = \Phi_{\text{hc}}(r) + \Phi_{\text{a}}(r) + \Phi_{\text{r}}(r), \quad (2.4)$$

$$\Phi_{\text{IR}}(r) = \begin{cases} \infty & r \leq \sigma \\ -\epsilon_{\text{a}} \frac{\sigma^2}{R_{\text{a}}^2} \exp\left(-\frac{r}{R_{\text{a}}}\right) + \epsilon_{\text{r}} \frac{\sigma^2}{R_{\text{r}}^2} \exp\left(-\frac{r}{R_{\text{r}}}\right) & r > \sigma \end{cases} \quad (2.5)$$

σ is the diameter of the hard core interaction, and ϵ_{a} (ϵ_{r}) and R_{a} (R_{r}) representing the strength and range of the attraction (repulsion), respectively. By setting $R_{\text{r}} < R_{\text{a}}$ it is even possible to shift the repulsion to lower distances than the attraction. Figure 2.1 shows the Imperio-Reatto model with potential parameters $R_{\text{a}} = 1\sigma$, $R_{\text{r}} = 2\sigma$ and $\epsilon_{\text{a}} = \epsilon_{\text{r}} = 4e/(4 - \sqrt{e})$ also used in Refs [9, 12, 17, 18, 19].

The most prominent effect of systems with short range attractive and long range repulsive interactions is the fact that under suitable external conditions (temperature, density) they form microphases, emergence of these strongly inhomogeneous phases is surprising, since the potential is spherical symmetric. However already Sear *et al.* [9] gave the following explanation for formation of microphases in systems with competing interactions:

- The attractive part of the potential leads to a decrease in energy for high densities, since the particles feel their mutual attraction at small separation, which fosters the formation of high density bulk phases and the classic liquid-gas phase separation scenario.
- However when in addition a long ranged repulsion comes into play the energetic argument mentioned above is only valid for bulk phases of small extent where particles located at the outer layer of the phase do not feel the repulsion arising from particles on the outer layer of the opposite side. As a result the high density phase is split up into multiple areas of high density (e.g. clusters) which are separated far enough from each other to minimize the increase in energy due to the repulsive part of the potential.

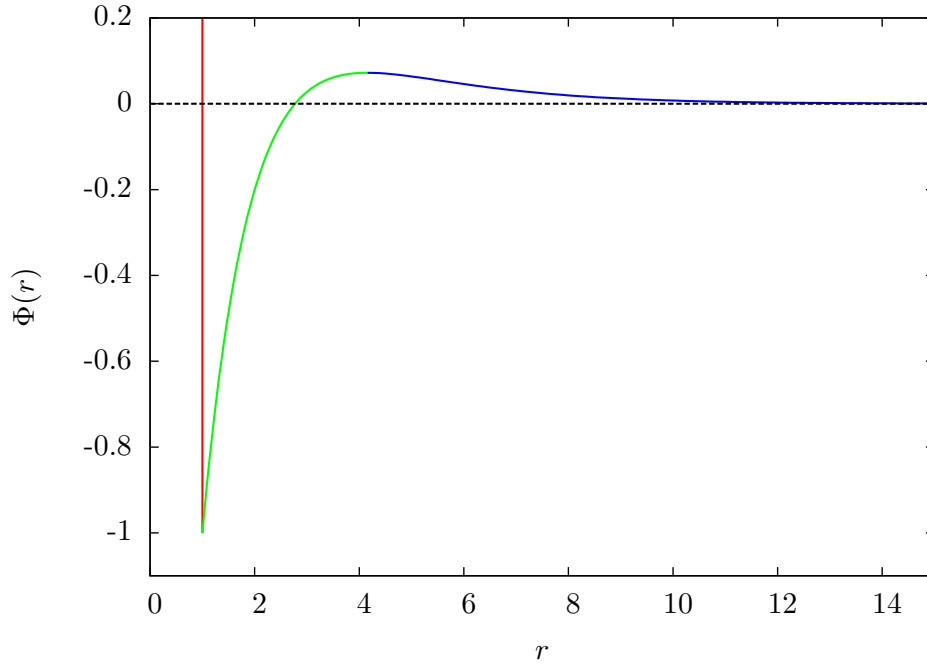


Figure 2.1: Imperio-Reatto potential with potential parameters $R_a = 1\sigma$, $R_r = 2\sigma$ and $\epsilon_a = \epsilon_r = 4e/(4 - \sqrt{e})$ also used in [9, 12, 17, 18, 19], red - hard sphere core, green - short range attractive part, blue - long range repulsive part, dashed black line - guide to the eye for $\Phi(r) = 0$

In two dimensions an increasing density leads to the emergence of the following microphases: clusters, stripes and bubbles (inverse clusters) (see figure 2.2). In three dimensions the emerging microphases change with increasing density from clusters to cylinders to lamellae to inverse cylinders to bubbles (inverse clusters) [28].

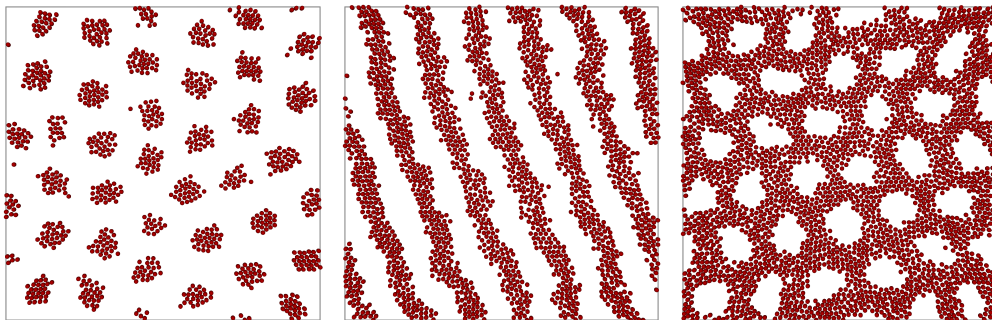


Figure 2.2: Simulation snapshots of the three different microphases encountered in the Imperio-Reatto model in 2D for different densities (from left to right $\rho = 0.20$, $\rho = 0.40$ and $\rho = 0.60$; $T = 0.40$ for all three snapshots).

Chapter 3

Theory - Statistical mechanics

This chapter presents the classical statistical mechanic principles on which the simulations (see section 4.1) and integral equation calculations (see section 4.2) of the present thesis are based on.

For this introduction into statistical mechanics we will follow chapter 2 of reference [27] and use the notation therein whenever possible.

Since only two-dimensional systems are investigated in this thesis, equations are presented for the two-dimensional case rather than for the three-dimensional case, whenever there is a dependence on the dimensionality. Keep in mind that the volume in these equations, while still denoted as V , represents an area in two dimensions.

3.1 General Concepts

The state of a classical, isolated, two-dimensional system of N spherical particles of mass m in an area V is completely defined by the $2N$ coordinates $\mathbf{r}^N \equiv \mathbf{r}_1, \mathbf{r}_2, \dots, \mathbf{r}_N$ and the $2N$ momenta $\mathbf{p}^N \equiv \mathbf{p}_1, \mathbf{p}_2, \dots, \mathbf{p}_N$ of these particles. The set $(\mathbf{r}^N, \mathbf{p}^N)$ containing the values of all these $4N$ variables is called phase-point and describes the state of the system at a certain time t . The $4N$ -dimensional space of all possible phase-points is called phase-space and will be denoted by Γ further on. Phase-space is the union of the configuration-space Γ_{conf} and the space of the momentum variables Γ_{mom}

$$\Gamma = \Gamma_{\text{conf}} \times \Gamma_{\text{mom}} \quad (3.1)$$

For reasons of simplicity we assume that the particles of the system are located in a box of side length L so $0 \leq r_i^{x/y} \leq L$ and the two dimensional volume $V = L^2$. The momenta on the other hand are not restricted by any external bounds so $-\infty \leq p_i^{x/y} \leq \infty$. The Hamiltonian \mathcal{H} of such a N -particle system is given by

$$\mathcal{H}(\mathbf{r}^N, \mathbf{p}^N) = \mathcal{K}_N(\mathbf{p}^N) + \mathcal{U}_N(\mathbf{r}^N) + \mathcal{W}(\mathbf{r}^N) \quad (3.2)$$

with $\mathcal{K}_N(\mathbf{p}^N)$ being the kinetic energy ($\mathcal{K}_N(\mathbf{p}^N) = \sum_{i=1}^N \frac{|\mathbf{p}_i|^2}{2m}$), $\mathcal{U}_N(\mathbf{r}^N)$ the potential energy due to particle-particle interactions and $\mathcal{W}(\mathbf{r}^N)$ the potential energy due to external fields.

The time-dependence of the phase-point along its trajectory within phase-space, is then governed by Hamilton's equations of motion

$$\dot{\mathbf{r}}_i = \frac{\partial \mathcal{H}}{\partial \mathbf{p}_i} \quad (3.3)$$

$$\dot{\mathbf{p}}_i = -\frac{\partial \mathcal{H}}{\partial \mathbf{r}_i}, \quad (3.4)$$

which can be solved given the $4N$ initial conditions of coordinates and momenta. Since the solution of Hamilton's equations of motion for specific initial conditions, is unique, the phase-space trajectory of the system cannot intersect itself, moreover two phase-space trajectories of the same Hamiltonian, solved with different initial conditions, cannot intersect; however they may come arbitrarily close to one another. The distribution of phase-points, for a system in equilibrium, along such a phase-space trajectory of infinite length is given by the equilibrium phase-space probability $f^{[N]}(\mathbf{r}^N, \mathbf{p}^N)$, which is defined as the probability that a phase-point of the system can be found in a (hyper)cube of volume $d\mathbf{r}^N \times d\mathbf{p}^N$ around the phase-point $(\mathbf{r}^N, \mathbf{p}^N)$. The equilibrium phase-space probability is normalized so that

$$\iint_{\Gamma} f^{[N]}(\mathbf{r}^N, \mathbf{p}^N) d\mathbf{r}^N d\mathbf{p}^N = 1. \quad (3.5)$$

Considering only a subset of n -particles of the N -particles system, with

$$\begin{aligned} \mathbf{r}^n &\equiv \mathbf{r}_1, \mathbf{r}_2, \dots, \mathbf{r}_n & \mathbf{p}^n &\equiv \mathbf{p}_1, \mathbf{p}_2, \dots, \mathbf{p}_n \\ \mathbf{r}^{(N-n)} &\equiv \mathbf{r}_{n+1}, \mathbf{r}_{n+2}, \dots, \mathbf{r}_N & \mathbf{p}^{(N-n)} &\equiv \mathbf{p}_{n+1}, \mathbf{p}_{n+2}, \dots, \mathbf{p}_N \end{aligned} \quad (3.6)$$

the equilibrium phase-space distribution function of this subset $f^{(n)}(\mathbf{r}^n, \mathbf{p}^n)$ can be computed by integration over the coordinates and momenta of the $(N - n)$ other particles

$$f^{(n)}(\mathbf{r}^n, \mathbf{p}^n) = \frac{N!}{(N-n)!} \iint f^{[N]}(\mathbf{r}^n, \mathbf{p}^n) d\mathbf{r}^{(N-n)} d\mathbf{p}^{(N-n)} \quad (3.7)$$

with $\frac{N!}{(n-n)!}$ being the combinatorial factor of choosing a subset of n particles out of a set of N indistinguishable particles. The resulting equilibrium phase-space distribution function $f^{(n)}(\mathbf{r}^n, \mathbf{p}^n)$ for the subset of n -particles is then called reduced equilibrium phase-space distribution function.

3.2 Time and Ensemble averages

Statistical mechanics offers two different ways to compute averages, namely time averages $\langle \dots \rangle_t$ and ensemble averages $\langle \dots \rangle_e$. The basic ideas of both averaging methods and the differences between them will be explained in the present section.

3.2.1 Time averages

If the initial positions and momenta of all particles of a system are known, the positions and momenta of the particles can, in principle, be computed for any given time t by solving Newton's equations of motion

$$m\ddot{\mathbf{r}}_i = \mathbf{F}_i = -\nabla_i \mathcal{U}_N(\mathbf{r}_i), \quad (3.8)$$

with \mathbf{F}_i being the total force acting on particle i .

Knowing the solution to Newton's equations of motion for the system, the time average of any mechanical property $B(\mathbf{r}^N, \mathbf{p}^N)$ can be obtained in a straight forward way as follows

$$\langle B \rangle_t = \lim_{\tau \rightarrow \infty} \frac{1}{\tau} \int_0^\tau B[\mathbf{r}^N(t'), \mathbf{p}^N(t')] dt'. \quad (3.9)$$

This approach is used in Molecular-Dynamics (MD) simulations to obtain averages of the observables of interest.

3.2.2 Ensemble averages

Ensemble averages, in contrast to time averages, are averages over a large number of possible representations of the system, where these representations of the system are characterized by the same macroscopic parameters (like e.g. the same particle number N , volume V and energy E), but occupy different microscopic states (the positions and momenta of the individual particles are different in all the system representations). The set of all the representations specified by the same macroscopic parameters is called an ensemble. Ensembles can be distinguished into types according to the set of macroscopic parameters, that are kept constant, throughout the constituting representations of the system. (See section 3.3 for details about the ensemble types used in the present work.) For an ensemble characterized by constant N, V, E (microcanonic ensemble) the ensemble average of an observable $B(\mathbf{r}^N, \mathbf{p}^N)$ can be calculated by

$$\langle B \rangle_e = \iint_{\Gamma} B(\mathbf{r}^N, \mathbf{p}^N) f^{[N]}(\mathbf{r}^N, \mathbf{p}^N) d\mathbf{r}^N d\mathbf{p}^N. \quad (3.10)$$

Where the equilibrium phase-space probability $f^{[N]}$ is given by

$$f^{[N]}(\mathbf{r}^N, \mathbf{p}^N) = C\delta(\mathcal{H} - E), \quad (3.11)$$

and C is a constant, so that the phase-space probability is normalized

$$\iint_{\Gamma} f^{[N]}(\mathbf{r}^N, \mathbf{p}^N) d\mathbf{r}^N d\mathbf{p}^N = 1. \quad (3.12)$$

Ensemble averaging is used in Monte-Carlo (MC) simulations. A detailed description of Monte Carlo simulations and the Monte Carlo methods used in the present work is given in section 4.1.

3.3 Types of Ensembles

The different types of ensembles can be characterized by the macroscopic thermodynamic parameters that are kept constant, which also characterizes, in some sense, the interaction of the systems with its environment (e.g. a heat bath).

The basic features of microcanonic ensembles, introduced above, as well as the basic features of all other ensemble types relevant in this work, namely the canonic ensembles (constant N, V, T) and the grand canonic ensembles (constant μ, V, T) are given in the following sections.

3.3.1 Microcanonic ensembles (NVE -ensembles)

Using the microcanonic ensemble type the systems are characterized by constant particle number N , volume V and energy E . Since all these values are constant the system can be considered as isolated from its environment.

The equilibrium phase-space probability density of the microcanonic ensembles is given by (see also equation (3.11))

$$f^{[N]}(\mathbf{r}^N, \mathbf{p}^N) = C\delta(\mathcal{H} - E). \quad (3.13)$$

The constant C is defined so that the equilibrium phase-space probability density is normalized (see also equation (3.12))

$$\iint_{\Gamma} f^{[N]}(\mathbf{r}^N, \mathbf{p}^N) d\mathbf{r}^N d\mathbf{p}^N = 1. \quad (3.14)$$

A microcanonic ensemble is represented by a set of phase-points located on the $(4N-1)$ -dimensional hypersurface of constant energy within the $4N$ dimensional phase-space. Without external potential $\mathcal{W}(\mathbf{r}^N)$ in the Hamiltonian \mathcal{H} (see equation (3.2)), this is the ensemble of Molecular dynamics simulations, since the total energy is conserved when solving Newtons equations of motion for such a system.

3.3.2 Canonic ensembles (NVT -ensembles)

Canonic ensembles share the same value of particle number N , volume V and temperature T . In contrast to microcanonic ensembles the energy is not constant. Systems described within the canonic ensemble are therefor in contact with a heat bath and constantly exchange energy with that heat bath. Thus the total energy E fluctuates around its average value.

The equilibrium phase-space probability density of canonic ensembles is given by

$$f^{[N]}(\mathbf{r}^N, \mathbf{p}^N) = \frac{1}{h^{2N} N!} \frac{\exp(-\beta\mathcal{H})}{Q_N}, \quad (3.15)$$

with the canonic partition function

$$Q_N = \frac{1}{h^{2N} N!} \iint_{\Gamma} \exp(-\beta\mathcal{H}) d\mathbf{r}^N d\mathbf{p}^N. \quad (3.16)$$

In the above equations h denotes Planck's constant. Introducing the factor h^{2N} ensures that the canonic phase-space probability density $f^{[N]}$ as well as the canonic partition function Q_N remain dimensionless, additionally they comply with their quantum statistical mechanics counterparts. The $N!$ factor corrects for the counting of indistinguishable particles. As in the microcanonic case, the canonic phase-space probability density is normalized

$$\iint_{\Gamma} f^{[N]}(\mathbf{r}^N, \mathbf{p}^N) d\mathbf{r}^N d\mathbf{p}^N = 1. \quad (3.17)$$

Combining equation (3.10) and equation (3.15) results in

$$\langle B \rangle_e = \frac{\int d\mathbf{p}^N d\mathbf{r}^N B(\mathbf{p}^N, \mathbf{r}^N) \exp[-\beta\mathcal{H}(\mathbf{p}^N, \mathbf{r}^N)]}{\int d\mathbf{p}^N d\mathbf{r}^N \exp[-\beta\mathcal{H}(\mathbf{p}^N, \mathbf{r}^N)]}, \quad (3.18)$$

the equation to compute averages of observables in canonical ensembles

Systems described within canonic ensembles are treated by the Monte Carlo simulations of the present work (see section 4.1).

The thermodynamic potential related to the canonical ensemble is the Helmholtz free energy

$$F(T, V, N) = U - TS, \quad (3.19)$$

with U and S denoting the total energy and entropy, respectively. The connection of thermodynamics and statistical mechanics is realized via

$$F = -k_B T \ln Q_N. \quad (3.20)$$

The total differential of the Helmholtz free energy can be written as

$$dF = -S dT - P dV + \mu dN. \quad (3.21)$$

While the connection to other thermodynamic variables is provided by

$$S = - \left(\frac{\partial F}{\partial T} \right)_{V, N} \quad (3.22)$$

$$P = - \left(\frac{\partial F}{\partial V} \right)_{T, N} \quad (3.23)$$

$$\mu = \left(\frac{\partial F}{\partial N} \right)_{T, V} \quad (3.24)$$

$$U = F + TS = \left(\frac{\partial (F/T)}{\partial (1/T)} \right)_{V, N}. \quad (3.25)$$

The integration of the momenta in equation (3.16) can be carried out analytically for Hamiltonians \mathcal{H} that separate into a kinetic and a potential part $\mathcal{H} = \mathcal{K} + \mathcal{U}$, with

$\mathcal{K} = \sum_{i=1}^N \frac{|\mathbf{p}_i|^2}{2m}$. Each of the $2N$ momenta yields a factor of $(2\pi mk_B T)^{1/2}$, thus and the canonical partition function can be written as

$$Q_N = \frac{1}{N!} \frac{Z_N}{\Lambda^{2N}}, \quad (3.26)$$

with the DeBroglie thermal wavelength Λ defined as

$$\Lambda = \sqrt{\frac{h^2}{2\pi k_B T m}} \quad (3.27)$$

and the configurational part of the canonic partition function being

$$Z_N = \int_{\Gamma_{\text{conf}}} \exp(-\beta \mathcal{U}_N) \mathbf{dr}^N. \quad (3.28)$$

For an ideal gas there is no particle-particle interaction and therefore $\mathcal{U}_N = 0$. The configurational part of the canonic partition function is then easily evaluated to

$$Z_N^{\text{id}} = \int_{\Gamma_{\text{conf}}} \dots \int \mathbf{dr}_1 \dots \mathbf{dr}_N = V^N \quad (3.29)$$

and the entire canonic partition function can be written as

$$Q_N^{\text{id}} = \frac{1}{N!} \frac{V^N}{\Lambda^{2N}}. \quad (3.30)$$

The Helmholtz free energy for the ideal gas can easily be derived by inserting equation (3.30) into equation (3.20) and using the Sterling approximation for $N!$

$$\ln N! = N \ln N - N + \mathcal{O}(\ln N). \quad (3.31)$$

$$\begin{aligned} F^{\text{id}} &= -k_B T \ln Q_N^{\text{id}} \\ &= -k_B T \ln \left(\frac{1}{N!} \frac{V^N}{\Lambda^{2N}} \right) \\ &= N k_B T \left[\ln \left(\frac{\Lambda^2}{V} (N!)^{\frac{1}{N}} \right) \right] \\ &= N k_B T \ln \left(\frac{\Lambda^2}{V} \right) + N k_B T \ln(N) - N k_B T \\ &= N k_B T [\ln(\Lambda^2 \rho) - 1] \end{aligned} \quad (3.32)$$

$$\frac{F^{\text{id}}}{N} = k_B T [\ln(\Lambda^2 \rho) - 1] \quad (3.33)$$

Inserting F^{id} into equation (3.24) gives the chemical potential for the ideal gas

$$\mu^{\text{id}} = k_B T \ln(\Lambda^2 \rho). \quad (3.34)$$

The canonical partition function can be expressed in terms of the canonic partition function for the ideal gas using equations (3.26) and (3.30) leading to

$$Q_N = Q_N^{\text{id}} \frac{Z_N}{V^N}. \quad (3.35)$$

Since the Helmholtz free energy is the logarithm of the canonic partition function (see equation (3.16)) it separates into an ideal and an excess part

$$F = F^{\text{id}} + F^{\text{ex}}, \quad (3.36)$$

with the ideal part defined by equation (3.33) and excess part given by

$$F^{\text{ex}} = -k_{\text{B}}T \ln \left(\frac{Z_N}{V^N} \right). \quad (3.37)$$

The total energy U can be separated into an ideal and excess part as well leading to

$$U = U^{\text{id}} + U^{\text{ex}} \quad (3.38)$$

$$U^{\text{id}} = Nk_{\text{B}}T \quad (3.39)$$

$$U^{\text{ex}} = \langle \mathcal{U}_N \rangle = \frac{1}{Z_N} \int_{\Gamma_{\text{conf}}} \mathcal{U}_N \exp(-\beta \mathcal{U}_N) d\mathbf{r}^N. \quad (3.40)$$

3.3.3 Grandcanonic ensembles (μVT -ensembles)

A system characterized by a grand canonic ensemble not only exchanges energy with a reservoir, but also particles. Therefore the particle number in such a system is not constant and fluctuates around an average value as well as the energy. The constant parameters in such a system are the chemical potential μ the volume V and the temperature T .

Since the particle number is not constant the phase-space of a grand canonic ensemble is given by the union of all the phase-spaces of canonic ensembles of the same volume V with particle numbers N ranging from zero to infinity.

The equilibrium phase-space probability density of grand canonic ensembles is given by

$$f(\mathbf{r}^N, \mathbf{p}^N; N) = \frac{\exp[-\beta(\mathcal{H} - N\mu)]}{\Xi}, \quad (3.41)$$

with the grand canonic partition function

$$\Xi = \sum_{N=0}^{\infty} \frac{\exp(N\beta\mu)}{h^{2N} N!} \iint_{\Gamma_N} \exp(-\beta\mathcal{H}) d\mathbf{r}^N d\mathbf{p}^N = \sum_{N=0}^{\infty} \frac{z^N}{N!} Z_N, \quad (3.42)$$

with Γ_N being the phase-space of the system with N particles. The activity z , used to express the grand canonic partition function above, is defined as

$$z = \frac{\exp(\beta\mu)}{\Lambda^2}, \quad (3.43)$$

while Z_N represents the configurational integral for particle number N (see equation (3.28)).

For an ideal gas the activity z is given by

$$z^{\text{id}} = \rho, \quad (3.44)$$

which can easily be seen by combining equations (3.34) and (3.43), while the grand canonic partition function for the ideal gas is given by

$$\begin{aligned} \Xi^{\text{id}} &= \sum_{N=0}^{\infty} \frac{(z^{\text{id}})^N}{N!} Z_N^{\text{id}} \\ &= \sum_{N=0}^{\infty} \frac{\rho^N V^N}{N!} \\ &= \exp(\rho V) \end{aligned} \quad (3.45)$$

As for the microcanonic and canonic ensembles the distribution function of the grand canonic ensembles is normalized

$$\sum_{N=0}^{\infty} \frac{1}{h^{2N} N!} \iint_{\Gamma_N} f(\mathbf{r}^N, \mathbf{p}^N; N) d\mathbf{r}^N d\mathbf{p}^N = 1. \quad (3.46)$$

Taking the variable particle number into account the grand canonic ensemble average of the observable $B(\mathbf{r}^N, \mathbf{p}^N)$ is given by

$$\langle B \rangle_e = \sum_{N=0}^{\infty} \frac{1}{h^{2N} N!} \iint_{\Gamma_N} B(\mathbf{r}^N, \mathbf{p}^N) f(\mathbf{r}^N, \mathbf{p}^N; N) d\mathbf{r}^N d\mathbf{p}^N. \quad (3.47)$$

The thermodynamic potential Ω is called grand potential. It is related to the Helmholtz free energy via

$$\Omega = F - \mu N. \quad (3.48)$$

Using the relations $U = TS - PV + \mu N$ and $F = U - TS$ this results in

$$\Omega = -PV. \quad (3.49)$$

The grand potential can also be expressed via the grand canonic partition function

$$\Omega = -k_B T \ln \Xi. \quad (3.50)$$

The total differential of the grand potential is given by

$$d\Omega = -SdT - PdV - Nd\mu, \quad (3.51)$$

Which results in the following differential expressions for entropy S , pressure P and particle number N

$$S = - \left(\frac{\partial \Omega}{\partial T} \right)_{V, \mu} \quad (3.52)$$

$$P = - \left(\frac{\partial \Omega}{\partial V} \right)_{T, \mu} \quad (3.53)$$

$$N = - \left(\frac{\partial \Omega}{\partial \mu} \right)_{T, V}. \quad (3.54)$$

Using the ideal gas values for the configurational integral $Z_N^{\text{id}} = V^N$ for particle number N and for the activity $z^{\text{id}} = \rho$ (equations (3.29) and (3.44)), the grand partition function for the ideal gas can be expressed as

$$\Xi^{\text{id}} = \sum_{N=1}^{\infty} \frac{\rho^N V^N}{N!} = \exp(\rho V). \quad (3.55)$$

The probability $p(N)$ that the equilibrated system consists of exactly N particles is given by

$$p(N) = \frac{1}{h^{2N} N!} \iint_{\Gamma_N} f(\mathbf{r}^N, \mathbf{p}^N; N) d\mathbf{r}^N d\mathbf{p}^N = \frac{1}{\Xi} \frac{z^N}{N!} Z_N \quad (3.56)$$

with $f(\mathbf{r}^N, \mathbf{p}^N; N)$ being the equilibrium grand canonic phase-space probability density. Thus the average particle number of the system can be written as

$$\langle N \rangle = \sum_{N=0}^{\infty} N p(N) = \frac{1}{\Xi} \sum_{N=0}^{\infty} N \frac{z^N}{N!} Z_N = \frac{\partial \ln \Xi}{\partial \ln z} \quad (3.57)$$

which is just a different formulation for equation (3.54). Taking the derivative of the above equation with respect to $\ln z$ results in

$$\begin{aligned} \frac{\partial \langle N \rangle}{\partial \ln z} &= z \frac{\partial}{\partial z} \left(\frac{1}{\Xi} \sum_{N=0}^{\infty} N \frac{z^N}{N!} Z_N \right) \\ &= \frac{1}{\Xi} \sum_{N=0}^{\infty} N^2 \frac{z^N}{N!} Z_N - \left(\frac{1}{\Xi} \sum_{N=0}^{\infty} N \frac{z^N}{N!} Z_N \right)^2 \\ &= \langle N^2 \rangle - \langle N \rangle^2 \\ &\equiv \langle (\Delta N)^2 \rangle \end{aligned} \quad (3.58)$$

with $\langle (\Delta N)^2 \rangle$ being a measure for the particle fluctuation in the grand canonic system. Using the definition of the activity equation (3.43) the derivative with respect to $\ln z$ above can be rewritten into an derivative with respect to μ resulting in

$$k_{\text{B}}T \frac{\partial \langle N \rangle}{\partial \mu} = \langle (\Delta N)^2 \rangle \quad (3.59)$$

Since $\frac{\partial \langle N \rangle}{\partial \mu}$ is an extensive quantity $\langle (\Delta N)^2 \rangle$ must be an extensive quantity as well. Therefor the root-mean-square deviation of the particle number $(\langle (\Delta N)^2 \rangle)^{1/2} / \langle N \rangle$ decreases when increasing the system size, while keeping all intensive parameters constant and ultimately going to zero in the thermodynamic limit ($N \rightarrow \infty$, $V \rightarrow \infty$ while $N/V = \rho = \text{const}$). Because of the vanishing root-mean-square deviation of the particle number in the thermodynamic limit, the thermodynamic variable N can be identified with its average value $\langle N \rangle$ within that limit.

Compressibility

Since the Helmholtz free energy is an extensive quantity in the thermodynamic limit it can be written as

$$F = N\phi(\rho, T). \quad (3.60)$$

in that regime with $\phi(\rho, T)$ being the free energy per particle. Expressing equations (3.23) and (3.24) in terms of the free energy per particle ϕ results in

$$\begin{aligned} \mu &= \left(\frac{\partial F}{\partial N} \right)_{V,T} & P &= - \left(\frac{\partial F}{\partial V} \right)_{T,N} \\ &= \left(\frac{\partial (N\phi(\rho, T))}{\partial N} \right)_{V,T} & &= - \left(\frac{\partial (N\phi(\rho, T))}{\partial V} \right)_{T,N} \\ &= \phi(\rho, T) + N \left(\frac{\partial \phi(\rho, T)}{\partial \rho} \right)_T \frac{\partial \rho}{\partial N} & &= -N \left(\frac{\partial \phi(\rho, T)}{\partial \rho} \right)_T \left(\frac{\partial \rho}{\partial V} \right) \\ &= \phi(\rho, T) + \rho \left(\frac{\partial \phi(\rho, T)}{\partial \rho} \right)_T & &= \rho^2 \left(\frac{\partial \phi(\rho, T)}{\partial \rho} \right)_T. \end{aligned} \quad (3.61)$$

Taking the derivative with respect to ρ of both of these results

$$\left(\frac{\partial \mu}{\partial \rho} \right)_T = 2 \left(\frac{\partial \phi}{\partial \rho} \right)_T + \rho \left(\frac{\partial^2 \phi}{\partial \rho^2} \right)_T \quad \left(\frac{\partial P}{\partial \rho} \right)_T = 2\rho \left(\frac{\partial \phi}{\partial \rho} \right)_T + \rho^2 \left(\frac{\partial^2 \phi}{\partial \rho^2} \right)_T \quad (3.62)$$

one can easily see that

$$\left(\frac{\partial P}{\partial \rho} \right)_T = \rho \left(\frac{\partial \mu}{\partial \rho} \right)_T. \quad (3.63)$$

The isothermal compressibility χ_T is defined as

$$\chi_T = -\frac{1}{V} \left(\frac{\partial V}{\partial P} \right)_T. \quad (3.64)$$

From that definition follows

$$\left(\frac{\partial P}{\partial \rho}\right)_T = -\frac{V^2}{N} \left(\frac{\partial P}{\partial V}\right)_{N,T} = \frac{1}{\rho \chi_T} \quad (3.65)$$

and by using the equality equation (3.63)

$$\begin{aligned} \frac{1}{\rho \chi_T} &= \left(\frac{\partial P}{\partial \rho}\right)_T \\ &= \rho \left(\frac{\partial \mu}{\partial \rho}\right)_T \\ &= \rho \left(\frac{\partial \mu}{\partial N}\right)_{V,T} \left(\frac{\partial N}{\partial \rho}\right)_T \\ &= N \left(\frac{\partial \mu}{\partial N}\right)_{V,T} \end{aligned} \quad (3.66)$$

Which can be rewritten to

$$\rho k_B T \chi_T = \frac{\langle (\Delta N)^2 \rangle}{\langle N \rangle} \quad (3.67)$$

by using equation (3.59) and expresses the isothermal compressibility χ_T in terms of particle fluctuations in a grand canonic ensemble. Equation (3.67) can be used to compute the isothermal compressibility in grand canonic Monte Carlo simulations.

Widom formula

Applying equation (3.24) for the excess parts of chemical potential and Helmholtz free energy and replacing the differential by a difference in the thermodynamic limit results in

$$\mu^{\text{ex}} = \left(\frac{\partial F}{\partial N}\right)_{T,V} \approx F^{\text{ex}}(N+1, V, T) - F^{\text{ex}}(N, V, T). \quad (3.68)$$

Which can be written as

$$\mu^{\text{ex}} = k_B T \ln \frac{V Z_N}{Z_{N+1}}. \quad (3.69)$$

using equation (3.37) to express the excess part of the free energy in terms of the configurational integrals (Z_N , Z_{N+1}) for systems containing N and $N+1$ particles. Assuming that the total potential energy of the $(N+1)$ -particle system \mathcal{U}_{N+1} can be written in terms of the total potential energy of the (N) -particle system \mathcal{U}_N as

$$\mathcal{U}_{N+1}(\mathbf{r}^{N+1}) = \mathcal{U}_N(\mathbf{r}^N) + \epsilon \quad (3.70)$$

the ratio of the configurational integrals Z_{N+1}/Z_N becomes

$$\begin{aligned}
\frac{Z_{N+1}}{Z_N} &= \frac{\int \exp[-\beta\mathcal{U}_{N+1}(\mathbf{r}^{N+1})] d\mathbf{r}^{N+1}}{\int \exp[-\beta\mathcal{U}_N(\mathbf{r}^N)] d\mathbf{r}^N} \\
&= \frac{V \int \exp(-\beta\epsilon) \exp(-\beta\mathcal{U}_N(\mathbf{r}^N)) d\mathbf{r}^N}{\int \exp(-\beta\mathcal{U}_N(\mathbf{r}^N)) d\mathbf{r}^N} \\
&= V \langle \exp(-\beta\epsilon) \rangle.
\end{aligned} \tag{3.71}$$

Inserting that ratio of the configurational integrals into equation (3.69) results in the Widom formula

$$\mu^{\text{ex}} = -k_{\text{B}}T \ln \langle \exp(-\beta\epsilon) \rangle \tag{3.72}$$

The Widom formula expresses the excess chemical potential μ^{ex} as the canonic ensemble average of the energy cost ϵ of inserting an additional particle (ghost particle) to the system.

3.4 Static Structure

For a system that is not subject to an external field the Hamiltonian can be written as $\mathcal{H} = \mathcal{K}_N + \mathcal{U}_N$, where the kinetic energy is the sum of independent terms $\mathcal{K}_N = \sum_{i=1}^N \frac{|\mathbf{p}_i|^2}{2m}$. It can be seen from its defining equation (3.7), that the reduced equilibrium phase-space distribution function $f^{(n)}(\mathbf{r}^n, \mathbf{p}^n)$ for such a system can be factorized

$$f^{(n)}(\mathbf{r}^n, \mathbf{p}^n) = \rho_N^{(n)}(\mathbf{r}^N) f_M^{(n)}(\mathbf{p}^N) \tag{3.73}$$

with

$$f_M^{(n)}(\mathbf{p}^n) = \frac{1}{(2\pi m k_{\text{B}}T)^n} \exp\left(-\beta \sum_{i=0}^n \frac{|\mathbf{p}_i|^2}{2m}\right) \tag{3.74}$$

and

$$\begin{aligned}
\rho_N^{(n)}(\mathbf{r}^n) &= \frac{N!}{(N-n)!} \frac{1}{h^{2N} N! Q_N} \iint \exp(-\beta\mathcal{H}) d\mathbf{r}^{(N-n)} d\mathbf{p}^N \\
&= \frac{N!}{(N-n)!} \frac{1}{Z_N} \int \exp(-\beta\mathcal{U}_N) d\mathbf{r}^{(N-n)}
\end{aligned} \tag{3.75}$$

called n -particle density. $\rho_N^{(n)}(\mathbf{r}^N) d\mathbf{r}^n$ is the probability of finding particles within a volume element $d\mathbf{r}^n$ around the positions given by \mathbf{r}^n irrespective of the coordinates of the other $(N-n)$ particles and all particle momenta.

In the grand canonic ensemble the n -particle density $\rho^{(n)}$ can be written as

$$\begin{aligned}
\rho^{(n)}(\mathbf{r}^n) &= \sum_{N \geq n} p(N) \rho_N^{(n)} \\
&= \frac{1}{\Xi} \sum_{N \geq n} \frac{z^N}{(N-n)!} \int \exp(-\beta \mathcal{U}_N) d\mathbf{r}^{(N-n)}.
\end{aligned} \tag{3.76}$$

It can easily be seen from equations (3.75) and (3.76) that the n -particle density is normalized in canonic ensembles

$$\int \rho_N^{(n)}(\mathbf{r}^n) d\mathbf{r}^n = \frac{N!}{(N-n)!}, \tag{3.77}$$

as well as in grand canonic ensembles

$$\int \rho^{(n)}(\mathbf{r}^n) d\mathbf{r}^n = \left\langle \frac{N!}{(N-n)!} \right\rangle. \tag{3.78}$$

In case of the one-particle density this results in

$$\int \rho_N^{(1)}(\mathbf{r}) d\mathbf{r} = N \tag{3.79}$$

for for canonic ensembles and

$$\int \rho^{(1)}(\mathbf{r}) d\mathbf{r} = \langle N \rangle \tag{3.80}$$

for grand canonic ensembles.

In case of a uniform fluid the one-particle density therefor becomes

$$\rho_N^{(1)}(\mathbf{r}) = \frac{N}{V} = \rho \qquad \rho^{(1)}(\mathbf{r}) = \frac{\langle N \rangle}{V} = \rho. \tag{3.81}$$

For an ideal gas, the configurational part of the canonic partition function becomes $Z_N^{\text{id}} = V^N$ (see equation (3.29)). The two-particle density in canonic ensembles can therefore be written as

$$\begin{aligned}
\rho_N^{(2)} &= \frac{N!}{(N-2)!} \frac{1}{V^N} V^{(N-2)} \\
&= \frac{N(N-1)}{V^2} \\
&= \rho^2 \left(1 - \frac{1}{N} \right).
\end{aligned} \tag{3.82}$$

The fact that the two-particle density for the ideal gas is given by $\rho^2 \left(1 - \frac{1}{N} \right)$ and not ρ^2 simply follows from the fact that while the probability of finding a particle in a volume element $d\mathbf{r}_1$ around \mathbf{r}_1 , without any other restrictions is $\frac{N}{V}$ (see equation (3.81)), the

probability to find a particle in a volume element $d\mathbf{r}_2$ around \mathbf{r}_2 while another particle is somewhere else is given by $\frac{N-1}{V}$. Combining these two probabilities gives exactly the result above.

However using the ideal gas values for the activity $z^{\text{id}} = \rho$ (see equation (3.44)) as well as for the configurational part of the canonic partition function $Z_N^{\text{id}} = V^N$ (see equation (3.29)) the n -particle density in grand canonic ensembles can be written as

$$\begin{aligned} \rho^{(n)}(\mathbf{r}^n) &= \frac{1}{\Xi^{\text{id}}} \sum_{N \geq n}^{\infty} \frac{\rho^N}{(N-n)!} V^{(N-n)} \\ &= \rho^n \exp(-\rho V) \sum_{N \geq n}^{\infty} \frac{\rho^{(N-n)} V^{(N-n)}}{(N-n)!} \\ &= \rho^n. \end{aligned} \quad (3.83)$$

This differs by a factor of $(1 - \frac{1}{N})$ from the value in canonic ensembles because, the particle number is not constant in grand canonic ensembles. However in the thermodynamic limit this difference vanishes.

The dimensionless n -particle distribution functions $g_N^{(n)}(\mathbf{r}^N)$ provides information on how far the particle distribution deviates from a complete random distribution. This function can be defined in terms of the corresponding n -particle density and the one-particle densities in canonic as well as in grand canonic ensembles via

$$g^{(n)}(\mathbf{r}^N) = \frac{\rho^{(n)}(\mathbf{r}_1, \dots, \mathbf{r}_n)}{\prod_{i=1}^n \rho^{(1)}(\mathbf{r}_i)}. \quad (3.84)$$

For homogeneous systems equation (3.84) reduces to

$$\rho^n g^{(n)}(\mathbf{r}^N) = \rho^{(n)}(\mathbf{r}^n). \quad (3.85)$$

If the system is not only homogeneous but also isotropic the 2-particle distribution function, or pair-distribution function $g^{(2)}(\mathbf{r}^N)$, is a function of the distance of the two particles $r_{12} = |\mathbf{r}_2 - \mathbf{r}_1|$ and does not depend on particle positions anymore. It is then called radial-distribution function $g(r)$.

For large separations (i.e. separations much larger than the interaction range) $g(r)$ approaches the limiting value $(1 - \frac{1}{N}) \approx 1$ in canonic ensembles and exactly the value 1 in grand canonic ensembles.

The one- and two-particle densities $\rho^{(1)}(\mathbf{r})$, $\rho^{(2)}(\mathbf{r}, \mathbf{r}')$ as well as the radial-distribution function $g(r)$ can be expressed as ensemble averages of observables consisting of delta-functions.

The one-particle density can be written in terms of ensemble averages of delta functions as

$$\rho^{(1)}(\mathbf{r}) = \left\langle \sum_{i=1}^N \delta(\mathbf{r} - \mathbf{r}_i) \right\rangle, \quad (3.86)$$

which can be easily verified by calculating the average of $\delta(\mathbf{r} - \mathbf{r}_1)$ and carrying out the integration of the variable \mathbf{r}_1

$$\begin{aligned}\langle \delta(\mathbf{r} - \mathbf{r}_1) \rangle &= \frac{1}{Z_N} \int \delta(\mathbf{r} - \mathbf{r}_1) \exp[-\beta \mathcal{U}_N(\mathbf{r}_1, \mathbf{r}_2, \dots, \mathbf{r}_N)] d\mathbf{r}^N \\ &= \frac{1}{Z_N} \int \dots \int \exp[-\beta \mathcal{U}_N(\mathbf{r}, \mathbf{r}_2, \dots, \mathbf{r}_N)] d\mathbf{r}_2 \dots d\mathbf{r}_N.\end{aligned}\quad (3.87)$$

Using any other particle index than 1 would yield the same result. Therefor the average of a sum of N delta functions containing all particles coordinates \mathbf{r}_i like the one in equation (3.86) would just result in N times the last line of equation (3.87), which exactly matches the definition of the one-particle density (see equation (3.75) for $n = 1$). The two-particle density can be written as average over delta-functions in a similar way

$$\rho^{(2)}(\mathbf{r}, \mathbf{r}') = \left\langle \sum_{i=1}^N \sum_{\substack{j=1 \\ i \neq j}}^N \delta(\mathbf{r} - \mathbf{r}_i) \delta(\mathbf{r}' - \mathbf{r}_j) \right\rangle. \quad (3.88)$$

The derivation is similar to the one of the one-particle density; however an average over a product of two delta-functions has to be taken

$$\begin{aligned}\langle \delta(\mathbf{r} - \mathbf{r}_1) \delta(\mathbf{r}' - \mathbf{r}_2) \rangle &= \frac{1}{Z_N} \int \delta(\mathbf{r} - \mathbf{r}_1) \delta(\mathbf{r}' - \mathbf{r}_2) \exp[-\beta \mathcal{U}_N(\mathbf{r}_1, \mathbf{r}_2, \mathbf{r}_3, \dots, \mathbf{r}_N)] d\mathbf{r}^N \\ &= \frac{1}{Z_N} \int \dots \int \exp[-\beta \mathcal{U}_N(\mathbf{r}, \mathbf{r}', \mathbf{r}_3, \dots, \mathbf{r}_N)] d\mathbf{r}_3 \dots d\mathbf{r}_N.\end{aligned}\quad (3.89)$$

The double sum in equation (3.88) leads to $N(N-1)$ equal factors, each corresponding to the last line in equation (3.89), comparison with with the definition of the two-particle density (see equation (3.75) for $n = 2$) leads to the result.

As mentioned above the radial-distribution function $g(r)$ can be expressed as an average as well

$$\begin{aligned}\left\langle \frac{1}{N} \sum_{i=1}^N \sum_{\substack{j=1 \\ i \neq j}}^N \delta(\mathbf{r} - \mathbf{r}_j + \mathbf{r}_i) \right\rangle &= \left\langle \frac{1}{N} \int \sum_{i=1}^N \sum_{\substack{j=1 \\ i \neq j}}^N \delta(\mathbf{r}' + \mathbf{r} - \mathbf{r}_j) \delta(\mathbf{r}' - \mathbf{r}_i) d\mathbf{r}' \right\rangle \\ &= \frac{1}{N} \int \rho^{(2)}(\mathbf{r}' + \mathbf{r}, \mathbf{r}') d\mathbf{r}'.\end{aligned}\quad (3.90)$$

For a homogeneous and isotropic system $\rho^{(2)}(\mathbf{r}' + \mathbf{r}, \mathbf{r}')$ can be replaced by $\rho^2 g^{(2)}(\mathbf{r}, \mathbf{r}')$ (see equation (3.85)) and the above relation reduces to

$$\begin{aligned}\left\langle \frac{1}{N} \sum_{i=1}^N \sum_{\substack{j=1 \\ i \neq j}}^N \delta(\mathbf{r} - \mathbf{r}_j + \mathbf{r}_i) \right\rangle &= \frac{\rho^2}{N} \int g^{(2)}(\mathbf{r}, \mathbf{r}') d\mathbf{r}' \\ &= \rho g(r).\end{aligned}\quad (3.91)$$

The radial-distribution function is of great importance in the physics of simple fluids because of several reasons:

- The radial-distribution function $g(r)$ can be measured in radiation scattering experiments [27]. The experimentally directly accessible quantity is the structure factor $S(k)$, this function can be converted into the radial-distribution function via Fourier transformation

$$\rho [g(\mathbf{r}) - 1] = \frac{1}{(2\pi)^2} \int [S(\mathbf{k}) - 1] \exp [i\mathbf{k} \cdot \mathbf{r}] d\mathbf{k} \quad (3.92)$$

$$S(\mathbf{k}) = 1 + \rho \int [g(r) - 1] \exp [-i\mathbf{k} \cdot \mathbf{r}] d\mathbf{r}. \quad (3.93)$$

- The form of the radial-distribution function $g(r)$ provides insight into the internal "structure" of the fluid. Peaks in $g(r)$ corresponds to shells of neighboring particles (the number of particles in a shell between r and $r + dr$ is $2\pi r \rho g(r) dr$ in 2D for a homogeneous isotropic system)
- For a homogeneous and isotropic system, with particle pair-interactions only, many thermodynamic properties of the system can be expressed in terms of integrals over $g(r)$ (see section 3.5).

The structure factor can not only be computed by Fourier transform of the pair-distribution function (see equation (3.93)), but also from the particle positions as

$$S(\mathbf{k}) = \frac{1}{N} \langle \rho_{\mathbf{k}} \rho_{-\mathbf{k}} \rangle, \quad (3.94)$$

with

$$\rho_{\mathbf{k}} = \int \rho_N^{(1)}(\mathbf{r}) \exp[-i\mathbf{k} \cdot \mathbf{r}] d\mathbf{r} = \sum_{j=1}^N \exp[-i\mathbf{k} \cdot \mathbf{r}_j] \quad (3.95)$$

the Fourier transform of the one-particle density defined in equation (3.86).

The representation of the structure factor as Fourier transform of the radial distribution function (equation (3.93)) can also be derived by using equations (3.94) and (3.95):

$$\begin{aligned} S(\mathbf{k}) &= \frac{1}{N} \left\langle \sum_{j=1}^N \sum_{l=1}^N \exp[-i\mathbf{k} \cdot \mathbf{r}_j] \exp[i\mathbf{k} \cdot \mathbf{r}_l] \right\rangle \\ &= 1 + \frac{1}{N} \left\langle \sum_{j=1}^N \sum_{l \neq j}^N \exp[-i\mathbf{k} \cdot (\mathbf{r}_j - \mathbf{r}_l)] \right\rangle \\ &= 1 + \frac{1}{N} \left\langle \sum_{j=1}^N \sum_{l \neq j}^N \iint \exp[-i\mathbf{k} \cdot (\mathbf{r} - \mathbf{r}')] \delta(\mathbf{r} - \mathbf{r}_j) \delta(\mathbf{r}' - \mathbf{r}_l) d\mathbf{r} d\mathbf{r}' \right\rangle \\ &= 1 + \frac{1}{N} \iint \exp[-i\mathbf{k} \cdot (\mathbf{r} - \mathbf{r}')] \rho_N^{(2)}(\mathbf{r}, \mathbf{r}') d\mathbf{r} d\mathbf{r}'. \end{aligned} \quad (3.96)$$

Using the translational invariance of the system and carrying out the \mathbf{r}' integration this becomes

$$\begin{aligned} S(\mathbf{k}) &= 1 + \rho \int g(r) \exp[-i \mathbf{k} \cdot \mathbf{r}] \, d\mathbf{r} \\ &= 1 + (2\pi)^2 \delta(\mathbf{k}) + \rho \int [g(r) - 1] \exp[-i \mathbf{k} \cdot \mathbf{r}] \, d\mathbf{r}. \end{aligned} \quad (3.97)$$

The last line of the above derivation is equivalent to equation (3.93), aside from the δ -function term. In case of radiation scattering this term is attributed to radiation passing through the sample without interaction and will be ignored further on since it affects $S(k)$ only at $\mathbf{k} = 0$.

3.5 Important observables

3.5.1 Energy

As mentioned in section 3.3.2 (equation (3.38)) the total energy of a system can be separated into an ideal and an excess part given by equations (3.39) and (3.40) respectively, if the Hamiltonian separates into a kinetic and a configurational part.

Assuming that the configurational part further splits up into pair-interactions

$$\mathcal{U}_N = \sum_{i=1}^N \sum_{j>i}^N \Phi(r_{ij}), \quad (3.98)$$

the excess part of the total energy can be written as

$$U^{\text{ex}} = \frac{N(N-1)}{2} \iint \Phi(\mathbf{r}_{12}) \left[\frac{1}{Z_N} \int \dots \int \exp(-\beta \mathcal{U}_N) \, d\mathbf{r}_3 \dots d\mathbf{r}_N \right] d\mathbf{r}_1 d\mathbf{r}_2 \quad (3.99)$$

by inserting equation (3.98) into equation (3.40) and taking into account that each of the $N(N-1)$ terms originating from the double sum in equation (3.98) gives rise to the same value after integration.

Comparing the term within the angular brackets of equation (3.99) to the right hand side of equation (3.89) results in

$$\begin{aligned} U^{\text{ex}} &= \frac{N(N-1)}{2} \iint \Phi(r_{12}) \langle \delta(\mathbf{r} - \mathbf{r}_1) \delta(\mathbf{r}' - \mathbf{r}_2) \rangle d\mathbf{r}_1 d\mathbf{r}_2 \\ &= \frac{N(N-1)}{2} \iint \Phi(r_{12}) \rho_N^{(2)}(\mathbf{r}, \mathbf{r}') \, d\mathbf{r}_1 d\mathbf{r}_2. \end{aligned} \quad (3.100)$$

Using the definition of the n -particle distribution function for homogeneous systems ($n = 2$), equation (3.85), the excess part of the energy becomes

$$U^{\text{ex}} = \frac{1}{2} \rho^2 \iint \Phi(r_{12}) g_N^{(2)}(\mathbf{r}_1, \mathbf{r}_2) \, d\mathbf{r}_1 d\mathbf{r}_2. \quad (3.101)$$

This expression can be further simplified for homogeneous and isotropic systems considering that the two-particle distribution function only depends on the separation $\mathbf{r}_{12} = \mathbf{r}_2 - \mathbf{r}_1$:

$$\begin{aligned} U^{\text{ex}} &= \frac{1}{2}\rho^2 \iint \Phi(r_{12}) g_N^{(2)}(\mathbf{r}_1, \mathbf{r}_2) d\mathbf{r}_1 d\mathbf{r}_2 \\ &= \frac{N^2}{2V^2} \iint \Phi(r_{12}) g(r_{12}) d\mathbf{r}_1 d\mathbf{r}_{12} \\ &= \frac{N^2}{2V} \int \Phi(r) g(r) dr. \end{aligned} \quad (3.102)$$

Finally for a 2D-system the excess energy per particle is given by

$$\frac{U^{\text{ex}}}{N} = \pi\rho \int_0^\infty \Phi(r)g(r)rdr. \quad (3.103)$$

3.5.2 Pressure

The pressure of a system can be expressed as the differential of the Helmholtz free energy with respect to the volume $P = -(\partial F/\partial V)_{T,N}$ (see equation (3.23)). Expressing the free energy in this equation in terms of the canonic partition function Q_N (see equation (3.20)) results in

$$P = k_B T \frac{\partial}{\partial V} \ln Q_N = k_B T \frac{1}{Q_N} \frac{\partial}{\partial V} Q_N. \quad (3.104)$$

The definitions for the canonic partition function Q_N and the configurational integral Z_N is given by equation (3.16) and equation (3.28) respectively, but will be repeated here for simpler reference

$$Q_N = \frac{Z_N}{N! \Lambda^{2N}} = \frac{1}{N! \Lambda^{2N}} \int_{\Gamma_{\text{conf}}} d\mathbf{r}^N \exp[-\beta\mathcal{U}(\mathbf{r}^N)] \quad (3.105)$$

$$Z_N = \int_{\Gamma_{\text{conf}}} d\mathbf{r}^N \exp[-\beta\mathcal{U}(\mathbf{r}^N)]. \quad (3.106)$$

The differential of the canonic partition function can therefore be written as

$$\frac{\partial}{\partial V} Q_N = \frac{\partial}{\partial V} \frac{1}{N! \Lambda^{2N}} \int_{\Gamma_{\text{conf}}} d\mathbf{r}^N \exp[-\beta\mathcal{U}(\mathbf{r}^N)] \quad (3.107)$$

Since the integration bounds of of the canonic partition function Q_N in equation (3.107) depend on the volume V , the differential cannot simply be switched with the integration. However a variable transformation of the form

$$\begin{aligned}\mathbf{r}_i &= \sqrt{V} \mathbf{r}'_i \\ d\mathbf{r}_i &= V d\mathbf{r}'_i\end{aligned}\tag{3.108}$$

removes the volume dependency of the integration bounds ($\Gamma_{\text{conf}} \rightarrow \Gamma'_{\text{conf}}$). To remind on the different variables the potential energy $\mathcal{U}(\mathbf{r}^N)$ depends on it is written as $\tilde{\mathcal{U}}(\mathbf{r}'^N)$ after the transformation

$$\begin{aligned}\frac{\partial}{\partial V} Q_N &= \frac{\partial}{\partial V} \frac{V^N}{N! \Lambda^{2N}} \int_{\Gamma'_{\text{conf}}} d\mathbf{r}'^N \exp[-\beta \tilde{\mathcal{U}}(\mathbf{r}'^N)] \\ &= \frac{NV^{N-1}}{N! \Lambda^{2N}} \int_{\Gamma'_{\text{conf}}} d\mathbf{r}'^N \exp[-\beta \tilde{\mathcal{U}}(\mathbf{r}'^N)] + \frac{V^N}{N! \Lambda^{2N}} \int_{\Gamma'_{\text{conf}}} d\mathbf{r}'^N \frac{\partial}{\partial V} \exp[-\beta \tilde{\mathcal{U}}(\mathbf{r}'^N)] \\ &= \frac{1}{N! \Lambda^{2N}} \frac{N}{V} Q_N + \frac{1}{N! \Lambda^{2N}} \int_{\Gamma_{\text{conf}}} d\mathbf{r}^N \exp[-\beta \mathcal{U}(\mathbf{r}^N)] (-\beta) \frac{\partial}{\partial V} \mathcal{U}(\mathbf{r}^N).\end{aligned}\tag{3.109}$$

The back-transformation to the non dashed r variables is performed on the last line of the above equation.

Using equation (3.109) the pressure can be written as

$$P = k_B T \frac{N}{V} - \frac{1}{N! \Lambda^{2N} Q_N} \int_{\Gamma_{\text{conf}}} d\mathbf{r}^N \exp[-\beta \mathcal{U}(\mathbf{r}^N)] \frac{\partial}{\partial V} \mathcal{U}(\mathbf{r}^N).\tag{3.110}$$

We assume that the potential energy \mathcal{U}_N can be written as a double-sum of pair potentials that only depend on the separation of the particles $r_{ij} = |\mathbf{r}_i - \mathbf{r}_j|$, as we did in the previous section

$$\mathcal{U}_N(\mathbf{r}^N) = \sum_{i=1}^N \sum_{j>i}^N \Phi(r_{ij}).\tag{3.111}$$

Therefor equation (3.110) is transformed to

$$\begin{aligned}P &= k_B T \frac{N}{V} - \frac{1}{Z_N} \int_{\Gamma_{\text{conf}}} d\mathbf{r}^N \exp[-\beta \mathcal{U}(\mathbf{r}^N)] \frac{\partial}{\partial V} \sum_{i=1}^N \sum_{j>i}^N \Phi(r_{ij}) \\ &= k_B T \frac{N}{V} - \frac{1}{Z_N} \int_{\Gamma_{\text{conf}}} d\mathbf{r}^N \exp[-\beta \mathcal{U}(\mathbf{r}^N)] \sum_{i=1}^N \sum_{j>i}^N \frac{\partial \Phi(r_{ij})}{\partial r_{ij}} \frac{\partial r_{ij}}{\partial V}.\end{aligned}\tag{3.112}$$

The factor $\partial r_{ij} / \partial V$ can be easily computed by using the variable transformation given in equation (3.108) and using the fact that the r' variables do not depend on the volume

$$\frac{\partial r_{ij}}{\partial V} = \frac{\partial(\sqrt{V}r'_{ij})}{\partial V} = \frac{r'_{ij}}{2\sqrt{V}} = \frac{r_{ij}}{2V}. \quad (3.113)$$

Using equation (3.113) the pressure can be finally written as

$$\begin{aligned} P &= k_B T \frac{N}{V} - \frac{1}{2V} \frac{1}{Z_N} \int_{\Gamma_{\text{conf}}} \mathbf{dr}^N \exp[-\beta \mathcal{U}(\mathbf{r}^N)] \sum_{i=1}^N \sum_{j>i}^N r_{ij} \frac{\partial \Phi(r_{ij})}{\partial r_{ij}} \\ &= k_B T \frac{N}{V} - \frac{1}{2V} \left\langle \sum_{i=1}^N \sum_{j>i}^N r_{ij} \frac{\partial \Phi(r_{ij})}{\partial r_{ij}} \right\rangle \end{aligned} \quad (3.114)$$

The first line of equation (3.114) can be also written as

$$P = k_B T \frac{N}{V} - \frac{N(N-1)}{4V} \iint r_{12} \frac{\partial \Phi(r_{12})}{\partial r_{12}} \left[\frac{1}{Z_N} \int \dots \int \exp[-\beta \mathcal{U}(\mathbf{r}^N)] \mathbf{dr}_3 \dots \mathbf{dr}_N \right] \mathbf{dr}_1 \mathbf{dr}_2 \quad (3.115)$$

taking into account that the $N(N-1)/2$ terms of the double-sum yield the same value after integration.

Using

$$\Phi'(r) \equiv \frac{\partial \Phi(r)}{\partial r} \quad (3.116)$$

and repeating the steps of the derivation of the excess energy leading from equation (3.98) to equation (3.103) with $r\Phi'(r)$ instead of $\Phi(r)$ results in

$$\frac{\beta P}{\rho} = 1 - \frac{\pi\beta\rho}{2} \int_0^\infty \Phi'(r) g(r) r^2 dr. \quad (3.117)$$

However different from equation (3.103) a discontinuity in the pair-potential is an issue here, since equation (3.117) includes the derivative of the pair-potential $\Phi'(r)$, which becomes infinite at the point of the discontinuity.

To resolve this issue the cavity distribution function $y(r)$ is introduced as

$$y(r) = \exp[\beta\Phi(r)] g(r). \quad (3.118)$$

It can be shown that the cavity distribution function is continuous, even if the pair-potential $\Phi(r)$ and, as a consequence, the radial-distribution function $g(r)$ are not [27]. Using the cavity distribution function defined above, equation (3.117) can be written as

$$\begin{aligned} \frac{\beta P}{\rho} &= 1 - \frac{\pi\beta\rho}{2} \int_0^\infty \Phi'(r) e(r) y(r) r^2 dr \\ &= 1 + \frac{\pi\rho}{2} \int_0^\infty e'(r) y(r) r^2 dr \end{aligned} \quad (3.119)$$

with $e(r) = \exp[-\beta\Phi(r)]$ the Boltzmann factor and $e'(r) = \frac{de(r)}{dr} = -\beta\Phi'(r) \exp[-\beta\Phi(r)]$. For a hard sphere systems with a particle diameter of σ the Boltzmann factor $e(r)$ is a step function and therefore its derivative $e'(r)$ is a delta function

$$e(r) = \begin{cases} 0 & r \leq \sigma \\ 1 & r > \sigma \end{cases} \quad (3.120)$$

$$e'(r) = \delta(r - \sigma). \quad (3.121)$$

Inserting $e'(r) = \delta(r - \sigma)$ into equation (3.119) results in

$$\begin{aligned} \frac{\beta P}{\rho} &= 1 + \frac{\pi\rho}{2} \int_0^\infty r^2 y(r) \delta(r - \sigma) dr \\ &= 1 + \frac{\pi\rho}{2} \lim_{r \rightarrow \sigma^+} r^2 y(r) \\ &= 1 + \frac{\pi\rho}{2} \sigma^2 g(\sigma) \end{aligned} \quad (3.122)$$

with $g(\sigma)$ being the value of the radial-distribution function at particle contact.

The pair-interaction potential used in the present work Φ_{IR} can be written as the sum of an hard core part and a tail part $\Phi(r) = \Phi_{\text{hc}}(r) + \Phi_{\text{tail}}(r)$ (see chapter 2). Obviously this is also valid for the derivative of the potential $\Phi'(r) = \Phi'_{\text{hc}}(r) + \Phi'_{\text{tail}}(r)$. Inserting this sum of potential parts into equation (3.117) the integral can be split into an integral over the hard core part of the interaction $\Phi'_{\text{hc}}(r)$ and an integral over the tail part of the interaction $\Phi'_{\text{tail}}(r)$.

Calculating the integral over the hard core part of the interaction as shown above, while leaving the integral over the tail interaction unchanged results in

$$\frac{\beta P}{\rho} = 1 + \frac{\pi\rho}{2} \sigma^2 g(\sigma) - \frac{\pi\beta\rho}{2} \int_\sigma^\infty \Phi'_{\text{tail}}(r) g(r) r^2 dr \quad (3.123)$$

with σ being the hard core diameter of the potential. The lower bound of the integral in equation (3.123) can be set to σ instead of zero because the radial-distribution function $g(r)$ within the core is zero anyway and does not contribute to the pressure.

Chapter 4

Methods

4.1 Monte-Carlo Simulations

4.1.1 General

Computer simulations are considered as a complementary access to physical properties together with experiments and theory. However theoreticians as well as experimentalists can benefit from computer simulations, because computer simulations separate the check of the approximations made in developing a theory from testing the validity of the underlying model [?].

To explain the basic principles of Monte Carlo simulations in condensed matter theory we will follow the argumentation (and notation) of [29].

The aim of computer simulations, applied to condensed matter systems, is to evaluate averages of observables (B), as defined in statistical mechanics, that can be expressed as functions of the positions (\mathbf{r}^N) and momenta (\mathbf{p}^N) of the N particles of the system. These particles interact via a known potential $\mathcal{U}(\mathbf{r}^N)$.

Most computer simulations try to achieve that by solving suitable equations of motion for the system and compute a time average of the observable (B). These can be Newtons equations of motion for Molecular Dynamics (MD) [29, 30], Langevin equations of motion for Brownian Dynamics (BD) [30] or Newtons equations of motion modified by a friction term and random noise for Stochastic Dynamics (SD) [31].

Monte Carlo simulations on the other hand do not compute the time average but the ensemble averages the observable.

In the canonical ensemble averages of a physical observable are given by (compare with equation (3.18))

$$\langle B \rangle = \frac{\int d\mathbf{p}^N d\mathbf{r}^N B(\mathbf{p}^N, \mathbf{r}^N) \exp[-\beta\mathcal{H}(\mathbf{p}^N, \mathbf{r}^N)]}{\int d\mathbf{p}^N d\mathbf{r}^N \exp[-\beta\mathcal{H}(\mathbf{p}^N, \mathbf{r}^N)]} \quad (4.1)$$

where the integrals are taken over the phase space and \mathcal{H} is the Hamilton function of the system.

Since the Hamiltonian depends on the momenta of the particles via

$$\mathcal{H}(\mathbf{p}^N, \mathbf{r}^N) = \mathcal{K}(\mathbf{p}^N) + \mathcal{U}(\mathbf{r}^N) = \sum_{i=1}^N \left(\frac{\mathbf{p}_i^2}{2m_i} \right) + \mathcal{U}(\mathbf{r}^N) \quad (4.2)$$

averages of observables depending on the particle positions only, can be computed via equation (4.3), since the contribution for the momenta cancel out.

$$\langle B \rangle = \frac{\int d\mathbf{r}^N B(\mathbf{r}^N) \exp[-\beta\mathcal{U}(\mathbf{r}^N)]}{\int d\mathbf{r}^N \exp[-\beta\mathcal{U}(\mathbf{r}^N)]} \quad (4.3)$$

Unfortunately averages like the ones in equation (4.3) can only be computed analytically for a few very simple systems, therefore they are calculated numerically using Monte Carlo simulations.

However due to the high number of particles, averages of the form of equation (4.3) are difficult to evaluate numerically as well. Using conventional quadrature approaches the integrand would be evaluated on a equidistantly spaced grid of m points in each dimension. The main disadvantage of this approach is obvious when considering the high dimensionality of the integrals. Even at a medium number of particles N the integrand has to be evaluated on an extremely high number of grid points. For example for a system of only $N = 100$ particles in $d = 3$ dimensions and evaluating only $m = 10$ points per dimension the integrand has to be evaluated at $m^{dN} = 10^{300}$ points. To evaluate the integrand at such a high number of points is not feasible with today's computers. Moreover due to the Boltzmann factor in the integrand most of the evaluated points would carry close to no weight or no weight at all because of the high energy of these configurations. For example if only two particles overlap in an hard sphere system the corresponding configuration has no weight due to its infinite potential energy.

Randomly selecting the sample points (brute force Monte Carlo) to evaluate the integral, will not reduce the problem of most sampling points having no weight. Therefore the sampling points have to be selected in a way that points having a relevant weight are sampled more often than those having a small weight. Doing so not only reduces the computational demand but also greatly reduces the variance of the result.

A one dimensional integral will serve as example to show how the sampling points should be chosen in order to reduce the resulting error ([29])

$$I = \int_0^1 dx f(x) \quad (4.4)$$

$$I \approx \frac{1}{m} \sum_{i=1}^m f(x_i). \quad (4.5)$$

An one-dimensional integral as equation (4.4) can be evaluated numerically by conventional quadrature by equation (4.5). For simplicity the boundaries of the integral have been chosen as $[0, 1]$. Clearly the integral can be expanded by a non-negative weight function $w(x)$ (see equation (4.6)). Assuming that the function $w(x)$ is the derivative of another function $u(x)$ and normalized on the interval $[0, 1]$ ($u(0) = 0$ as

well as $u(1) = 1$), the integration variable can be changed from x to u . The resulting integral (equation (4.7)) can be computed by conventional quadrature using u as the integration variable instead of x resulting in equation (4.8)

$$I = \int_0^1 dx w(x) \frac{f(x)}{w(x)} \quad (4.6)$$

$$I = \int_0^1 du \frac{f(x(u))}{w(x(u))} \quad (4.7)$$

$$I \approx \frac{1}{m} \sum_{i=1}^m \frac{f(x(u_i))}{w(x(u_i))}. \quad (4.8)$$

The gain of this weighted sampling crucially depends on the choice of the weight function $w(x)$. The variance of I (evaluated via equation (4.8)) can be written as

$$\sigma_I^2 = \frac{1}{m^2} \sum_{i=1}^m \sum_{j=1}^m \left\langle \left(\frac{f(x(u_i))}{w(x(u_i))} - \langle f/w \rangle \right) \left(\frac{f(x(u_j))}{w(x(u_j))} - \langle f/w \rangle \right) \right\rangle \quad (4.9)$$

where $\langle f/w \rangle$ represents the true average of $w(x)/f(x)$. Since the cross terms of independent samples ($i \neq j$) are zero, equation (4.9) reduces to

$$\sigma_I^2 = \frac{1}{m^2} \sum_{i=1}^m \left\langle \left(\frac{f(x(u_i))}{w(x(u_i))} - \langle f/w \rangle \right)^2 \right\rangle. \quad (4.10)$$

Equation (4.10) shows that the magnitude of the variance can be greatly reduced when choosing the weight function $w(x)$ in a way that the fraction $f(x)/w(x)$ is a smooth function. An appropriate choice to achieve this is to choose $w(x)$ as the Boltzmann factor.

Unfortunately there is no general recipe to construct the transformation equivalent to the one from x to u in a multidimensional integral. This makes it impossible to compute the configurational part of the partition function Z (see equation (4.11)) directly by Monte Carlo simulations.

$$Z \equiv \int d\mathbf{r}^N \exp[-\beta(\mathcal{U}(\mathbf{r}^N))] \quad (4.11)$$

However as Metropolis *et al.* showed [32] it is possible to compute fractions of integrals like the average in equation (4.3) using Monte Carlo simulations.

The ratio between the Boltzmann factor and the configurational part of the partition function $\mathcal{N}(\mathbf{r}^N) = \exp[-\beta(\mathcal{U}(\mathbf{r}^N))]/Z$ is the probability of finding the system in an configuration around \mathbf{r}^N .

Assuming it is possible to randomly create a series of points according to the probability distribution $\mathcal{N}(\mathbf{r}^N)$, would mean that the number of points in a unit volume around the point \mathbf{r}^N is $n = m\mathcal{N}(\mathbf{r}^N)$ (with m being the total number of points created). Ensemble averages (equation (4.3)) could then simply be computed as follows

$$\langle B \rangle \approx \frac{1}{m} \sum_{i=1}^m n_i B(\mathbf{r}_i^N) \quad (4.12)$$

Unfortunately the absolute probability is unknown since Z cannot be computed (see above). In [32] Metropolis *et al.* showed how it is still possible to construct a series of sampling points with a relative probability proportional to the Boltzmann factor. Starting from a old configuration (denoted by o) with a nonzero Boltzmann factor a new configuration (denoted by n) is derived. (How this is done practically will be explained in section 4.1.2). The assumption of Metropolis *et al.* is that such a move from an old configuration to a new one does not destroy the equilibrium distribution $\mathcal{N}(\mathbf{r}^N)$ once it has been established. In equilibrium the probability of finding the system in configuration o is proportional to $\mathcal{N}(o)$. If the probability of going from configuration o to configuration n is now denoted by $\pi(o \rightarrow n)$ then on average the probability to leave configuration o to some other configuration (left side of equation (4.13)) must be equal to the probability of reaching configuration o from some other configuration (right side of equation (4.13)), in an effort to preserve equilibrium,

$$\sum_n \mathcal{N}(o) \pi(o \rightarrow n) = \sum_n \mathcal{N}(n) \pi(n \rightarrow o) \quad |\forall o, \quad (4.13)$$

The condition formulated in equation (4.13) is called "global balance". For practical purposes it is much more convenient to impose a much stronger condition namely "detailed balance", which states that in equilibrium the probability to go from any configuration o to any other configuration n (left side of equation (4.14)) must be equal to the probability of returning from configuration n to configuration o (right side of equation (4.14)).

$$\mathcal{N}(o) \pi(o \rightarrow n) = \mathcal{N}(n) \pi(n \rightarrow o) \quad |\forall (o, n) \quad (4.14)$$

The transition probability from configuration o to configuration n ($\pi(o \rightarrow n)$) can be split into the probability of selecting the move from o to n ($\alpha(o \rightarrow n)$) and the probability of accepting such a move ($\text{acc}(o \rightarrow n)$)

$$\pi(o \rightarrow n) = \alpha(o \rightarrow n) \times \text{acc}(o \rightarrow n). \quad (4.15)$$

If the probability of selecting the move from configuration o to configuration n ($\alpha(o \rightarrow n)$) is chosen to be symmetric ($\alpha(o \rightarrow n) = \alpha(n \rightarrow o) \quad |\forall (o, n)$), then the acceptance ($\text{acc}(o \rightarrow n)$) has to fulfill the condition given in equation (4.16)

$$\mathcal{N}(o) \text{acc}(o \rightarrow n) = \mathcal{N}(n) \text{acc}(n \rightarrow o) \quad |\forall (o, n). \quad (4.16)$$

Reordering of equation (4.16) and substituting the probability density \mathcal{N} with its definition leads to

$$\frac{\text{acc}(o \rightarrow n)}{\text{acc}(n \rightarrow o)} = \frac{\mathcal{N}(n)}{\mathcal{N}(o)} = \frac{Z \exp[-\beta \mathcal{U}(\mathbf{r}_n^N)]}{Z \exp[-\beta \mathcal{U}(\mathbf{r}_o^N)]} = \exp[-\beta(\mathcal{U}(\mathbf{r}_n^N) - \mathcal{U}(\mathbf{r}_o^N))] \quad (4.17)$$

It should be noted that the configurational part of the partition function cancels out in equation (4.17). This finally shows how it is possible to construct a series of points with a probability density proportional to the Boltzmann factor without knowing the absolute probability. It also shows that this is only possible by selecting an initial configuration and to continue from this configuration to the next and so on.

Since equation (4.17) only gives the fraction between two acceptance values it can be fulfilled in more than one ways. Obviously the acceptance value must lie in the interval $[0, 1]$. The choice of Metropolis *et al.*, which is still used in many Monte Carlo simulation implementations, is to set the acceptance $\text{acc}(o \rightarrow n)$ to unity if the probability density of the new configuration $\mathcal{N}(n)$ is bigger than the probability density of the old configuration $\mathcal{N}(o)$. The acceptance probability is thus given by equations (4.18) and (4.19),

$$\text{acc}(o \rightarrow n) = 1 \quad \text{if } \mathcal{N}(n) \geq \mathcal{N}(o) \quad (4.18)$$

$$\text{acc}(o \rightarrow n) = \mathcal{N}(n)/\mathcal{N}(o) \quad \text{if } \mathcal{N}(n) < \mathcal{N}(o). \quad (4.19)$$

In terms of the potential energy (easily available within the simulation) the acceptance criterion can be written as

$$\text{acc}(o \rightarrow n) = \min \{ \exp[-\beta(\mathcal{U}(\mathbf{r}_n^N) - \mathcal{U}(\mathbf{r}_o^N))], 1 \}. \quad (4.20)$$

4.1.2 Monte Carlo Moves

Obviously there are many different ways to construct Monte Carlo moves fulfilling the detailed balance request (equation (4.14)). Therefore this chapter is restricted to the Monte Carlo moves used in this work.

One of the characteristic features of Monte Carlo simulations is that the particle moves are not imposed by the intrinsic dynamics of the Hamiltonian equations of motion. Thus changes in the system are possible that are not possible in a real system (like changing the identity/type of two particles in a multi-component mixture). Such "unphysical" moves can drastically decrease the computational effort needed in simulations.

A number of N attempted MC moves (N being the number of mobile particles in the simulation) will be called MC step, it is used as a system-size independent measure of MC time.

Additionally we will define a MC sweep as the duration of the simulation between two snapshots (the recording of all particle positions), as such a MC sweep consists of n_{skip} MC steps.

Displacement Moves

Displacement moves are the most simple and common moves in MC simulations and thus are used by nearly all (statistical physics) MC codes. A displacement move is preformed (in principle) by the following steps:

1. randomly select one single particle (its position is denoted by \mathbf{r}_o)

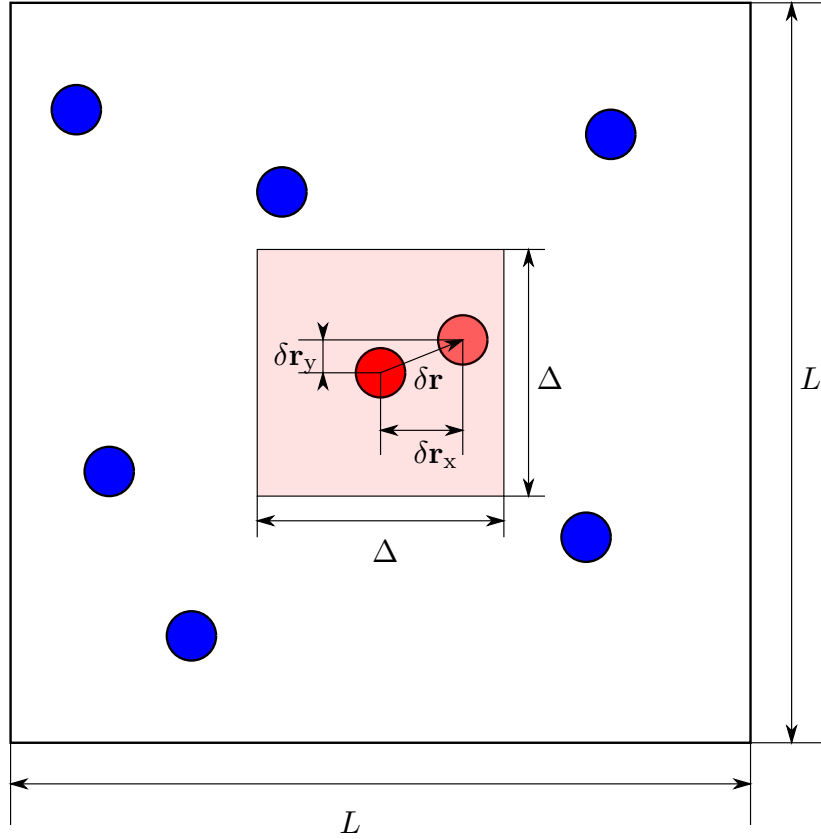


Figure 4.1: Displacement move: The selected particle is shown in red, the trial particle position after a move of $\delta \mathbf{r}$ is shown in a lighter shade of red. The light red square around the selected particle shows the possible particle positions with a maximum displacement of $\Delta/2$.

2. compute the potential energy of the configuration $\mathcal{U}(\mathbf{r}_o^N)$
3. create displacement vector $\delta \mathbf{r}$ by randomly selecting the Cartesian components from the interval $[-\Delta/2, +\Delta/2]$, with $\Delta/2$ being the maximum displacement which is a parameter of constant value during the duration of the simulation. The new particle position therefore is $\mathbf{r}_n = \mathbf{r}_o + \delta \mathbf{r}$.
Side note: the displacement vector can be created differently as well [33].
4. compute the potential energy of the new configuration $\mathcal{U}(\mathbf{r}_n^N)$
5. accept the move with a probability

$$\text{acc}(o \rightarrow n) = \min \{ \exp[-\beta(\mathcal{U}(\mathbf{r}_n^N) - \mathcal{U}(\mathbf{r}_o^N))], 1 \}$$

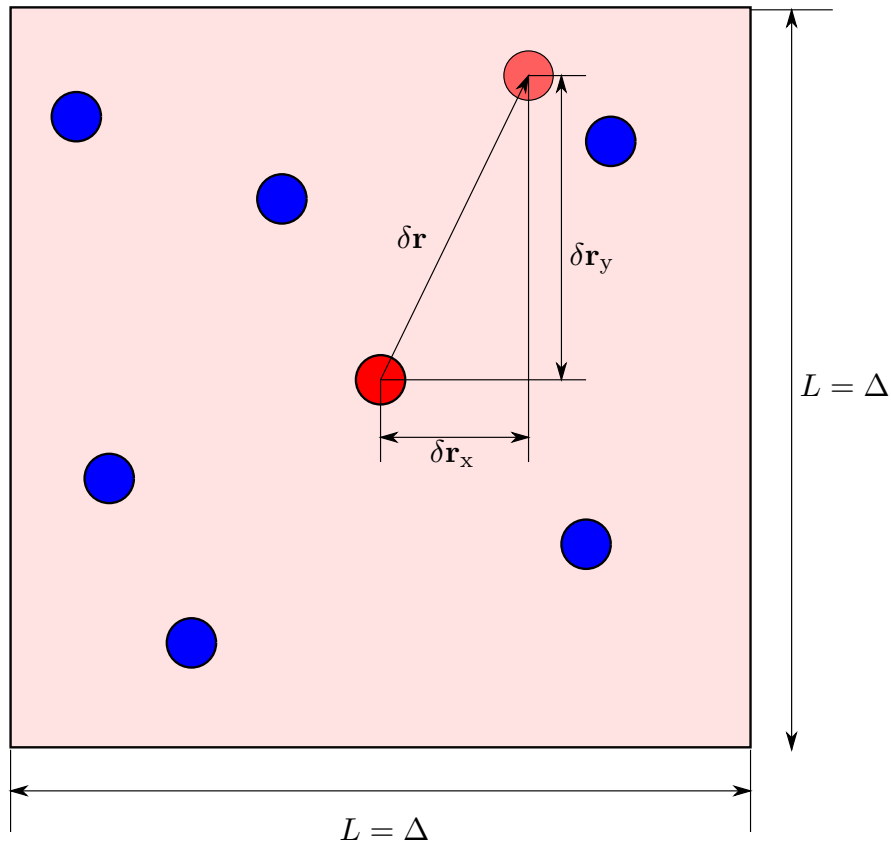


Figure 4.2: Jump Move: Selected Particle is shown in red, the trial particle position after a move with $\delta \mathbf{r}$ is shown in a lighter shade of red. The light red square filling the entire simulation box shows the possible new particle positions.

Jump Moves

Jump moves are a special case of the displacement moves in which the particle can move/jump to any place in the simulation box, meaning the maximum displacement $\Delta/2$ coincides with the half length of the simulation box.

In general the maximum displacement $\Delta/2$ is chosen small as to keep the acceptance rate at the desired values (about 20 to 50% as a rule of thumb [29]). When selecting the maximum displacement $\Delta/2$ as the half simulation box length, which is the highest value compatible with periodic boundary conditions, there is no way tuning the acceptance rate, which then can be low in dense systems. However by mixing jump moves with displacement moves the equilibration rate of the system can be improved.

4.1.3 Implementation Details

This section lists technical details, that were integrated in the MC simulation code used in the present work. Some of these are applied to (nearly) all MC simulations in statistical physics (like the periodic boundary conditions), while the use of others (like the Lattice Monte Carlo explained in section 4.1.3) is not that widespread.

Periodic Boundary Conditions

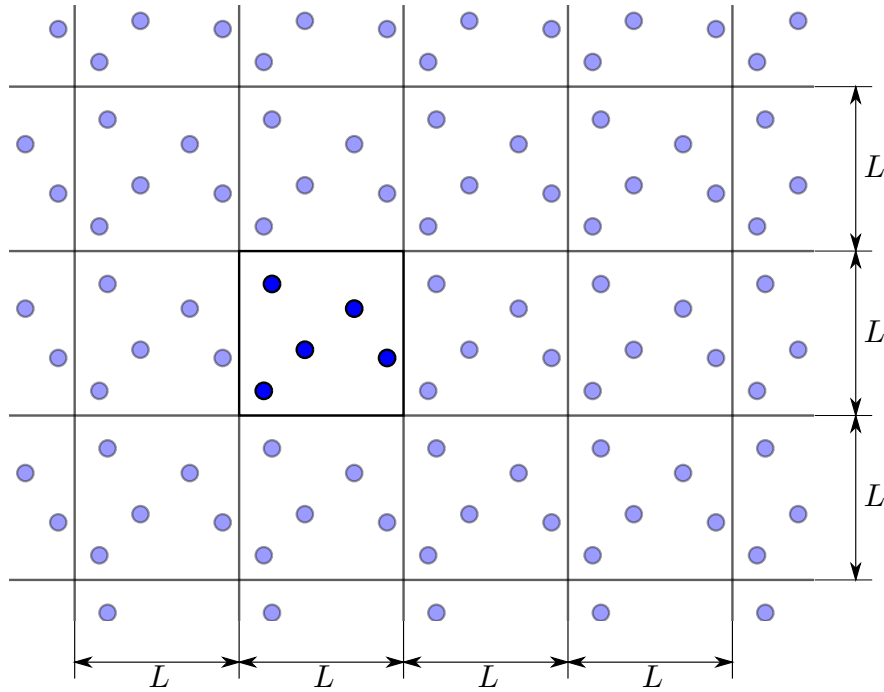


Figure 4.3: Periodic boundary conditions: Image of the infinite grid of simulation boxes (simulation box side length L). The copies of the original box are shown in a lighter shade.

MC simulations are limited to a few thousand up to a few million particles, due to the computer power available today. Even if that number appears to be high it is still very low compared to bulk systems found in nature (compare to Avogadro/Loschmidt number $N_A = 6.02210^{23}$). As a result surface effects have a noticeable influence on the computed averages when considering the simulation cell alone. To solve this problem many MC simulations try to mimic a bulk environment around each particle in the simulation by (virtually) filling space with identical copies of the original simulation box. This technique is called "periodic boundary conditions" since whenever a particle is leaving the simulation box its periodic image enters the simulation box from the opposite side. The potential energy of a particle is then computed not only with the

particles of the original simulation box but also with the periodic images of the particles in all other copies of the simulation box on the infinite lattice (including its own periodic image). A restriction to the amount of particles interactions considered is commonly made by truncating the interaction used in the simulation (see section 4.1.3).

The application of periodic boundary conditions is a widely used and efficient technique to compute bulk properties of systems while using only a limited number of particles. However problems may still arise if the wavelength of fluctuations of observables is not compatible with the periodicity of the simulation boxes. This is especially important if fluctuations of observables are expected to have a wavelength equal or greater than the side length of the simulation box, which is the case in the vicinity of a continuous phase transition for example.

Truncation of Interaction

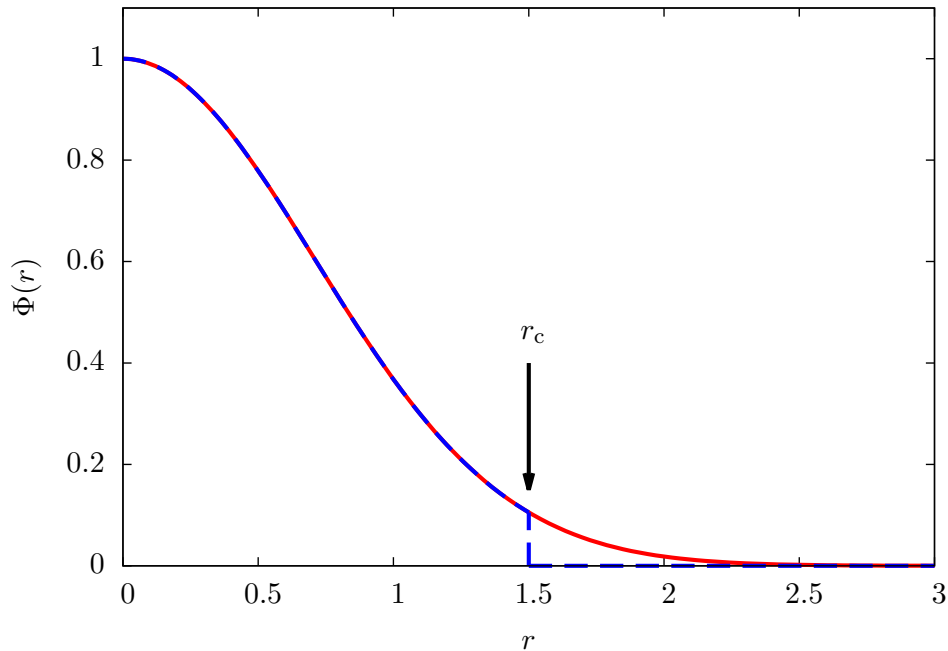


Figure 4.4: Truncation of the interaction for the example of the Gaussian Core model. Red - original potential, blue - simple truncation. In all cases ($r_c = 1.5$) was used.

The application of periodic boundary conditions as introduced in section 4.1.3 suggests to compute the interactions of the particles in the simulation box not only with all the other particles of the simulation box but also with an infinite number of periodic images of the simulation box. However this would mean that a particle also interacts with an infinite number of periodic images of itself. Luckily in general the interaction of a particle with its close environment is more important than the interaction with particles further away. If the interaction potential decays fast enough with increasing

distance, thus the interaction with particles further away can be ignored.

Simple Truncation

In the simple truncation method also used in this work the (radially symmetric) potential is set to zero at a suitable distance, the so called cutoff radius (r_c)

$$\Phi_{\text{trunc}}(r) = \begin{cases} \Phi(r) & r \leq r_c \\ 0 & r > r_c \end{cases} . \quad (4.21)$$

Naturally in using this modified interaction potential introduces an error in the computed energy, however if the potential decays fast enough (i.e. faster than $1/r^{d-1}$ with d being the dimensionality of the system) a correction to the energy can be computed as follows. Assuming a uniform radial distribution ($g(r) = 1$) for particle-particle distances bigger than the cutoff radius ($r > r_c$) the tail corrections for the potential energy in two and three dimensions are given by

$$U_{\text{tail}}^{3\text{D}} = 2\pi\rho \int_{r_c}^{\infty} dr r^2 \Phi(r) \quad (4.22)$$

$$U_{\text{tail}}^{2\text{D}} = \pi\rho \int_{r_c}^{\infty} dr r \Phi(r). \quad (4.23)$$

A suitable choice of the cutoff radius (r_c) not only guarantees that the value of the potential at the cutoff radius ($\Phi(r_c)$) is small compared to the maximum/minimum value of the potential, but also that the tail correction (equation (4.22) or equation (4.23)) is small compared to the total value of the energy.

The case of the cutoff radius being smaller than the half simulation box length ($r_c < L/2$) is of special interest since only interactions of a tagged particle with the closest periodic image of other particles are taken into account. In this work $r_c < L/2$ was always the case.

Equilibration

In a MC simulation the obtained averages should not depend on the initial particle positions used in the simulation. However even for an arbitrary starting configuration compatible with the potential (e.g. no hard overlaps) and an ergodic system, this is only true in general for an infinite simulation time, since the chosen starting configuration may be very unlikely in equilibrium and the development towards an equilibrium state might be slow. Observables obtained during that time may be far from their mean value at equilibrium. If these fare from the mean values are included into the averaging procedure, more simulation steps at an equilibrium state are necessary to obtain the correct average accurately.

To avoid problems with starting configurations far from equilibrium, without increasing the length of the simulations, the acquisition of averages can be deferred until configurations closer to equilibrium have been reached and the desired observables fluctuate around their mean value.

If not stated otherwise random particle positions were used as starting configuration for the MC simulations in the present work. Equilibration of these starting configurations was used to avoid the accuracy problems in obtaining averages discussed above.

Reduced Units

MC simulation quantities are often expressed in reduced units. After choosing a suitable unit of length, energy and mass all other quantities can be expressed in terms of these units.

The usual choice is

- unit of length σ (characteristic length/range of interaction potential)
- unit of energy ϵ (characteristic amplitude of interaction potential)
- unit of mass m (mass of the simulation particles)

With that choice of units other important simulation quantities follow as

quantity	symbol	2D	3D
distance	r^*	$= r/\sigma$	$= r/\sigma$
energy	U^*	$= U/\epsilon$	$= U/\epsilon$
density	ρ^*	$= \rho\sigma^2$	$= \rho\sigma^3$
pressure	P^*	$= P\sigma^2/\epsilon$	$= P\sigma^3/\epsilon$
temperature	T^*	$= k_B T/\epsilon$	$= k_B T/\epsilon$

with (*) denoting the reduced unit quantity.

By using reduced units most of the computed averages should have a value in the range between 10^{-3} to 10^3 . This eliminates the possible occurrence of an overflow/underflow with one of the floating point variables involved. Additionally the numeric precision should be roughly constant for these floating point variables.

Reduced units will be used in the remainder of this work, for simplicity of notation the (*) will be omitted further on.

Cell Lists

Cell lists are a method to improve the performance of (MC) simulations. The most time consuming step in a MC simulation is the computation of the potential energy of a configuration. Assuming only pair interactions between the particles and without the use of advanced methods (such as cell lists) this computation scales with N^2 . Even when truncating the interaction (see section 4.1.3) the distance between all particle pairs has to be computed in order to evaluate if there is an interaction at all.

The cell lists method reduced the number of particle pairs that need to be evaluated by splitting up the simulation box in cells with a side length greater or equal than the cutoff radius of the potential ($l_{cl} \geq r_c$). A given particle therefore interacts only with particles located in the same or neighboring cell list cells. The number of these particles

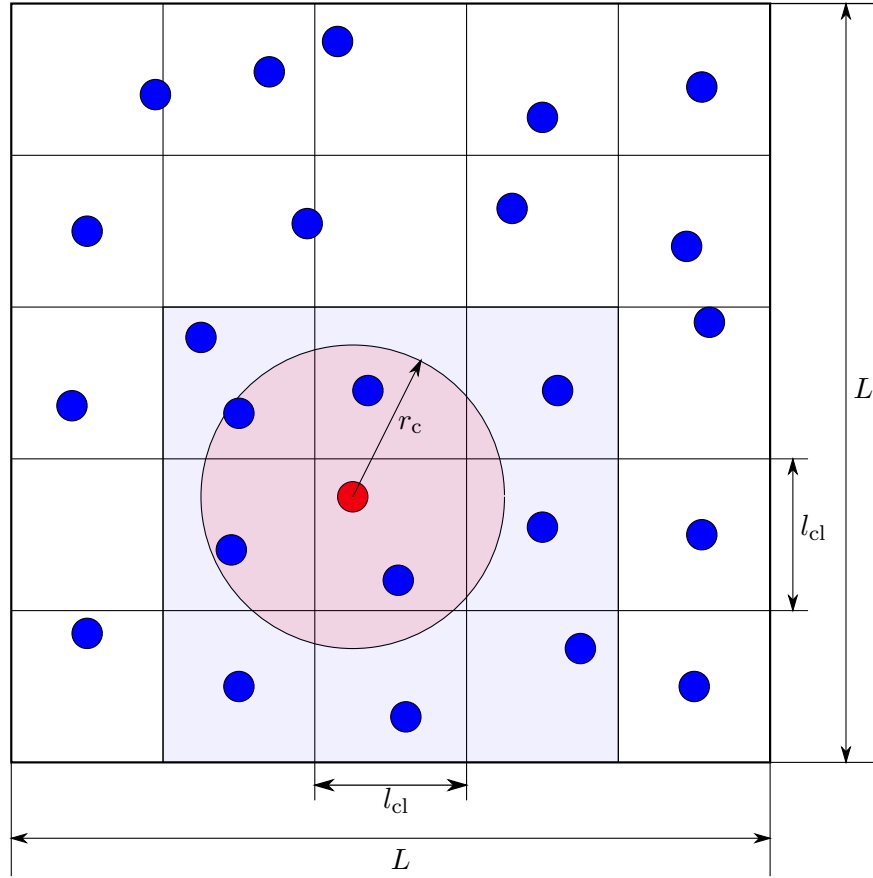


Figure 4.5: Cell list method: Selected particle shown in red. The light red circle around the particle has a radius equivalent to the interaction range or the cutoff radius (r_c), respectively. Interaction takes place only between the selected particle and particles within this radius. The cell of the selected particle as well as the neighboring cells are shaded in blue. Distances have to be computed between the selected particle and the ones in the blue area only.

is independent of the system size and therefore the scaling factor of the energy computation is reduced to N . The number of neighboring cells depends on the dimensionality of the simulation and is $3^d - 1$ ($d = 2 \rightarrow 8$; $d = 3 \rightarrow 26$). The identity of the cell a particle is located in is uniquely defined by the coordinates of the particle, and can be updated once the particle has moved.

Clearly cell lists only offer a speed gain if the cutoff radius of the interaction potential is less or equal than a quarter of the simulation box.

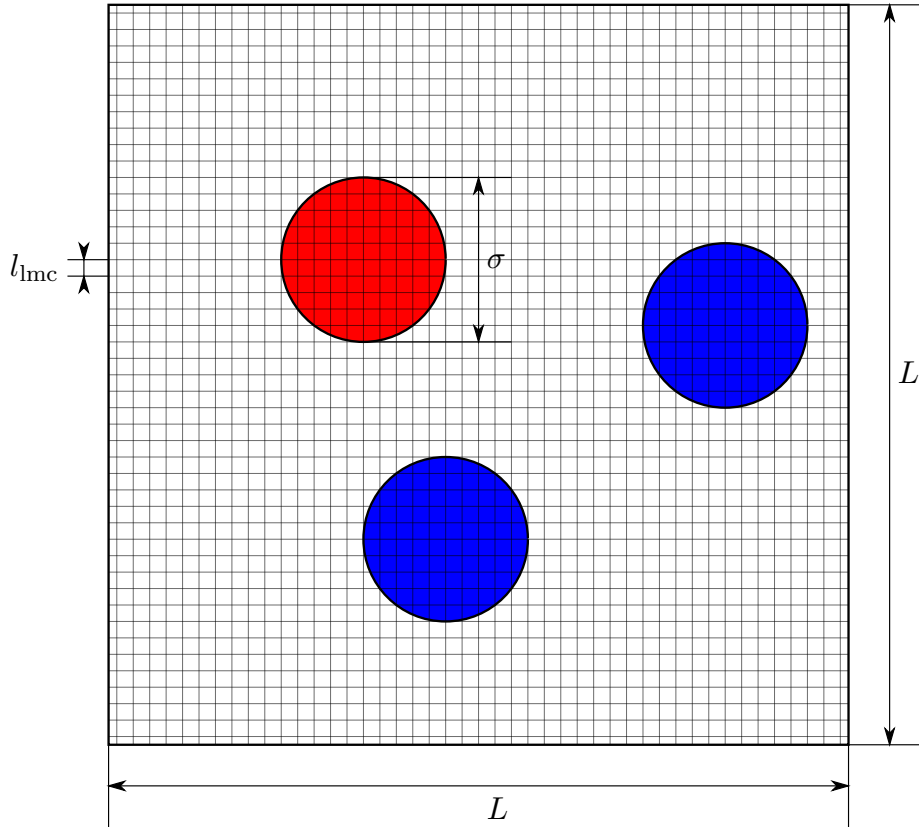


Figure 4.6: Lattice MC method: grid spacing (l_{lmc}) and particle diameter (σ) shown for a lattice discretisation parameter of $\zeta = 10$.

Lattice Monte Carlo

The advantage of lattice MC simulations compared to continuum simulations is their computational efficiency due to the possible tabulation of the interaction potential. It is obvious that on a square lattice the squared distance between two arbitrary lattice points (r^2) is always an integer multiple of the square of the lattice spacing (l_{lmc}^2). Therefore the interaction $\Phi(r)$ for all possible distances can be computed at the beginning of the simulation and stored in an array (of suitable size), the computationally expensive evaluation of the interaction potential can then be replaced by a simple look-up operation on that array.

However in order to replace a continuum simulation by a simulation on a lattice one has to ensure that both yield the same results. The equivalence of continuum models and suitable lattice models was first investigated by Panagiotopolous [34, 35]. Here the term "suitable" means that the lattice has to be spaced fine enough so that the results match the ones of continuum simulations. To quantify the approach towards

continuum Panagiotopoulos *et al.* introduced the dimensionless lattice discretisation parameter (ζ), which they defined as

$$\zeta = \frac{\text{particle diameter } (\sigma)}{\text{lattice spacing } (l_{\text{lmc}})}. \quad (4.24)$$

It is obvious that the lattice discretisation parameter controls how close the lattice resembles continuum conditions. Clearly lattice artifacts should decrease with increasing lattice discretisation parameter.

Panagiotopoulos *et al.* found out that lattice simulations with a lattice discretisation parameter of $\zeta = 1$ or 2 result in a qualitative different phase behavior than continuum models, whereas lattice simulations with $\zeta \geq 3$ yield the qualitative correct continuum phase behavior for the restricted primitive model [34]. In a following up work [35] Panagiotopoulos stated that ζ has to be equal or greater than 10 for a lattice MC simulation to produce the same critical parameters and radial distribution functions (within simulation accuracy) as a continuum simulation (given a Lennard-Jones or Buckingham exponential-6 potential in three dimensions).

Panagiotopoulos *et al.* report that the computational gain of lattice MC simulations compared to simple continuum simulations is approximately a factor of 100 for ionic solutions (due to the replacing of the computationally costly Ewald summation) [34] and a factor of about 10 and 20 for Lennard-Jones and Buckingham exponential-6 potentials, respectively [35]. This computational gain can be invested to simulate larger systems or longer time scales, which is both important in this work.

4.1.4 MC Dynamics

First attempts to use MC simulations to study *dynamic* properties were made as early as 1991 [36], but this study is limited to one-dimensional systems.

In 1998 Gleim *et al.* reported that the long time relaxation, namely the α -relaxation, of a supercooled Lennard-Jones mixture is independent of the microscopic dynamics [31]. The authors compared Newtonian dynamics and stochastic dynamics for their system and found that the curves of the self intermediate scattering function coincided in the α -relaxation regime, when the time-scale was adjusted accordingly. In the same year Huitema *et al.* tested this idea to use Monte Carlo simulations on a Lennard-Jones system to compute the velocity auto-correlation function [33]. They used the equivalence of the self diffusion coefficient computed by MC simulations and Molecular Dynamics simulations respectively to adjust the time scale of the MC simulations, calibrating the time scale of the MC simulations in that way. Moreover they argued that the configurational changes in the MC simulations have to correspond to real events in the stochastic system, limiting MC simulations to displacement moves with small maximum displacement. As expected the velocity auto-correlation showed different behavior in the short time regime, due to the different underlying dynamics, namely the memory effect observed in Molecular Dynamics simulations in contrast to the fact that the direction of a move in MC simulations is not correlated to the direction of the previous move. Nevertheless the study showed that the behavior of the velocity auto-correlation function in the long time regime was similar.

In the light of these studies MC simulations are used in this thesis to compute dynamic properties of the systems under investigation. Since our system represents a colloid with effective interactions (solvent degrees of freedom are integrated out see chapter 2) a stochastic dynamic is more appropriate than Newtonian Dynamics, in addition we are mainly interested in the long time behavior which is similar for the different types of dynamics. Moreover different studies [37, 38] suggest that MC simulations are computational more efficient since larger steps can be used than in algorithms solving the equations of motion.

4.2 Integral Equations

4.2.1 Ornstein-Zernike Equation

To derive the Ornstein-Zernike equations, a system in the presence of an external field $w(\mathbf{r})$ is considered here, following chapter 3 of [27]. As in previous chapters equations will be given for the two-dimensional case, when depending on the dimensionality. The microscopic particle density $\rho(\mathbf{r})$ can be written as a sum of δ -functions

$$\rho(\mathbf{r}) = \sum_{i=1}^N \delta(\mathbf{r} - \mathbf{r}_i), \quad (4.25)$$

with the N particles at positions \mathbf{r}_i ($1 \leq i \leq N$). The one-particle density $\rho^{(1)}(\mathbf{r})$ can then be identified as the ensemble average of the microscopic particle density $\rho(\mathbf{r})$ via equation (3.86)

$$\rho^{(1)}(\mathbf{r}) = \langle \rho(\mathbf{r}) \rangle = \left\langle \sum_{i=1}^N \delta(\mathbf{r} - \mathbf{r}_i) \right\rangle. \quad (4.26)$$

Using the microscopic particle density given in equation (4.25) the potential energy due to the external field $\mathcal{W}_N(\mathbf{r}^N)$ can be written as

$$\mathcal{W}_N(\mathbf{r}^N) = \sum_{i=1}^N w(\mathbf{r}_i) = \int \rho(\mathbf{r}) w(\mathbf{r}) d\mathbf{r}, \quad (4.27)$$

resulting in a Hamiltonian of the system given by

$$\mathcal{H}(\mathbf{r}^N, \mathbf{p}^N) = \mathcal{K}_N(\mathbf{p}^N) + \mathcal{U}_N(\mathbf{r}^N) + \mathcal{W}_N(\mathbf{r}^N) \quad (4.28)$$

Density fluctuations in the system can be quantified by the density-density correlation function $H^{(2)}(\mathbf{r}, \mathbf{r}')$, which is defined as

$$\begin{aligned} H^{(2)}(\mathbf{r}, \mathbf{r}') &= \left\langle [\rho(\mathbf{r}) - \langle \rho(\mathbf{r}) \rangle] [\rho(\mathbf{r}') - \langle \rho(\mathbf{r}') \rangle] \right\rangle \\ &= \rho^{(2)}(\mathbf{r}, \mathbf{r}') + \rho^{(1)}(\mathbf{r})\delta(\mathbf{r} - \mathbf{r}') - \rho^{(1)}(\mathbf{r})\rho^{(1)}(\mathbf{r}') \\ &= \rho^{(1)}(\mathbf{r})\rho^{(1)}(\mathbf{r}')h^{(2)}(\mathbf{r}, \mathbf{r}') + \rho^{(1)}(\mathbf{r})\delta(\mathbf{r} - \mathbf{r}'), \end{aligned} \quad (4.29)$$

where $\rho^{(2)}(\mathbf{r}, \mathbf{r}')$ denotes the two-particle density introduced by equations (3.75) and (3.76) for $n = 2$, while the total pair-correlation function $h^{(2)}(\mathbf{r}, \mathbf{r}')$ is related to the pair-distribution function $g^{(2)}(\mathbf{r}, \mathbf{r}')$ (introduced in section 3.4, equation (3.84)) via the simple relation

$$h^{(2)}(\mathbf{r}, \mathbf{r}') = g^{(2)}(\mathbf{r}, \mathbf{r}') - 1. \quad (4.30)$$

In order to obtain an expression for the grand-canonical partition function of the system, interacting with the external field, the Hamiltonian from equation (4.28) has to be inserted into equation (3.42) resulting in

$$\Xi = \sum_{N=0}^{\infty} \frac{1}{N!} \int \dots \int \exp(-\beta\mathcal{U}_N) \left(\prod_{i=1}^N z \exp[-\beta w(\mathbf{r}_i)] \right) d\mathbf{r}_1 \dots d\mathbf{r}_N, \quad (4.31)$$

with the activity z given by equation (3.43). Defining the intrinsic chemical potential $\psi(\mathbf{r})$ as

$$\psi(\mathbf{r}) = \mu - w(\mathbf{r}), \quad (4.32)$$

the grand-canonical partition function can be rewritten as

$$\Xi = \sum_{N=0}^{\infty} \frac{1}{N!} \int \dots \int \exp(-\beta\mathcal{U}_N) \left(\prod_{i=1}^N \frac{1}{\Lambda^2} \exp[\beta\psi(\mathbf{r}_i)] \right) d\mathbf{r}_1 \dots d\mathbf{r}_N. \quad (4.33)$$

Incorporating the Hamiltonian from equation (4.28) into the definition of the n -particle density given by equation (3.75) results in

$$\rho^{(n)}(\mathbf{r}_1 \dots \mathbf{r}_n) = \frac{1}{\Xi} \sum_{N=n}^{\infty} \frac{1}{(N-n)!} \int \dots \int \exp(-\beta\mathcal{U}_N) \left(\prod_{i=1}^N z \exp[-\beta w(\mathbf{r}_i)] \right) d\mathbf{r}_{n+1} \dots d\mathbf{r}_N \quad (4.34)$$

In the following it is assumed that the interaction of the particles of the system with the confining walls is included in the external potential $w(\mathbf{r})$ by setting $w(\mathbf{r}) = \infty$ outside the accessible area V of the system.

In that way an infinitesimal change in the system area dV , of a system under the influence of an external field $w(\mathbf{r})$, can also be written in terms of a variation in the function of the external field $\delta w(\mathbf{r})$. The total differential of the Helmholtz free energy, given by equation (3.21), can therefore be written as

$$\delta F = -S\delta T + \int \rho^{(1)}(\mathbf{r})\delta w(\mathbf{r})d\mathbf{r} + \mu\delta N, \quad (4.35)$$

in terms of the variation in the functional form of the external field $\delta w(\mathbf{r})$.

Defining the intrinsic free energy \mathcal{F} as the contribution of the Helmholtz free energy not explicitly dependent on the external potential $w(\mathbf{r})$

$$\mathcal{F} = F - \int \rho^{(1)}(\mathbf{r})w(\mathbf{r})d\mathbf{r}, \quad (4.36)$$

in analogy to the intrinsic chemical potential $\psi(\mathbf{r})$, results in a total differential of \mathcal{F} given by

$$\begin{aligned} \delta\mathcal{F} &= -S\delta T - \int \delta\rho^{(1)}(\mathbf{r})w(\mathbf{r})d\mathbf{r} - \mu\delta N \\ &= -S\delta T + \int \delta\rho^{(1)}(\mathbf{r})\psi(\mathbf{r})d\mathbf{r}, \end{aligned} \quad (4.37)$$

using the intrinsic chemical potential $\psi(\mathbf{r})$ defined in equation (4.32).

The grand potential of the system can then be written as

$$\Omega = \mathcal{F} + \int \rho^{(1)}(\mathbf{r})w(\mathbf{r})d\mathbf{r} - \mu N, \quad (4.38)$$

with its total differential given by

$$\begin{aligned} \delta\Omega &= -S\delta T + \int \rho^{(1)}(\mathbf{r})\delta w(\mathbf{r})d\mathbf{r} - N\delta\mu \\ &= -S\delta T - \int \rho^{(1)}(\mathbf{r})\delta\psi(\mathbf{r})d\mathbf{r}. \end{aligned} \quad (4.39)$$

Combining the Hamiltonian of equation (4.28) with equations (3.41) and (3.50) the logarithm of the grand canonical probability density $f(\mathbf{r}^N, \mathbf{p}^N; N)$ can be expressed as

$$\ln f(\mathbf{r}^N, \mathbf{p}^N; N) = \beta\Omega - \beta\mathcal{K}_N - \beta\mathcal{U}_N - \beta\mathcal{W}_N + \beta N\mu. \quad (4.40)$$

By reordering, averaging and use of equations (4.27) and (4.32) the above relation can be rewritten as

$$\left\langle \mathcal{K}_N + \mathcal{U}_N + k_B T \ln f(\mathbf{r}^N, \mathbf{p}^N; N) \right\rangle = \Omega + \int \rho^{(1)}(\mathbf{r})\psi(\mathbf{r})d\mathbf{r} = \mathcal{F}. \quad (4.41)$$

Without particle-particle interactions the intrinsic chemical potential $\psi(\mathbf{r})$ is given by

$$\psi^{\text{id}}(\mathbf{r}) = k_B T \ln \left[\Lambda^2 \rho^{(1)}(\mathbf{r}) \right]. \quad (4.42)$$

The (total) chemical potential of an ideal gas interacting with the external potential $w(\mathbf{r})$ is then given by

$$\mu^{\text{id}} = k_B T \ln \left[\Lambda^2 \rho^{(1)}(\mathbf{r}) \right] + w(\mathbf{r}), \quad (4.43)$$

which can be rewritten as

$$\rho^{(1)}(\mathbf{r}) = z^{\text{id}} \exp[-\beta w(\mathbf{r})], \quad (4.44)$$

using $z^{\text{id}} = \exp(\beta\mu^{\text{id}})/\Lambda^2$ (see equation (3.43)) for the activity of the ideal gas. To calculate the intrinsic free energy of the ideal gas, we use equation (4.41)

$$\mathcal{F} = \Omega + \int \rho^{(1)}(\mathbf{r})\psi(\mathbf{r})d\mathbf{r}. \quad (4.45)$$

The grand potential of the ideal gas is given by

$$\Omega^{\text{id}} = -k_B T \rho V, \quad (4.46)$$

it can be rewritten for the inhomogeneous case as

$$\Omega^{\text{id}} = -k_B T \int \rho^{(1)}(\mathbf{r})d\mathbf{r}. \quad (4.47)$$

Finally the intrinsic free energy of the ideal gas can be written as

$$\mathcal{F}^{\text{id}} = k_{\text{B}}T \int \rho^{(1)}(\mathbf{r}) \left(\ln \left[\Lambda^2 \rho^{(1)}(\mathbf{r}) \right] - 1 \right) \mathrm{d}\mathbf{r}, \quad (4.48)$$

which is equivalent to equation (3.33) for the homogeneous case $\rho(\mathbf{r}) = \rho$.

It can be immediately seen from equation (4.37), that the functional derivative of the intrinsic free energy $\mathcal{F}[\rho^{(1)}]$ with respect to $\rho^{(1)}$ at constant temperature T is given by

$$\frac{\delta \mathcal{F}[\rho^{(1)}]}{\delta \rho^{(1)}(\mathbf{r})} = \psi(\mathbf{r}), \quad (4.49)$$

the intrinsic chemical potential. For an introduction of functional derivatives see section 3.2 of [27]. Similar as the free energy, the intrinsic free energy can be split into an ideal and an excess part

$$\mathcal{F}[\rho^{(1)}] = \mathcal{F}^{\text{id}}[\rho^{(1)}] + \mathcal{F}^{\text{ex}}[\rho^{(1)}], \quad (4.50)$$

where the ideal part is given by equation (4.48). Using the above equations, it is easy to verify that the functional derivative of the intrinsic free energy of the ideal gas with respect to the one-particle density $\rho^{(1)}(\mathbf{r})$ is given by

$$\frac{\delta \mathcal{F}^{\text{id}}[\rho^{(1)}]}{\delta \rho^{(1)}(\mathbf{r})} = k_{\text{B}}T \ln \left[\Lambda^2 \rho^{(1)}(\mathbf{r}) \right] = \psi^{\text{id}}(\mathbf{r}), \quad (4.51)$$

the intrinsic chemical potential of the ideal gas (compare with equation (4.42)).

The functional derivative of the grand potential $\Omega[\psi]$ with respect to the intrinsic chemical potential $\psi(\mathbf{r})$ can be easily obtained from equation (4.39) as

$$\frac{\delta \Omega[\psi]}{\delta \psi(\mathbf{r})} = -\rho^{(1)}(\mathbf{r}). \quad (4.52)$$

Combining equations (4.45) and (4.52) one can see that the functionals for the intrinsic free energy $\mathcal{F}[\rho^{(1)}]$ and the grand potential $\Omega[\psi]$ are connected by a generalized Laplace transform

$$\Omega[\psi] - \int \psi(\mathbf{r}) \frac{\delta \Omega[\psi]}{\delta \psi(\mathbf{r})} \mathrm{d}\mathbf{r} = \Omega[\psi] + \int \psi(\mathbf{r}) \rho^{(1)}(\mathbf{r}) \mathrm{d}\mathbf{r} = \mathcal{F}[\rho^{(1)}]. \quad (4.53)$$

In the limit of vanishing external field $w \rightarrow 0$ the one-particle density $\rho^{(1)}$ is given by $\langle N \rangle / V$ and the intrinsic free energy ψ is given by the chemical potential μ . In this limit, the functional derivatives in equations (4.49) and (4.52) are replaced by the thermodynamic standard relations $\partial F / \partial N = \mu$ and $\partial \Omega / \partial \mu = -N$.

In order to compute higher order functional derivatives of the grand potential $\Omega[w]$ with respect to the intrinsic chemical potential ψ the functional derivative $\delta \Omega[\psi] / \delta \psi(\mathbf{r})$ is expressed in a different way utilizing $\Omega = -k_{\text{B}}T \ln \Xi$ (equation (3.50)).

Using the local activity $z^*(\mathbf{r})$ given by

$$z^*(\mathbf{r}) = \frac{\exp[\beta \psi(\mathbf{r})]}{\Lambda^2} = z \exp[-\beta w(\mathbf{r})], \quad (4.54)$$

the grand partition function Ξ (equation (4.33)) can be written as

$$\Xi = \sum_{N=0}^{\infty} \frac{1}{N!} \int \dots \int \exp(-\beta\mathcal{U}_N) \left(\prod_{i=1}^N z^*(\mathbf{r}_i) \right) d\mathbf{r}_1 \dots d\mathbf{r}_N. \quad (4.55)$$

It can be seen from the definition of the local activity $z^*(\mathbf{r})$ (equation (4.54)), that the functional differential of a thermodynamic quantity with respect to the intrinsic chemical potential ψ can be rewritten as a functional differential with respect to the local activity z^*

$$\frac{\delta}{\delta\psi(\mathbf{r})} = \beta z^*(\mathbf{r}) \frac{\delta}{\delta z^*(\mathbf{r})} \quad (4.56)$$

at constant temperature T . The functional derivative $\delta\Omega[\psi]/\delta\psi$ is thus given by

$$\frac{\delta\Omega[\psi]}{\delta\psi(\mathbf{r}_1)} = -k_B T \frac{\delta \ln \Xi}{\delta\psi(\mathbf{r}_1)} = -\frac{z^*(\mathbf{r}_1)}{\Xi} \frac{\delta\Xi}{\delta z^*(\mathbf{r}_1)} \quad (4.57)$$

with

$$\frac{\delta\Xi}{\delta z^*(\mathbf{r}_1)} = \sum_{N=1}^{\infty} \frac{1}{(N-1)!} \int \dots \int \exp(-\beta\mathcal{U}_N) \left(\prod_{i=2}^N z^*(\mathbf{r}_i) \right) d\mathbf{r}_2 \dots d\mathbf{r}_N. \quad (4.58)$$

Combining equations (4.57) and (4.58) with the definition of the one-particle density (equation (4.34) for $n=1$) shows that equation (4.52) is indeed fulfilled.

More generally the grand partition functional acts as generating function for the n -particle densities via

$$\rho^{(n)}(\mathbf{r}_1 \dots \mathbf{r}_n) = \frac{z^*(\mathbf{r}_1) \dots z^*(\mathbf{r}_n)}{\Xi} \frac{\delta^n \Xi}{\delta z^*(\mathbf{r}_1) \dots \delta z^*(\mathbf{r}_n)}, \quad (4.59)$$

which can be seen from higher order functional derivatives of the grand partition function Ξ with respect to the local activity z^* and equation (4.34).

The second functional derivative of the grand potential Ω with respect to the intrinsic chemical potential is given by

$$\begin{aligned} \frac{\delta^2\Omega[\psi]}{\delta\psi(\mathbf{r}_1)\delta\psi(\mathbf{r}_2)} &= -\beta z^*(\mathbf{r}_2) \frac{\delta}{\delta z^*(\mathbf{r}_2)} \left(\frac{1}{\Xi} z^*(\mathbf{r}_1) \frac{\delta\Xi}{\delta z^*(\mathbf{r}_1)} \right) \\ &= -\beta \left[-\frac{1}{\Xi^2} z^*(\mathbf{r}_1) z^*(\mathbf{r}_2) \frac{\delta\Xi}{\delta z^*(\mathbf{r}_1)} \frac{\delta\Xi}{\delta z^*(\mathbf{r}_2)} \right. \\ &\quad \left. + \delta(\mathbf{r}_1 - \mathbf{r}_2) \frac{1}{\Xi} z^*(\mathbf{r}_2) \frac{\delta\Xi}{\delta z^*(\mathbf{r}_1)} \right. \\ &\quad \left. + \frac{1}{\Xi} z^*(\mathbf{r}_1) z^*(\mathbf{r}_2) \frac{\delta^2\Xi}{\delta z^*(\mathbf{r}_1)\delta z^*(\mathbf{r}_2)} \right] \end{aligned} \quad (4.60)$$

which can be rewritten as

$$\frac{\delta^2\Omega[\psi]}{\delta\psi(\mathbf{r}_1)\delta\psi(\mathbf{r}_2)} = \beta \left[\rho^{(1)}(\mathbf{r}_1)\rho^{(1)}(\mathbf{r}_2) - \rho^{(1)}(\mathbf{r}_1)\delta(\mathbf{r}_1 - \mathbf{r}_2) - \rho^{(2)}(\mathbf{r}_1, \mathbf{r}_2) \right] \quad (4.61)$$

using equation (4.59). However equation (4.61) can be further simplified to

$$\frac{\delta^2\Omega[\psi]}{\delta\psi(\mathbf{r}_1)\delta\psi(\mathbf{r}_2)} = -\beta H^{(2)}(\mathbf{r}_1, \mathbf{r}_2) \quad (4.62)$$

by using the definition of the density-density correlation function $H(\mathbf{r}_1, \mathbf{r}_2)$ (equation (4.29)).

More generally, the higher order functional derivatives of the grand potential Ω are related to the higher order density-density correlation functions $H^{(n)}(\mathbf{r}_1, \dots, \mathbf{r}_n)$ via

$$-H^{(n)}(\mathbf{r}_1, \dots, \mathbf{r}_n) = \frac{\delta^n \beta \Omega[\psi]}{\delta(\beta\psi(\mathbf{r}_1)) \dots \delta(\beta\psi(\mathbf{r}_n))}. \quad (4.63)$$

The n -particle direct correlation functions can be defined as functional derivatives of the intrinsic free energy \mathcal{F}^{ex} with respect to the one-particle density $\rho^{(1)}(\mathbf{r})$. For the one-particle direct correlation function $c^{(1)}$ this is given by

$$c^{(1)}(\mathbf{r}) = -\beta \frac{\delta \mathcal{F}^{\text{ex}}[\rho^{(1)}]}{\delta \rho^{(1)}(\mathbf{r})}. \quad (4.64)$$

The two-particle direct-correlation function is related to the second-order functional derivative of \mathcal{F}^{ex} with respect to the one-particle $\rho^{(1)}(\mathbf{r})$ density via

$$c^{(2)}(\mathbf{r}, \mathbf{r}') = \frac{\delta c^{(1)}(\mathbf{r})}{\delta \rho^{(1)}(\mathbf{r}')} = -\beta \frac{\delta^2 \mathcal{F}^{\text{ex}}[\rho^{(1)}]}{\delta \rho^{(1)}(\mathbf{r}) \delta \rho^{(1)}(\mathbf{r}')}. \quad (4.65)$$

N -particle direct-correlation functions are constructed from the lower order ones similar to equation (4.65).

Combining equations (4.49), (4.51) and (4.64) results in

$$\beta\psi(\mathbf{r}) = \beta \frac{\delta \mathcal{F}[\rho^{(1)}]}{\delta \rho^{(1)}(\mathbf{r})} = \ln \left[\Lambda^2 \rho^{(1)}(\mathbf{r}) \right] - c^{(1)}(\mathbf{r}), \quad (4.66)$$

with $k_B T \ln [\Lambda^2 \rho^{(1)}(\mathbf{r})]$ being the ideal part of the chemical potential μ^{id} as well as the ideal part of the intrinsic chemical potential ψ^{id} , the term $-k_B T c^{(1)}(\mathbf{r})$ can be identified as the excess part of the intrinsic chemical potential $\psi^{\text{ex}}(\mathbf{r})$. Using the definition of the activity $z = \exp(\beta\mu)/\Lambda^2$ together with $\psi(\mathbf{r}) = \mu - w(\mathbf{r})$, equation (4.66) can be rewritten to

$$\rho^{(1)}(\mathbf{r}) = z \exp \left[-\beta w(\mathbf{r}) + c^{(1)}(\mathbf{r}) \right]. \quad (4.67)$$

Without external field $w(\mathbf{r}) = 0$, equation (4.66) can be written as

$$-k_B T c^{(1)} = \mu - k_B T \ln [\Lambda^2 \rho] = \mu^{\text{ex}}, \quad (4.68)$$

in this case the quantity $-k_B T c^{(1)}$ is also equal to the excess chemical potential μ^{ex} . The density-density correlation function $H^{(2)}(\mathbf{r}, \mathbf{r}')$ can be written in terms of a first order functional derivative of the one-particle density $\rho^{(1)}(\mathbf{r})$ with respect to the intrinsic chemical potential $\psi(\mathbf{r})$ as

$$H(\mathbf{r}, \mathbf{r}') = k_B T \frac{\delta \rho^{(1)}(\mathbf{r})}{\delta \psi(\mathbf{r}')}, \quad (4.69)$$

omitting the superscript (2) in equation (4.69) and the following derivation to improve the readability.

The inverse of the density-density correlation can be defined by means of

$$\int H^{-1}(\mathbf{r}, \mathbf{r}'') H(\mathbf{r}'', \mathbf{r}') d\mathbf{r}'' = \delta(\mathbf{r} - \mathbf{r}') \quad (4.70)$$

with

$$H^{-1}(\mathbf{r}, \mathbf{r}') = \beta \frac{\delta \psi(\mathbf{r})}{\delta \rho^{(1)}(\mathbf{r}')}. \quad (4.71)$$

Using equation (4.66), $H^{-1}(\mathbf{r}, \mathbf{r}')$ can be written as

$$\begin{aligned} H^{-1}(\mathbf{r}, \mathbf{r}') &= \frac{\delta}{\delta \rho^{(1)}(\mathbf{r}')} (\beta \psi(\mathbf{r})) \\ &= \frac{\delta}{\delta \rho^{(1)}(\mathbf{r}')} \left(\ln \left[\Lambda^2 \rho^{(1)}(\mathbf{r}) \right] - c^{(1)}(\mathbf{r}) \right) \\ &= \frac{1}{\rho^{(1)}(\mathbf{r})} \delta(\mathbf{r} - \mathbf{r}') - c^{(2)}(\mathbf{r}, \mathbf{r}'). \end{aligned} \quad (4.72)$$

Substituting $H^{-1}(\mathbf{r}, \mathbf{r}')$ and $H(\mathbf{r}, \mathbf{r}')$ in equation (4.70) with equations (4.29) and (4.72) and carrying out the integration over \mathbf{r}'' results in

$$\begin{aligned} \delta(\mathbf{r} - \mathbf{r}') &= \int \left(\frac{1}{\rho^{(1)}(\mathbf{r})} \delta(\mathbf{r} - \mathbf{r}'') - c^{(2)}(\mathbf{r}, \mathbf{r}'') \right) \times \\ &\quad \times \left(\rho^{(1)}(\mathbf{r}'') \rho^{(1)}(\mathbf{r}') h^{(2)}(\mathbf{r}'', \mathbf{r}') + \rho^{(1)}(\mathbf{r}'') \delta(\mathbf{r}'' - \mathbf{r}') \right) d\mathbf{r}'' \\ &= \rho^{(1)}(\mathbf{r}') h^{(2)}(\mathbf{r}, \mathbf{r}') + \delta(\mathbf{r} - \mathbf{r}') - \rho^{(1)}(\mathbf{r}') c^{(2)}(\mathbf{r}, \mathbf{r}') \\ &\quad - \rho^{(1)}(\mathbf{r}') \int c^{(2)}(\mathbf{r}, \mathbf{r}'') \rho^{(1)}(\mathbf{r}'') h^{(2)}(\mathbf{r}'', \mathbf{r}') d\mathbf{r}'', \end{aligned} \quad (4.73)$$

which finally leads to the Ornstein-Zernike equation

$$h^{(2)}(\mathbf{r}, \mathbf{r}') = c^{(2)}(\mathbf{r}, \mathbf{r}') + \int c^{(2)}(\mathbf{r}, \mathbf{r}'') \rho^{(1)}(\mathbf{r}'') h^{(2)}(\mathbf{r}'', \mathbf{r}') d\mathbf{r}''. \quad (4.74)$$

The total correlation function $h^{(2)}(\mathbf{r}, \mathbf{r}')$ on the right-hand side of the Ornstein-Zernike equation can be recursively substituted by the left-hand side of the Ornstein-Zernike equation resulting in

$$\begin{aligned}
h^{(2)}(\mathbf{r}_1, \mathbf{r}_2) &= c^{(2)}(\mathbf{r}_1, \mathbf{r}_2) \\
&+ \int c^{(2)}(\mathbf{r}_1, \mathbf{r}_3) \rho^{(1)}(\mathbf{r}_3) h^{(2)}(\mathbf{r}_3, \mathbf{r}_2) d\mathbf{r}_3 \\
&+ \iint c^{(2)}(\mathbf{r}_1, \mathbf{r}_3) \rho^{(1)}(\mathbf{r}_3) c^{(2)}(\mathbf{r}_3, \mathbf{r}_4) \rho^{(1)}(\mathbf{r}_4) c^{(2)}(\mathbf{r}_4, \mathbf{r}_2) d\mathbf{r}_3 d\mathbf{r}_4 \\
&+ \dots
\end{aligned} \tag{4.75}$$

The interpretation of this formal solution to the Ornstein-Zernike equation is that the total correlation $h^{(2)}(\mathbf{r}_1, \mathbf{r}_2)$ is given by the direct correlation $c^{(2)}(\mathbf{r}_1, \mathbf{r}_2)$ between the particles in question and terms arising from indirect correlations transmitted via an increasing number of intermediate particles. This makes it plausible to assume that the range of the direct correlation function $c^{(2)}(\mathbf{r}_1, \mathbf{r}_2)$ is the same order of magnitude as the range of the pair potential, while the range of the total correlation function $h^{(2)}(\mathbf{r}_1, \mathbf{r}_2)$ can be much larger.

For an uniform and isotropic fluid the Ornstein-Zernike equation (4.74) reduces to

$$h(r) = c(r) + \rho \int c(|\mathbf{r} - \mathbf{r}'|) h(r') d\mathbf{r}', \tag{4.76}$$

which becomes an algebraic equation when transferred to k -space via Fourier transformation

$$\hat{h}(k) = \hat{c}(k) + \rho \hat{c}(k) \hat{h}(k). \tag{4.77}$$

4.2.2 Closure Relations

The Ornstein-Zernike equation (4.76) by itself is of limited use, since both the total correlation function $h(r)$ as well as the direct correlation function $c(r)$ are unknown. Therefor another independent equation, combining the total and direct correlation functions, using the interaction potential $\Phi(r)$ of the particles, a so called closure relation, is needed, in order to obtain a solvable system of equations. Unfortunately, up to now, no exact closure relation for the Ornstein-Zernike equation has been found, that would allow the solution of the resulting system of equations with reasonable (computational) effort. However, there exist a number of approximate closure relations, that can be used to obtain a solvable system of equations together with the Ornstein-Zernike relation. The two (approximate) closure relations used in this work, namely the hypernetted chain closure (HNC) and the Percus-Yevick closure (PY) will be introduced in this section.

The approximate nature of the integral equations used in this thesis purely arises from the approximations made in the closure relations.

For the derivation of the hypernetted chain and the Percus-Yevick closure we will follow section 4.3 and 4.4 of [27] which uses the idea of Percus, placing a particle (index 0) of the system at the coordinate $\mathbf{r} = 0$ in an otherwise homogeneous system of N particles and calculating its effects on the system [39].

The external field $w(\mathbf{r})$ created by the 0-particle fixed at $\mathbf{r} = 0$ is given by

$$w(\mathbf{r}) = \Phi(0, \mathbf{r}), \quad (4.78)$$

where $\Phi(\mathbf{r}, \mathbf{r}')$ is the particle-particle interaction of the system. The total potential energy of the system is then the sum of the potential energy due to the pair interaction of the particles, \mathcal{U}_N , and the potential energy due to the external field of particle 0 at position $\mathbf{r} = 0$. Since the interaction of the 0-particle is the same as the interaction between all the other particles, the total potential energy can also be written as sum of the particle-particle interactions of a system of $N + 1$ particles (\mathcal{U}_{N+1}) without an external field

$$\mathcal{U}_N + \sum_{i=1}^N w(\mathbf{r}_i) = \sum_{i=1}^N \sum_{j>i}^N \Phi(\mathbf{r}_i, \mathbf{r}_j) + \sum_{i=1}^N \Phi(0, \mathbf{r}_i) = \sum_{i=1}^{N+1} \sum_{j>i}^{N+1} \Phi(\mathbf{r}_i, \mathbf{r}_j) = \mathcal{U}_{N+1}. \quad (4.79)$$

Using equation (4.31) the grand partition function of this system can be written as

$$\begin{aligned} \Xi[w] &= \sum_{N=0}^{\infty} \frac{1}{N!} \int \dots \int \exp(-\beta \mathcal{U}_N) \left(\prod_{i=1}^N z \exp(-\beta \Phi(0, \mathbf{r}_i)) \right) d\mathbf{r}_1 \dots d\mathbf{r}_N \\ &= \sum_{N=0}^{\infty} \frac{z^N}{N!} \int \dots \int \exp(-\beta \mathcal{U}_{N+1}) d\mathbf{r}_1 \dots d\mathbf{r}_N \\ &= \frac{\Xi_0}{z} \sum_{N=0}^{\infty} \frac{1}{\Xi_0} \frac{z^{N+1}}{N!} \int \dots \int \exp(-\beta \mathcal{U}_{N+1}) d\mathbf{r}_1 \dots d\mathbf{r}_N, \end{aligned} \quad (4.80)$$

with Ξ_0 being the grand partition function of the system without the "external" field due to particle 0.

Replacing N by $N - 1$ in the last line of equation (4.80) changes the lower bound of the sum from zero to one, the respective change from \mathcal{U}_{N+1} to \mathcal{U}_N is possible because the particle-particle interaction $\Phi(\mathbf{r}, \mathbf{r}')$ for the 0-particle is the same than for the other particles and therefor the structure of the potential energy is the same for a $(N + 1)$ -particle system without external field (compare equation (4.79))

$$\Xi[w] = \frac{\Xi_0}{z} \sum_{N=1}^{\infty} \frac{1}{\Xi_0} \frac{z^N}{(N-1)!} \int \dots \int \exp(-\beta \mathcal{U}_N) d\mathbf{r}_1 \dots d\mathbf{r}_{N-1}. \quad (4.81)$$

The sum in equation (4.81) can be identified as the grand canonical one-particle density $\rho^{(1)}(\mathbf{r})$ of the homogeneous system (without particle 0), using the definition of the n -particle density equation (3.76) with $n = 1$,

$$\Xi[w] = \frac{\Xi_0}{z} \rho^{(1)}(\mathbf{r}|w = 0). \quad (4.82)$$

Equation (4.82) relates the grand partition function of the inhomogeneous system $\Xi[w]$ with the grand partition function Ξ_0 and the one-particle density $\rho^{(1)}(\mathbf{r}|w = 0)$ of the homogeneous system.

Adopting the idea of Percus for the one-particle density of the inhomogeneous system using equation (4.34) results in

$$\begin{aligned}\rho^{(1)}(r|w) &= \frac{1}{\Xi[w]} \sum_{N=1}^{\infty} \frac{1}{(N-1)!} \int \dots \int \exp(-\beta\mathcal{U}_N) \left(\prod_{i=1}^N z \exp(-\beta\Phi(0, \mathbf{r}_i)) \right) d\mathbf{r}_1 \dots d\mathbf{r}_{N-1} \\ &= \frac{1}{\rho(\mathbf{r}|w=0)} \frac{1}{\Xi_0} \sum_{N=1}^{\infty} \frac{z^{N+1}}{(N-1)!} \int \dots \int \exp(-\beta\mathcal{U}_{N+1}) d\mathbf{r}_1 \dots d\mathbf{r}_{N-1},\end{aligned}\tag{4.83}$$

while applying equation (4.82) to replace $\Xi[w]$ by Ξ_0 and equation (4.79) to replace \mathcal{U}_N by \mathcal{U}_{N+1} respectively. Substituting N by $N-1$ in the last line of equation (4.83), similar as above, changes the lower bound of the sum from one to two, leading to

$$\begin{aligned}\rho^{(1)}(r|w) &= \frac{1}{\rho(\mathbf{r}|w=0)} \sum_{N=2}^{\infty} \frac{1}{\Xi_0} \frac{z^N}{(N-2)!} \int \dots \int \exp(-\beta\mathcal{U}_N) d\mathbf{r}_1 \dots d\mathbf{r}_{N-2} \\ &= \frac{1}{\rho(\mathbf{r}|w=0)} \rho^{(2)}(\mathbf{r}, \mathbf{r}'|w=0).\end{aligned}\tag{4.84}$$

We identify the sum in the first line of equation (4.84) as the two-particle density $\rho^{(2)}(\mathbf{r}, \mathbf{r}'|w=0)$ of the homogeneous system, using the definition of the n -particle density equation (3.76) with $n=2$. Applying the definition of the pair-distribution function equation (3.85) finally leads to

$$\rho^{(1)}(\mathbf{r}|w) = \rho g(0, \mathbf{r}),\tag{4.85}$$

which relates the one-particle density of the inhomogeneous system $\rho^{(1)}(\mathbf{r}|w)$ to the density of the homogeneous system ρ and its pair distribution function $g(0, \mathbf{r})$. The change in the one-particle density $\Delta\rho^{(1)}(\mathbf{r})$ due to the interaction with the particle at position 0 is then given by

$$\Delta\rho^{(1)}(\mathbf{r}) = \rho^{(1)}(\mathbf{r}|w) - \rho^{(1)}(\mathbf{r}|w=0) = \rho g(0, \mathbf{r}) - \rho = \rho h(0, \mathbf{r}).\tag{4.86}$$

Hypernetted Chain closure [HNC]

The hypernetted chain closure (HNC) can be derived by expanding the single particle direct correlation $c^{(1)}(\mathbf{r})$ of the inhomogeneous system into a Taylor series with respect to the density difference $\Delta\rho^{(1)}(\mathbf{r})$ between the inhomogeneous and homogeneous system following section 4.4 of [27].

A more complex derivation of the HNC closure, by minimizing an approximate free energy functional, is given in section 4.3 of [27].

The Taylor series of single particle direct correlation $c^{(1)}(\mathbf{r})$ of the inhomogeneous system up to first order with respect to the deviation of the one-particle density $\rho^{(1)}(\mathbf{r})$ to that of a homogeneous system is given by

$$\begin{aligned}
c^{(1)}(\mathbf{r}) &\approx c_0^{(1)} + \int \Delta\rho^{(1)}(\mathbf{r}') \left. \frac{\delta c^{(1)}(\mathbf{r})}{\delta \rho^{(1)}(\mathbf{r}')} \right|_{w=0} d\mathbf{r}' \\
&= c_0^{(1)} + \int \Delta\rho^{(1)}(\mathbf{r}') c_0^{(2)}(\mathbf{r}, \mathbf{r}') d\mathbf{r}',
\end{aligned} \tag{4.87}$$

with $c_0^{(1)}$ denoting the single particle direct correlation of the homogeneous system and using the definition of the second order direct correlation function equation (4.65) to replace the functional derivative in the first line of equation (4.87).

Inserting the above result into equation (4.67), while assuming that the system is isotropic and by applying equation (4.86) to replace $\Delta\rho^{(1)}(\mathbf{r})$ with $\rho_0 h(\mathbf{r})$ results in

$$\begin{aligned}
\rho^{(1)}(\mathbf{r}) &\approx z \exp \left[c_0^{(1)} \right] \exp \left[-\beta w(\mathbf{r}) + \int \Delta\rho^{(1)}(\mathbf{r}) c^{(2)}(\mathbf{r}, \mathbf{r}') d\mathbf{r}' \right] \\
&= \rho_0 \exp \left[-\beta w(\mathbf{r}) + \int \Delta\rho^{(1)}(\mathbf{r}) c^{(2)}(|\mathbf{r} - \mathbf{r}'|) d\mathbf{r}' \right] \\
&= \rho_0 \exp \left[-\beta w(\mathbf{r}) + \int \rho_0 h(\mathbf{r}) c^{(2)}(|\mathbf{r} - \mathbf{r}'|) d\mathbf{r}' \right]
\end{aligned} \tag{4.88}$$

with ρ_0 denoting the density of the homogeneous system. Applying equation (4.85) the above can be written as

$$\begin{aligned}
g(\mathbf{r}) &\approx \exp[-\beta w(\mathbf{r})] \exp \left[\int \rho_0 h(\mathbf{r}) c^{(2)}(|\mathbf{r} - \mathbf{r}'|) d\mathbf{r}' \right] \\
&= \exp[-\beta w(\mathbf{r})] \exp[h(\mathbf{r}) - c(\mathbf{r})],
\end{aligned} \tag{4.89}$$

taking advantage of the Ornstein-Zernike equation (4.76) to replace the integral by $(h(\mathbf{r}) - c(\mathbf{r}))$.

Substituting the external field w by the pair interaction in equation (4.89), due to the initial presumption of an additional particle causing this field, finally leads to the hypernetted chain closure given by

$$g(\mathbf{r}) \approx \exp[-\beta\phi(\mathbf{r})] \exp[h(\mathbf{r}) - c(\mathbf{r})], \tag{4.90}$$

with " \approx " denoting the approximate nature of this closure relation due to the Taylor expansion of $c^{(1)}(\mathbf{r})$.

Percus-Yevick closure [PY]

Following section 4.4 of [27] again, the Percus-Yevick closure can be derived in much the same way as the hypernetted chain closure in the previous subsection. However, the Taylor series of the exponential of the direct-correlation function $\exp[c^{(1)}(\mathbf{r})]$ is used instead of the Taylor series of the direct correlation function $c^{(1)}(\mathbf{r})$ only. Up to first order this Taylor expansion is given by

$$\begin{aligned}
\exp[c^{(1)}(\mathbf{r})] &\approx \exp[c_0^{(1)}] + \int \Delta\rho^{(1)}(\mathbf{r}') \frac{\delta \exp[c^{(1)}(\mathbf{r})]}{\delta \rho^{(1)}(\mathbf{r}')} \Big|_{w=0} d\mathbf{r}' \\
&= \exp[c_0^{(1)}] + \exp[c^{(1)}(\mathbf{r})] \int \Delta\rho^{(1)}(\mathbf{r}') c^{(2)}(\mathbf{r}, \mathbf{r}') d\mathbf{r}',
\end{aligned} \tag{4.91}$$

applying equation (4.65) again to replace the functional derivative. Reordering the terms leads to

$$\exp[c^{(1)}(\mathbf{r})] \left[1 - \int \Delta\rho^{(1)}(\mathbf{r}') c^{(2)}(\mathbf{r}, \mathbf{r}') d\mathbf{r}' \right] \approx \exp[c_0^{(1)}] \tag{4.92}$$

which can be written as

$$\exp[c^{(1)}(\mathbf{r})] \approx \exp[c_0^{(1)}] \left[1 + \int \Delta\rho^{(1)}(\mathbf{r}') c^{(2)}(\mathbf{r}, \mathbf{r}') d\mathbf{r}' \right], \tag{4.93}$$

utilizing the approximation $\frac{1}{1-ax} = 1 + ax + \mathcal{O}(x^2)$. Taking advantage of equation (4.67) the one-particle density is thus given by

$$\begin{aligned}
\rho^{(1)}(\mathbf{r}) &\approx z \exp[c_0^{(1)}] \exp[-\beta w(\mathbf{r})] \left[1 + \int \Delta\rho^{(1)}(\mathbf{r}') c^{(2)}(\mathbf{r}, \mathbf{r}') d\mathbf{r}' \right] \\
&= \rho_0 \exp[-\beta w(\mathbf{r})] \left[1 + \int \rho_0 h(\mathbf{r}') c^{(2)}(|\mathbf{r} - \mathbf{r}'|) d\mathbf{r}' \right],
\end{aligned} \tag{4.94}$$

while replacing $\Delta\rho^{(1)}(\mathbf{r}')$ by its definition (equation (4.86)).

Using equation (4.85) together with the Ornstein-Zernike equation (4.76) leads to the Percus-Yevick closure relation

$$g(\mathbf{r}) \approx \exp[-\beta\phi(\mathbf{r})] [1 + h(\mathbf{r}) - c(\mathbf{r})]. \tag{4.95}$$

As with the hypernetted chain closure the "≈" in equation (4.95) denotes the approximate nature of the Percus-Yevick closure relation.

Comparing the hypernetted chain (HNC) and Percus-Yevick (PY) closure relations (equations (4.90) and (4.95) respectively), one can see that the Percus-Yevick closure can be derived directly from the hypernetted chain closure by replacing $\exp[h(\mathbf{r}) - c(\mathbf{r})]$ by its Taylor series with respect to the indirect correlation function $\gamma(\mathbf{r}) = (h(\mathbf{r}) - c(\mathbf{r}))$ up to first order.

4.2.3 Algorithm for Solving the Ornstein-Zernike Equations

In combination with a closure relation (equations (4.90) and (4.95)) the Ornstein-Zernike equation (4.76) can be solved in an iterative way. A common method, also used in [40], takes advantage of the fact that the Fourier transform of the Ornstein-Zernike equation (4.77) is an simple algebraic equation. In terms of the (Fourier transformed)

direct and indirect correlation functions $\hat{c}(k)$ and $\hat{\gamma}(k)$, where $\hat{h}(k) = \hat{c}(k) + \hat{\gamma}(k)$, the Fourier transformed Ornstein-Zernike equation can be written as

$$\hat{\gamma}(k) = \frac{\rho \hat{c}^2(k)}{1 - \rho \hat{c}(k)}. \quad (4.96)$$

The iterative solutions, starting from an initial "guess" of the indirect correlation function $\gamma(r)$, is then performed as follows:

1. Calculate the direct correlation $c(r)$ function from the indirect correlation function $\gamma(r)$ using a closure relation (equation (4.90) or (4.95)) including the pair potential $\Phi(r)$.
2. Compute the Fourier transform of the direct-correlation function $c(r) \rightarrow \hat{c}(k)$. (Details on the Fourier transform in two dimensions are given in section 4.2.4)
3. From the Fourier-transformed direct correlation function $\hat{c}(k)$ calculate the Fourier transform of the indirect correlation function $\hat{\gamma}(k)$ using the Ornstein-Zernike equation in the form of equation (4.96)
4. Take the inverse-Fourier-transform of $\hat{\gamma}(k)$ getting an new (improved) guess for the indirect correlation function $\gamma(r)$.
5. Repeat steps 1-4 until sufficient consistency between two successive iterations is achieved.

In mathematics this solution method is often referred to as "Picard circle" or "Picard iteration" [41]. A diagrammatic picture of the Picard circle for solving the Ornstein-Zernike equation is given in figure 4.7.

The initial "guess" for the indirect correlation function $\gamma(r)$ is usually taken from the solution of the Ornstein-Zernike equation of a state-point close to desired one (similar density and temperature). If no such solution exists, the Ornstein-Zernike equation can be solved for a state-point close to the ideal gas (low density and/or high temperature) taking $\gamma(r) = 0$ as an initial guess for the indirect correlation function. By computing the solutions of the Ornstein-Zernike for a series of state-points successively increasing the density or lowering the temperature the desired state-point can be reached. However, care has to be taken, that this series of state-points does not pass trough a region where the Ornstein-Zernike equation (together with a suitable closure relation) does not converge. For an Lennard Jones system E. Lomba found out that the area of no-solution using the Ornstein-Zernike equation in combination with the reference-HNC closure (not discussed here), mostly lies within the two-phase region, but is not identical with it [42], while the part of the no-solution area outside the two-phase region is in the vicinity of the critical point.

In the present work, the maximum value of the difference between the indirect correlation function $\gamma(r)$ of two successive iterations of the Picard circle is used to test for consistency of the solution. If this maximum difference drops below a certain predefined absolute value (10^{-5}) the Picard circle is aborted. The pair distribution function and the structure factor can then be calculated via

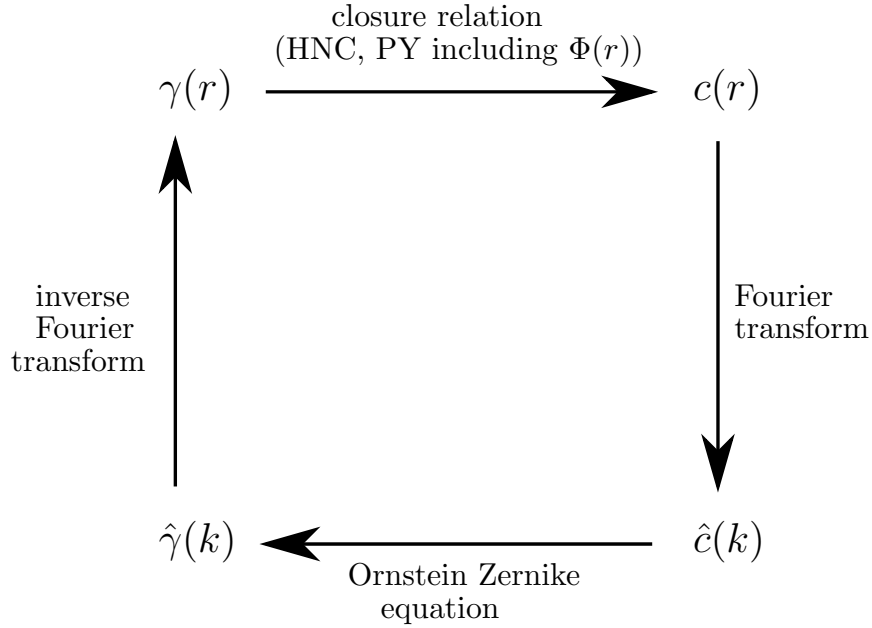


Figure 4.7: Picard circle for the iterative solution of the Ornstein-Zernike equation. The Fourier transformed direct and indirect correlation functions are denoted by $\hat{c}(k)$ and $\hat{\gamma}(k)$ respectively.

$$g(r) = h(r) + 1 = c(r) + \gamma(r) + 1 \quad (4.97)$$

and

$$S(k) = 1 + \rho \hat{h}(k) = 1 + \rho (\hat{c}(k) + \hat{\gamma}(k)). \quad (4.98)$$

(see equation (3.93)).

Thermodynamic properties can then be computed via the appropriate equations (e.g. equations (3.103) and (3.123)). However, if a certain property is computed via two different routes the results of these two routes will not coincide in general, due to the approximate nature of the closure relations [27]. This discrepancy is called the thermodynamic inconsistency of the integral equations.

A simple way to improve the convergence of the Picard iteration in practice, is to "mix" the solution of two successive iterations ($\gamma_i(r)$, $\gamma_{i-1}(r)$) by a fixed mixing factor α via

$$\gamma_i^{\text{new}}(r) = \alpha \gamma_i(r) + (1 - \alpha) \gamma_{i-1}(r) \quad (4.99)$$

and use the resulting function $\gamma_i^{\text{new}}(r)$ as an input for the next iteration [43].

A better, however more elaborate, method to improve the convergence of the Picard circle was first described in the Appendix of Reference [44]. This method will be described in the following section and was also used in the present work.

Ng's Method

The Ng method is used in the present work to speed up the convergence of the iterative solution of the Ornstein-Zernike equation. This method was first presented in [44] and will be outlined here for completeness.

The solution of an iterative problem, like the solution of the Ornstein-Zernike equation combined with a suitable closure relation, can be written as

$$f = Af \quad (4.100)$$

with the operator A describing one Picard iteration and function f being a correlation function (e.g. the indirect correlation function $\gamma(r)$). Denoting the input of the i -th iteration as f_i and the output of this iteration as g_i the iteration procedure can be written as

$$f_{i+1} = g_i = Af_i. \quad (4.101)$$

Denoting the difference between the input and the output of the i -th iteration step by

$$d_i = g_i - f_i = (A - 1)f_i \quad (4.102)$$

a measure for the convergence is given by

$$\|d_i\| = \sqrt{\left(\int |d_i(x)|^2 dx\right)}. \quad (4.103)$$

A solution \bar{f} of the Picard iteration can be approximated by a linear combination of the inputs of previous iterations (f_i , f_{i-1} and f_{i-2})

$$\bar{f} = (1 - c_1 - c_2) f_i + c_1 f_{i-1} + c_2 f_{i-2}. \quad (4.104)$$

Using the iteration-operator A on \bar{f} from the ansatz in equation (4.104) results in

$$\begin{aligned} A\bar{f} &= (1 - c_1 - c_2) Af_i + c_1 Af_{i-1} + c_2 Af_{i-2} \\ &= (1 - c_1 - c_2) g_i + c_1 g_{i-1} + c_2 g_{i-2} \end{aligned} \quad (4.105)$$

assuming that the operator A is linear with respect to the input function f . The linearity of the operator A is only an approximation that holds close to the final solution, of course.

The error in \bar{f} by the ansatz in equation (4.104) can be measured by

$$\begin{aligned} \Delta &= \|A\bar{f} - \bar{f}\| \\ &= \|d_i - c_1(d_i - d_{i-1}) - c_2(d_i - d_{i-2})\| \\ &= \|d_i - c_1 d_{01} - c_2 d_{02}\|, \end{aligned} \quad (4.106)$$

with d_i defined by equation (4.102) and $d_{01} = d_i - d_{i-1}$ as well as $d_{02} = d_i - d_{i-2}$, using the same notation as in [44] and omitting the arguments of the error Δ . The square of the error Δ is then given by

$$\begin{aligned}
\Delta^2 &= \|d_i - c_1 d_{01} - c_2 d_{02}\|^2 \\
&= \int (d_i - c_1 d_{01} - c_2 d_{02})(d_i - c_1 d_{01} - c_2 d_{02}) dx \\
&= \int (d_i^2 - 2c_1 d_{01} d_i - 2c_2 d_{02} d_i + 2c_1 c_2 d_{01} d_{02} + c_1^2 d_{01}^2 + c_2^2 d_{02}^2) dx \\
&= \{d_i, d_i\} - 2c_1 \{d_{01}, d_i\} - 2c_2 \{d_{02}, d_i\} \\
&\quad + 2c_1 c_2 \{d_{01}, d_{02}\} + c_1^2 \{d_{01}, d_{01}\} + c_2^2 \{d_{02}, d_{02}\},
\end{aligned} \tag{4.107}$$

while using

$$\{A, B\} = \int A(x)B(x)dx \tag{4.108}$$

for the inner product in the last line of equation (4.107). The square error Δ^2 can now be minimized with respect to c_1 and c_2 by

$$\frac{\partial \Delta^2}{\partial c_1} = -2 \{d_{01}, d_i\} + 2c_2 \{d_{01}, d_{02}\} + 2c_1 \{d_{01}, d_{01}\} = 0 \tag{4.109}$$

$$\frac{\partial \Delta^2}{\partial c_2} = -2 \{d_{02}, d_i\} + 2c_1 \{d_{01}, d_{02}\} + 2c_2 \{d_{02}, d_{02}\} = 0. \tag{4.110}$$

This results in a set of linear equations given by

$$\begin{aligned}
\{d_{01}, d_{01}\} c_1 + \{d_{01}, d_{02}\} c_2 &= \{d_{01}, d_i\} \\
\{d_{01}, d_{02}\} c_1 + \{d_{02}, d_{02}\} c_2 &= \{d_{02}, d_i\}.
\end{aligned} \tag{4.111}$$

The solution of equation (4.111) can be written as

$$\begin{aligned}
c_1 &= \frac{\{d_{01}, d_i\} \{d_{02}, d_{02}\} - \{d_{02}, d_i\} \{d_{01}, d_{02}\}}{\{d_{01}, d_{01}\} \{d_{02}, d_{02}\} - \{d_{01}, d_{02}\}^2} \\
c_2 &= \frac{\{d_{02}, d_i\} \{d_{01}, d_{01}\} - \{d_{01}, d_i\} \{d_{01}, d_{02}\}}{\{d_{01}, d_{01}\} \{d_{02}, d_{02}\} - \{d_{01}, d_{02}\}^2}.
\end{aligned} \tag{4.112}$$

Using c_1 and c_2 from equation (4.112) the refined input for iteration step $i + 1$ can be written as

$$f_{i+1} = (1 - c_1 - c_2) g_i + c_1 g_{i-1} + c_2 g_{i-2}. \tag{4.113}$$

Note that in equation (4.113) the output functions g_i , g_{i-1} and g_{i-2} are used rather than the input functions f_i , f_{i-1} and f_{i-2} as in the ansatz, equation (4.104), to prevent that the refined input of the $(i + 1)$ -th iteration step is always a linear combination of the first three input functions f_1 , f_2 and f_3 .

As mentioned in [44] higher order approximations in an ansatz similar to equation (4.104) (including the solutions of more previous iterations) are possible, but have not been used in the present work.

4.2.4 Integral Equations in Two Dimensions

The Fourier transform mentioned in sections 4.2.1 and 4.2.2 can be written as

$$\hat{f}(\mathbf{k}) = \int d\mathbf{r} f(\mathbf{r}) \exp[-i \mathbf{k} \cdot \mathbf{r}], \quad (4.114)$$

see [45], where the integration is performed on the entire two-dimensional space. However due to the homogeneity of the system, assumed when deriving the Ornstein-Zernike equation (4.76), the correlation functions depend on the absolute value of \mathbf{r} only, so $f(\mathbf{r}) = f(r)$. The Fourier transform is thus given by

$$\begin{aligned} \hat{f}(\mathbf{k}) = \hat{f}(k) &= \int_0^\infty dr r f(r) \int_0^{2\pi} d\phi \exp[-i kr \cos(\phi)] \\ &= 2\pi \int_0^\infty dr r f(r) J_0(-kr) \end{aligned} \quad (4.115)$$

using the definition of the 0-th order spherical Bessel function

$$\begin{aligned} J_0(kr) &= \int_0^{2\pi} d\phi \exp[-i kr \cos(\phi)] \\ &= \frac{\sin(kr)}{kr}. \end{aligned} \quad (4.116)$$

From equation (4.116) it can be easily seen that the spherical Bessel function of the 0-th order is a symmetric function $J_0(x) = J_0(-x)$. The two dimensional Fourier transform of a spherical symmetric function (also called Hankel transform) can therefore be written as

$$\hat{f}(k) = 2\pi \int_0^\infty dr r f(r) J_0(kr). \quad (4.117)$$

The inverse transformation

$$f(\mathbf{r}) = \frac{1}{(2\pi)^2} \int d\mathbf{k} \hat{f}(\mathbf{k}) \exp[i \mathbf{k} \cdot \mathbf{r}], \quad (4.118)$$

can be derived equivalently [45] and is given by

$$f(r) = \frac{1}{2\pi} \int_0^\infty dk k \hat{f}(k) J_0(kr). \quad (4.119)$$

A fast algorithm to numerically compute the Hankel transformation as well as its inverse, by two successive Fourier transformations was first introduced in [46] and is also used in [47, 48]. The details of this algorithm are repeated here for completeness. Equation (4.117) is rewritten in terms of the new variables \mathcal{R} and \mathcal{K} which are connected to r and k via the variable transform

$$r = \exp(\mathcal{R}) \quad dr = \exp(\mathcal{R}) d\mathcal{R} \quad (4.120)$$

$$k = \exp(\mathcal{K}) \quad dk = \exp(\mathcal{K}) d\mathcal{K}. \quad (4.121)$$

The integration in equation (4.117) can therefore be written as

$$\begin{aligned} \int dr f(r) J_0(kr) &= \int_{-\infty}^{\infty} d\mathcal{R} \exp(\mathcal{R}) \exp(\mathcal{R}) f(\exp(\mathcal{R})) J_0(\exp(\mathcal{K} + \mathcal{R})) \\ &= \exp(-\mathcal{K}) \int_{-\infty}^{\infty} d\mathcal{R} \exp(\mathcal{R}) \exp(\mathcal{R} + \mathcal{K}) f(\exp(\mathcal{R})) J_0(\exp(\mathcal{K} + \mathcal{R})) \\ &= 4\pi \exp(-\mathcal{K}) \Re \left[\int_0^{\infty} dt \Theta(t) M(t) \exp(i\mathcal{K}t) \right], \end{aligned} \quad (4.122)$$

with $\Re[x]$ denoting the real part of x and the two functions $\Theta(t)$ and $M(t)$ defined as

$$\Theta(t) = \frac{1}{2\pi} \int_{-\infty}^{\infty} d\mathcal{R} \exp(\mathcal{R}) f(\exp(\mathcal{R})) \exp(i\mathcal{R}t) \quad (4.123)$$

and

$$M(t) = \frac{1}{2\pi} \int_{-\infty}^{\infty} d\mathcal{R}' \exp(\mathcal{R}') J_0(\exp(\mathcal{R}')) \exp(-i\mathcal{R}'t). \quad (4.124)$$

The last equality in equation (4.122) can be proved easily by inserting the functions $\Theta(t)$ and $M(t)$ given by equations (4.123) and (4.124) into the last line of equation (4.122) resulting in

$$\begin{aligned} &4\pi \exp(-\mathcal{K}) \Re \left[\int_0^{\infty} dt \Theta(t) M(t) \exp(i\mathcal{K}t) \right] \\ &= \frac{4\pi}{(2\pi)^2} \exp(-\mathcal{K}) \Re \left[\int_0^{\infty} dt \int_{-\infty}^{\infty} d\mathcal{R} \exp(\mathcal{R}) f(\exp(\mathcal{R})) \exp(i\mathcal{R}t) \times \right. \\ &\quad \left. \times \int_{-\infty}^{\infty} d\mathcal{R}' \exp(\mathcal{R}') J_0(\exp(\mathcal{R}')) \exp(-i\mathcal{R}'t) \exp(i\mathcal{K}t) \right] \quad (4.125) \\ &= \frac{1}{\pi} \exp(-\mathcal{K}) \int_{-\infty}^{\infty} d\mathcal{R} \exp(\mathcal{R}) f(\exp(\mathcal{R})) \int_{-\infty}^{\infty} d\mathcal{R}' \exp(\mathcal{R}') J_0(\exp(\mathcal{R}')) \times \\ &\quad \times \Re \left[\int_0^{\infty} dt \exp(i(\mathcal{R} + \mathcal{K} - \mathcal{R}')t) \right], \end{aligned}$$

making use of the fact that $f(r)$ and $\hat{f}(k)$ are real functions. The term $\int_0^{\infty} dt \exp(i(\mathcal{R} + \mathcal{K} - \mathcal{R}')t)$ on the last line of equation (4.125) can be identified as a Dirac-delta function via

$$\Re \left[\int_0^{\infty} dt \exp(i(\mathcal{R} + \mathcal{K} - \mathcal{R}')t) \right] = \frac{2\pi}{2} \delta(\mathcal{R} + \mathcal{K} - \mathcal{R}'). \quad (4.126)$$

Equation (4.126) can be derived from the integral-form of the Dirac-delta function and Euler's formula by

$$\begin{aligned}
\delta(x - x') &= \frac{1}{2\pi} \int_{-\infty}^{\infty} dt \exp(i(x - x')t) \\
&= \frac{1}{2\pi} \int_{-\infty}^{\infty} dt [\cos((x - x')t) + i \sin((x - x')t)] \\
&= \frac{1}{2\pi} \int_{-\infty}^{\infty} dt [\cos((x - x')t)] \\
&= \frac{2}{2\pi} \int_0^{\infty} dt [\cos((x - x')t)] \\
&= \frac{2}{2\pi} \Re \left[\int_0^{\infty} dt \exp(i(x - x')t) \right],
\end{aligned} \tag{4.127}$$

taking into account that only the real part gives a contribution, since sine is an odd function. Additionally, the restriction to the x -interval $[0, \infty]$ is possible, because cosine is an even function, therefore $\int_{-\infty}^{\infty} dx \cos(x) = 2 \int_0^{\infty} dx \cos(x)$.

Using equation (4.126), equation (4.125) can further be simplified resulting in

$$\begin{aligned}
&4\pi \exp(-\mathcal{K}) \Re \left[\int_0^{\infty} dt \Theta(t) M(t) \exp(i\mathcal{K}t) \right] \\
&= \frac{1}{\pi} \exp(-\mathcal{K}) \int_{-\infty}^{\infty} d\mathcal{R} \exp(\mathcal{R}) f(\exp(\mathcal{R})) \int_{-\infty}^{\infty} d\mathcal{R}' \exp(\mathcal{R}') J_0(\exp(\mathcal{R}')) \times \\
&\quad \times \pi \delta(\mathcal{R} + \mathcal{K} - \mathcal{R}') \\
&= \exp(-\mathcal{K}) \int_{-\infty}^{\infty} d\mathcal{R} \exp(\mathcal{R}) \exp(\mathcal{R} + \mathcal{K}) f(\exp(\mathcal{R})) J_0(\exp(\mathcal{R} + \mathcal{K})),
\end{aligned} \tag{4.128}$$

which is equivalent to the first line of equation (4.122).

The integration on the last line of equation (4.122) can be computed by a Fourier transform. In the present work a Fast-Fourier algorithm was used to compute this integral, as was the case in [46, 47, 48].

The function $M(t)$ can be simplified to

$$\begin{aligned}
M(t) &= \frac{1}{2\pi} \int_{-\infty}^{\infty} d\mathcal{R} \exp(\mathcal{R}) J_0(\exp(\mathcal{R})) \exp(-i\mathcal{R}t) \\
&= \frac{1}{2\pi} \int_{-\infty}^{\infty} d\mathcal{R} \exp(\mathcal{R}) J_0(\exp(\mathcal{R})) \exp(\mathcal{R})^{-it} \\
&= \frac{1}{2\pi} \int_0^{\infty} dr J_0(r) r^{-it} \\
&= \frac{1}{2\pi} 2^{-it} \frac{\Gamma(\frac{1}{2} - \frac{it}{2})}{\Gamma(\frac{1}{2} + \frac{it}{2})} \\
&= \frac{1}{2\pi} 2^{-it} \exp(i\psi(t)),
\end{aligned} \tag{4.129}$$

with the phase $\psi(t)$ given by

$$\psi(t) = \Im \left[\ln \frac{\Gamma\left(\frac{1}{2} - \frac{it}{2}\right)}{\Gamma\left(\frac{1}{2} + \frac{it}{2}\right)} \right], \quad (4.130)$$

with $\Im[x]$ denoting the imaginary part of x . The unitary phase $\psi(t)$ can be approximated by

$$\begin{aligned} \psi(t) \approx \lim_{n \rightarrow \infty} & \left[2 \sum_{k=1}^n \arctan \left(\frac{t}{2k-1} \right) - t \ln(x) + t \right. \\ & \left. - 2n\alpha + \frac{\sin(\alpha)}{6x} - \frac{\sin(3\alpha)}{180x^3} + \frac{\sin(5\alpha)}{630x^5} - \frac{\sin(7\alpha)}{840x^7} \right] \end{aligned} \quad (4.131)$$

[47], using

$$x = \sqrt{\left(n + \frac{1}{2}\right)^2 + \frac{t^2}{4}} \quad (4.132)$$

and

$$\alpha = \arctan \left(\frac{t}{2n+1} \right) \quad (4.133)$$

The path from equation (4.130) to equation (4.131) is outlined in appendix A with comments on the validity of the limit in equation (4.131) given in appendix A.1.

In the present work $n = 5$ was used to approximate the phase using equation (4.131). The same value for n was also used in [47, 48] and found to give sufficient accuracy there.

The function $\Theta(t)$ in the last line of equation (4.122) can be computed by splitting the integration in two parts

$$\begin{aligned} \Theta(t) &= \frac{1}{2\pi} \int_{-\infty}^{\infty} d\mathcal{R} \exp(\mathcal{R}) f(\exp(\mathcal{R})) \exp(i\mathcal{R}t) \\ &= \frac{1}{2\pi} \int_{-\infty}^{\mathcal{R}_m} d\mathcal{R} \exp(\mathcal{R}) f(\exp(\mathcal{R})) \exp(i\mathcal{R}t) \\ &\quad + \frac{1}{2\pi} \int_{\mathcal{R}_m}^{\infty} d\mathcal{R} \exp(\mathcal{R}) f(\exp(\mathcal{R})) \exp(i\mathcal{R}t) \\ &= \frac{1}{2\pi} \int_{-\infty}^{\mathcal{R}_m} d\mathcal{R} \exp(\mathcal{R}) f(\exp(\mathcal{R})) \exp(i\mathcal{R}t) \\ &\quad + \frac{1}{2\pi} \exp(i\mathcal{R}_m) \int_0^{\infty} d\mathcal{R} \exp(\mathcal{R} + \mathcal{R}_m) f(\exp(\mathcal{R} + \mathcal{R}_m)) \exp(i\mathcal{R}t). \end{aligned} \quad (4.134)$$

The first integration term on the right hand side of equation (4.134) can be calculated directly in the interval $[-\infty, \mathcal{R}_m]$ assuming $\mathcal{R}_m < -1$ and therefore $r_m \ll 1$ ($r_m = \exp(\mathcal{R}_m)$), by approximating $f(r)$ as $f(r_m)$ within this interval, resulting in

$$\begin{aligned}\Theta_1(t) &= \frac{1}{2\pi} \int_{-\infty}^{\mathcal{R}_m} d\mathcal{R} \exp(\mathcal{R}) f(\exp(\mathcal{R})) \exp(i\mathcal{R}t) \\ &\approx \frac{1}{2\pi} \exp(\mathcal{R}_m) f(\exp(\mathcal{R}_m)) \frac{\exp(i\mathcal{R}_m t)}{1+it}.\end{aligned}\quad (4.135)$$

The second integration term on the right side of equation (4.134) is a convolution integral and can be computed by a Fast-Fourier transform, similar to the convolution integral in equation (4.122).

In the present work $\mathcal{R}_m = -7$ was used resulting in $r_m \approx 10^{-3}$, similar to References [47, 48] justifying the approximation ($\mathcal{R}_m < -1$, $r_m \ll 1$) made above.

Summarizing, the Hankel transform, given by equation (4.117), can be computed by two subsequent Fast-Fourier transforms. However, the necessary shift from r and k to \mathcal{R} and \mathcal{K} requires the representation of the structure functions as values spaced equidistantly in \mathcal{R} and \mathcal{K} rather than in r and k . Therefore the spacing between two values of such a structure function increases as the distance from the origin increases. For the calculations in the present work the structure functions were computed on $N = 2^{13} = 8192$, points with an equidistant spacing in \mathcal{R} of $\Delta\mathcal{R} = 0.002$, if not explicitly stated otherwise.

Due to the need of two subsequent Fast Fourier transforms, instead of only one Sine-transform in the three-dimensional case [45], the two-dimensional Fourier transform (Hankel transform) is computationally more demanding. Additionally it is not as accurate because of the approximations made in the computation of the functions $\Theta(t)$ and $M(t)$.

4.2.5 Chemical potential μ

An exact, closed and single-state expression is desired for computing the chemical potential, using the structure functions, obtained by the Ornstein-Zernike equations in combination with the closure relations.

Closed in this sense implies that the expression contains no infinite sums or products, while single-state indicates, that said expression only depends on the properties of a single state-point. Obviously such an expression can only yield exact results except for the approximations already introduced by the closure relation used.

A suitable expression for the chemical potential μ for HNC closure-relation was first derived in [49] and later via another method in [50] and is given by

$$\beta\mu_{\text{HNC}}^{\text{ex}} = \rho \int d\mathbf{r} \left[\gamma(r) - h(r) + \frac{1}{2}h(r)\gamma(r) \right]. \quad (4.136)$$

The respective expression for the PY closure-relation was derived in [50] and is given by

$$\beta\mu_{\text{PY}}^{\text{ex}} = \rho \int d\mathbf{r} \ln(1 + \gamma(r)) \left[\frac{\gamma(r) - h(r)}{\gamma(r)} \right]. \quad (4.137)$$

Expressions for a broader range of closure relations can be found in [51], an extension to quenched-annealed systems (QA systems) in [52].

4.3 Cluster Analysis

This section describes how clusters are identified and how they are tracked from one simulation step to the next. In addition, the computation of some cluster properties is described here.

4.3.1 Cluster Identification

Clusters are identified from single configurations of Monte Carlo simulations using the known coordinates of the particles. In this work a simple distance-based definition for clusters is used [17]. First a starting particle is defined to be part of a new cluster. The distance-based cluster definition can then be applied iteratively. Particles i and j belong to the same cluster if their distance is equal or smaller than a fixed distance parameter d_{cl} (i.e. $\sqrt{(x_i - x_j)^2 + (y_i - y_j)^2} \leq d_{cl}$). A distance parameter of $d_{cl} = 1.85$ is used in the present work, if not explicitly stated otherwise. It is important to note, that a distance smaller than d_{cl} to just one particle of a cluster is a sufficient criterion for another particle to belong to the same cluster and it is not necessary that the distance criterion $\sqrt{(x_i - x_j)^2 + (y_i - y_j)^2} \leq d_{cl}$ is fulfilled for every pair of particles i and j of a cluster. The linear extension (e.g. diameter) of a cluster can therefore be much larger than the cluster parameter d_{cl} itself.

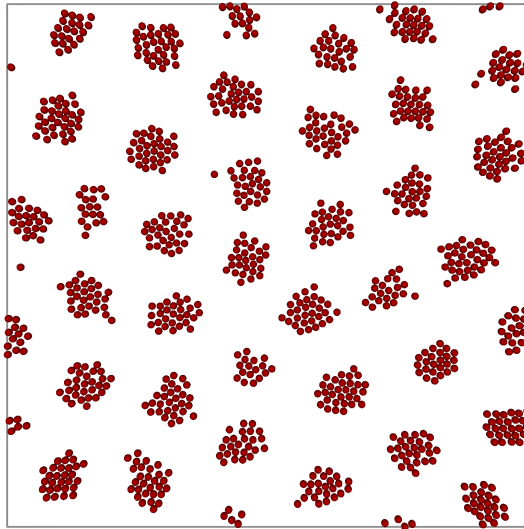


Figure 4.8: Typical simulation snapshots of the cluster micro-phases encountered in the Imperio-Reatto model (see chapter 2) in 2D ($\rho = 0.20$, $T = 0.40$). The clusters can be identified easily using bare eye and intuition only.

Algorithm

The algorithm used for the cluster identification is outlined below and depicted in figure 4.9.

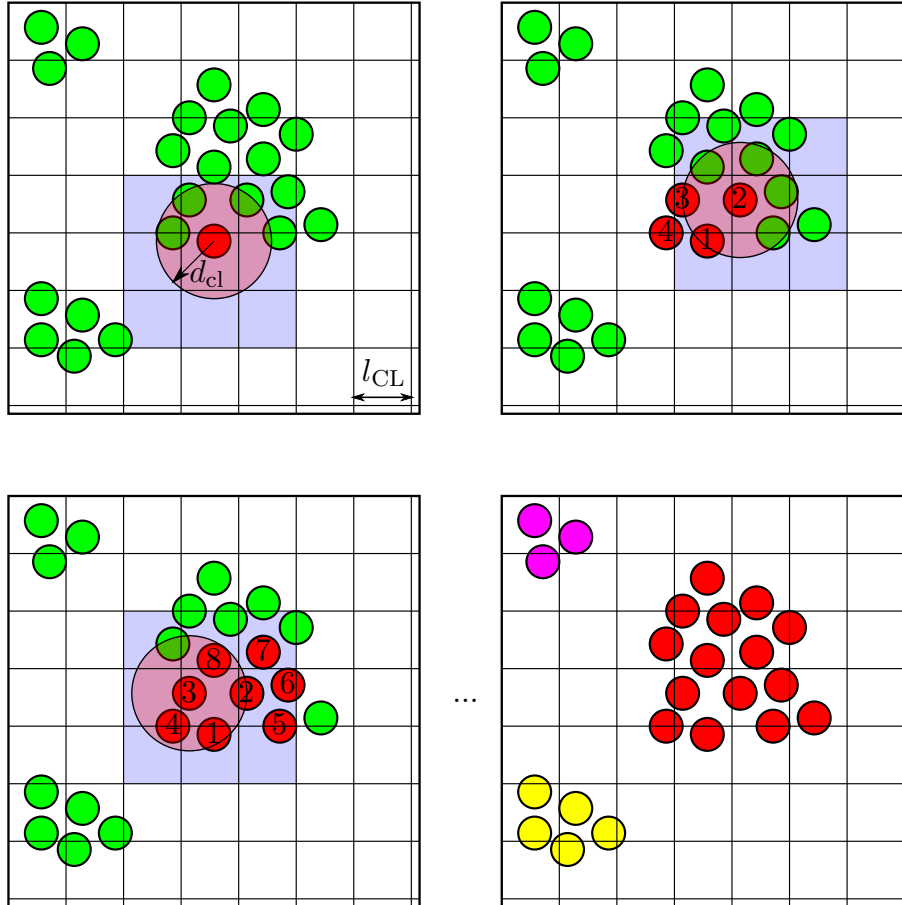


Figure 4.9: Cluster Identification: (from top left to bottom right)

top left: The green particles have not been associated to a cluster by now. The red particle is the starting particle of the new cluster, it is selected at random. The light red disk around the red starting particle marks the distance parameter d_{cl} , while the light blue square marks the nine cell-list cells which are searched for additional cluster particles (see text). Note that the light red circle lies entirely within the light blue square.

top right: The red particles are associated with the new cluster, their centers lie within the light red circular area of the top-left panel. The numbers mark the order of their finding (within the code). At the present step the code seeks particles close to particle number 2 (see the light red disk).

bottom left: The code seeks particles close to particle number 3 (see the light red disk) at this step.

bottom right: After some more iterations the cluster is complete. The other clusters (identified in the same way) are distinguished from the first by color (yellow and purple).

1. In a first step all particles are sorted into cell-lists (for an explanation of cell-lists see section 4.1.3). The side length of the cell-lists is greater or equal to the cluster distance parameter $l_{CL} \geq d_{cl}$. The cell-lists are used here to improve the speed of the present algorithm.
2. The first particle in the first cell-list cell is then selected as starting-particle for the first candidate-cluster (see figure 4.9 top left panel). The term "*candidate-cluster*" is explained further below, it can be read as "*cluster*" for the time being. The specific choice for the starting-particle is made for convenience only, the final result of the algorithm will not depend on it.
3. The selected particle is removed from the cell-list and added to a list for the particles of the new candidate-cluster.
4. The cell-list cell of the selected particle and all neighboring cell-list cells are searched for particles whose distance to the currently selected particle is equal or smaller than the distance parameter d_{cl} . (The center of mass of these particles lies in the red shaded area shown in the top left panel of figure 4.9.)

Without the use of cell-lists all particles of the simulation snapshot would have to be checked instead of only the fraction located in the same or neighboring cell-list cells. Even with the overhead of sorting the particles into the cell-list this results in a massive speed gain.

5. All particles matching the distance criterion $\sqrt{(x_i - x_j)^2 + (y_i - y_j)^2} \leq d_{cl}$ of the previous step are removed from the cell-lists and added to the list of the current candidate-cluster. (The red particles (nr. 2, 3, 4) in the top right panel of figure 4.9)
6. The next particle in the candidate-cluster is selected (if it exists) together with the cell-list cell it is located in.
7. Steps 4 to 6 are repeated until the last particle of the candidate-cluster is reached and no new particles belonging to that candidate-cluster can be found (see figure 4.9 bottom left for another step).
8. If no new particles can be added to a candidate-cluster, the first particle in the first non empty cell-list cell is selected as starting-point for the next candidate-cluster. (Remember that particles already belonging to candidate-clusters are removed from the cell-list cells.) This cell-list cell can also be the first one since the criterion for the side length of the cell-list cells is $l_{CL} \geq d_{cl}$. Again the specific choice for the starting particle of the next candidate-cluster is made because of convenience and does not change the result.
9. Steps 3 to 8 are repeated until no particle remains in any of the cell-list cells and every particle of the simulation step is assigned to a candidate-cluster (see figure 4.9 bottom right).

10. In a follow-up step only candidate-clusters with a size (number of particles) greater or equal to a size parameter n_{cl} are accepted as clusters. The remaining candidate-clusters (which are often single particles) are treated as free particles. A size parameter of $n_{cl} = 5$ is used in the present work, if not explicitly stated otherwise.

Of course the periodic boundary conditions used in the Monte-Carlo simulations have to be taken into account when calculating particle distances and computing the center of mass of clusters.

The use of cell-lists drastically reduces the number of particles that have to be tested as potential cluster members. Additionally cluster members already identified are removed from the cell-list cells and thus do not have to be tested again. As a result the algorithm is exceptionally fast (20 million particles are processed in a few seconds on a state-of-the-art computer). Moreover it shall be emphasized that the assignment of a particle to a cluster is unambiguous.

However there are also a few drawbacks to this method. Single particles with no neighbors closer than d_{cl} are identified as clusters of size one by the algorithm. This is easily overcome in the present work by only accepting clusters of a minimum size of $n_{cl} = 5$ particles as valid clusters, which in turn is the reason the term "candidate-clusters" was used above. The inability of the algorithm to disentangle clusters that are connected by a bridging particle is another disadvantage. However the effect of this problem is minimized by a sensible choice of the distance parameter d_{cl} . The alternative solution of an additional, time consuming post-processing step to disentangle such connected clusters was not pursued in the present work.

4.3.2 Cluster Tracking

Since the cluster identification described in section 4.3.1 yields no information about the movement of the clusters, other means have been implemented to relate the clusters of one simulation-snapshot with those of the next simulation-snapshot. Obviously there are various approaches to solve that problem. However, some properties of the system complicate the task of tracking the clusters for the entire length of a simulation run:

- The clusters can (in principal) move through the entire simulation box, since they are not fixed to a site like the cluster crystals in Refs. [53, 54]. A tracking based on the position of the clusters is therefore not possible.
- Particles can join or leave the cluster, therefore a cluster cannot be defined by the particles it contains at a certain simulation-snapshot.
- The number of clusters is not constant, meaning it is possible that clusters form and dissolve or even merge and split during a simulation run.
- Single particles can exist outside of clusters. Therefore a minimum size for clusters has been imposed with the minimum particle number n_{cl} in the cluster identification algorithm to distinguish between clusters and free particles (see section 4.3.1).

To overcome the problems listed above it is assumed, that the clusters, or more specific the cluster centers of mass (cluster-CMs), do not move more than half the smallest distance between two cluster-CMs during the time elapsing between two simulation-snapshots (a MC-sweep). If the above assumption is valid, the distance of a specific cluster-CM in simulation-snapshot n to the CM of the same cluster in simulation-snapshot $n - 1$ is smaller than the distance from the CM of the cluster in simulation-snapshot n to all other cluster-CMs of simulation-snapshot $n - 1$ (at least if that specific cluster still exists in snapshot n , see point three in the list above).

Unfortunately, a one to one identification of clusters-CMs with the ones of the previous simulation-snapshot is not always possible and some special cases have to be taken into account.

An overview of these cases treated by the code of the present work is given in table 4.1. In a first step to distinguish between these cases, all candidates for inheriting the cluster-identity are identified. This is done for all the clusters in snapshot $n - 1$. The candidates for inheriting the cluster-identity (within snapshot n) of a certain cluster \mathcal{A} in snapshot $n - 1$ shall be called follow-up clusters of cluster \mathcal{A} . A cluster in snapshot n is a follow-up cluster of cluster \mathcal{A} , if cluster \mathcal{A} is closer to its coordinates than any other cluster in snapshot $n - 1$. Obviously cluster \mathcal{A} (in snapshot $n - 1$) can have any non-negative number of follow-up clusters in snapshot n . In practice however only a low number of follow-up clusters is relevant, consequently only cases of up to three follow up clusters are treated by the code produced in the course of the present thesis. Events with four ore more follow-up clusters, not covered by the cases given in table 4.1, only occurred at higher temperatures ($T \geq 0.50$), however at these temperatures clusters were already hard to identify from snapshot pictures using bare eyes only. Moreover at temperatures not much higher ($T > 0.60$) it was impossible to identify the clusters computationally (using the code described in section 4.3.1).

Taking a look at table 4.1 it becomes obvious, that the number of follow-up clusters (given in the last column) is not sufficient to distinguish between the seven cases given in this table.

An additional criterion has to be used to differentiate, for instance, a combination of case 1 and case 2 from case 3. Other distinctions have to be made between case 4 and case 5 as well as case 6 and case 7. The distance based criterion(s) used in this work and the consequences to the assignment of cluster identities are outlined below.

case 1 & 2 vs. case 3:

A combination of case 1 and 2 as well as case 3 are both characterized by the fact that one of the two clusters of simulation snapshot $n - 1$ involved has no follow up cluster. This cluster shall be called \mathcal{B}_{n-1} for now. In order to differentiate between these two possibilities the closest cluster of snapshot n with respect to \mathcal{B}_{n-1} is identified. It shall be called \mathcal{A}_n After that its parent-cluster \mathcal{A}_{n-1} , the one closest to it in snapshot $n - 1$, is identified as well. It is assumed in this work that the cluster \mathcal{B}_{n-1} dissolves into single particles or groups of particles that are to small to be considered as a cluster (i.e. particle number < 5), if the distance from \mathcal{B}_{n-1} to \mathcal{A}_n is greater or equal than twice the distance from \mathcal{A}_{n-1} to \mathcal{A}_n . This would be a combination of cases 1 and 2: In such a situation the cluster \mathcal{A}_n inherits the cluster-identity from cluster \mathcal{A}_{n-1} , while

case nr.	snapshot $n - 1$	→	snapshot n	remark	number of follow-up clusters
1	●	→	●		1
2	●	→		cluster dissolving	0
3	● ●	→	●	cluster merging	1/0*
4	●	→	● ●	new cluster	2
5	●	→	● ●	cluster splitting	2
6	●	→	● ● ●	two new clusters	3
7	●	→	● ● ● ● ● ●	cluster splitting into three or cluster splitting and new cluster	3

Table 4.1: The different cases treated by the cluster tracking code:

Each case is assigned a case-number it is referenced to in the text. The second and third column show the state of the clusters in snapshot $n - 1$ and n respectively. The blue spheres represent new or disappearing clusters, whereas the yellow spheres represent clusters which continue to exist as single clusters, split clusters or merged clusters. How these cases are distinguished in this thesis is explained in the text. The last column gives the number of follow-up clusters to each of the cases. How the number of follow up clusters is obtained is also explained in the text.

* two numbers for the follow up clusters are given for the two clusters of simulation snapshot $n - 1$

the cluster-identity of \mathcal{B}_{n-1} is not used any longer. This situation is illustrated in the left two panels of figure 4.10. If on the other hand the distance from \mathcal{B}_{n-1} to \mathcal{A}_n is smaller than twice the distance from \mathcal{A}_{n-1} to \mathcal{A}_n , it is assumed that the two clusters \mathcal{A}_{n-1} and \mathcal{B}_{n-1} merged into the cluster \mathcal{A}_n . This constitutes case 3 and is illustrated in the right two panels of figure 4.10. In such a situation neither the cluster-identity of \mathcal{A}_{n-1} nor the identity of \mathcal{B}_{n-1} are used any longer and the new cluster \mathcal{A}_n is assigned a new identity.

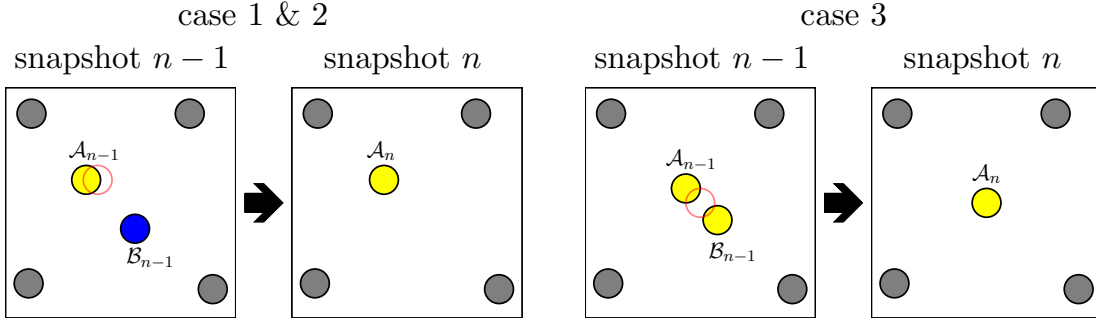


Figure 4.10: Comparison between a combination of case 1 and case 2 (the two panels to the left) to case 3 (the two panels to the right). The black arrow symbolizes the propagation from snapshot $n - 1$ (left of the arrow) to snapshot n (right of the arrow). The red circle indicates the position of the cluster in snapshot n , in order to simplify the judgment of distances

case 4 vs. case 5:

Case 4 as well as case 5 are characterized by the fact that the cluster of simulation snapshot $n - 1$ involved (\mathcal{A}_{n-1}) has two follow-up clusters. To distinguish between the two cases the two follow-up clusters, \mathcal{A}_n and \mathcal{B}_n , in simulation snapshot n are identified as described in the main text of section 4.3.2. Without loss of generality it is assumed that \mathcal{A}_n is closer to \mathcal{A}_{n-1} . The distance criterion applied now is similar to the one before. If the distance between \mathcal{B}_n and \mathcal{A}_{n-1} is greater or equal than twice the distance between \mathcal{A}_n and \mathcal{A}_{n-1} it is assumed that the cluster \mathcal{B}_n has spontaneously formed from free particles and therefore the event is classified as case 4. The identity of cluster \mathcal{A}_{n-1} is then inherited by cluster \mathcal{A}_n , while cluster \mathcal{B}_n is assigned a new cluster identity. This situation is illustrated in the left two panels of figure 4.11. If on the other hand the distance between \mathcal{B}_n and \mathcal{A}_{n-1} is smaller than twice the distance between \mathcal{A}_n and \mathcal{A}_{n-1} however, it is assumed that the cluster \mathcal{A}_{n-1} has split up into the two parts \mathcal{A}_n and \mathcal{B}_n . In that case \mathcal{A}_n as well as \mathcal{B}_n are assigned new cluster identities, while the identity of \mathcal{A}_{n-1} is not used any longer. This situation constitutes case 5 and is illustrated in the right two panels of figure 4.11.

It shall be stressed here that case 4 is the exact inverse of the combination of cases 1 and 2, while case 5 is the exact inverse of case 3.

case 6 vs. case 7:

Case 6 and case 7 are characterized by the fact that the cluster of snapshot $n - 1$ involved in the process (\mathcal{A}_{n-1}) has three follow-up clusters. Similar as for the cases

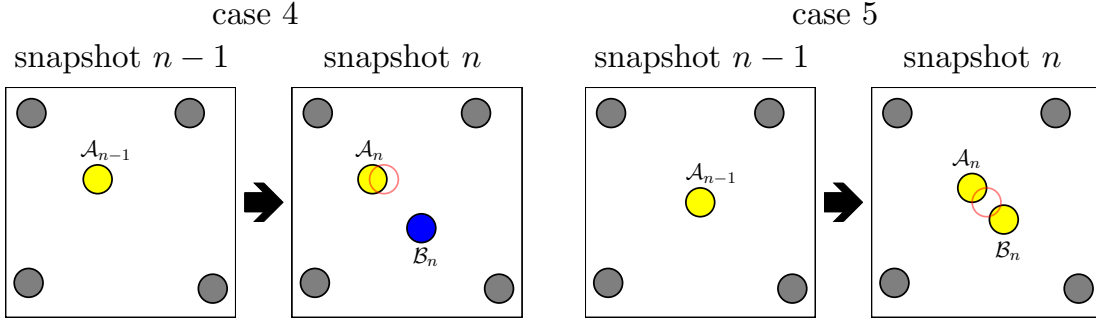


Figure 4.11: Comparison between case 4 (the two panels to the left) to case 5 (the two panels to the right). The black arrow symbolizes the propagation from snapshot $n-1$ (left of the arrow) to snapshot n (right of the arrow). The red circle indicates the position of the cluster in snapshot $n-1$, in order to simplify the judgment of distances.

where two follow-up clusters emerge, all the follow-up clusters of \mathcal{A}_{n-1} are identified as described in the main text of section 4.3.2. Without loss of generality they are called \mathcal{A}_n , \mathcal{B}_n and \mathcal{C}_n in order of increasing distance to \mathcal{A}_{n-1} . If the distance between \mathcal{B}_n and \mathcal{A}_{n-1} as well as the distance between \mathcal{C}_n and \mathcal{A}_{n-1} is equal or greater than twice the distance between \mathcal{A}_n and \mathcal{A}_{n-1} , it is assumed that both the clusters \mathcal{B}_n and \mathcal{C}_n have been formed from free particles. This constitutes case 6 of table 4.1. In such a situation (shown in the left two panels of figure 4.12) cluster \mathcal{A}_n inherits the identity of cluster \mathcal{A}_{n-1} , while the clusters \mathcal{B}_n and \mathcal{C}_n are assigned new identities. If on the other hand distance between \mathcal{B}_n and \mathcal{A}_{n-1} as well as the distance between \mathcal{C}_n and \mathcal{A}_{n-1} are both smaller than twice the distance between \mathcal{A}_n and \mathcal{A}_{n-1} , it is assumed that the cluster \mathcal{A}_{n-1} split up into the three clusters \mathcal{A}_n , \mathcal{B}_n and \mathcal{C}_n . This constitutes the first possibility of case 7 (case 7a) of table 4.1. In this situation (shown in the right two panels of figure 4.12) all three follow-up clusters are assigned new identities and the identity of cluster \mathcal{A}_{n-1} is not used any longer. However if the distance between \mathcal{C}_n and \mathcal{A}_{n-1} is greater or equal than twice distance between \mathcal{A}_n and \mathcal{A}_{n-1} , but the distance between \mathcal{B}_n and \mathcal{A}_{n-1} is smaller than that, it is assumed that the cluster \mathcal{A}_{n-1} split into the clusters \mathcal{A}_n and \mathcal{B}_n while \mathcal{C}_n did form from free particles (case 7b not shown in figure 4.12). Since all follow-up clusters are assigned a new identity the same as in the situation described above, these two cases (7a and 7b) are not differentiated by the code used in the present work.

4.3.3 Voronoi tessellation

The idea of a Voronoi tessellation is to partition a space, containing a certain number of objects (clusters or particles in case of this work), into subspaces (Voronoi cells / Voronoi polygons) belonging to those objects. This is achieved in a way, that each subspace contains all points in space whose distance to the associated object (of the subspace) is smaller or equal than their distances to all other objects within the space. In two dimensional systems points associated to two objects (i.e. having the same distance to two objects) form the border between two Voronoi cells, such a border is called

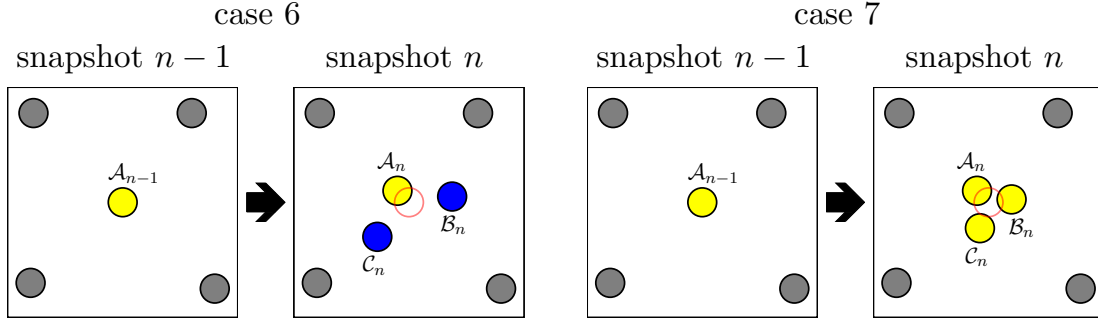


Figure 4.12: Comparison between case 6 (the two panels to the left) to case 7 (the two panels to the right). The black arrow symbolizes the propagation from snapshot $n - 1$ (left of the arrow) to snapshot n (right of the arrow). The red circle indicates the position of the cluster in snapshot $n - 1$, in order to simplify the judgment of distances.

Voronoi edge. Points associated to three and more objects form the intersecting points of Voronoi edges, they are called Voronoi vertices. If a Voronoi vertex is associated with four or more objects the vertex is called degenerate.

A mathematical definition for the Voronoi tessellation and Voronoi polygons can be found in [55, 56, 57, 58].

The Voronoi tessellation is essential for this work to identify if pairs of particles or clusters are nearest neighbors or not. This can easily be detected from the Voronoi tessellation since only the Voronoi cells of nearest neighbors share a Voronoi border or a Voronoi vertex in case the vertex is not degenerate. In turn, the nearest neighbor information is needed to compute the bond order parameters (see section 4.3.4).

Algorithm

To compute the Voronoi tessellation the code F35 from Ref. [30] was adapted for use in the present work. This code identifies the Voronoi polygons to a number of objects (e.g. clusters or particles) as follows.

An object of the simulation snapshot is selected as center object A . Then candidates for the nearest neighbors to the center object A are selected by simply choosing all those objects with a distance to center object A closer than a sufficiently large cutoff radius (r_c^{vor}). The cutoff radius r_c^{vor} has to be large enough so that at least three objects are found within this distance for each center object, which is the minimum number of points to construct a polygon in 2D.

Starting from the two closest of these candidates (B and C) the coordinates of the candidate-Voronoi vertex $V^{\{BC\}}$ (i.e. the point with equal distance to objects A , B and C) of this pair of objects relative to the center object A is computed via:

$$\overline{AV\{BC\}}_x = \frac{1}{2} \frac{\overline{AC}_y |\overline{AB}|^2 - \overline{AB}_y |\overline{AC}|^2}{\overline{AB}_x \overline{AC}_y - \overline{AC}_x \overline{AB}_y} \quad (4.138)$$

$$\overline{AV\{BC\}}_y = \frac{1}{2} \frac{\overline{AB}_x |\overline{AC}|^2 - \overline{AC}_x |\overline{AB}|^2}{\overline{AB}_x \overline{AC}_y - \overline{AC}_x \overline{AB}_y} \quad (4.139)$$

with \overline{AB} representing a vector from object A to object B and $\overline{AV\{BC\}}_x$, $\overline{AV\{BC\}}_y$ being the x and y components of the vector from the center object A to the candidate-vertex $V\{BC\}$. The obtained candidate-Voronoi vertex $V\{BC\}$ is a valid Voronoi vertex of the Voronoi cell, if the projection of $2\overline{AV\{BC\}}$ onto the unit vector $\widehat{\overline{AK}_i}$ from the central object A to any other candidate object K_i is smaller than than $|\overline{AK}_i|$:

$$2\overline{AV\{BC\}} \cdot \widehat{\overline{AK}_i} \leq |\overline{AK}_i| \quad \forall i. \quad (4.140)$$

Figure 4.13 shows the the situation with K_1 and K_2 being additional candidate objects, where $2\overline{AV\{BC\}} \cdot \widehat{\overline{AK}_2} < |\overline{AK}_2|$ and $2\overline{AV\{BC\}} \cdot \widehat{\overline{AK}_1} > |\overline{AK}_1|$. If a candidate-Voronoi vertex of a center particle turns out to be a valid vertex of its Voronoi cell, the vertex is stored along with the corresponding objects (B and C).

The number of valid Voronoi vertices associated to two objects (e.g. center object A and object B) should be zero, if they are not nearest neighbors, or two if they are nearest neighbors (one at each endpoint of the shared Voronoi edge). If however only one valid Voronoi vertex is associated to two objects, this vertex must be degenerate. An example of a degenerate Voronoi vertex is the point in the center of four objects placed on the corners of a square. The objects at the end of a diagonal of that square share only this single point as a Voronoi vertex and are not nearest neighbors. Obviously such an arrangement of objects is realized in a square lattice.

Since a special treatment of degenerate Voronoi vertices would be needed the current algorithm stops with an error in such a case. However since the present work is not dealing with regular structures such degeneracies should be seldom and did not occur in practice.

The set of all vertices belonging to a specific object make up the Voronoi polygon (Voronoi cell) of that object.

The computation of the Voronoi vertices is repeated with the next object as the center object A , until the Voronoi polygon of all objects in the simulation snapshot has been determined.

4.3.4 Bond-Order Parameters

Bond-order parameters are a measure of crystalline order in a system and are computed in this work to monitor the freezing of the particles and clusters into an ordered structure.

For a single particle or cluster the bond-order parameters $\Psi_6^{[1]}$ and $\Psi_4^{[1]}$ can be computed for hexagonal and square order [59, 60, 61, 62] via

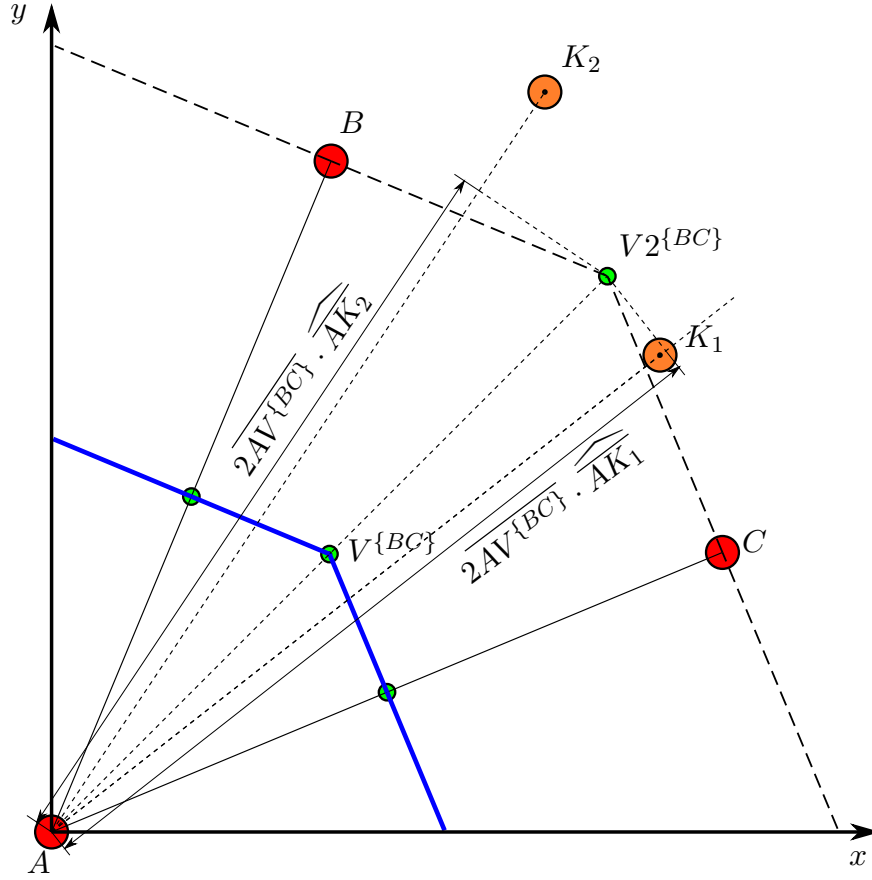


Figure 4.13: Voronoi tessellation: A denotes the central object, V denotes the candidate vertex with respect to objects B and C . $V2^{BC}$ denotes the intersection of the line perpendicular to the vector \overline{AB} running through object B with the line perpendicular to the vector \overline{AC} running through object C . The candidate Voronoi vertex V^{BC} is located in the middle of the distance $\overline{AV2^{BC}}$. Other candidate objects are shown as K_1 and K_2 (see text).

$$\Psi_6^{[1]} = \left| \frac{1}{M} \sum_{m=1}^M e^{6i\Phi_m} \right| \quad (4.141)$$

$$\Psi_4^{[1]} = \left| \frac{1}{M} \sum_{m=1}^M e^{4i\Phi_m} \right|, \quad (4.142)$$

with Φ_m being the angle between the vector from the central particle to its nearest neighbor with index m with respect to a fixed axis (e.g. the x -axis), and M being the number of these nearest neighbors (i denotes the imaginary unit here). The su-

perscript ^[1] in $\Psi_6^{[1]}$ and $\Psi_4^{[1]}$ indicates that the bond-order parameters computed via equations (4.141) and (4.142) are single particle properties.

For all the configurations in a simulation, with many particles or clusters in each configuration the bond order parameters for hexagonal and and square order, Ψ_6 and Ψ_4 can be computed via

$$\Psi_6 = \frac{1}{\sum_{j=1}^J N_j} \left| \sum_{j=1}^J \sum_{n=1}^{N_j} \frac{1}{M_{j,n}} \sum_{m=1}^{M_{j,n}} e^{6i\Phi_{j,n,m}} \right| \quad (4.143)$$

$$\Psi_4 = \frac{1}{\sum_{j=1}^J N_j} \left| \sum_{j=1}^J \sum_{n=1}^{N_j} \frac{1}{M_{j,n}} \sum_{m=1}^{M_{j,n}} e^{4i\Phi_{j,n,m}} \right|, \quad (4.144)$$

with J being the number of snapshots in the simulation, N_j being the number of particles/clusters in snapshot j , $M_{j,n}$ being the number of neighbors of particle/cluster n in snapshot j and $\Phi_{j,n,m}$ being the angle between the vector from central particle/cluster n to its nearest neighbor m in snapshot j with respect to a fixed axis.

4.3.5 Radius of gyration

The radius of gyration R_g is a measure of the linear extent of a cluster. In polymer-physics the radius of gyration of a polymer or cluster is defined as

$$R_g = \sqrt{\frac{1}{n^2} \sum_{i>j}^n d_{ij}^2}, \quad (4.145)$$

with d_{ij} being the distance between particles i and j belonging to the same cluster and n the number of particles within that cluster. Equation (4.145) was also used by Imperio *et al.* to compute the radius of gyration in Ref. [17].

Chapter 5

Results

5.1 Static Properties and Phase Diagrams

This section presents the potential-parameter regions (R_r, ϵ_r) where fluids, interacting via the Imperio-Reatto potential Φ_{IR} introduced in chapter 2, undergo microphase separation, in contrast to the regions where liquid-vapor phase separation occurs. More detailed results for either scenario is presented in sections 5.1.3 and 5.1.4 of this chapter. The results of section have been published in [63].

5.1.1 Computation of Phase Diagrams

Phase diagrams can be computed, using the Ornstein-Zernike equations, together with a suitable closure relation (like HNC or PY). For the present work the Percus-Yevick (PY) closure has been used for this purpose, if not explicitly stated otherwise. The computation of phase diagrams is performed in this work as follows. Solving the Ornstein-Zernike equations for a specific system at a certain particle density ρ and a certain temperature T yields the static structure information for this specific system, like the radial distribution function $g(r)$, the total correlation function $h(r) = g(r) - 1$ and the indirect correlation function $\gamma(r)$. Thermodynamic information of the system (pressure, chemical potential) can be computed from the static structure functions using suitable relations like equation (3.123) for the pressure and equations (4.136) and (4.137) for the chemical potential. Using the pressure and chemical potential, computed in this way, systems fulfilling the consistency equations

$$\begin{aligned} T^{\text{gas}} &= T^{\text{liq}} \\ P^{\text{gas}} &= P^{\text{liq}} \\ \mu^{\text{gas}} &= \mu^{\text{liq}}, \end{aligned} \tag{5.1}$$

while $\rho^{\text{gas}} \neq \rho^{\text{liq}}$, can be identified.

The numerical algorithm starts from a sufficiently high temperature, in order to ensure the convergence of the Ornstein-Zernike equation, together with the chosen closure

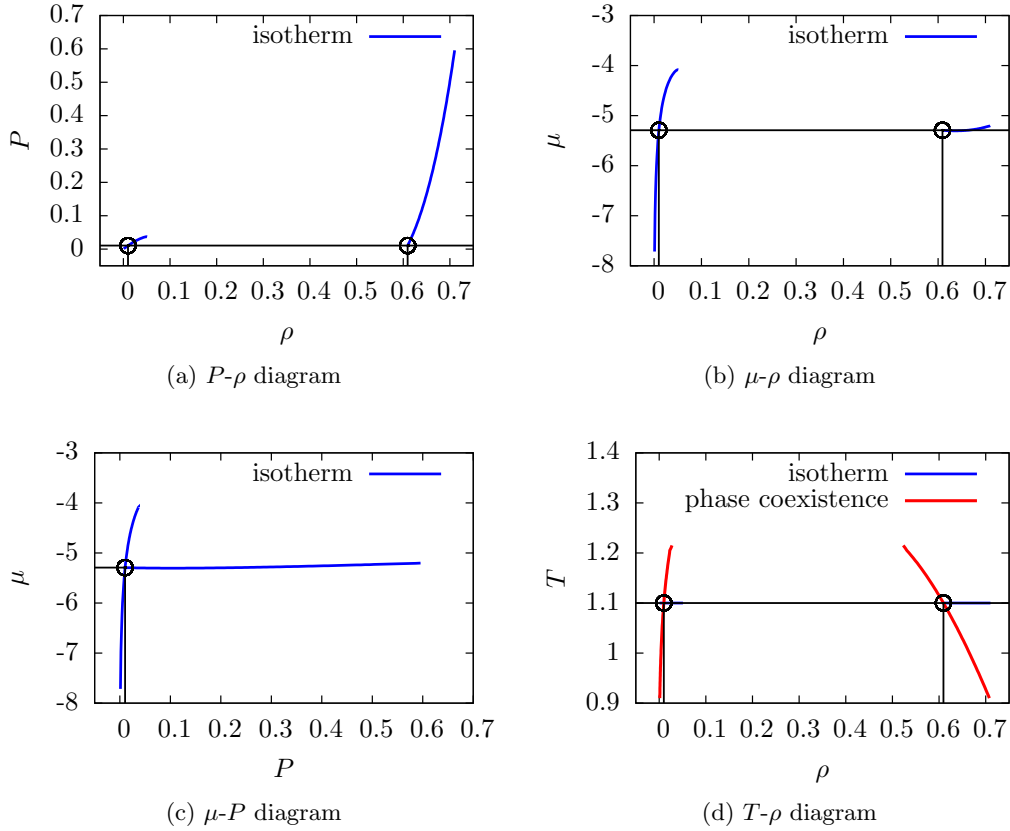


Figure 5.1: Procedure for computing the phase diagram used in the present work. The parameters of the potential are $R_r = 1.4$ and $\epsilon_r = 0.375$, the temperature is $T = 1.1$.

relation. For the current investigations a temperature of $T^{\text{start}} = 3.5$ was found to be sufficient for that purpose.

The Ornstein-Zernike equation is solved at this temperature for a low density ($\rho_{\text{gas}}^{\text{start}}$), as well as a high density ($\rho_{\text{liq}}^{\text{start}}$). The low density ($\rho_{\text{gas}}^{\text{start}}$) has to be chosen lower than the lowest coexistence density in the gas branch of the phase diagram, within the investigated temperature region. In the present investigation we have used $\rho_{\text{gas}}^{\text{start}} = 0.001$. Similarly, the higher density ($\rho_{\text{liq}}^{\text{start}}$), has to be chosen higher than the highest coexistence density in the liquid branch of the phase diagram, within the investigated temperature region.

In contrast to the lower density $\rho_{\text{gas}}^{\text{start}}$ however, the high starting density $\rho_{\text{liq}}^{\text{start}}$ has to be optimized in order to explore as much of the phase diagram as possible. In the present investigation this is achieved by using $\rho_{\text{liq}}^{\text{start}} = 0.75$ in a first run and refining $\rho_{\text{liq}}^{\text{start}}$ in subsequent runs by estimating the density of intersection of the high density coexistence line with the no-solution line of the Ornstein-Zernike equation. See figure 5.15 for a typical phase diagram and a typical no-solution line. The estimated intersection between the high density coexistence line and the no solution line would be

$\rho \approx 0.70$ in case of that figure. A value of $0.735 \leq \rho_{\text{liq}}^{\text{start}} \leq 0.8$ has been found suitable for most cases, with only a few exceptions of $\rho_{\text{liq}}^{\text{start}}$ being as low as 0.62.

Beginning from these two starting state-points $(\rho_{\text{gas}}^{\text{start}}, T^{\text{start}})$, $(\rho_{\text{liq}}^{\text{start}}, T^{\text{start}})$, the Ornstein-Zernike equation is solved, for a series of decreasing temperatures, down to the temperature where the first gas-liquid phase coexistence occurs. Then the Ornstein-Zernike equation is solved for increasing density, for the low density branch, starting from $\rho_{\text{gas}}^{\text{start}}$ at constant temperature T , until the solution algorithm does not converge anymore. In most cases, the breakdown of convergence is related to entering the two phase or the micro-phase region. The pressure P , and the chemical potential μ are evaluated for all visited state-points, using equation (3.123) and equations (4.136) and (4.137), respectively. Typical values for the pressure and the chemical potential as functions of the density are shown as blue lines on the low density branch of figure 5.1a and figure 5.1b.

For the high density (liquid) branch, the Ornstein-Zernike equation is solved for decreasing densities starting from $\rho_{\text{liq}}^{\text{start}}$ at constant temperature T . Values for the pressure P and the chemical potential μ as function of the densities of this branch, are shown as blue lines on high density side of figure 5.1a and figure 5.1b.

The phase coexistence can be easily identified as the point where pressure P and chemical potential μ (the difference between excess chemical potential and chemical potential is important here), are equal for the two branches. The temperature T of the two state-points is equal here, since we are working at isothermal conditions. The phase-coexistence is the intersection point of the low (gas) and the high (liquid) density branches at the pressure P as a function of the chemical potential μ , as the one shown in figure 5.1c. Computing the coexistence densities $\rho_{\text{gas}}^{\text{coex}}$, $\rho_{\text{liq}}^{\text{coex}}$ for several temperatures T in a similar way, the coexistence lines for the investigated system can be found. An example of these coexistence lines is shown in figure 5.1d.

In general those parts of the coexistence lines close to the critical point and the parts at very low temperatures are not accessible by this method because the Ornstein-Zernike equation (together with the closure relation) cannot be solved in those regions.

Approximation of the critical point

The critical point can be approximated by fitting the data obtained for the gas and the liquid branches of the coexistence lines, via a critical scaling law introducing the critical exponent β (see e.g. [27])

$$\rho_{\text{liq}}^{\text{coex}}(T) - \rho_{\text{gas}}^{\text{coex}}(T) \propto (|T^{\text{crit}} - T|)^{\beta}. \quad (5.2)$$

The unknown critical temperature is denoted by T^{crit} in equation (5.2).

Equation (5.2) is only valid in the vicinity of the critical point, thus only coexistence points with $T^{\text{coex}} \geq 0.9 T^{\text{crit}}$ were taken into account in the fitting procedure. Since T^{crit} is a priori unknown a guess has to be used to determine the data for a first fit. The critical temperature T^{crit} is then refined by repeating the fitting procedure three times, using the critical temperature of the previous fit to determine the coexistence data used in the next step of the fitting procedure.

The critical density ρ^{crit} , can then be obtained, by fitting the data of the gas and of the liquid branches of the phase diagram to

$$\rho_{\text{gas}}^{\text{coex}}(T) = \rho_{\text{gas}}^{\text{crit}} - \frac{1}{2} C_{\text{gas}} (T^{\text{crit}} - T)^{\beta} \quad (5.3)$$

and

$$\rho_{\text{liq}}^{\text{coex}}(T) = \rho_{\text{liq}}^{\text{crit}} + \frac{1}{2} C_{\text{liq}} (T^{\text{crit}} - T)^{\beta} \quad (5.4)$$

respectively, where $\rho_{\text{gas}}^{\text{crit}}$ and $\rho_{\text{liq}}^{\text{crit}}$ should yield the same value for the critical density ρ^{crit} and C_{gas} as well as C_{liq} are constants.

5.1.2 Overview

In order to demonstrate the effect of varying the potential-parameters of the Imperio-Reatto model (see chapter 2), as well as to display the range of potentials used in this investigation, the shapes of the Imperio-Reatto model potential with constant repulsion strength ($\epsilon_r = 1.0$) and different values of the repulsion range (R_r) are shown in figure 5.2. Shapes of the the Imperio-Reatto model potential at a constant repulsion range ($R_r = 2.0$) and different values of the repulsion strength (ϵ_r) are shown in figure 5.3.

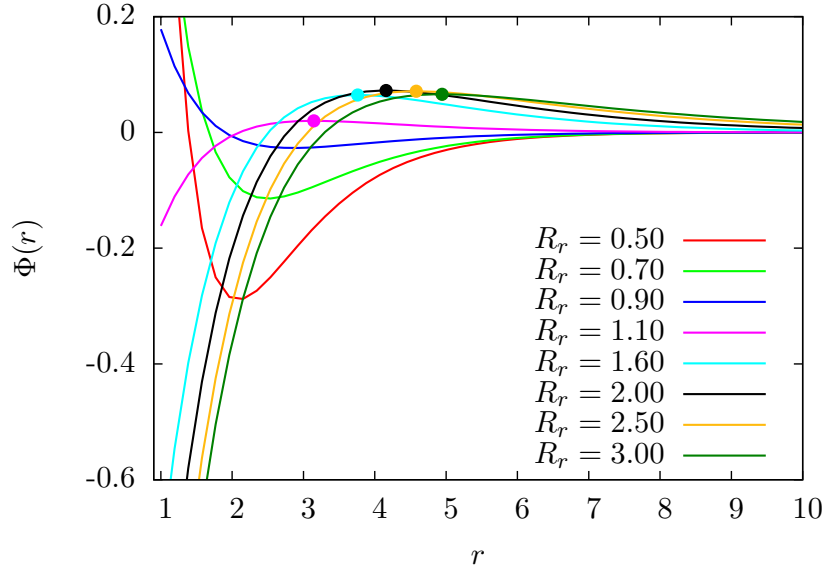


Figure 5.2: Selected potentials with a repulsion strength of $\epsilon_r = 1.0$ and different values of the repulsion range R_r as labeled. The potential used by Imperio and Reatto (e.g. in [12, 17, 18]) is given by the black line. The dots mark the maximum of the repulsion.

It can be seen immediately from figure 5.2, that the distance r_{\max} where the potential attains its maximum value is shifted to larger r with increasing repulsion range R_r . The potential value at the maximum $\Phi_{\text{IR}}(r_{\max})$ however, increases up to a repulsion range of $R_r \sim 2.0$, while increasing the repulsion range and decreases slowly, for even larger values of the repulsion range R_r .

Figure 5.3 on the other hand shows, that using a fixed repulsion range of $R_r = 2.0$ and increasing the repulsion strength (ϵ_r), shifts the position of the maximum of the repulsive potential hump r_{\max} to smaller values of r , while the potential value at this maximum, $\Phi_{\text{IR}}(r_{\max})$, increases monotonically.

The maximum of the repulsive potential hump, within the entire parameter space investigated in this work ($0.5 \leq R_r \leq 3.0$ and $0.0 \leq \epsilon_r \leq 1.0$), can be found at a repulsion range of $R_r = 2.144$, and a repulsion strength of $\epsilon_r = 1.0$ at the position $r_{\max} = 4.288$, with an value of $\Phi_{\text{IR}}(r_{\max}) = 0.0726$ (computed using [64]).

An overview of the different phase behaviors identified for our systems is shown in figure 5.4. In dependence of the values of R_r and ϵ_r this figure provides information if

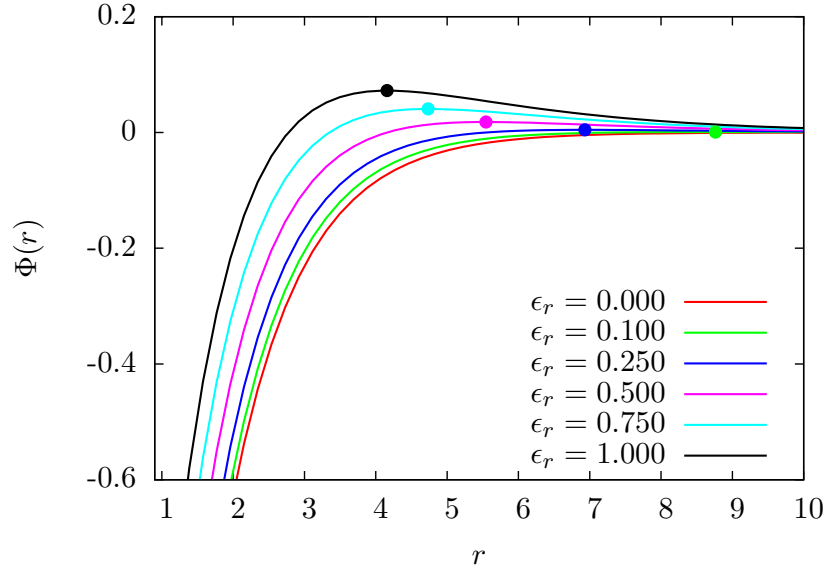


Figure 5.3: Selected potentials with a repulsion range of $R_r = 2.0$ and different values of the repulsion strength ϵ_r as labeled. The potential used by Imperio and Reatto (e.g. in [12, 17, 18]) is given by the black line. The dots mark the maximum of the repulsion.

the corresponding system shows a liquid-vapor separation or a microphase formation. The black rectangle (■) marks the parameter-set used by Imperio and Reatto in their works (e.g. [12, 17, 18, 19]), while the black bullets (●) mark the additional parameter sets investigated in this work via integral equations and Monte-Carlo simulations.

The sets of potential parameters (R_r, ϵ_r) of the Imperio-Reatto potential, where the corresponding system shows a liquid-vapor phase transition below a density dependent temperatures, are marked by the green area in figure 5.4. For these sets of parameters, it was possible to find at least one liquid-vapor phase coexistence, using the method explained in section 5.1.1. More detailed results for these systems are given in section 5.1.4.

Potential parameters, where the corresponding systems show microphase formation below a density dependent temperatures, are marked by the red area in figure 5.4. The yellow stripe between the red and green area in this figure marks sets of potential parameters, where no conclusive result for either of the two scenarios could be found. More detailed results for microphase forming systems can be found in section 5.1.3.

This classification of systems into phase-separating and microphase forming systems was confirmed by Monte Carlo simulations.

In [20] Archer managed to derive a closed expression for the wave-number k_c , using a Density Functional Theory (DFT) approach. According to his work, systems featuring the Imperio-Reatto potential form microphases with a periodicity characterized by the wave-number k_c at low temperatures.

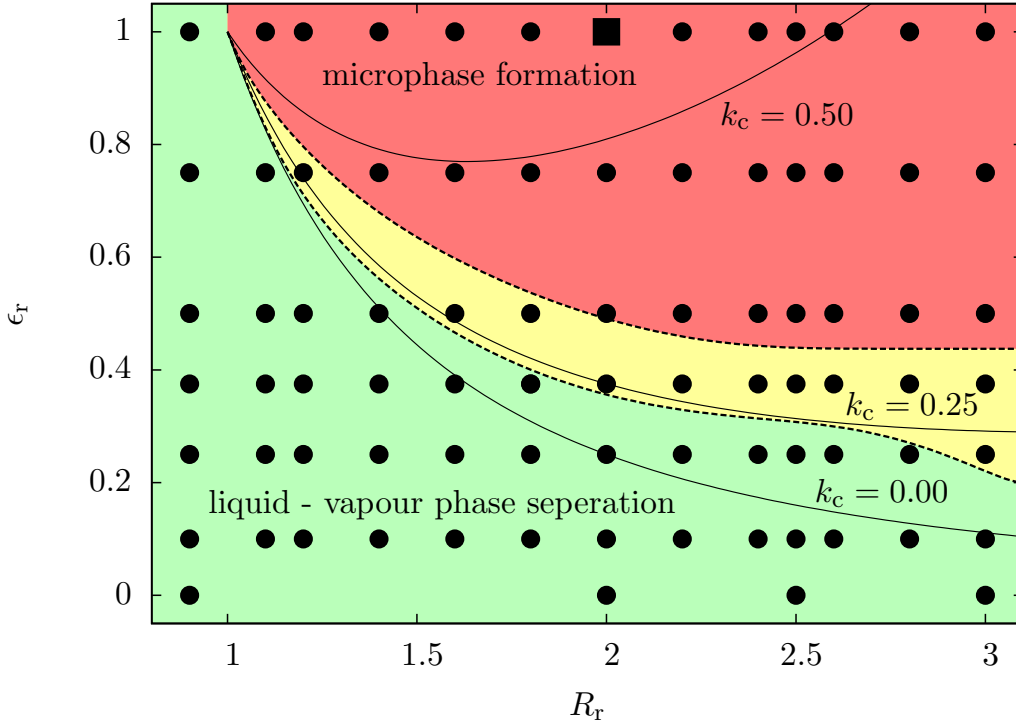


Figure 5.4: Overview of the investigated systems (\bullet and \blacksquare) specified by R_r and ϵ_r . Systems in the green area show a liquid-vapor phase separation. Systems in the red area show microphase formation. For the systems in the yellow area in between, no conclusive answer could be given. The lines in this figure run along states with constant k_c (see equation (5.5) as labeled).

The expression derived for the wave-number k_c is given by

$$k_c = \sqrt{\frac{\Gamma - 1}{R_r^2 - \Gamma R_a^2}} \quad (5.5)$$

$$\Gamma = \left(\frac{\epsilon_r R_r^2}{\epsilon_a R_a^2} \right)^{\frac{2}{5}}.$$

Lines of constant k_c are shown in figure 5.4.

As can be seen from equation (5.5), the value of k_c only depends on the potential parameters (i.e. the range and strength of the attraction and the repulsion), but is independent of the state parameters (i.e. density and temperature). The implications of the independence of k_c from the state of the system are investigated in more detail in section 5.1.3.

If $k_c = 0$, one would obviously expect the conventional liquid vapor phase separation scenario. Therefore, the line where $k_c = 0$ should coincide with the upper boundary of the green area below which the systems undergo liquid-vapor phase separation. The

obvious difference of the two lines (see figure 5.4) indicates the limitations of the DFT approach. On the other hand the position of the peak associated with microphase formation, that is found in the structure factors computed via Monte-Carlo simulations or the Ornstein-Zernike equation was very well predicted by the value of k_c calculated via equation (5.5) in all investigated cases, as can be seen in figures 5.9 to 5.11 and 5.13 in section 5.1.3.

In figure 5.5 we use the same color code as figure 5.4. Now the curves connect pairs of potential parameters for which the max of the repulsive potential, r_{\max} occurs at the same position.

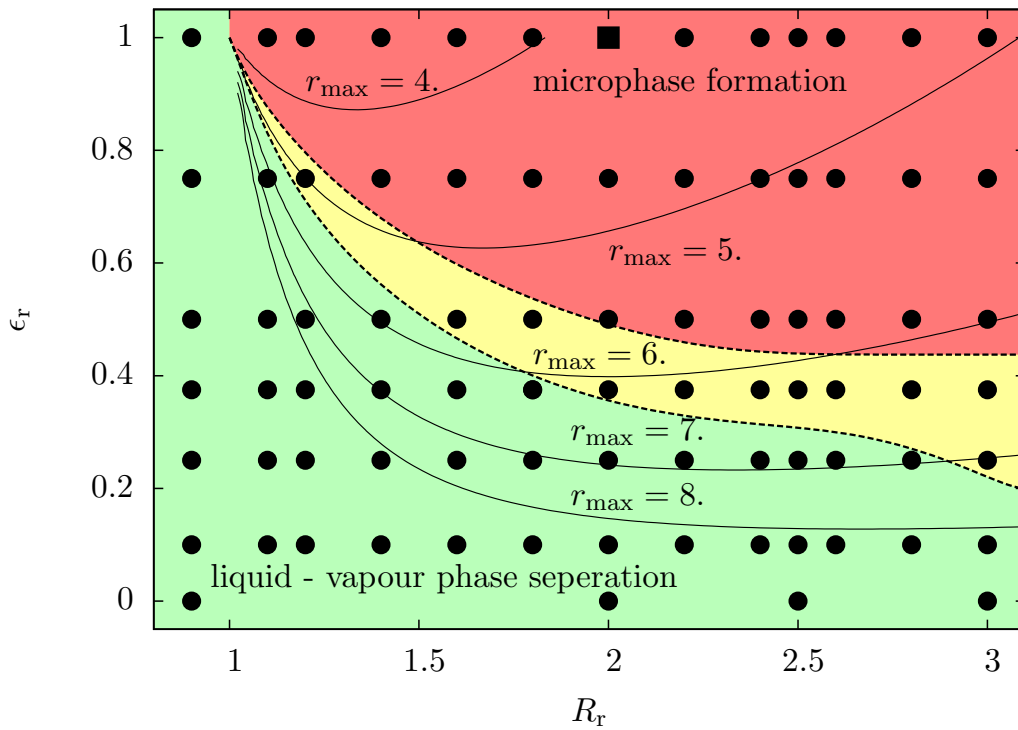


Figure 5.5: Overview of the investigated systems (\bullet and \blacksquare) specified by R_r and ϵ_r . Systems in the green area show a liquid-vapor phase separation. Systems in the red area show microphase formation. For the systems in the yellow area in between, no conclusive answer could be given. The lines in this figure connect states with equal position of the maximum r_{\max} in the potential as labeled.

From this figure we can see, that within the given parameter space ($0.0 \leq \epsilon_r \leq 1.0$ and $0.5 \leq R_r \leq 3.0$), microphase formation only occurs, if the position of the repulsive potential hump, r_{\max} , is less than ~ 6.5 . This means, that the distance of the maximum of the repulsion, r_{\max} must not be too large, in order to guarantee microphase formation. In figure 5.6 we use the same color code as in figures 5.4 and 5.5. Here, the black curves connect sets of potential parameters with the same height of the repulsive potential hump, $\Phi_{\text{IR}}(r_{\max})$.

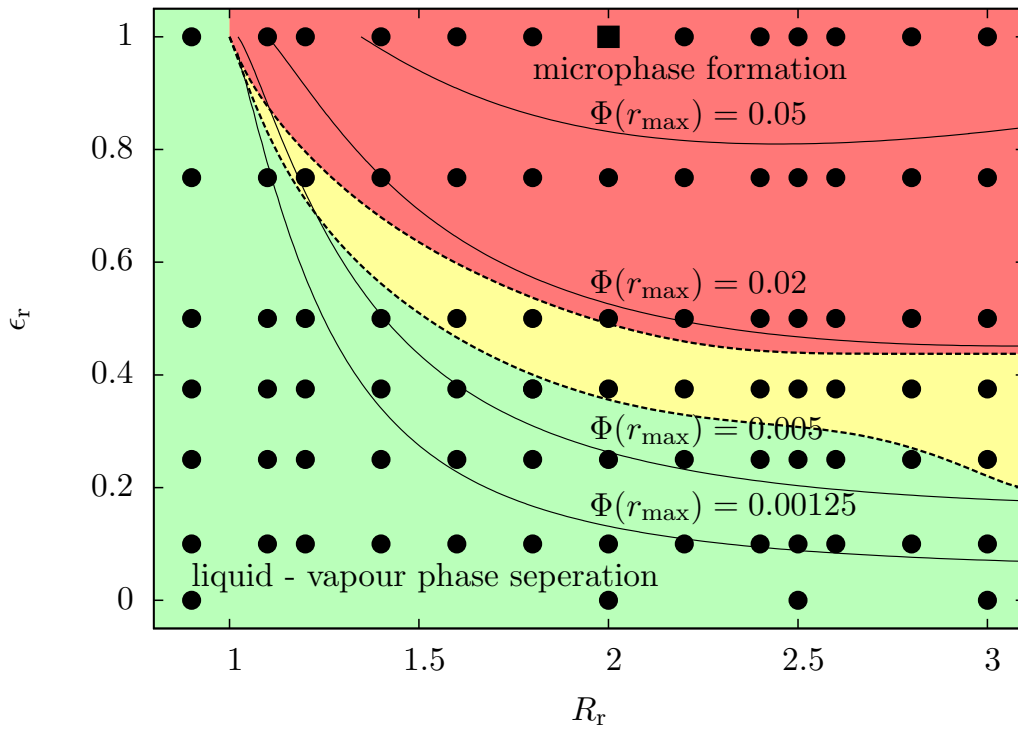


Figure 5.6: Overview of the investigated systems (\bullet and \blacksquare) specified by R_r and ϵ_r . Systems in the green area show a liquid-vapor phase separation. Systems in the red area show microphase formation. For the systems in the yellow area in between, no conclusive answer could be given. The lines in this figure connect states with equal height the potential maximum $\Phi(r_{\max})$ (as labeled).

From this figure we can see, that microphase formation only occurs, if the height of the repulsive potential hump, $\Phi_{\text{IR}}(r_{\max})$, is larger than ~ 0.02 .

5.1.3 Systems showing microphase formation

As already stated in the previous section, the region of potential-parameters (R_r , ϵ_r) where the system shows microphase formation, below a density dependent temperature, is marked by the red area in figure 5.4. Above this transition temperature, these systems form a homogeneous fluid phase.

Since the microphase formation of the original system used by Imperio and Reatto ($R_r = 2.0$, $\epsilon_r = 1.0$), has already been investigated in great detail in [12, 17, 18, 19], this work focuses on four state-points within the fluid phase of this system.

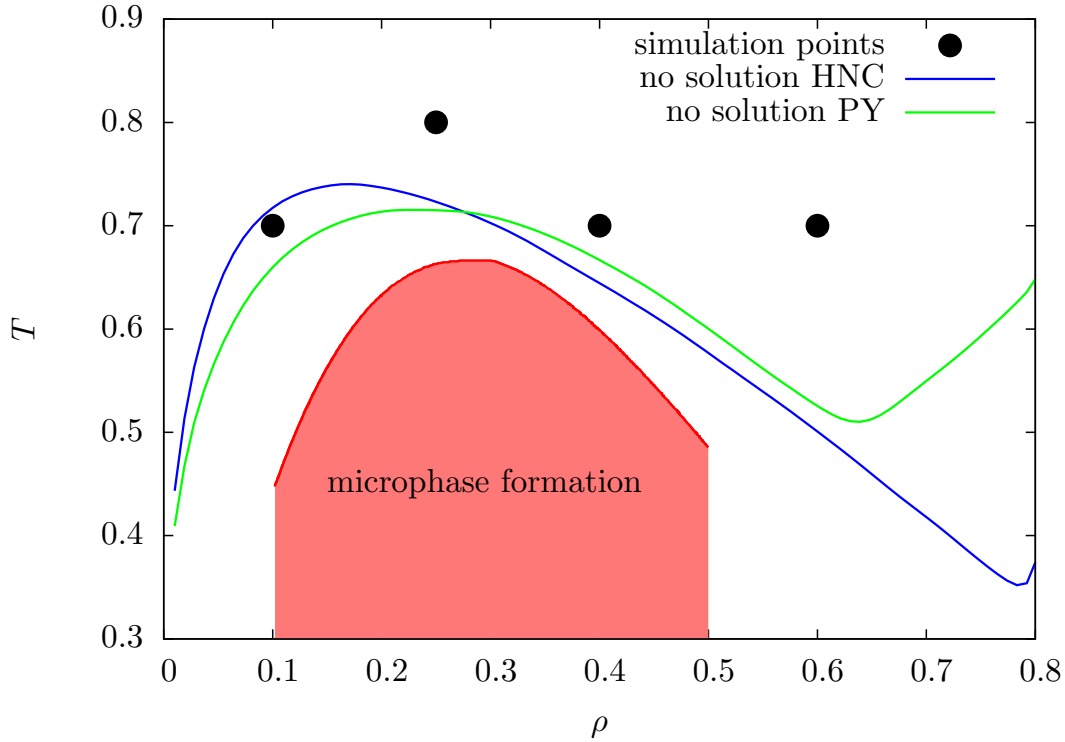


Figure 5.7: State-points of the system characterized by $R_r = 2.0$ and $\epsilon_r = 1.0$ investigated via Monte Carlo simulation \bullet . Further the no-solution line of the Ornstein-Zernike equation along with the HNC (blue line) and the PY (green line) closure relations are shown. The red area represents an estimate for the region where microphase formation occurs (taken from [12]).

The four selected state-points ($\rho = 0.10$, $T = 0.70$; $\rho = 0.25$, $T = 0.80$; $\rho = 0.40$, $T = 0.70$; $\rho = 0.60$, $T = 0.70$), are marked as black bullets in figure 5.7. In addition, an estimate for the region where microphase formation shows (red area), is given in this figure. The blue and green lines in figure 5.7 represent the no-solution lines for the Ornstein-Zernike equation, in combination with the HNC and the PY closure relation, respectively. These no-solution lines mark the limit, below which the numerical solution of the Ornstein-Zernike equation, does not converge any more.

All selected state-points marked in figure 5.7 are chosen to be located close to the no-solution lines of the integral equation approach. The state-point ($\rho = 0.10$, $T = 0.70$), even lies within the region where the HNC approximation does not converge.

A comparison of the radial distribution functions $g(r)$, for the four selected state-points is shown in figure 5.8.

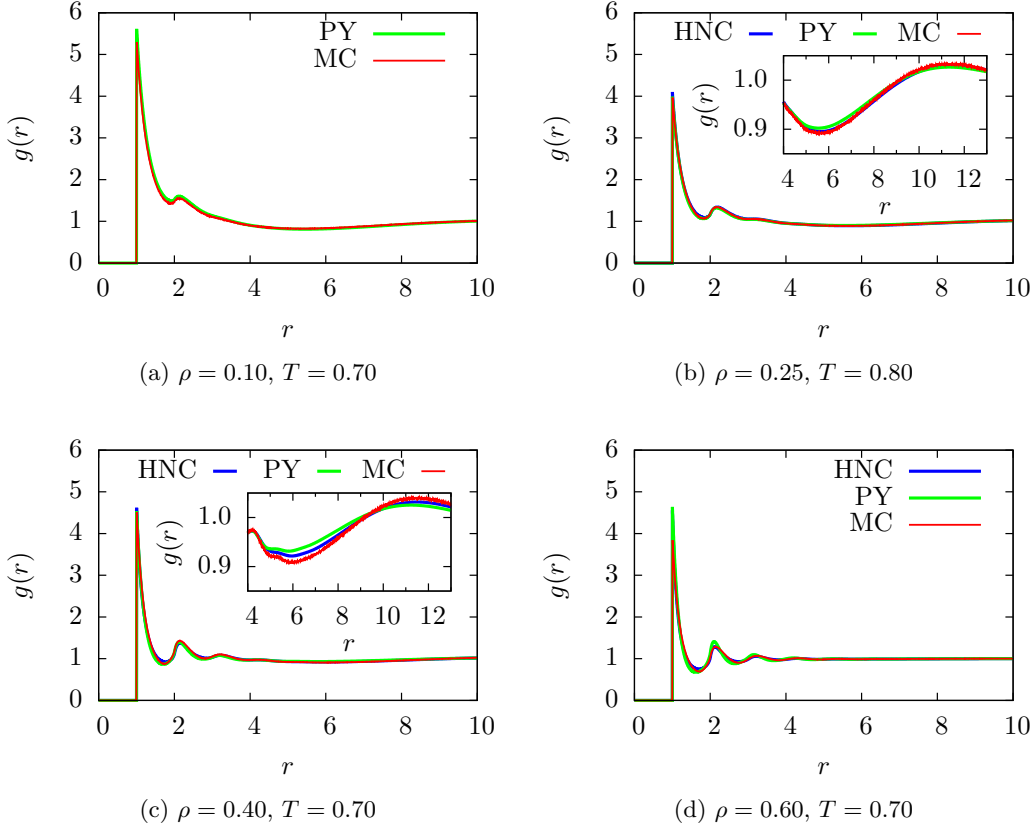


Figure 5.8: Comparison between the radial distribution functions $g(r)$, obtained by Monte Carlo simulation and integral equations (as labeled), for systems characterized by the potential-parameters $R_r = 2.0$ and $\epsilon_r = 1.0$. The insets in (b) and (c) show the the first minimum and the subsequent maximum of the long range oscillations in $g(r)$ (see text for further details).

For all four investigated state points, the $g(r)$ show a good agreement between the Monte Carlo simulation data and the integral equation results. results, for all four investigated state-points.

This observation is especially surprising for state-points that are located that close to the no-solution lines of the Ornstein-Zernike equation. The agreement between the integral equation results, computed with the HNC and PY closure respectively, is also remarkable, since it is well known, that for many simple liquids, these two closure relations lead to distinctively different results for the structure functions [27].

In addition to a pronounced main peak, the radial distribution functions in figure 5.8 also show a side peak at $r \sim 2.0$. This structural feature in combination with the long range oscillations at low density ($\rho \lesssim 0.40$) indicates the onset of the microphase formation reported for this systems at lower temperature. The first minimum of the long range oscillation on $g(r)$ is visible in the inset of figures 5.8b and 5.8c as a minimum in the radial distribution function at $r \sim 5.5$ and $r \sim 6.0$ respectively the distance to the subsequent maximum is ≈ 5.5 in both cases which leads to a wavelength of the long range oscillations of ~ 11.0 . This wavelength is consistent with the wavenumber $k_c = 0.573$ derived for the potential-parameters of the original Imperio-Reatto system since $2\pi/0.573 \approx 11.0$. The usual behavior of decaying oscillations around unity, with a wavelength in the order of the particle size, seen in many simple liquids, is only present at the highest of the four investigated densities ($\rho = 0.60$).

Figure 5.9 shows a comparisons of the static structure factors $S(k)$, from Monte Carlo simulations and for the Ornstein-Zernike equation in combination with the HNC and PY closure relation respectively, for the state-points marked in figure 5.7.

The structure factors $S(k)$, presented in figure 5.9, show a pronounced first peak at $k < 1.0$. The position of this peak coincides with the value of $k_c = 0.573$ calculated for the potential-parameters of this system (marked by the black vertical arrow in figure 5.9), indicating the formation of a microphase at lower temperatures.

Another clue to the connection of this peak to the microphase formation is given by the distinct non-monotonic behavior of its height while increasing the density (even when not considering the state $\rho = 0.25, T = 0.80$ because of the different temperature). The first peak of the structure factor at about $k_c = 0.573$ is highest at $\rho = 0.40$, which also is the statepoint closest to the microphase region as can be seen in figure 5.7.

The second peak of the static structure factor $S(k)$ at $k \approx 6.0$ is related to the oscillations of the radial distribution function $g(r)$ with a wavelength of ≈ 1.0 . Therefore it originates from particles that are in direct contact with other particles.

Similar as for the radial distribution function, there is good agreement between the data from Monte Carlo simulations and the results from integral equations (PY, HNC). Notable discrepancies in the structure factor $S(k)$ are only visible at higher densities (see figures 5.9c and 5.9d).

To further test the independence of k_c on the system state, the results for the static structure factors $S(k)$ of a system with $R_r = 1.2$, $\epsilon_r = 1.0$, are compared at different temperatures and densities, according to equation (5.5) this should lead to $k_c = 0.745$ irrespective of temperature and density.

Figure 5.10 shows the static structure factors, for this system obtained by Monte Carlo simulations at different temperatures ($T = 0.10, T = 0.15, T = 0.20$), well inside the microphase forming region for the featured densities ($\rho = 0.20$ figure 5.10a and $\rho = 0.40$ figure 5.10b).

The height of the peaks differs substantially, however the peak position does not vary with temperature and in addition coincides with the predicted value of k_c .

Figure 5.11 shows a similar comparison, however the static structure factors (obtained by Monte Carlo simulations) are compared for different densities ($\rho = 0.20, \rho = 0.40$ and $\rho = 0.60$). These states correspond to different morphologies of microphases (clusters, stripes/lamellae, bubbles/inverse clusters). Two different temperatures $T = 0.15$ and

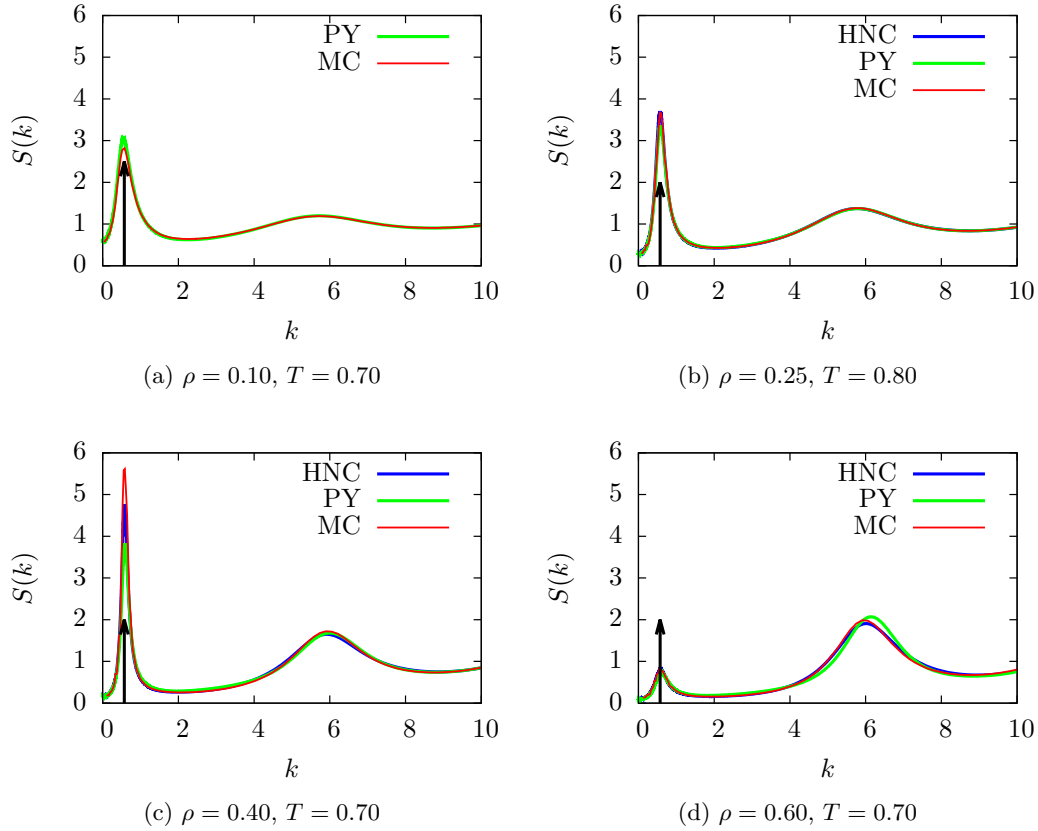


Figure 5.9: Comparison between the structure factors $S(k)$, obtained by Monte Carlo simulation and integral equations (as labeled), for systems characterized by the potential-parameters $R_r = 2.0$ and $\epsilon_r = 1.0$. The vertical arrow marks the position of $k_c = 0.573$.

$T = 0.20$ are considered.

As in the preceding case, it can be seen that the positions the peak of the structure factors do not depend on the state and in addition coincide with the value predicted by equation (5.5).

To provide additional evidence for the validity of k_c obtained from equation (5.5) four sets of potential-parameters (A, B, C and D) have been chosen in such a way, that each set yields a similar value for k_c ($k_c \approx 0.485$). The potential-parameters, as well as the exact values of k_c are listed in table 5.1.

The location of the four systems (A, B, C, D) are also shown in the (R_r, ϵ_r) plane in figure 5.12.

The data for the static structure factor $S(k)$, obtained by Monte Carlo simulations for the systems A, B, C and D at two different temperatures ($T = 0.50$ and $T = 0.70$), is shown in figure 5.13.

As can be seen from this figure the position of the peak of the static structure factor

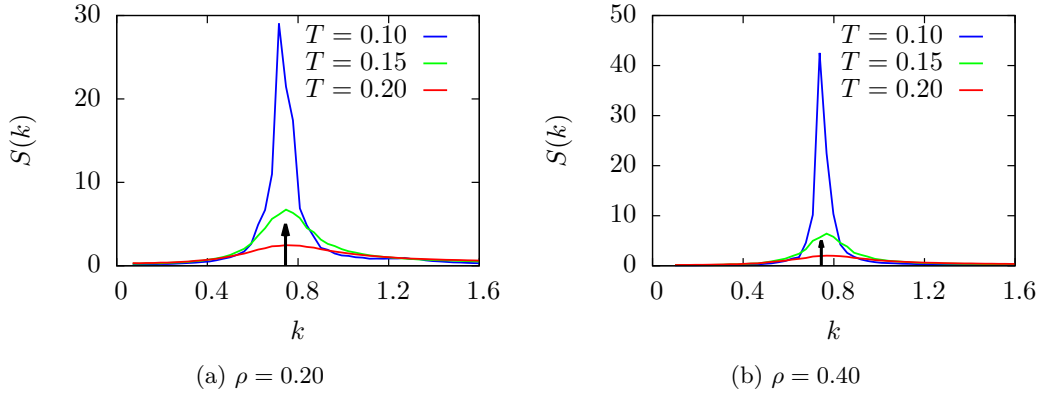


Figure 5.10: Static structure factors for systems with $R_r = 1.2$ and $\epsilon_r = 1.0$, calculated from Monte-Carlo simulations for different temperature (as labeled) and two values of the density (left and right panel). The vertical arrow marks the position of $k_c = 0.745$.

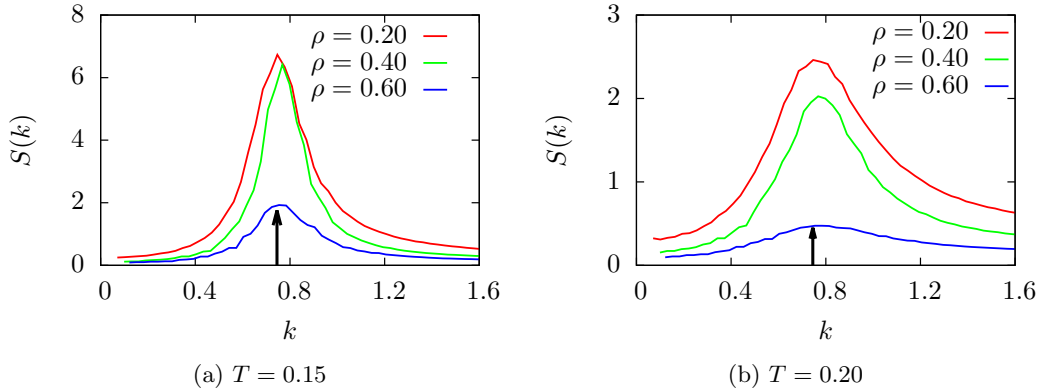


Figure 5.11: Static structure factors for systems with $R_r = 1.2$ and $\epsilon_r = 1.0$, calculated from Monte-Carlo simulations for different densities (as labeled) and two values of the temperature (left and right panel). The vertical arrow marks the position of $k_c = 0.745$.

coincides reasonably well with the value $k_c = 0.485$. Deviations from the predicted value visible in figures 5.13a and 5.13b can be at least partly attributed to the limited k -resolution of the static structure factor in this wave-number region. The low k -resolution is also responsible that some of the peaks in the structure factor are not sampled at their maximum height therefore some of the peaks in figure 5.13 seem to be lower at low temperature than at higher temperature.

Simulation snapshots of the systems A, B, C and D are shown in figure 5.14.

From a visual inspection figures 5.14a to 5.14d look similar, especially concerning cluster

	R_r	ϵ_r/ϵ_a	k_c
A	1.60	0.750	0.4861
B	1.80	0.750	0.4849
C	2.50	0.905	0.4850
D	2.74	1.000	0.4851

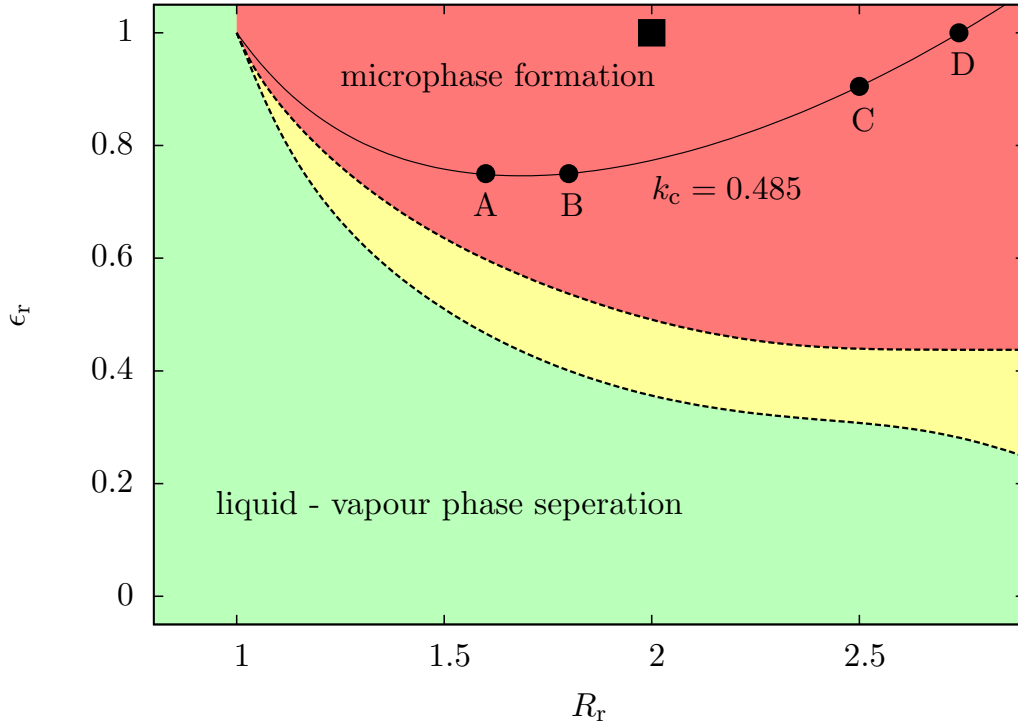
Table 5.1: Potential-parameter sets A, B, C and D yielding $k_c \approx 0.485$.

Figure 5.12: Overview of the systems characterized by $k_c \approx 0.485$ (●). See table 5.1 for the potential parameters and exact value of k_c of these systems. The system investigated by Imperio and Reatto ($R_r = 2.0$, $\epsilon_r = 1.0$) is shown as a reference point (■).

size and the distance between the individual clusters. This also is evidence that the parameters of the potentials involved in creating systems A,B,C and D, yield the same k_c , using equation (5.5), which in turn lead to the formation of microphases with similar structure. Please note that the not all snapshots in figure 5.14 where produced using the same temperature.

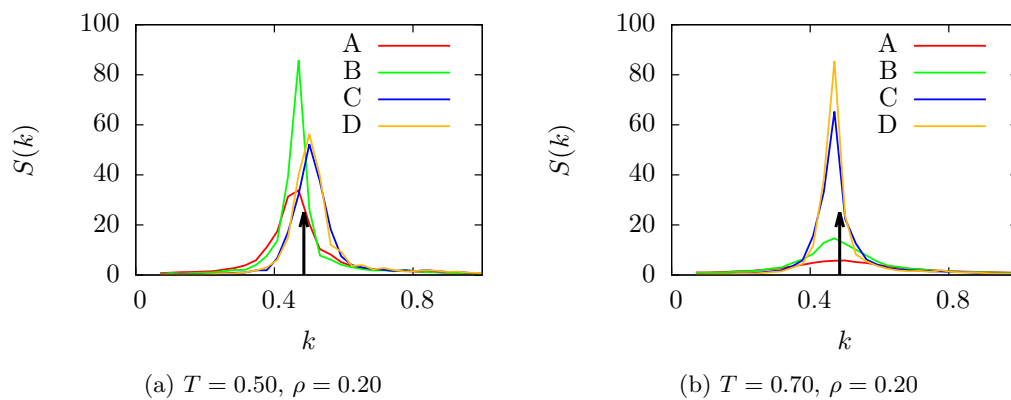


Figure 5.13: Structure factor comparison for the systems A, B, C and D, calculated from Monte-Carlo simulations for different systems (as labeled) and two values of the temperature (left and right panel). The vertical arrow marks the position of $k_c = 0.485$.

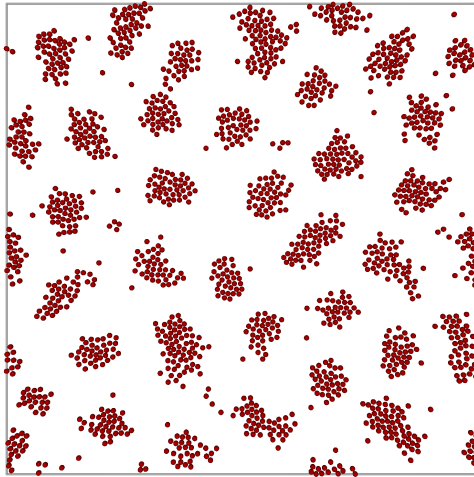
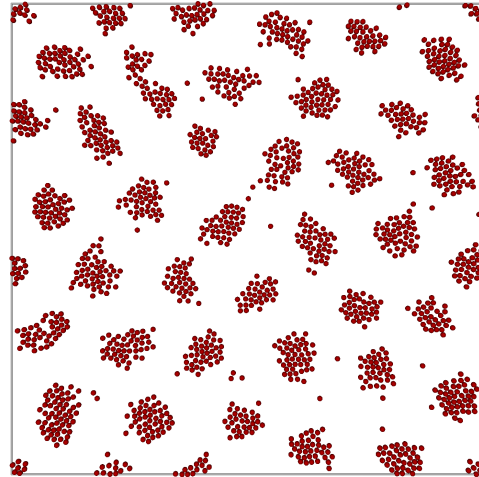
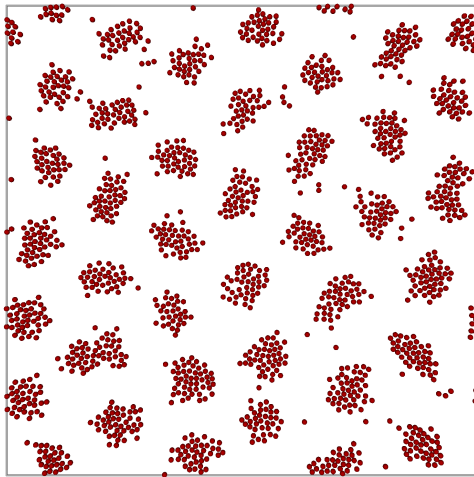
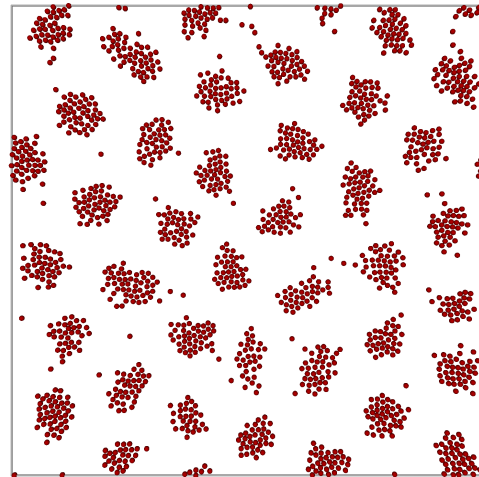
(a) A: $R_r = 1.60$, $\epsilon_r = 0.750$, $T = 0.50$ (b) B: $R_r = 1.80$, $\epsilon_r = 0.750$, $T = 0.50$ (c) C: $R_r = 2.50$, $\epsilon_r = 0.905$, $T = 0.70$ (d) D: $R_r = 2.74$, $\epsilon_r = 1.000$, $T = 0.70$

Figure 5.14: Monte Carlo simulation snapshots of systems A, B, C and D. Please note that the temperature is $T = 0.50$ for figures 5.14a and 5.14b, while $T = 0.70$ for figures 5.14c and 5.14d.

5.1.4 Systems showing liquid-vapor phase separation

In this section we summarize concentrates on the results of systems with competing interactions, showing the usual liquid-vapor phase separation behavior at sufficiently low temperatures. The potential-parameters sets (R_r, ϵ_r) that guarantee liquid-vapor phase separation are located in the green area shown in figure 5.4.

Figure 5.15 shows a typical phase diagram for such a system ($R_r = 1.40$, $\epsilon_r = 0.375$).

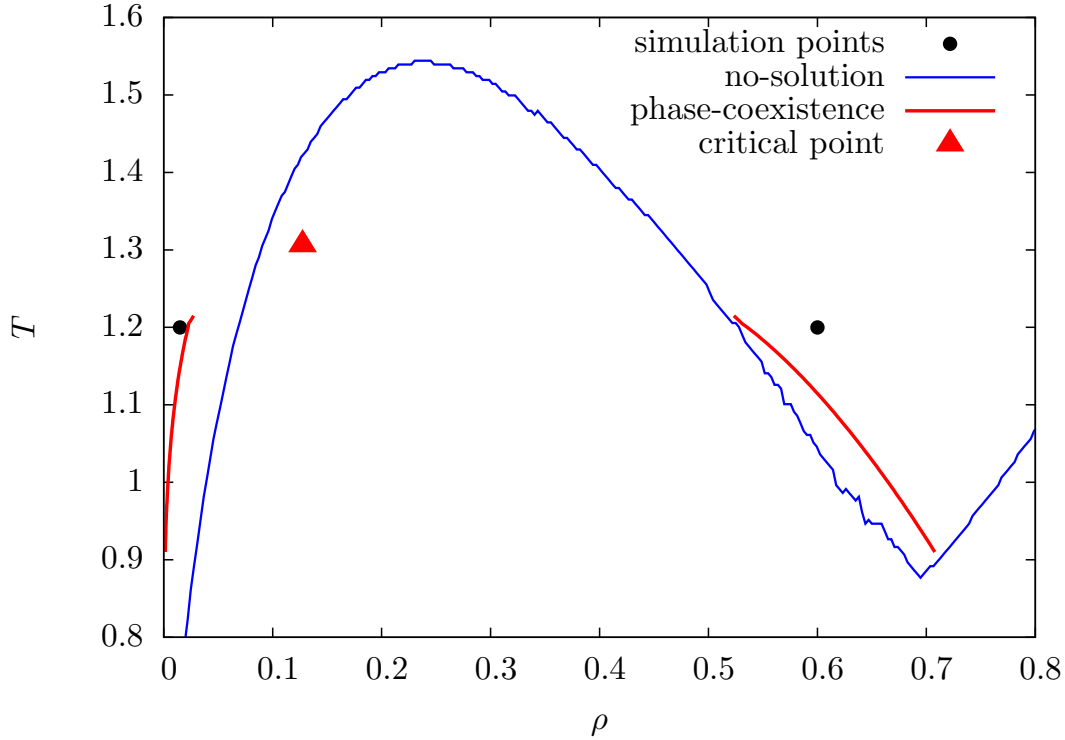


Figure 5.15: Phase coexistence lines, no solution line and an estimation of the critical point (\blacktriangle) for a typical system with competing interactions ($R_r = 1.4$, $\epsilon_r = 0.375$). The black dots (\bullet) specify the state-points for which the Monte Carlo simulations, have been computed in order to compare the structure functions $g(r)$ and $S(k)$ (see figures 5.16 and 5.17).

The coexistence lines that were found using the procedure described in section 5.1.1 are represented by the red lines in figure 5.15. The closure relation used in this case was the PY closure, while the red triangle (\blacktriangle) in figure 5.15 marks the position of the critical point estimated by the procedure given in section 5.1.1. The blue line in figure 5.15, on the other hand marks the no-solution line of the Ornstein-Zernike equation together with the PY closure relation. Below that line the solution algorithm outlined in section 4.2.3 did not converge.

The radial distribution function $g(r)$, as well as the static structure factor $S(k)$ have been compared for two state-points of the system in order to check the accuracy of the

integral equation approach. These two state-points, are specified via as black dots (●) in figure 5.15, they have been chosen to lie close to the coexistence lines of the system.

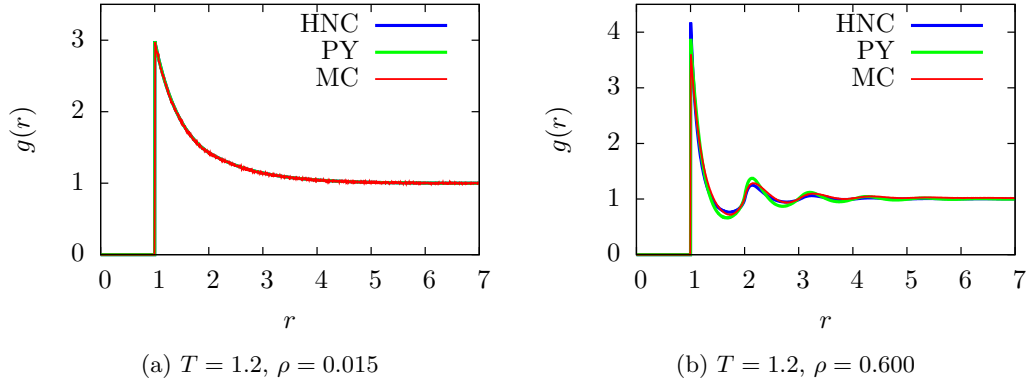


Figure 5.16: Comparison of the radial distribution function $g(r)$ of systems characterized by the potential-parameters $R_r = 1.4$ and $\epsilon_r = 0.375$, obtained via the Ornstein-Zernike equation in combination with the HNC (blue line) and PY (green line) closure respectively, as well as Monte Carlo simulations (red line).

Figure 5.16 shows the radial distribution functions $g(r)$ for a system with potential-parameters $R_r = 1.2$ and $\epsilon_r = 0.375$ at $T = 1.2$ densities of $\rho = 0.015$ (left) and $\rho = 0.60$ (right). The radial distribution functions $g(r)$ shown in figure 5.16a have a pronounced main peak of considerable height at the hard core of the particles, in the low density vapor phase ($\rho = 0.015$). The height of this peak may be that pronounced, due to the adjacent attractive interaction of the potential. The height of the peak is reproduced very well by the integral equations, irrespective of the closure relation. The radial distribution for the liquid phase ($\rho = 0.60$), has an asymmetric peak at $r \approx 2$ in addition to the pronounced main peak. The agreement of the simulation data with the results from integral equations is not as good as for the low density vapor phase, however the positions of all the peaks as well as the peak heights are quite well reproduced still.

A comparison of the static structure factors $S(k)$, obtained by Monte Carlo simulations as well as by integral equations for the same system and state-points is given in figure 5.17.

Similar as for the radial distribution function, all features of the static structure factor are in excellent agreement between the simulation data and the integral equation results for the low density state-point ($\rho = 0.015$). We find also good agreement for the high density state-point ($\rho = 0.60$), with the only notable exception of the peak height at $k = 0$ (see figure 5.17b).

The coexistence lines of systems interacting via the Imperio-Reatto potential and computed via the Ornstein-Zernike equation in combination with the Percus-Yevick closure relation are shown in figures 5.18 and 5.19. In addition to these coexistence lines (solid lines), an estimate of the critical points (dots) is given, whenever there was sufficient

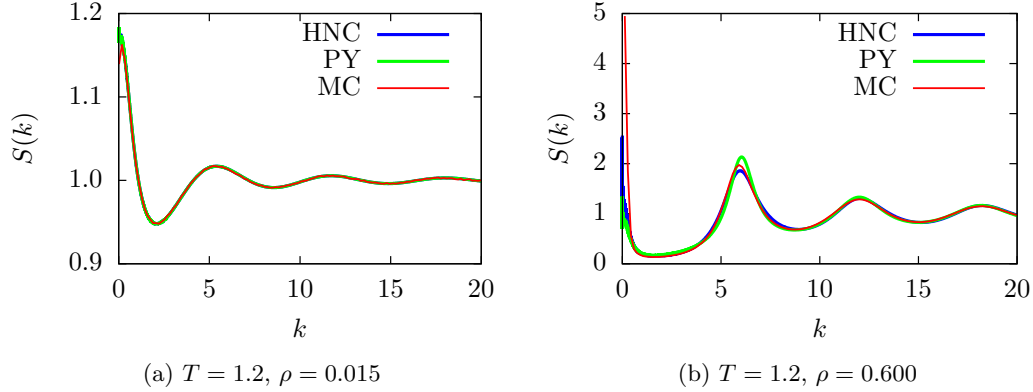


Figure 5.17: Comparison of the structure factor $S(k)$ of systems characterized by the potential-parameters $R_r = 1.4$ and $\epsilon_r = 0.375$, obtained via the Ornstein-Zernike equation in combination with the HNC (blue line) and PY (green line) closure respectively, as well as Monte Carlo simulations (red line).

data available. The no-solution lines for the systems are shown in figures 5.18 and 5.19. as dashed lines.

In each of the panels of figure 5.18, the value of the repulsion strength ϵ_r was kept constant, at the value stated at the bottom of the panel where R_r was varied. It can be easily seen from this figure that an increase in the repulsion range R_r (while keeping ϵ_r fixed) leads to a monotonic decrease in the critical temperature T^{crit} . There is also an monotonic decrease in the critical density ρ^{crit} as long as the repulsion range $R_r > 1.0$. In each of the panels of figure 5.19, the value of the repulsion range R_r was kept constant, at the value stated at the bottom of the panel where ϵ_r was varied. Figure 5.19 shows, that increasing the repulsion strength ϵ_r (while keeping R_r constant) leads to a decrease of the critical temperature T^{crit} and a flattening of the coexistence curve. A drastic example of the flattening of the coexistence curve can be seen in the phasediagram using the potential-parameters $R_r = 0.9$, $\epsilon_r = 1.0$ in figure 5.19b (orange curve).

As already discussed in section 5.1.1, the approximate position of the critical point lies within the no-solution region in nearly all of the investigated cases. It shall be also noted, that the critical density ρ^{crit} tends to zero for potential-parameter sets close to the boundary of the microphase region (e.g. $R_r = 1.6$, $\epsilon_r = 0.375$ in figures 5.18d and 5.19d), which is also due to the fact that we approach the region of microphase formation.

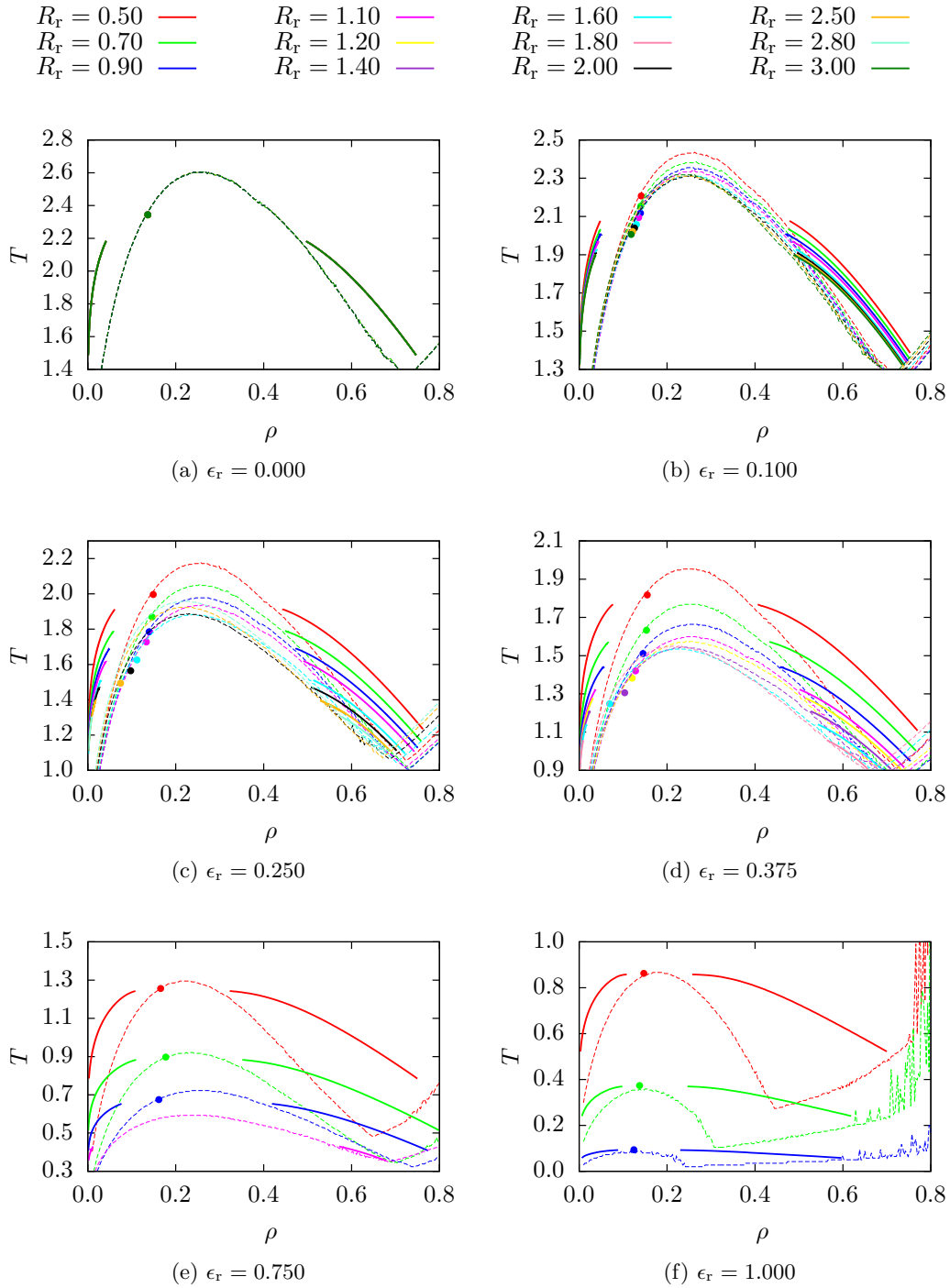


Figure 5.18: Phase coexistence lines (solid lines), no-solution lines (dotted lines) and estimates for the critical points (dots) for systems interacting via the Imperio-Reatto potential. The repulsion strength ϵ_r is constant in each panel and stated at the bottom. The repulsion range R_r is varied as labeled at the top of the figure.

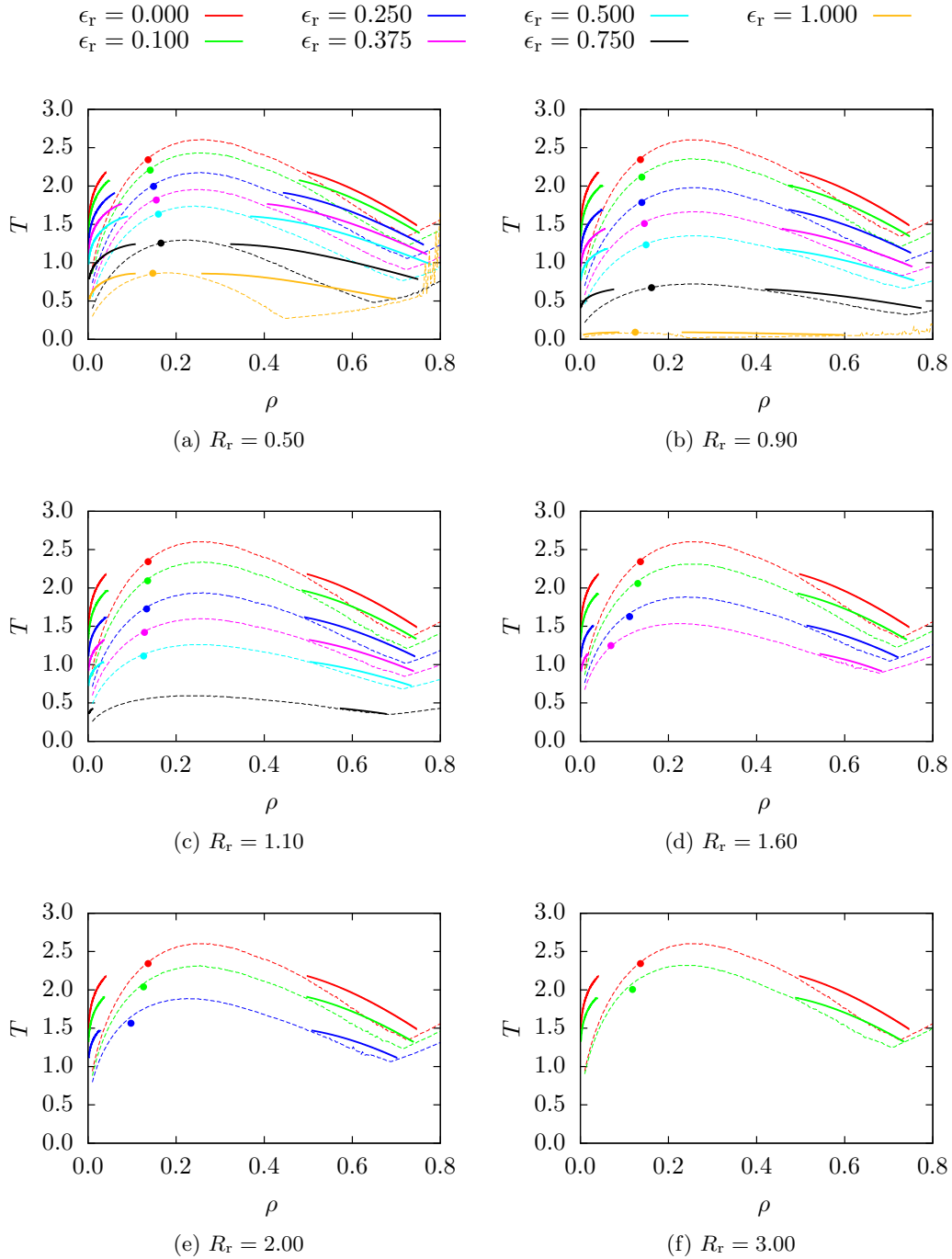


Figure 5.19: Phase coexistence lines (solid lines), no-solution lines (dotted lines) and estimates for the critical points (dots) for systems interacting via the Imperio-Reatto potential. The repulsion range R_r is constant in each panel and stated at the bottom. The repulsion strength ϵ_r is varied as labeled at the top of the figure.

5.2 Clusters and Dynamic Properties

This section is dedicated to the static and dynamic properties of the clusters, as well as the dynamic properties of the particles. Special emphasis is put on the slowing down of the dynamics of clusters and particles, while lowering the temperature of the system (see section 5.2.4). In order to identify the clusters, and to calculate and track their centers of mass, the methods described in section 4.3 have been used. For a justification of using Monte-Carlo simulations to obtain dynamic properties see section 4.1.4 and the references therein.

To gain data comparable to results already published in literature, a single component system of particles interacting via the Imperio-Reatto potential (see chapter 2) is used in this section, unless explicitly stated otherwise. The parameters of the potential are set to $R_r = 2.0$ and $\epsilon_r = 1.0$, respectively.

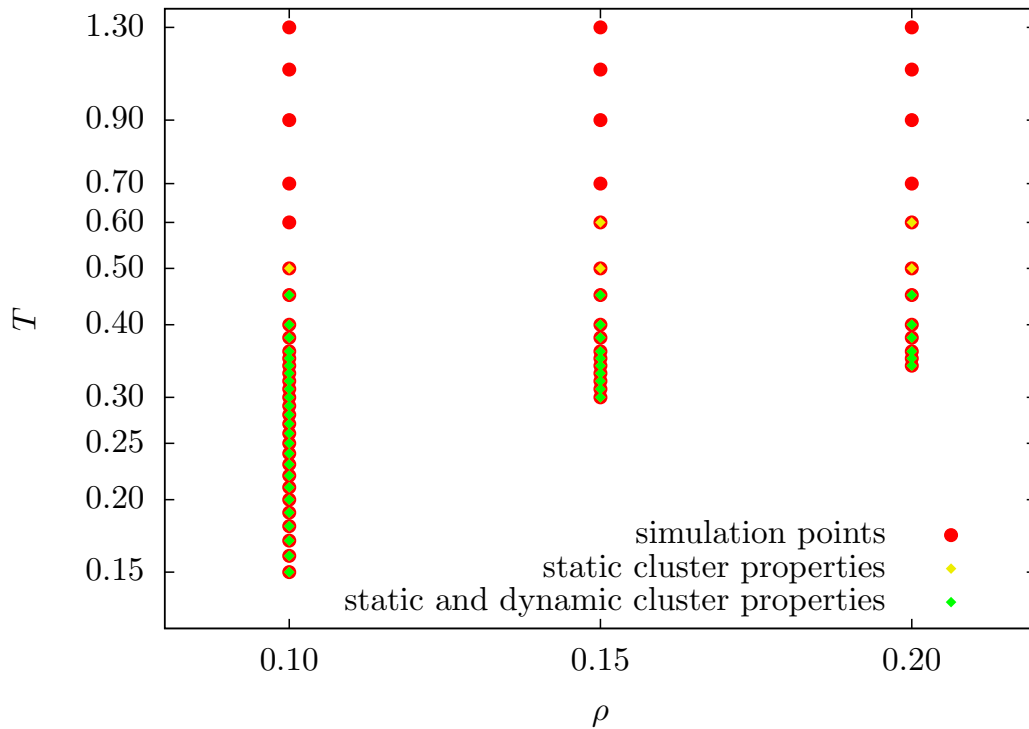


Figure 5.20: Statepoints considered to investigate the particle and cluster dynamics. The temperature was reduced for three different particle densities ($\rho = 0.10$, $\rho = 0.15$ and $\rho = 0.20$) in successive steps (quenches), starting from a temperature of $T = 1.3$. To average over potentially frozen configurations, ten independent simulations have been executed for every statepoint. For simulation points with an additional yellow dot static cluster properties are available, while for those marked with an additional green dot static and dynamic cluster properties are available.

The simulations of the present section were carried out as follows: ten independent

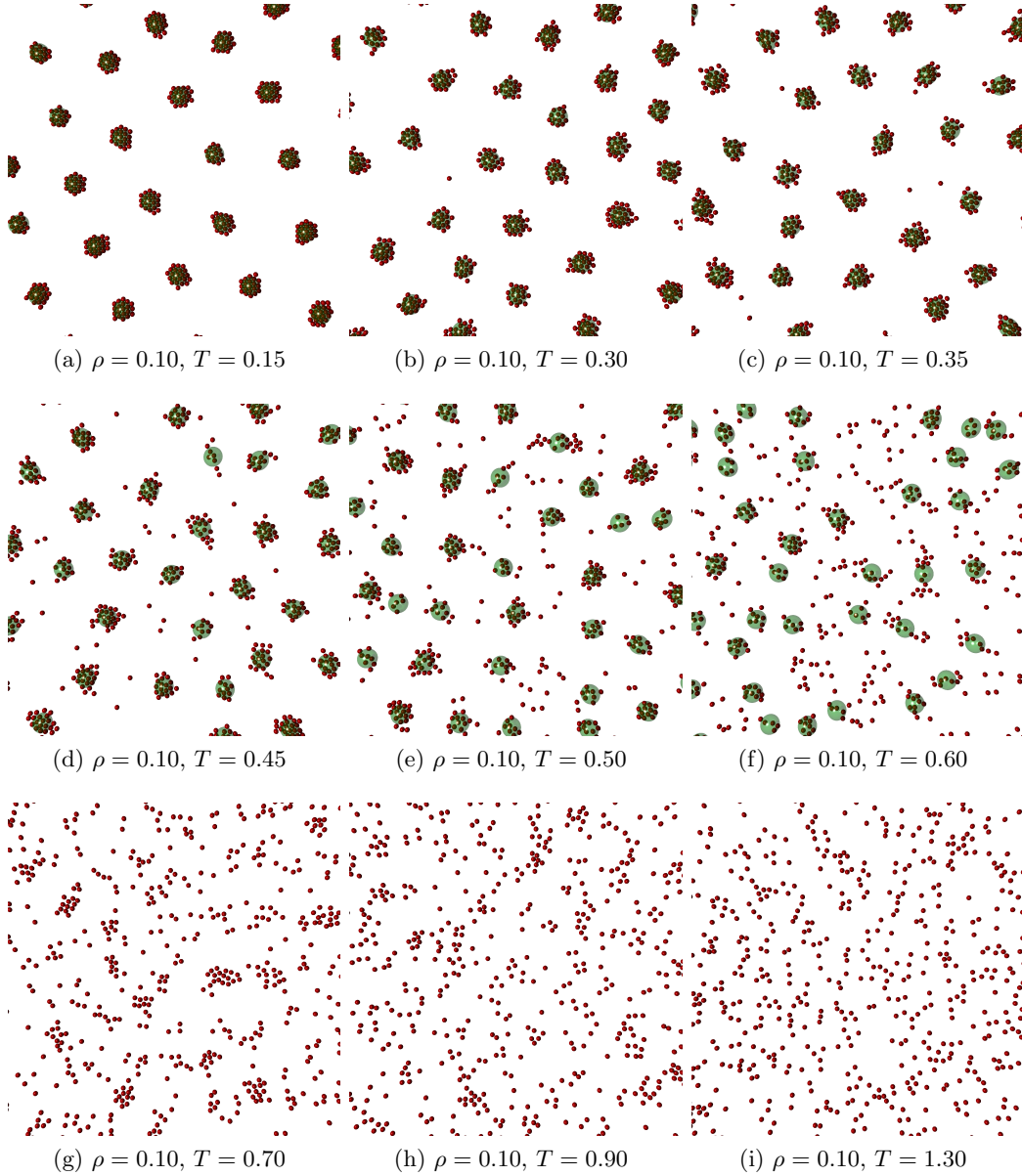


Figure 5.21: Simulation snapshots of the system with $\rho = 0.10$ at different temperatures. The small red dots mark the position of individual particles, with the diameter of these dots matching the hard sphere diameter σ of the interaction potential $\Phi_{\text{IR}}(r)$, while the green transparent spheres represent the positions of the cluster centers of mass computed via the algorithm described in section 4.3.1. The sections of the simulation boxes shown in this figure are of the same size as the simulation box sections shown in figures 5.22 and 5.23.

random configurations of the system, each containing 4000 particles interacting via the Imperio-Reatto potential have been equilibrated at a temperature of $T = 1.30$ at

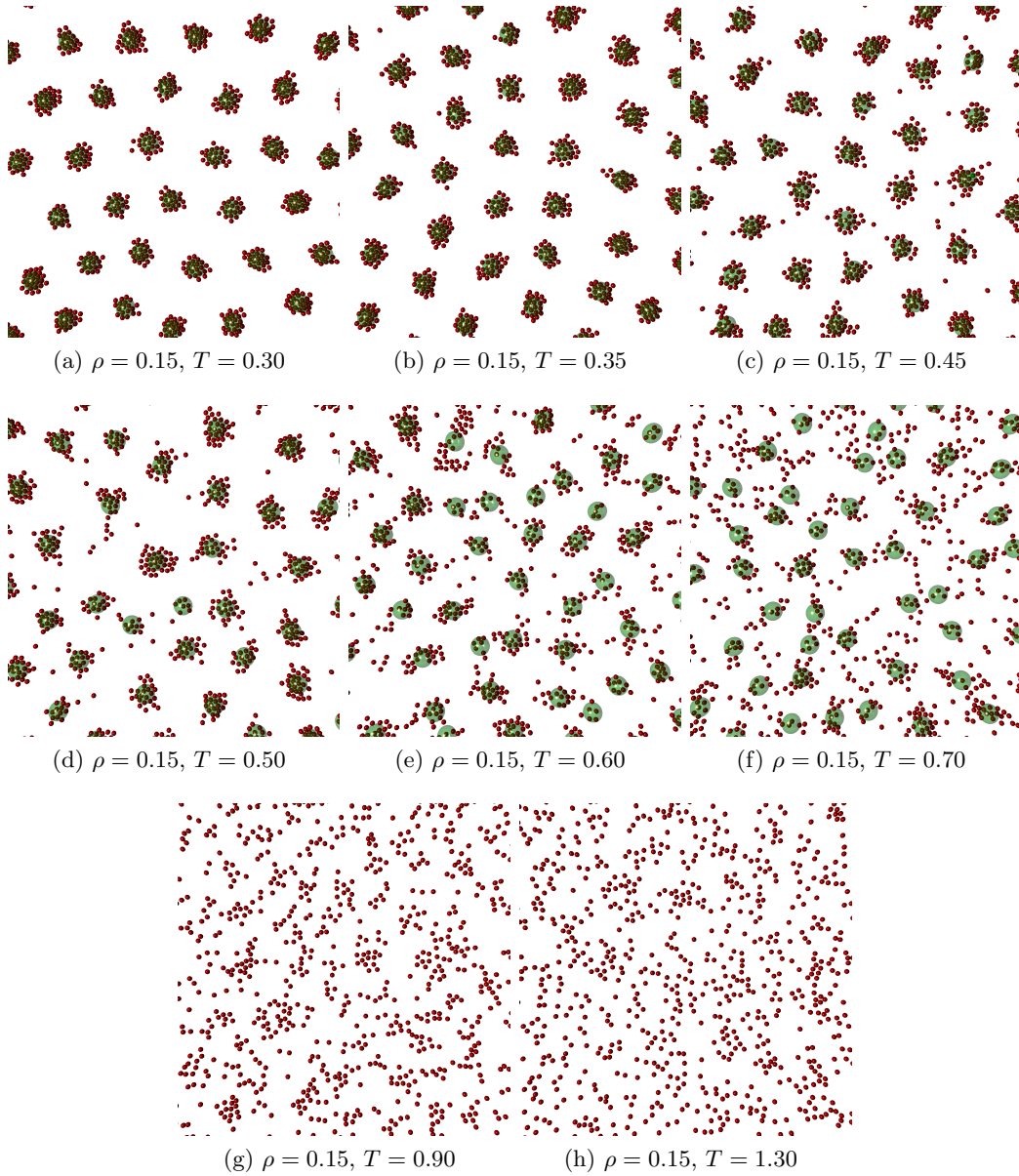


Figure 5.22: Simulation snapshots of the system with $\rho = 0.15$ at different temperatures. The small red dots mark the position of individual particles, with the diameter of these dots matching the hard sphere diameter σ of the interaction potential $\Phi_{\text{IR}}(r)$, while the green transparent spheres represent the positions of the cluster centers of mass computed via the algorithm described in section 4.3.1. The sections of the simulation boxes shown in this figure are of the same size as the simulation box sections shown in figures 5.22 and 5.23.

the densities $\rho = 0.10$, $\rho = 0.15$ and $\rho = 0.20$. The equilibrated configurations have been used as initial configurations of subsequent Monte-Carlo simulations to obtain the

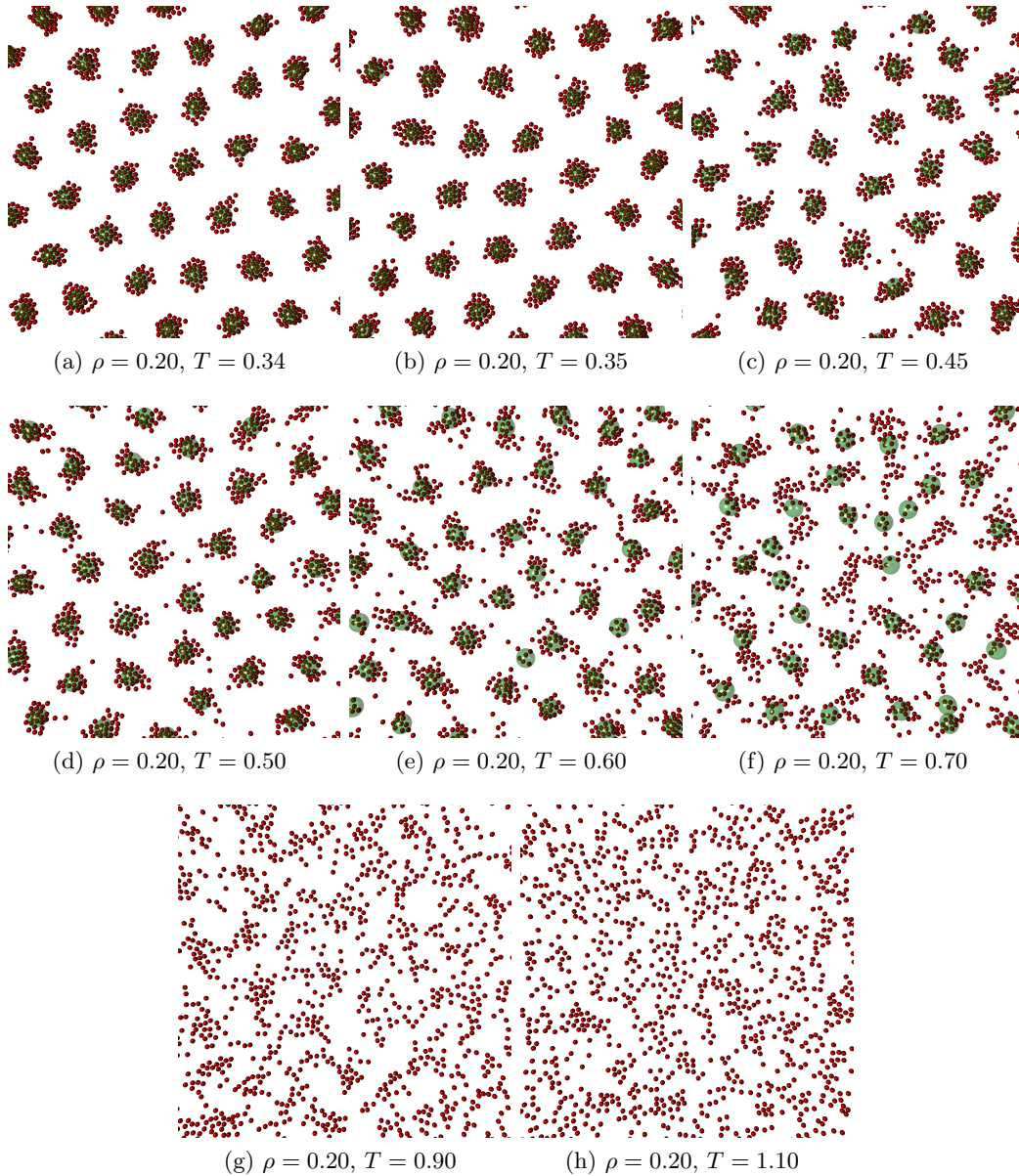


Figure 5.23: Simulation snapshots of the system with $\rho = 0.20$ at different temperatures. The small red dots mark the position of individual particles, with the diameter of these dots matching the hard sphere diameter σ of the interaction potential $\Phi_{\text{IR}}(r)$, while the green transparent spheres represent the positions of the cluster centers of mass computed via the algorithm described in section 4.3.1. The sections of the simulation boxes shown in this figure are of the same size as the simulation box sections shown in figures 5.22 and 5.23.

desired observables (like e.g. the pair distribution function $g(r)$ and the static structure factor $S(k)$) and additionally, as initial configurations for the equilibration at $T = 1.10$.

The above procedure is repeated for all ten independent initial conditions, at each density and for all temperatures marked by the points in figure 5.20, thereby obtaining ten independent quenches at each of these densities.

In order to save time and to run more simulations in parallel, some exceptions to the strictly sequential equilibration at the next lower temperature have been made. At $\rho = 0.10$ up to four of the next lower temperature initial conditions have been created out of the equilibrated configuration of a certain temperature for $T < 0.30$. For example equilibrated configurations for $T = 0.26 - 0.29$ have been created from the equilibrated configuration at $T = 0.30$ of their quench.

To efficiently cover the huge number of MC-steps (corresponding to time) required for this investigation, while also resolving effects occurring at a short timescale (i.e. during only a few MC-steps), two MC-simulation runs are started from each of the equilibrated initial configuration mentioned above, to acquire the observables for $T \leq 0.70$. While the first of these runs covers a short time window (using $n_{\text{skip}} = 1$, so the number of MC steps and MC sweeps is equal) the second (long) simulation run extends over the entire time window (using 5000 MC sweeps and a rather large n_{skip} value of up to 8500, to cover the up to 42 500 000 MC steps at $T = 0.15$). Graphs of time-dependent properties, like the mean-square displacement and the intermediate scattering functions depicted in section 5.2.4 are combinations of these "short" and "long" simulation runs, averaged over the ten independent quenches.

The time independent observables discussed in this section, have been averaged over the ten independent quenches, after taking the mean over the configurations of the long simulation runs covering the entire time window only.

Figures 5.21 to 5.23 display equally sized sections of the simulation box, showing a typical particle configuration of the Monte-Carlo simulations at different temperatures and different densities, respectively. The green, semi-transparent spheres in these figures, mark the positions of clusters, found via the algorithm described in section 4.3.1, while the red, opaque spheres mark the positions of individual particles.

At low temperatures distinct clusters are well discernible (see figures 5.21 to 5.23) and the algorithm indeed locates the centers of mass of these clusters correctly (see transparent green spheres in figures 5.21 to 5.23). Single particles moving between these clusters can also be seen in most of the panels of figures 5.21 to 5.23. These "free" particles are not considered as part of the clusters by the algorithm and are encountered more frequently with increasing temperatures (see panels for $T \geq 0.40$). For $T \geq 0.70$ it becomes increasingly hard to identify individual clusters in the simulation snapshots with the naked eye, since the cluster microphase vanishes and the system becomes practically homogeneous in this temperature range. A more detailed discussion about the transition from the microphase separated phase to the homogeneous phase will be presented in sections 5.2.1 and 5.2.3. Because of the transition to a homogeneous phase, the cluster positions obtained by the cluster identification algorithm are not marked in panels with $T \geq 0.70$ in figure 5.21 and $T \geq 0.90$ in figures 5.22 and 5.23.

5.2.1 General Cluster Properties

In this section the static properties of the clusters are discussed. Figure 5.24 shows the cluster size distribution in terms of the number of particles that form the cluster for several temperatures at the three investigated densities (panels a-c).

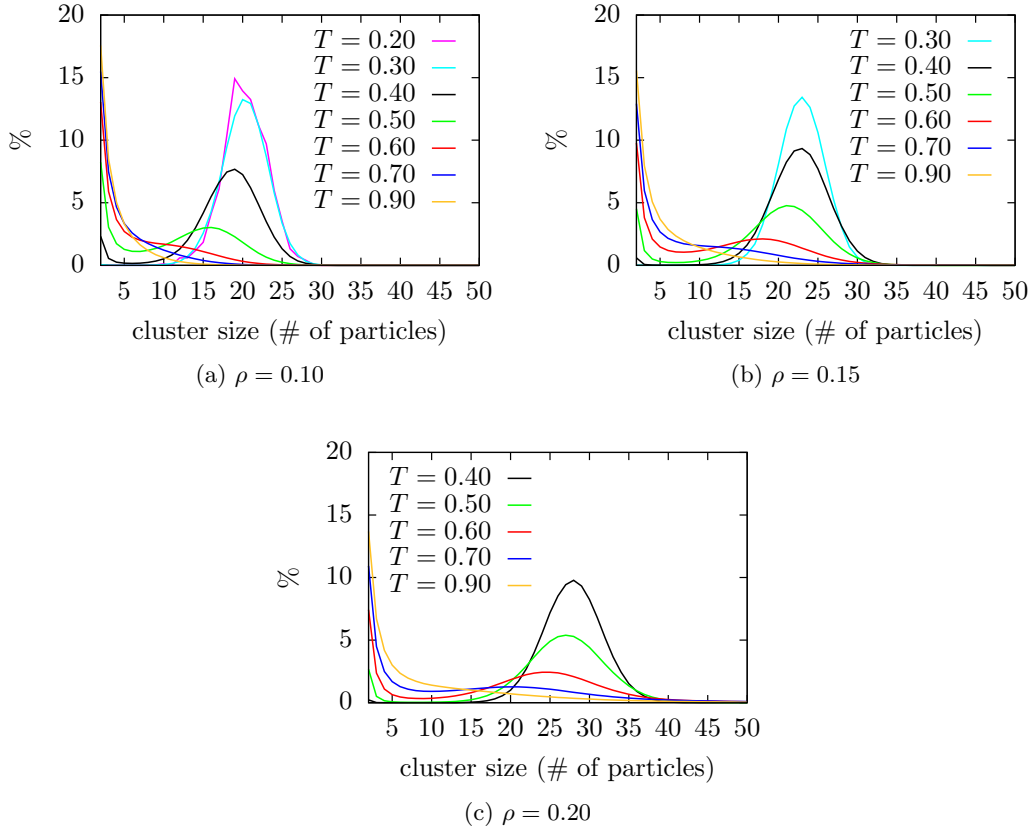


Figure 5.24: Cluster size distribution at different temperatures as labeled (cluster size in terms of particle number). In the following we will speak of clustering, if the cluster size distribution has a relative maximum at a cluster size larger than one (cluster size distribution criterion see text).

One can see from figure 5.24 that the cluster size distribution only shows a relative maximum at a cluster size > 1 for temperatures below a certain limit. Above this temperature this distribution drops strictly monotonically with increasing cluster size. Since the appearance of the relative maximum at a cluster sizes > 1 marks the existence of clusters of a particular size in a qualitative manner, it will be used in the following as a criterion to separate clustering systems from non-clustering systems (the so-called cluster size distribution criterion) [17].

The temperatures, at which clustering occurs according to this cluster size distribution criterion, are given in table 5.2.

ρ	clustering for
0.10	$T \leq 0.50$
0.15	$T \leq 0.60$
0.20	$T \leq 0.70$

Table 5.2: Temperatures below which clustering occurs for a given density ρ , using the cluster size distribution criterion (see text).

These temperatures, are in good agreement with the expectations from visual inspection of the simulation snapshots displayed in figures 5.21 to 5.23. As can be seen from table 5.2 clustering breaks down at lower temperatures as we decrease the particle densities.

Figure 5.25 shows the average percentage of particles which are not part of any cluster as a function of temperature for the three investigated densities.

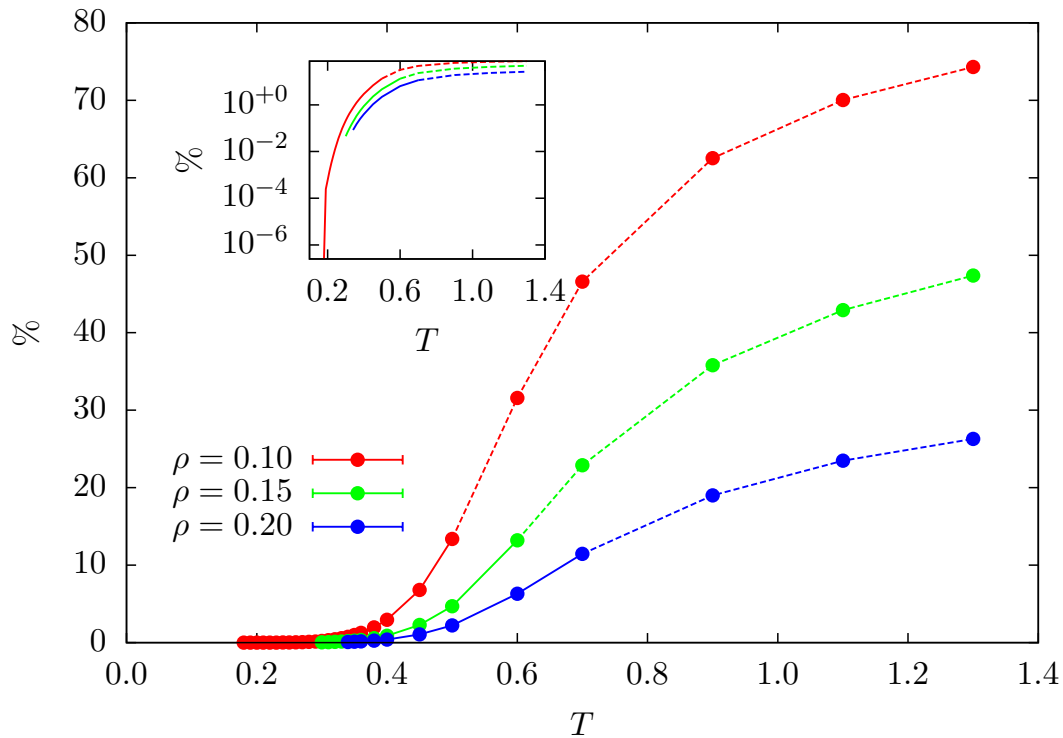


Figure 5.25: Percentage of particles not belonging to any cluster of size ≥ 5 (free particles). The dotted line marks the part of the curve where the cluster size distribution does not have a relative maximum at a cluster size larger than one anymore.

Form this figure, one can see that the percentage of particles not belonging to any

cluster increases significantly in the temperature range where clustering brakes down according to the cluster size distribution argument mentioned before. The curves in figure 5.25 are therefor drawn as dashed lines for temperatures above which clustering is no longer observed. It is also interesting to note, that clustering seems to break down if more than $\sim 12\%$ of the particles do not belong to any cluster, irrespective of the particle density.

Figure 5.26 shows the size of the clusters as a function of temperature.

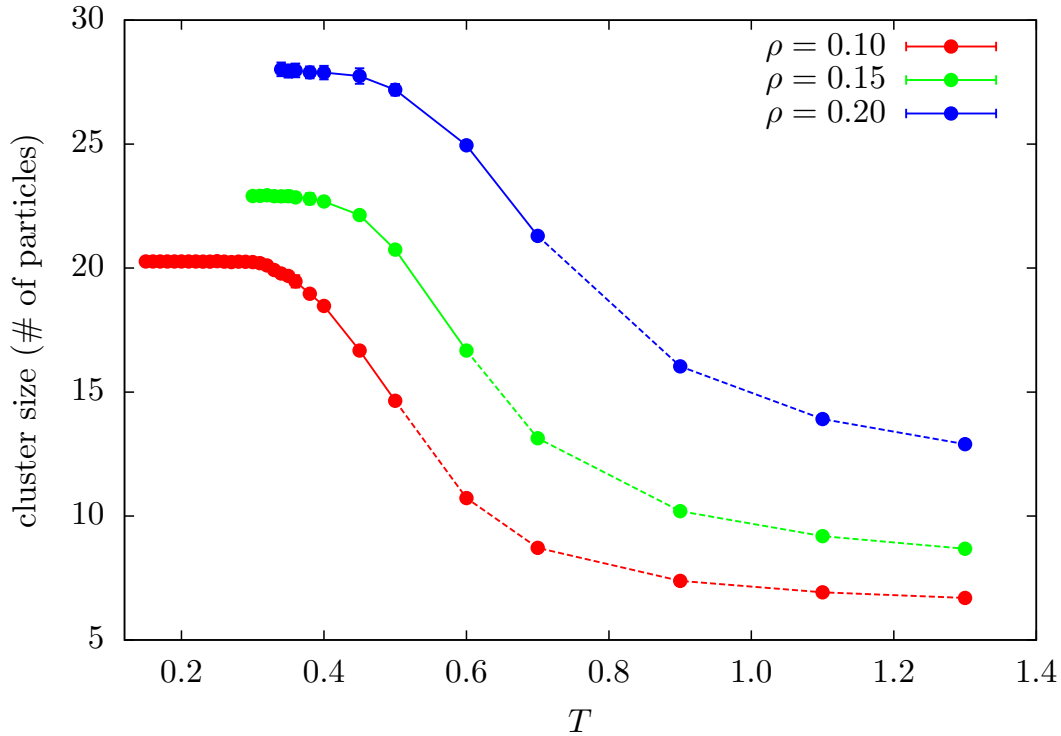


Figure 5.26: Average cluster size as a function of the temperature. The dotted line marks the part of the curve where the cluster size distribution does not have a relative maximum at a cluster size larger than one anymore.

It can easily be seen from figure 5.26 that the average number of particles within a cluster remains constant for a considerable temperature range that is part of the clustering regime. However when approaching the transition temperature to the homogeneous phase, the average particle number per cluster starts to drop. This trend is continued for temperatures above the transition temperature (see dashed part of the lines in figure 5.26). Obviously the average cluster size is bigger for systems of higher density, this can be seen from figures 5.21 to 5.23 from the snapshots of the systems.

Finally figure 5.27 shows the average size of the clusters in terms of the gyration radius R_g , which can be computed via equation (4.145).

In contrast to the cluster size the average value of R_g increases with rising temperatures: this is due to the increased space required by the individual particles of the

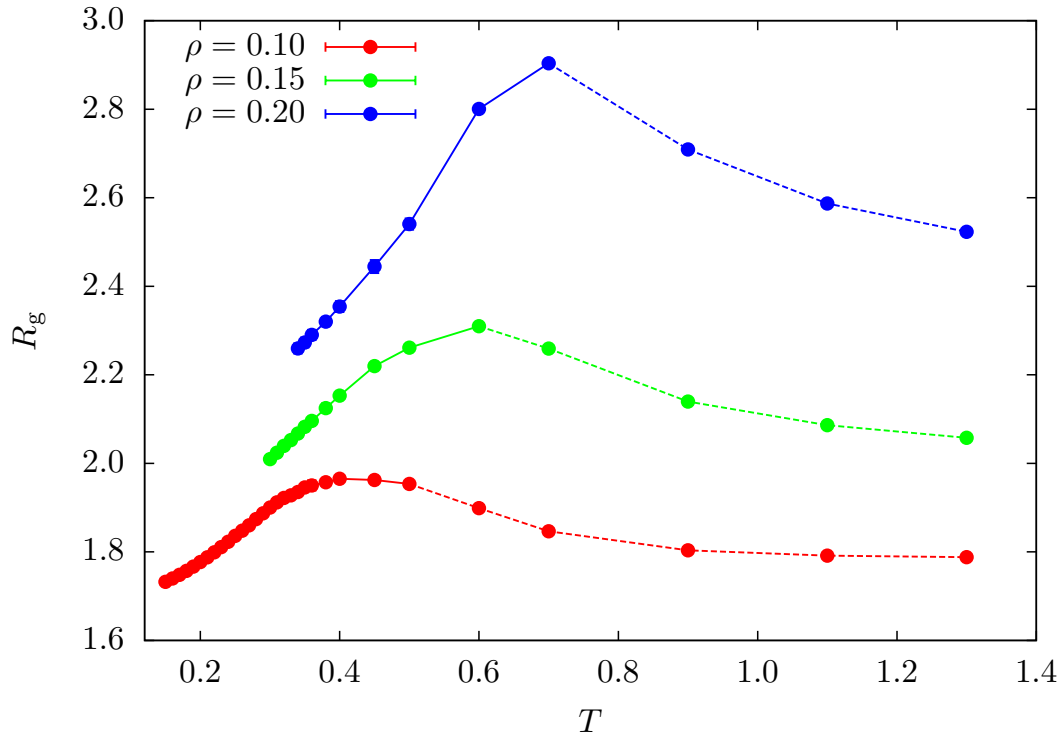


Figure 5.27: Gyration radius of the clusters of the system versus temperature. The dotted line marks the part of the curve where the cluster size distribution does not have a relative maximum at a cluster size larger than one anymore. Clustering occurs up to the maximum in R_g .

cluster caused by their higher mobility. R_g reaches a maximum close to the transition temperature to the homogeneous phase. For temperatures above the transition temperature R_g decreases again, due to the reduced number of particles within the clusters.

Figure 5.28 shows the rate of occurrence of the different cluster tracking cases defined in section 4.3.2 (see in particular table 4.1) and briefly recapped in the caption of figure 5.28.

Apart from the most common, but also trivial case 1 (translational move of the cluster only), which is not considered in figure 5.28, one can see that the different cluster tracking cases occur at the same rate respective counterparts (see panel (a) of figure 5.28 for cases 2 and 4, panel (b) of figure 5.28 for cases 3 and 5 and the caption of figure 5.28 for a brief explanation of the cases). Except for the trivial case 1, the combination of cases 2 and 4 (cluster dissolving, new cluster), basically involving only one cluster, is the most common, while the combination of cases 3 and 5 (cluster merging/cluster splitting), involving two clusters, is roughly by one order of magnitude less frequent. Cases 6 and 7 (two new clusters/cluster splitting in three parts), involving three clusters, are roughly by one order of magnitude less frequent than cases 3/5. As explained in

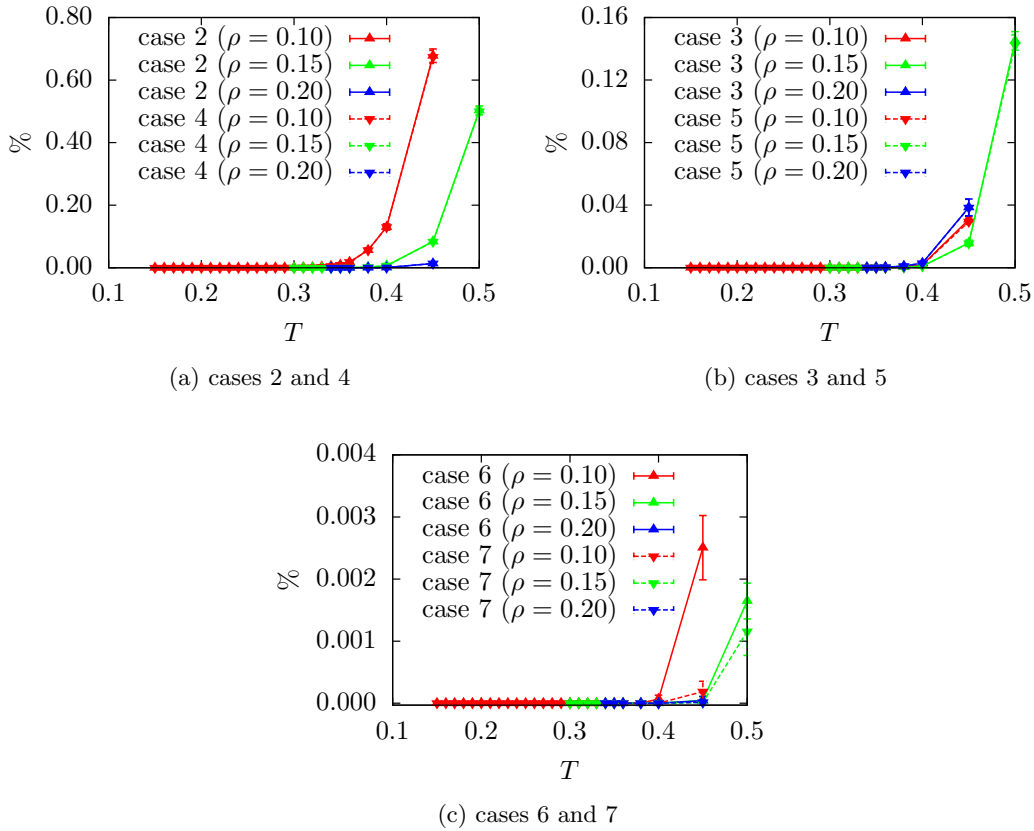


Figure 5.28: Rate of occurrence of the different cluster tracking cases versus temperature. A simple translation of a cluster (case 1), which is the most common but trivial case is considered here. Note that the dissolving cluster case (case 2) occurs as often as its counterpart, i. e. the forming of a new cluster (case 4). The observation holds for the merging of two clusters (cases 3) and the splitting of a cluster in two fragments (case 5). Case 6, the simultaneous forming of two new clusters, and case 7 representing either a cluster splitting into three fragments or a cluster splitting into two fragments with the additional formation of a cluster close by, are not inverse cases.

section 4.3.2, the cluster tracking algorithm, as used in this work, aborts if events involving four or more clusters are recognized. Fortunately no such occurrences were observed in our simulations for $T \leq 0.45$.

5.2.2 Structural Particle and Cluster Properties

Figure 5.29 shows the comparisons of radial distribution functions $g(r)$ computed from particle and cluster positions respectively, for a density of $\rho = 0.10$ at various temperatures. To improve visibility, the short range parts ($0 < r < 6$) are shown in the insets of the panels, while only the long range parts ($6 < r < 100$) of the radial distribution functions are depicted in the main plot.

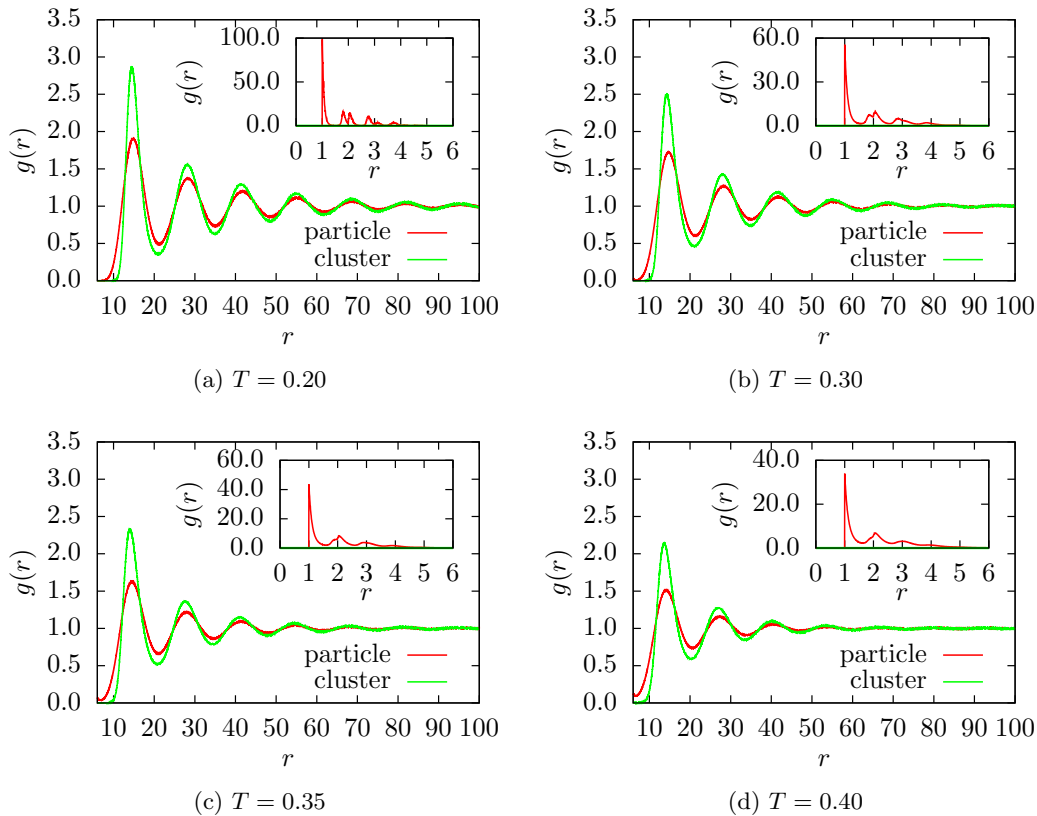


Figure 5.29: Comparisons of $g(r)$ of particles (red) and clusters (green) for $\rho = 0.10$ at different temperatures. Note that for $r > 6$ the peaks for particles and clusters are at exactly the same position.

It can be seen from figure 5.29, that the maxima and minima of the long range ($r > 6$) oscillations of the radial distribution functions computed from particle and cluster positions are located at the same positions in the temperature range $0.20 \leq T \leq 0.40$. This is not very surprising since the clusters are composed of the particles. For $r < 6$ however, the radial distribution function of the clusters is zero, while the radial distribution function of the particles shows a very distinct structure. This different behavior of the cluster- and particle- $g(r)$ at small r stems from the fact that the centers of mass of two clusters cannot come this close to one another without the merging of the clusters. The distinct peaks of the particle- $g(r)$ at $r < 6$ on the other hand originate

from the particle distances within the same cluster.

With increasing temperature, the amplitude of the long range oscillations ($r > 6$) decreases and less oscillations are visible in the radial distribution functions. This is the usual behavior for the radial distribution function in fluids, when increasing the temperature. However, for $T = 0.35$ the second peak of the particle- $g(r)$ at $r \sim 2$ shows a distinctive shoulder towards lower r (see insets of the panels of figure 5.29). This shoulder evolves into a double peak at $T = 0.30$, becoming more pronounced at even lower temperatures (see also [12]). The double peak structure in the second peak of the radial distribution function strongly indicates that the particles form an ordered structure within the clusters for $T \leq 0.30$, which is in agreement with results from [17]. The exact positions of the maxima of the double peak at $r \sim 2$ coincide with those of an hexagonal lattice, which agrees with the particle configuration seen in simulation snapshots (see panels (a)-(c) of figure 5.21).

Figure 5.30 shows a comparison of radial distribution functions $g(r)$ computed from the particle and cluster positions for a density of $\rho = 0.15$ at various temperatures.

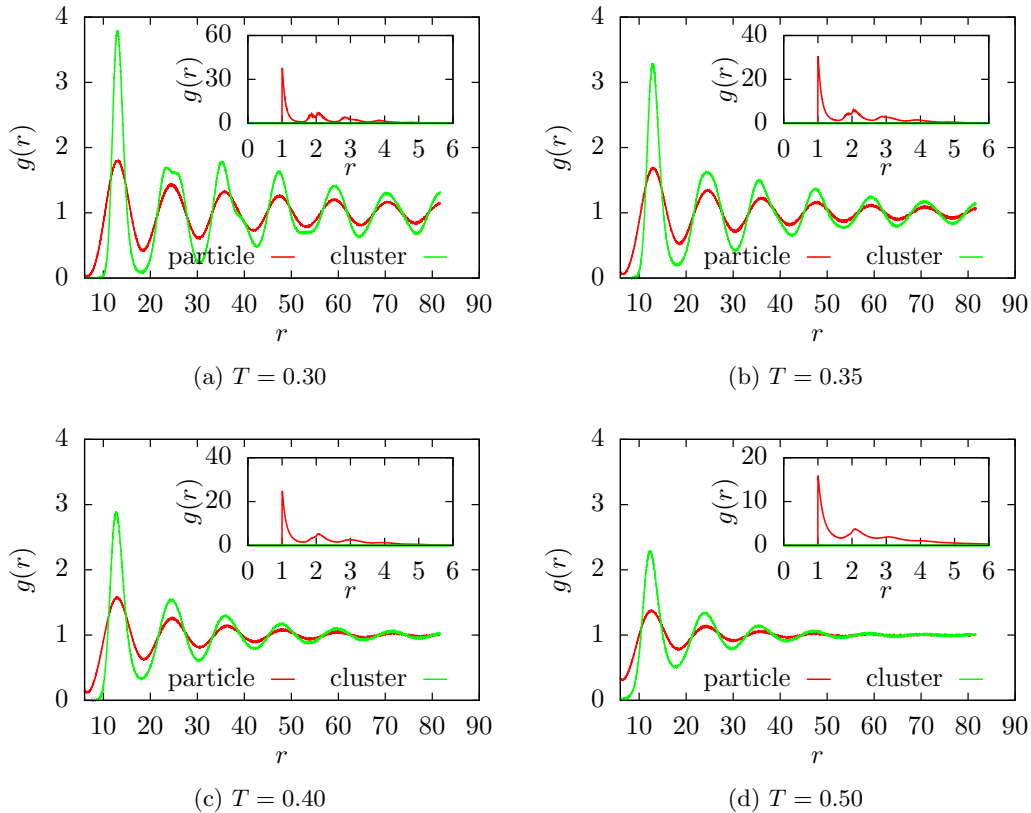


Figure 5.30: Comparisons of $g(r)$ of particles (red) and clusters (green) for $\rho = 0.15$ at different temperatures. Note that for $r > 6$ the peaks for particles and clusters are at exactly the same position. The shoulder of the second peak for the cluster- $g(r)$ at low T is discussed in the text.

As in figure 5.29, the second peak of the radial distribution function of the particles is split at the lowest temperatures investigated (see insets of figure 5.30 (a) and (b)). In contrast to the lower density case, however, the peak splitting is already visible for $T \leq 0.35$. A shoulder in the second peak of the particle- $g(r)$ can be seen at $T = 0.40$, marking the onset of the peak splitting mentioned above [17].

Moreover, the second and third peak of the radial distribution function of the clusters, at $r \approx 24$ and $r \approx 36$ respectively, feature distinct shoulders at a temperature of $T = 0.30$. These shoulders are not present in any of the cluster- $g(r)$ peaks at a density of $\rho = 0.10$, for the entire investigated temperature range ($T \geq 0.15$).

The shoulder in the second and third peak of the radial distribution function of the clusters is a hint that the clusters themselves freeze into an ordered structure at sufficiently low temperature for a density of $\rho = 0.15$, while this does not happen at $\rho = 0.10$. A similar result was obtained in [17] by analyzing the static structure factor $S(\mathbf{k})$ computed from the particle positions. Further evidence of this freezing of the clusters will be presented later in this section.

The agreement of the peak positions of the particle- and the cluster- $g(r)$ for $r \leq 6$ has already been observed for $\rho = 0.10$ (see figure 5.29) and will not be discussed again here.

Figure 5.31 shows the comparison of radial distribution functions $g(r)$ computed from particle and cluster positions for a density of $\rho = 0.20$ at various temperatures.

As in figures 5.29 and 5.30, the second peak of the radial distribution function of the particles is split for the lowest temperatures investigated (see insets of figure 5.31 (a)). The peak splitting is present at $T \leq 0.35$ and a shoulder can be observed at $T = 0.40$. It has to be pointed out that the same features can be seen in systems with $\rho = 0.15$ at the same temperatures.

The onset of peak splitting in the second peak of the radial distribution function of the clusters, mentioned for $\rho = 0.15$ (figure 5.30 (a)), can already be seen at $T = 0.40$ for $\rho = 0.20$ (see main panel of figure 5.31 (b)), while a clear peak splitting for this peak is visible at $T = 0.35$ (see main panel of figure 5.31 (a)). This indicates that at higher density the clusters themselves tend to freeze into ordered structures and that an increase in density shifts the freezing temperature to higher values.

In order to precisely determine the transition temperature of the particles within the clusters into a hexagonal lattice, the second and third peak of the radial distribution function of the particles are shown in the left panels of figure 5.32 ($1.3 \leq r \leq 4.0$). In order to determine the ordering temperature of the clusters into a hexagonal lattice with higher precision, the second and third peak of the radial distribution function of the clusters is shown in the right panels of figure 5.32 ($20 \leq r \leq 50$).

At $\rho = 0.10$, the second peak in the particle- $g(r)$ is split for $T \leq 0.33$, while showing a very prominent, horizontal shoulder at $T = 0.34$ (see figure 5.32 (a)). The onset of this shoulder is already visible at $T = 0.40$, while the third peak shows a shoulder only for $T \leq 0.35$, which becomes a double peak at $T \leq 0.25$. The best estimate for the transition temperature of the particles within the clusters, into an ordered structure is $0.33 \leq T_{\text{part}}^{\text{freeze}} \leq 0.34$, mainly taking the formation of the double peak structure of the second peak as a criterion for freezing. This transition temperature is in good agreement with results from [12, 17].

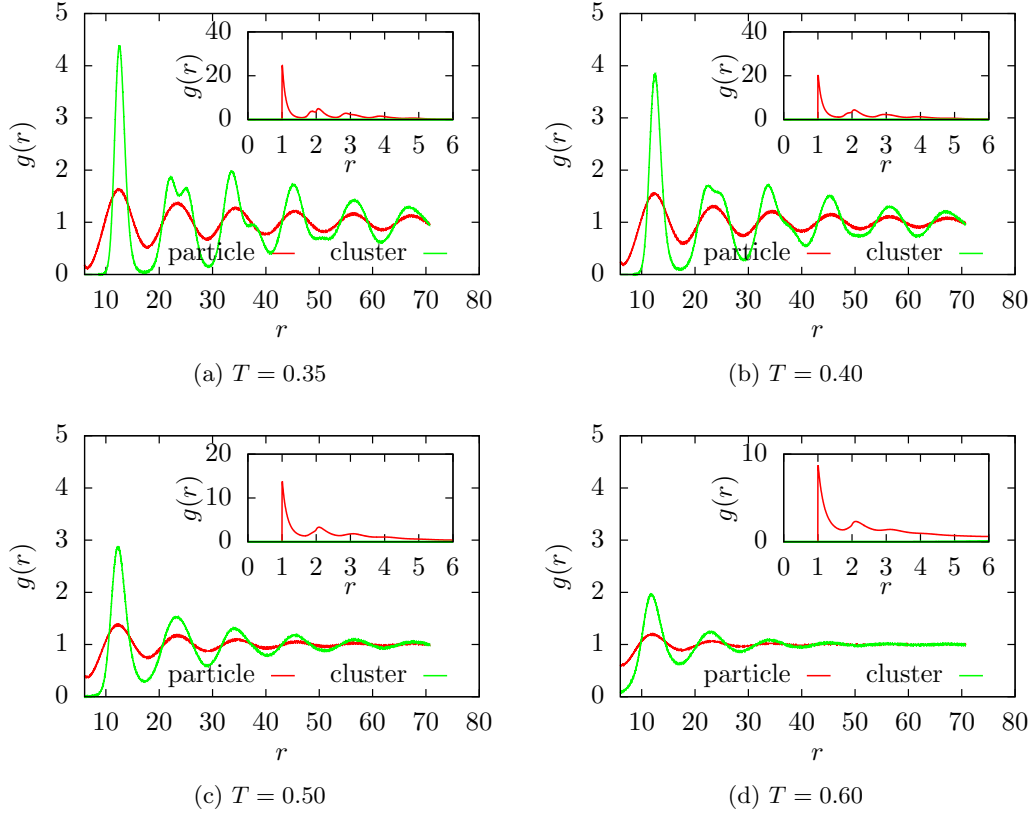


Figure 5.31: Comparisons of $g(r)$ of particles (red) and clusters (green) for $\rho = 0.20$ at different temperatures. Note that for $r > 6$ the peaks for particles and clusters are at exactly the same position. The shoulder of the second peak for the cluster- $g(r)$ at low T is discussed in the text.

As already mentioned before, neither double peaks nor shoulders can be found in the second and third peak of the cluster- $g(r)$ at a density of $\rho = 0.10$ (see figure 5.32 (b)), which means that the clusters do not form an ordered structure at that density for $T \geq 0.15$.

Panels (c) and (d) of figure 5.32 show the situation for a density of $\rho = 0.15$, with the pair distribution functions of the particles displayed in panel (c). The second peak in this panel has a double peak structure for $T \leq 0.35$, while showing a prominent, nearly horizontal, shoulder at $T = 0.36$. An onset of the shoulder on this peak is visible up to a temperature of $T = 0.40$. The third peak of the particle- $g(r)$ only shows a shoulder in the temperature region $0.30 \leq T \leq 0.36$, but no double peak structure. Therefore the best estimate for the transition temperature of the particles into a hexagonal structure for $\rho = 0.15$ is $0.35 \leq T_{\text{part}}^{\text{freeze}} \leq 0.36$, which is also in good agreement with results from [17].

The second peak of the cluster- $g(r)$, displayed in panel (d) of figure 5.32, shows a horizontal shoulder at $T = 0.30$, this shoulder is visible for all temperatures $T \leq 0.32$.

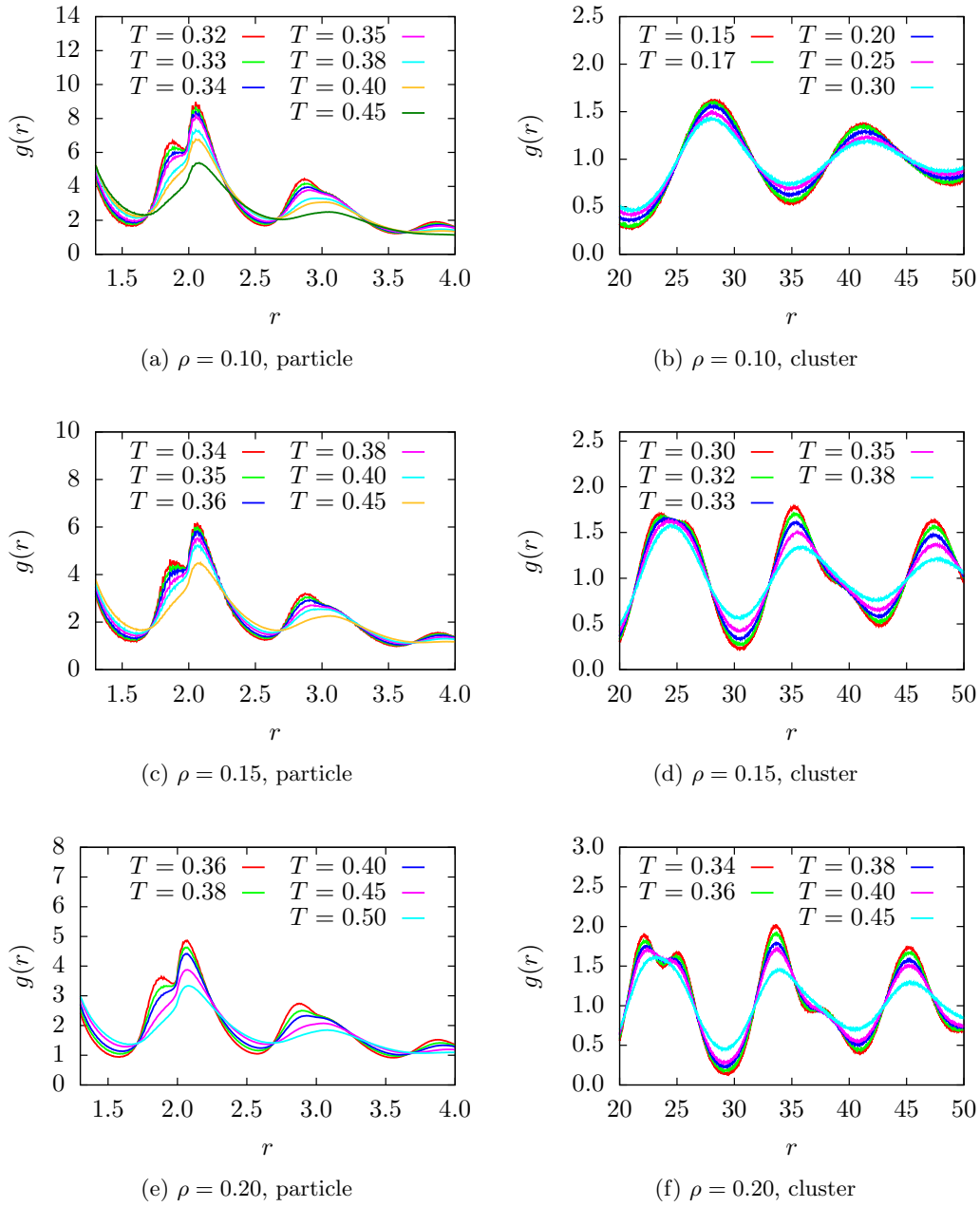


Figure 5.32: Peak splitting for the second peak in $g(r)$ for particles (right) and clusters (left). Note that no peak splitting or shoulder can be observed for the cluster- $g(r)$ at $\rho = 0.10$, while peak splitting is clearly visible for the cluster- $g(r)$ at $\rho = 0.20$ ($T \leq 0.40$). A shoulder is present for the second and third peak of the cluster- $g(r)$ at $\rho = 0.15$ ($T \leq 0.32$).

Similar to that, the third peak of the cluster- $g(r)$ shows a shoulder in the temperature region $0.30 \leq T \leq 0.32$ for $\rho = 0.15$ as well, however, the shoulder of this peak is not as prominent as the one of the second cluster- $g(r)$ peak. The best estimate for the transition temperature to an ordered structure for the clusters at $\rho = 0.15$ therefor is $T_{\text{cluster}}^{\text{freeze}} \lesssim 0.30$. This estimate is also in good agreement with results from [17], analyzing the static structure factor $S(\mathbf{k})$ of the particles.

Pair distribution functions for the particles and clusters at a density of $\rho = 0.20$ are shown in panels (e) and (f) of figure 5.32. The particle- $g(r)$, displayed in panel (e) features a double peak structure on the second peak ($r \sim 2$) at a temperature of $T = 0.36$ as well as a horizontal shoulder at a temperature of $T = 0.38$. An onset of the shoulder of the second particle- $g(r)$ peak is visible already at $T = 0.40$. The third peak of the particle- $g(r)$ also features a shoulder for $0.36 \leq T \leq 0.38$, however this shoulder is not as prominent as the one visible at the second peak of the particle $g(r)$, similar to the case for $\rho = 0.15$. An estimate for the transition temperature of the particles into an ordered structure within the clusters at $\rho = 0.20$, therefor is given by $0.36 \leq T_{\text{part}}^{\text{freeze}} \leq 0.38$, using the appearance of a double peak in $g(r)$ as a criterion for such a transition, as found in [17].

The pair distribution function of the clusters at $\rho = 0.20$, shown in panel (f) of figure 5.32, features a double peak structure in the second peak ($r \sim 24$) for $T \leq 0.38$ and an prominent, however not horizontal, shoulder for $T = 0.40$. The third peak of the cluster- $g(r)$ features a double peak structure for $T \leq 0.35$, which is reduced to a horizontal shoulder at $T = 0.36$ with the onset of this shoulder visible up to $T = 0.40$. The best estimate for the transition temperature to an ordered structure for clusters at $\rho = 0.20$ therefor is $0.38 \leq T_{\text{cluster}}^{\text{freeze}} \leq 0.40$. For $\rho = 0.20$ [17] predicts a transition temperature $T \approx 0.60$ for the freezing of the clusters from the static structure factor. This estimate is considerably higher than our estimate and would rule out liquid like clusters at that density.

Estimates of the transition temperatures of particles and clusters into ordered structures are summarized in table 5.3.

ρ	particles	clusters
0.10	$0.33 \leq T \leq 0.34$	-
0.15	$0.35 \leq T \leq 0.36$	$T \sim 0.30$
0.20	$0.36 \leq T \leq 0.38$	$0.38 \leq T \leq 0.40$

Table 5.3: Transition temperatures to ordered structures of particles and clusters estimated from features of the pair distribution function. Our results are in good agreement with [17], with the exception of the cluster transition temperature for $\rho = 0.20$ (see text).

The structural order of the system can be quantified by the bond order parameters introduced in section 4.3.4. Since the clusters seem to arrange primarily into a hexagonal structure at low temperature, judging from the respective snapshots in figures 5.21 to 5.23, the bond order parameter Ψ_6 is the most appropriate to identify the transition into an ordered structure.

Figure 5.33 shows the bond order parameter Ψ_6 of the clusters, computed via equation (4.143), as a function of temperature for the three investigated densities ($\rho = 0.10$; $\rho = 0.15$ and $\rho = 0.20$).

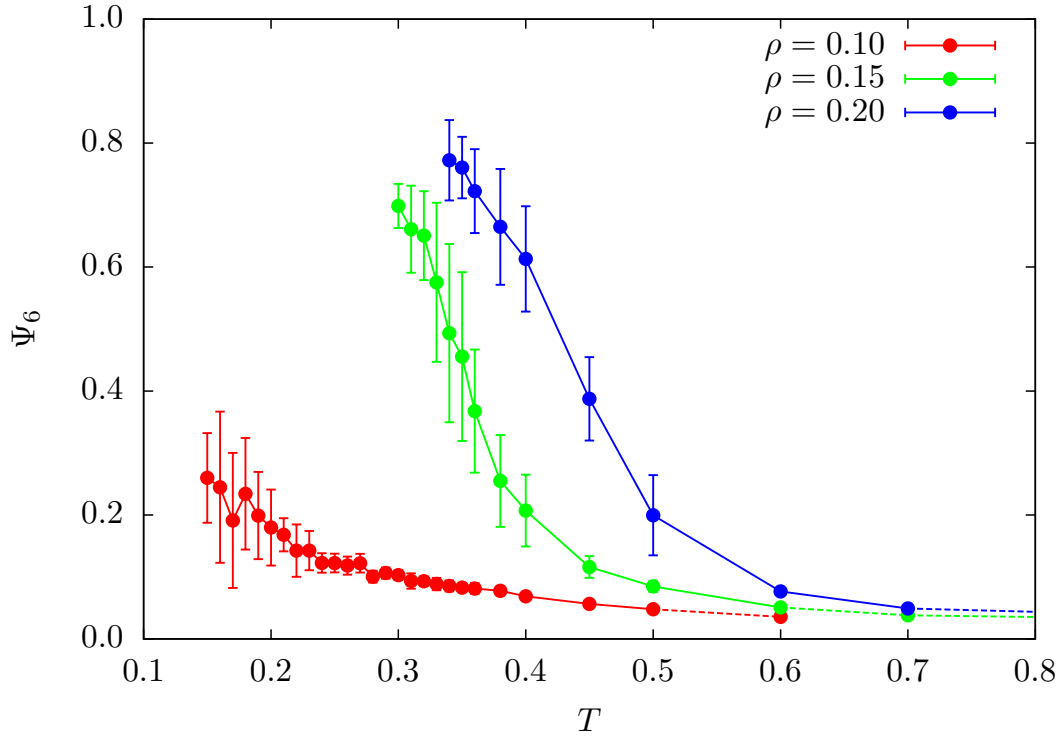


Figure 5.33: Bond order parameter Ψ_6 for the clusters of the system as a function of temperature.

It can be seen from figure 5.33, that the systems with a density of $\rho = 0.15$ and $\rho = 0.20$ shows a step increase in hexagonal order when lowering the temperature. The bond order parameter increases from close to zero up to $\Psi_6 \sim 0.8$ when decreasing the temperature. In systems with $\rho = 0.10$, on the other hand, Ψ_6 also increases when lowering the temperature, however Ψ_6 does not exceed a value of ~ 0.30 in the entire investigated temperature range.

The step increase of the bond ordering parameter, when lowering the temperature, seen at $\rho = 0.15$ and $\rho = 0.20$ indicates that the positions of the centers of mass of the clusters freeze in these systems, as already stated before in this section. At a density of $\rho = 0.10$, on the other hand, no step increase of the value of Ψ_6 is visible, therefore it can be argued that the clusters do not freeze at this density, within the investigated temperature range ($0.15 \leq T \leq 1.30$).

It can also be seen from figure 5.33 that the step increase in Ψ_6 occurs at higher temperatures for systems with $\rho = 0.20$ when comparing to systems with $\rho = 0.15$. However, the steepest increase of Ψ_6 is found at temperatures above the cluster freezing temperature $T_{\text{cluster}}^{\text{freeze}}$, estimated by the splitting of the second peak in cluster- $g(r)$.

Figures 5.34 to 5.36 show the positions of the clusters within the simulation box at the end of the respective simulation run, at different temperatures and for the densities $\rho = 0.10$, $\rho = 0.15$ and $\rho = 0.20$. The spheres representing the clusters in these snapshots are colored according to their individual bond order parameter $\Psi_6^{[1]}$ (see color code) which is computed via equation (4.141).

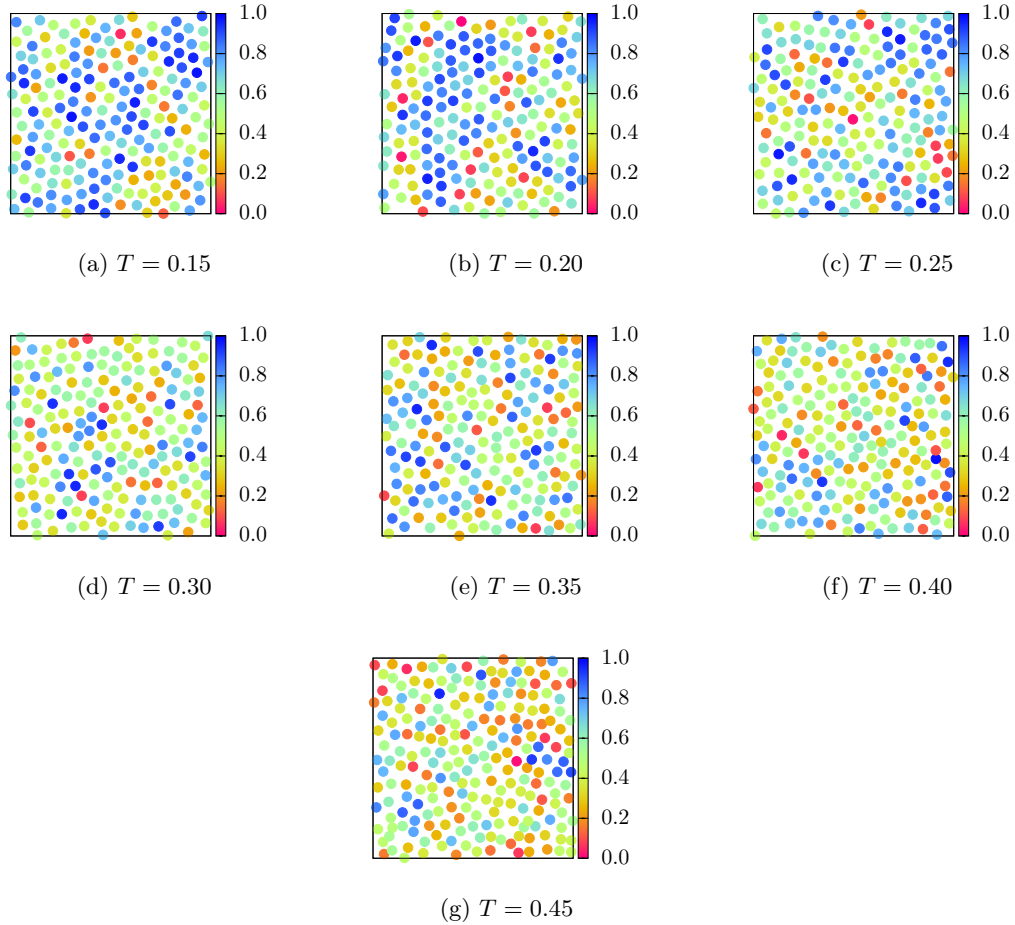


Figure 5.34: Cluster bond order parameter $\Psi_6^{[1]}$ for the individual clusters at the end of the simulations for $\rho = 0.10$ at various temperatures. The spheres mark the position of the clusters, while their color represents the value of $\Psi_6^{[1]}$ (red low $\Psi_6^{[1]}$, blue high $\Psi_6^{[1]}$). Snapshots of the entire simulation box are displayed here. The size of the spheres is *not* related to the actual cluster size.

At a temperature of $T = 0.45$ and a density of $\rho = 0.10$, shown in figure 5.34g, there are only a few clusters with a high bond order parameter $\Psi_6^{[1]}$ organized in small groups (blue spheres), while most of the clusters have a low to medium $\Psi_6^{[1]}$ (red to green colored spheres). When lowering the temperature the groups of clusters with high $\Psi_6^{[1]}$ grow, however, the majority of clusters still have a low to medium bond order

parameter (see figures 5.34g to 5.34d). Only at temperatures $T \leq 0.25$ the amount of clusters with a sizable bond order parameter ($\Psi_6^{[1]} \geq 0.7$) becomes comparable to the amount of clusters with low to medium $\Psi_6^{[1]}$ ($\Psi_6^{[1]} \leq 0.70$). Even down to the lowest temperature $T = 0.15$ a significant amount of clusters has only a low to medium bond order parameter $\Psi_6^{[1]}$ (see figure 5.34a).

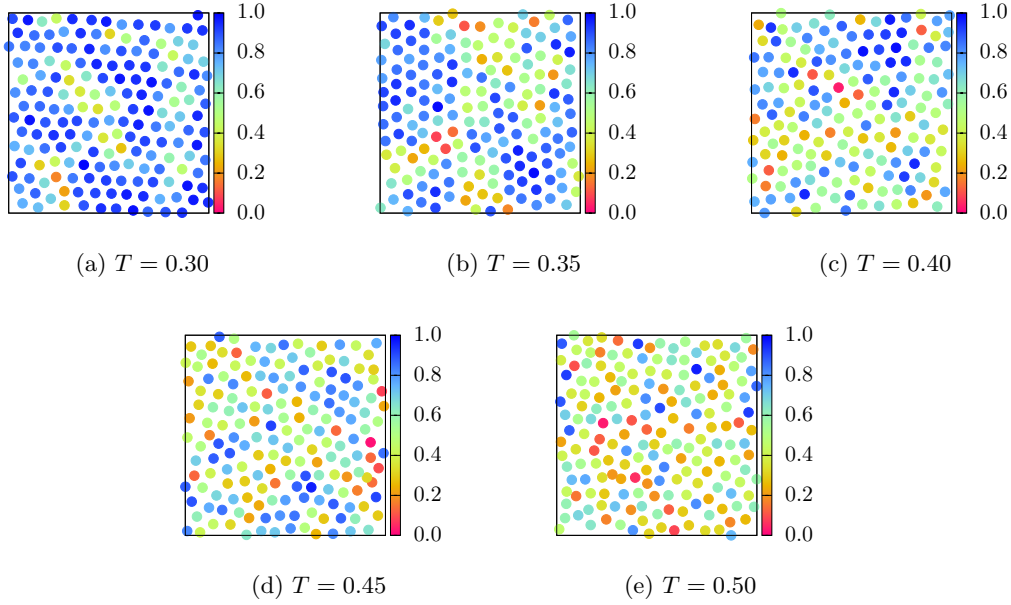


Figure 5.35: Cluster bond order parameter $\Psi_6^{[1]}$ for the individual clusters at the end of the simulations for $\rho = 0.15$ at various temperatures. The spheres mark the position of the clusters, while their color represents the value of $\Psi_6^{[1]}$ (red low $\Psi_6^{[1]}$, blue high $\Psi_6^{[1]}$). Snapshots of the entire simulation box are displayed here. The size of the spheres is *not* related to the actual cluster size.

Systems with a density of $\rho = 0.15$ mainly consist of clusters with a low to medium bond order parameter $\Psi_6^{[1]}$ at a temperature of $T = 0.50$ (red to green spheres in figure 5.35e). Only a small fraction of the clusters has a high $\Psi_6^{[1]}$ (blue spheres). Similar as for systems with $\rho = 0.10$, these clusters organize in small groups. As the temperature is decreased for systems of $\rho = 0.15$, the size of these high $\Psi_6^{[1]}$ cluster-groups increases quite rapidly (see figures 5.35e to 5.35c). At a temperature of $T = 0.35$ approximately half of the clusters show a high value of $\Psi_6^{[1]}$ ($\Psi_6^{[1]} \geq 0.7$) and therefore high hexagonal ordering (see figure 5.35b). In contrast to the lower temperatures at $\rho = 0.15$, the majority of clusters possess a high bond order parameter $\Psi_6^{[1]}$ at $T = 0.30$ (see figure 5.35a), only small groups of clusters with low to medium $\Psi_6^{[1]}$ remain immersed within the bulk of the hexagonally ordered clusters (blue spheres).

At a density of $\rho = 0.20$, most of the clusters show a bond order parameter $\Psi_6^{[1]} \geq 0.7$ already at a temperature of $T = 0.45$. Only a few groups of clusters with low to medium

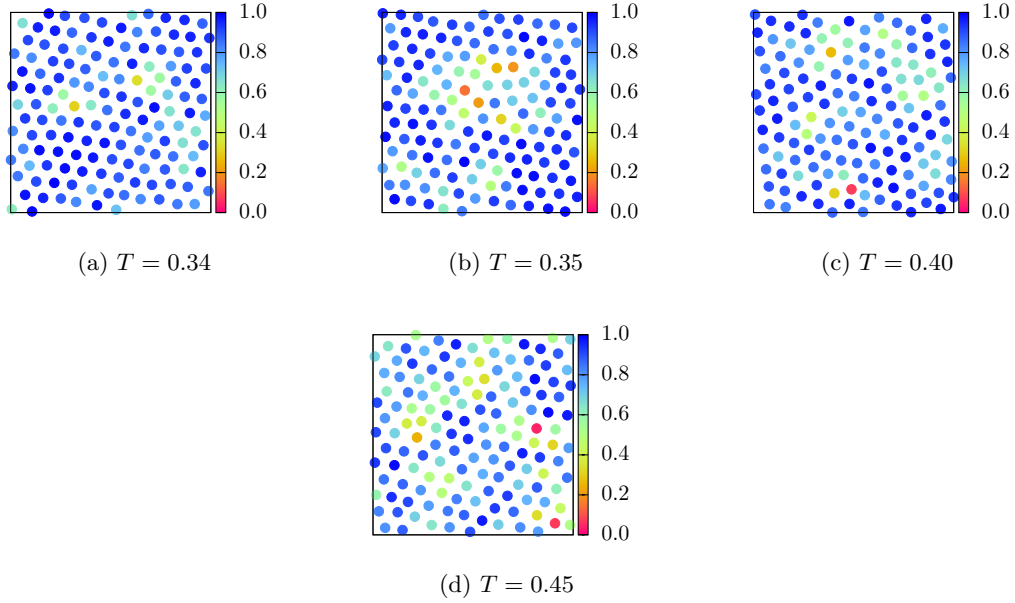


Figure 5.36: Cluster bond order parameter $\Psi_6^{[1]}$ for the individual clusters at the end of the simulations for $\rho = 0.20$ at various temperatures. The spheres mark the position of the clusters, while their color represents the value of $\Psi_6^{[1]}$ (red low $\Psi_6^{[1]}$, blue high $\Psi_6^{[1]}$). Snapshots of the entire simulation box are displayed here. The size of the spheres is *not* related to the actual cluster size.

$\Psi_6^{[1]}$ are present at that temperature (see figure 5.36d). As for the systems with lower density, the amount of clusters with a high value of $\Psi_6^{[1]}$ increases when lowering T . At the lowest investigated temperature for this density ($T = 0.34$), only two small groups of clusters with a medium $\Psi_6^{[1]}$ ($0.3 \leq \Psi_6^{[1]} \leq 0.7$) remain in the simulations snapshot shown. The hexagonal order of the clusters, spanning the entire simulation box, can clearly be seen in the snapshot at this temperature (figure 5.36a).

Obviously the bond order parameters of the individual clusters shown in the simulation snapshots of figures 5.34 to 5.36 coincides with the bond order parameter averaged over the entire simulation run, depicted as a function of temperature in figure 5.33. As in this figure, the snapshots show that the systems with $\rho = 0.10$ do not freeze within the investigated temperature region, and that systems with $\rho = 0.20$ freeze at higher temperatures than those with $\rho = 0.15$. However the snapshots in figures 5.34 to 5.36 also show, that the value of the bond order parameter exhibits large deviations between the individual clusters contained in the simulation box. Moreover these figures suggest that the average bond order parameter does not rise by a simultaneous increase of the bond order parameter of the individual clusters, but by the growth of the groups of cluster, where a high value of $\Psi_6^{[1]}$ is already present at higher temperature (nucleation centers).

5.2.3 Thermal Particle and Cluster Properties

The excess specific heat C_V^{ex} can be computed via

$$C_V^{\text{ex}} = \frac{dU^{\text{ex}}}{dT}, \quad (5.6)$$

as a derivative of the excess energy U^{ex} (given by equation (3.40)) with respect to the temperature T .

Figure 5.37 shows the excess specific heat per particle C_V^{ex}/N as a function of temperature for the three investigated densities. The black line in this figure represents the specific heat computed in an earlier investigation of Imperio and Reatto [12] for this system at $\rho = 0.10$.

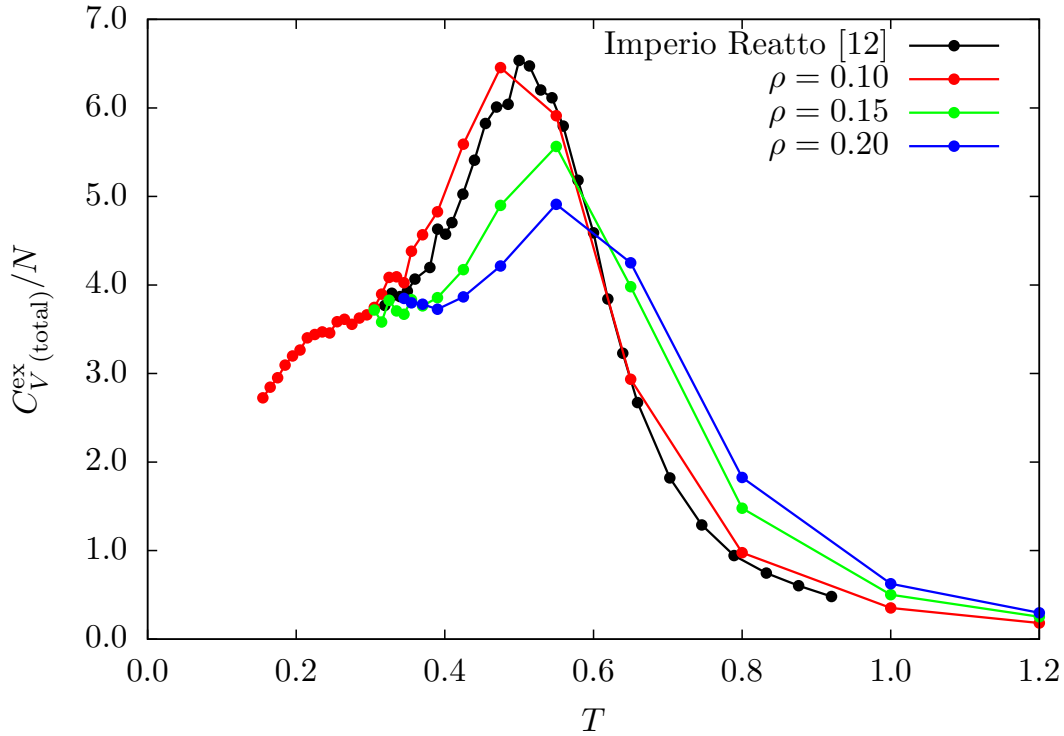


Figure 5.37: Excess specific heat per particle for $\rho = 0.10$, $\rho = 0.15$ and $\rho = 0.20$. The specific heat presented here has been obtained by computing the differential of the potential energy of the particles with respect to the temperature dU/dT . The black graph from [12] has been added as reference data for $\rho = 0.10$.

One can see from figure 5.37, that the total excess specific heat C_V^{ex}/N for $\rho = 0.10$ computed during the current investigation (red line in figure 5.37) is in good agreement with the data published in [12]. Differences mainly originate from the larger temperature steps in the current investigation.

As already stated by Imperio and Reatto in [12], the main peak in C_V^{ex}/N located at

$T \sim 0.50$ arises from the formation of the clusters out of the homogeneous phase upon cooling.

High peaks, due to the cluster formation, are also found in the specific heat curves for the densities $\rho = 0.15$ and $\rho = 0.20$. For the higher densities, the maximum of the peaks of the specific heat is shifted towards higher temperatures. This is in agreement with the statement of section 5.2.1, that the cluster formation occurs at higher temperatures in systems with higher densities.

Aside from the main peak in C_V^{ex}/N at $T \sim 0.50$, there is also a small peak visible for $\rho = 0.10$ at $T \sim 0.34$. There is also some indication of a peak in the vicinity of this temperature for $\rho = 0.15$ and $\rho = 0.20$. Due to the location of the peak at $T \sim 0.34$, it could indicate the freezing of the particles within the clusters to a hexagonal structure (see table 5.3). Indications of this ordering into a hexagonal structure, were also found in the pair distribution functions shown in figure 5.32. For systems with a density of $\rho = 0.40$ Imperio *et al.* found a similar, yet much more pronounced peak in C_V^{ex}/N [12, 17]. In this work Imperio *et al.* also argued that this peak stems from the transition of the particles into a hexagonal structure within the stripes, based on the additional information from structure functions.

5.2.4 Dynamic Particle and Cluster Properties

This subsection treats the dynamic properties of particles and clusters of systems with competing interactions, like the mean square displacement (MSD, $\langle \delta r^2(t) \rangle$), the diffusion coefficient (D) and the intermediate scattering function $f(k, t)$.

The gathering of dynamic information of the system via Monte Carlo simulations is treated in section 4.1.4 and the citations within that subsection. In absence of a better quantity, Monte Carlo steps, introduced in section 4.1.2, are used as a measure of time here, while the hard-core diameter σ of the potential is used as the unit of length.

Mean square displacement

The mean square displacement at the time t can be computed via

$$\langle \delta r^2(t) \rangle = \langle |\mathbf{r}(t) - \mathbf{r}(0)|^2 \rangle, \quad (5.7)$$

with $\langle \dots \rangle$ denoting the ensemble average over all particles, while $\mathbf{r}(t)$ and $\mathbf{r}(0)$ is the particle position at time t and time 0 respectively.

Another interesting quantity can be computed from the mean square displacement by building its logarithmic derivative [65] via

$$z(t) = \frac{d[\log \delta r^2(t)]}{d[\log t]}. \quad (5.8)$$

The value of $z(t)$ characterizes the type of the particle motion in the system (e.g. ballistic, diffusive, frozen). The most important types of motion and their corresponding value of $z(t)$ are listed in table 5.4 [65].

$z(t)$	type of motion
2	ballistic
1	diffusive
0	frozen

Table 5.4: Meaning of different values of the logarithmic derivative of the mean square displacement $z(t)$.

Due to the random direction of each individual Monte Carlo move (see section 4.1.2), $z(t)$ cannot exceed a value of 1 in Monte Carlo simulation for times exceeding several MC-steps, opposed to the short term ballistic flight regime visible in molecular dynamics simulation. However, as argued in section 4.1.4 and references therein, the long time behavior of molecular dynamics as well as Monte Carlo and Brownian dynamics simulations should coincide.

$\rho = 0.10$:

Figure 5.38 shows the mean square displacement and $z(t)$ as a function of time (in MC-steps) for the particles as well as the clusters, at a particle density of $\rho = 0.10$ and at various temperatures below the cluster-formation limit.

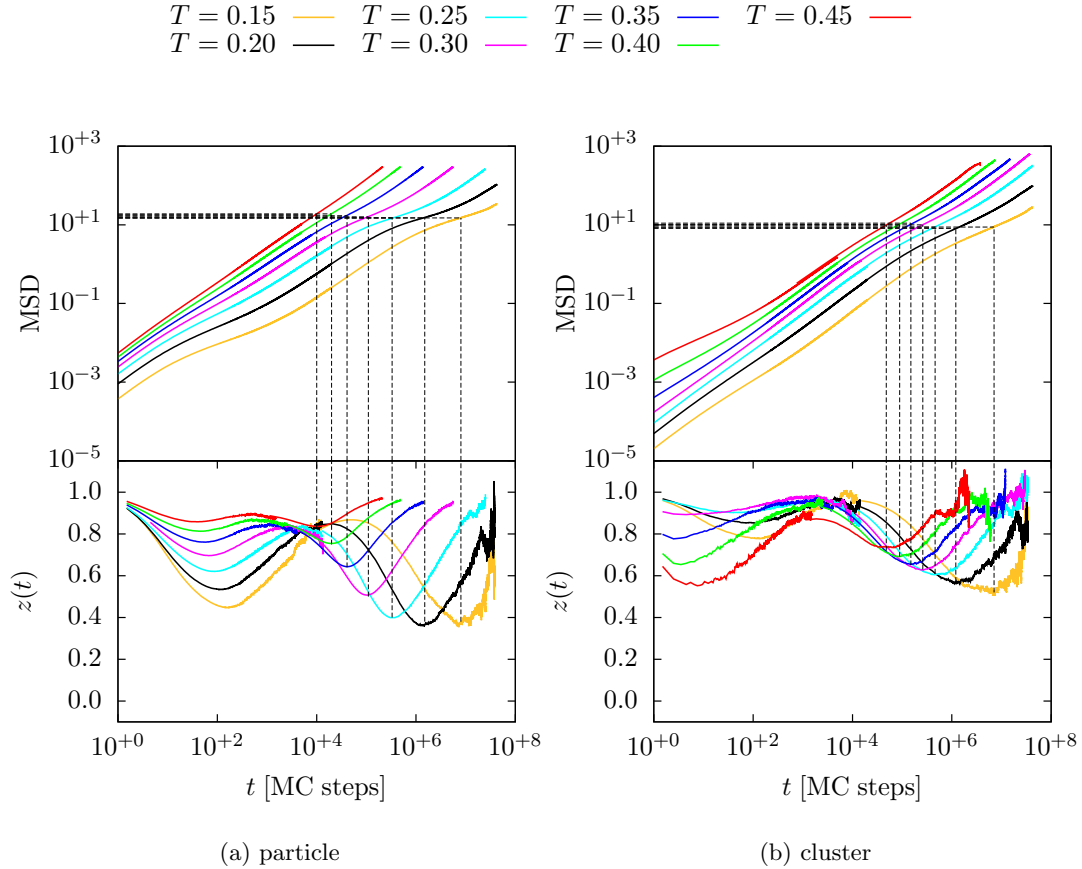


Figure 5.38: Mean square displacement as a function of time (top) and logarithmic derivative of the mean square displacement $z(t)$ as a function of time (bottom), for particles (left) and clusters (right) at a density of $\rho = 0.10$.

At the highest shown temperature ($T = 0.45$), the particles behaves close to purely diffusive, as can be seen from the mean square displacement curve, as well as from the value of $z(t)$ close to 1 (see top left panel of figure 5.38).

When lowering the temperature, deviations from the pure diffusive behavior become more apparent. While the double logarithmic plot of the mean square displacement curve is not a straight line anymore, the $z(t)$ as a function of time shows two dips. The depth of these dips, i.e. the deviation of $z(t)$ from the purely diffusive value of 1, grows with decreasing temperature. The minimum of the first dip of the particle- $z(t)$ is located at about $3.5 \cdot 10^{+1} \leq t \leq 1.5 \cdot 10^{+2}$ MC steps, which translates to a mean square displacement value of $1.3 \cdot 10^{-2} \leq \langle \delta r^2(t) \rangle \leq 1.3 \cdot 10^{-1}$ (see left panels of figure 5.38), with the lower value of this range occurring at $T = 0.15$. The decreasing MSD value of the first dip in $z(t)$, with decreasing temperature, as well as the absolute MSD value significantly below 1 suggest, that this dip in $z(t)$ originates from the restriction of the motion of the individual particles by neighboring particles in the cluster. The reduction of the mean square displacement value of the particles by one order of magnitude, when

reducing T , can be explained by the more compact (hexagonal) structure of the clusters at lower temperature, severely restricting the movement of the particles in the cluster. The minimum of the second dip of the particle- $z(t)$ is located at $t \approx 1 \cdot 10^4$ MC steps for a temperature of $T = 0.45$ and is shifted to larger values t with decreasing temperature, reaching a value of $t \approx 8.0 \cdot 10^6$ MC steps for a temperature of $T = 0.15$. This corresponds to a rather narrow range of MSD values of $\langle \delta r^2(t) \rangle \sim 1.7 \cdot 10^{+1} \pm 0.2 \cdot 10^{+1}$ at the location of these $z(t)$ -minima, for all investigated temperatures (see left panels of figure 5.38). Since a mean square displacement of $\langle \delta r^2(t) \rangle \sim 1.7 \cdot 10^{+1}$ approximately equals a mean traveled distance of $\delta r \sim 4$, which is in the order of the cluster size (R_g), therefore the second dip in $z(t)$ originates from the cumulative attractive forces of the cluster particles hindering particles to leave the cluster. The nearly temperature invariant mean square displacement value associated with the second dip in the particle- $z(t)$ also supports that explanation, especially since the location of the minimum shifts three orders of magnitude in time. The noise visible in $z(t)$ especially at high values of t originates from the differential, calculated from the mean square displacement of the simulation (see equation (5.8)). This differential amplifies the noise present in the mean square displacement data, which is more prominent at the end of the simulation, due to the smaller number of possible starting points available to calculate $\langle \delta r^2(t) \rangle$ (see [30]).

The right panels of figure 5.38 show the mean square displacement and $z(t)$ of the clusters at $\rho = 0.10$ as a function of time. As with the particles, the function $z(t)$ shows two dips for the clusters (see bottom right panel of figure 5.38). However, the first dip of the cluster- $z(t)$ exhibits a non-monotonous behavior in its depth as well as in its location, when lowering the temperature. For high temperatures a deep dip is located at low t ($t \leq 10$ MC steps). The depth of this dip decreases while lowering the temperature down to $T \approx 0.30$, where it nearly vanishes. For temperatures lower than $T = 0.30$ a new dip at about $t \sim 1 \cdot 10^{+2}$ MC steps appears. This dip has its minimum at the same time t as the first dip of the particle- $z(t)$. Similar as in the particle- $z(t)$, the depth of of this minimum increases with decreasing temperature. The discontinuity in the behavior of the first minimum in the cluster- $z(t)$ (non-monotonous behavior) occurs roughly at a temperature ($T \approx 0.30$), where the particles freeze into a hexagonal ordered structure within the cluster. The minima at $t \leq 10$ MC steps are clearly influenced by the by the dynamics imposed by the Monte-Carlo simulations and would show differently in molecular dynamics and Brownian dynamics simulations (see section 4.1.4).

The minimum of the second dip in the cluster- $z(t)$ is located at $t \approx 4.8 \cdot 10^{+4}$ for $T = 0.45$ and $t \approx 7.1 \cdot 10^{+6}$ for $T = 0.15$. Surprisingly, the more than two orders of magnitude difference in the location of the second minimum of the cluster- $z(t)$ translate to approximately the same mean square displacement value at this minima of $8.1 \leq \langle \delta r^2(t) \rangle \leq 11.0$. This mean square displacement value is equivalent to a distance of $\delta r \sim 3$, which is roughly the distance the cluster center of mass can travel before being hindered by the surrounding clusters.

$\rho = 0.15$:

Similar to figure 5.38, figure 5.39 displays the mean square displacement and $z(t)$ as a

function of time (MC-steps) for the particles as well as the clusters at a particle density of $\rho = 0.15$ and at various temperatures below the cluster formation limit.

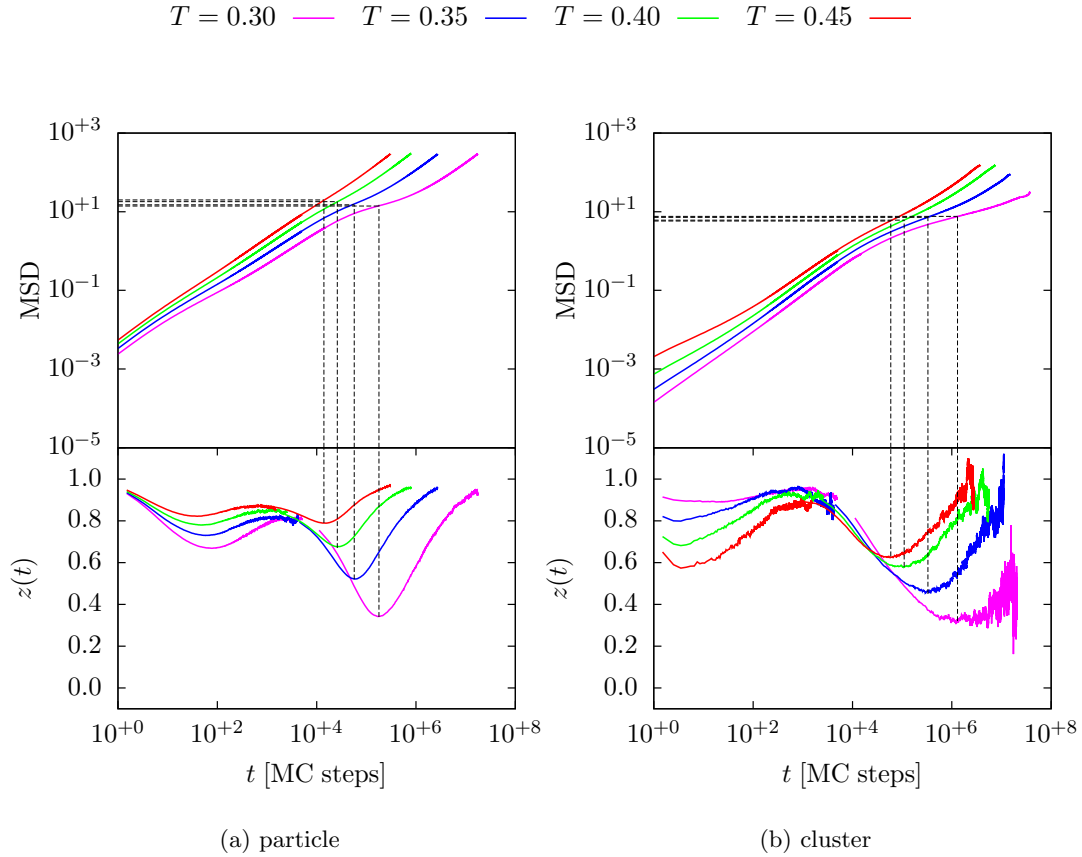


Figure 5.39: Mean square displacement as a function of time (top) and logarithmic derivative of the mean square displacement $z(t)$ as a function of time (bottom), for particles (left) and clusters (right) at a density of $\rho = 0.15$.

The panels on the left side of figure 5.39 show the mean square displacement and $z(t)$ for the particles. The behavior of these properties is essentially the same as for a density of $\rho = 0.10$. For the highest investigated temperature $T = 0.45$ the system behaves mostly diffusive, which is visible from the mean square displacement (top left panel of figure 5.39) and the fact that the value of the function $z(t)$ (bottom left panel of figure 5.39) is close to one for the entire time range. However two dips in the particle- $z(t)$ are already visible at that temperature. The depth of these minima increases when lowering the temperature. The minimum of the first dip in the particle- $z(t)$ is located at $t \approx 3.5 \cdot 10^{+1}$ MC steps, at a temperature of $T = 0.45$, while moving to $t \approx 8.2 \cdot 10^{+1}$ for a temperature of $T = 0.30$. The mean square displacement at the location of these minima in the particle- $z(t)$ lies in the range of $7.7 \cdot 10^{-2} \leq t \leq 1.2 \cdot 10^{-1}$, with the smaller mean square displacement value applying to the smaller temperature. The locations, as well as the mean square displacement values at these minima in the particle- $z(t)$

are comparable to the ones for a density of $\rho = 0.10$, supporting the assumption that they also originate from the confinement due to the surrounding particles in the same cluster.

The second dip of the particle- $z(t)$ is located at $t \approx 1.4 \cdot 10^4$ for a temperature of $T = 0.45$ and $t \approx 1.8 \cdot 10^5$ for $T = 0.30$. As before this translates to a mean square displacement value in the rather narrow range of $14 \leq \langle \delta r^2(t) \rangle \leq 20$. The roughly temperature-independent mean square displacement value at the minimum of the second dip in the particle- $z(t)$ is comparable to the respective value at $\rho = 0.10$. However, the location of the minimum of the second dip in the particle- $z(t)$ is shifted to larger t when comparing to the minimum of the second dip in the particle $z(t)$ for $\rho = 0.10$ at the same temperature. Since clusters are larger at a density of $\rho = 0.15$, than at $\rho = 0.10$, the particles are trapped for a longer time by these bigger clusters, while the area accessible to the particle within the cluster roughly stays the same. Figure 5.40 shows the binding energy of the particles in clusters at the investigated densities ($\rho = 0.10$, $\rho = 0.15$ and $\rho = 0.20$) as a function of temperature. The binding energy is defined as the difference of the potential energy of a particle outside the cluster $U_{(\text{free})}^{\text{ext}}/N$ and a particle inside a cluster $U_{(\text{cluster})}^{\text{ext}}/N$.

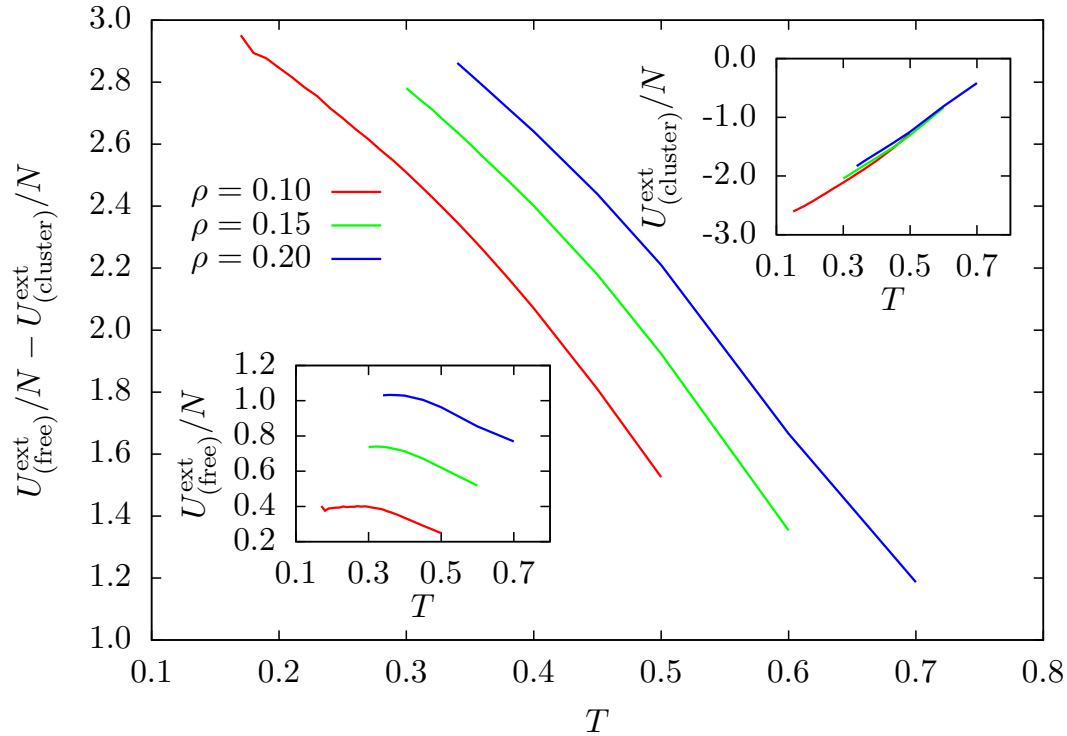


Figure 5.40: Binding energy of the particles in the clusters for $\rho = 0.10$, $\rho = 0.15$ and $\rho = 0.20$ as a function of temperature. The binding energy is defined as the difference in the average potential energy of a free (non-cluster) particle (bottom left inset) and a particle in a cluster (top right inset). Mind the different y-scale on the insets.

Figure 5.40 shows that the binding energy increases with the density. However it can be seen from the insets of figure 5.40 that this increase in binding energy mainly originates from the increase of the potential energy of the particles outside the clusters, $U_{(\text{free})}^{\text{ext}}/N$. The mean square displacement and $z(t)$ for the clusters is shown in the panels on the right side of figure 5.39. Due to the smaller temperature range compared to the $\rho = 0.10$ case, a non-monotonous behavior for the minimum of the first dip in the cluster- $z(t)$ is not visible here. The locations of the minimum of the first dip of the cluster- $z(t)$ range from $3.6 \leq t \leq 26$ with values of the mean square displacement at the location of the minimum from $2.6 \cdot 10^{-3} \leq \langle \delta r^2(t) \rangle \leq 4.5 \cdot 10^{-3}$.

The second minimum in the cluster- $z(t)$ is located between $t \approx 5.9 \cdot 10^4$ for $T = 0.45$ and $t \approx 1.3 \cdot 10^6$ for $T = 0.30$, covering 1.5 orders of magnitude (see figure 5.39). However all mean square displacement values at the location of these minima fall into the comparably narrow range of $5.8 \leq \langle \delta r^2(t) \rangle \leq 7.6$, which is less than the respective value at $\rho = 0.10$, because the larger size of the clusters restricts their movement to a higher degree.

$\rho = 0.20$:

Figure 5.41 shows the mean square displacement and $z(t)$ as functions of time for the particles and clusters of systems with a density of $\rho = 0.20$ at different temperatures. The particle properties are displayed in the panels on the left side, and show the same features (two dips in $z(t)$) as in systems with $\rho = 0.10$ and $\rho = 0.15$. The location of the minimum in the particle- $z(t)$ varies from $t \approx 4.3 \cdot 10^1$ MC steps for $T = 0.45$ to $t \approx 8.1 \cdot 10^1$ MC steps for $T = 0.34$. The mean square displacement values at the position of these $z(t)$ -minima lie in the range of $9.5 \cdot 10^{-2} \leq \langle \delta r^2(t) \rangle \leq 1.2 \cdot 10^{-1}$. At a constant temperature, the location of the first minimum in $z(t)$ for the particles, as well as the particle mean square displacement value at this minimum is approximately the same for all three investigated densities.

The second dip in the particle- $z(t)$ is located between $t \approx 2.2 \cdot 10^4$ MC steps at $T = 0.45$ and $t \approx 1.3 \cdot 10^5$ MC steps at $T = 0.34$ for a density of $\rho = 0.10$. Similar to the other investigated densities, the mean square displacement value at the location of this minimum lies in the comparably narrow range of $1.6 \cdot 10^1 \leq \langle \delta r^2(t) \rangle \leq 2.1 \cdot 10^1$. Comparing the location of the second minimum in the particle- $z(t)$, as well as the mean square displacement value at this minimum for all investigated densities at constant temperatures one can see that the location of the minimum is shifted towards larger values of t with increasing ρ , while the corresponding mean square displacement value stays nearly constant. This trend, already mentioned before, originates from the fact, that the larger cluster at higher densities, trap the particles more efficiently, while the space available for the particles within the clusters is roughly of equal size for all densities.

The mean square displacement and $z(t)$ of the clusters at a density of $\rho = 0.20$ are shown as functions of time in the right panels of figure 5.41. The first dip in the cluster $z(t)$ occurs at short times ($t < 10$) and shows the same behavior as for $\rho = 0.15$, therefore it will not be discussed here again.

The second dip in the cluster- $z(t)$ is located between $t \approx 2.2 \cdot 10^5$ MC steps for $T = 0.45$ and $t \approx 6.0 \cdot 10^5$ MC steps for $T = 0.34$. Again the widely distributed

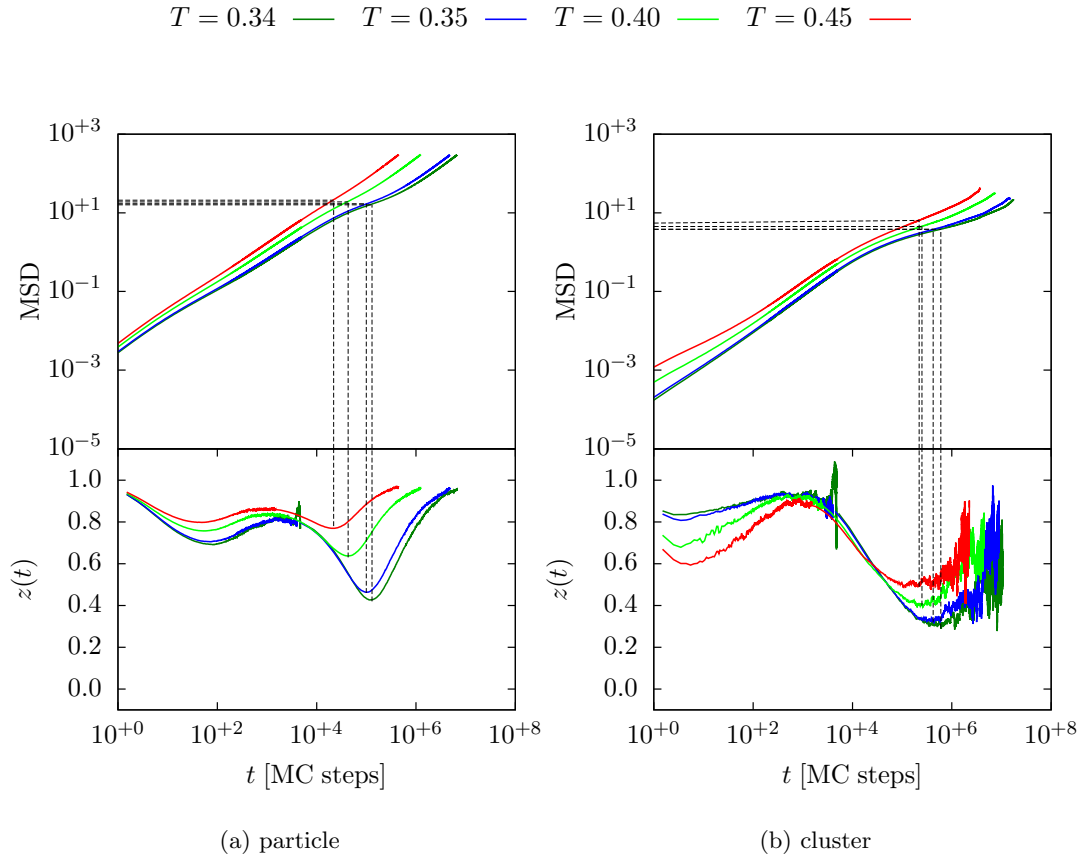


Figure 5.41: Mean square displacement as a function of time (top) and logarithmic derivative of the mean square displacement $z(t)$ as a function of time (bottom), for particles (left) and clusters (right) at a density of $\rho = 0.20$.

locations of the minima in $z(t)$ translate into a rather narrow range of mean square displacement values, at the location of these minima. The minima of these cluster- $z(t)$ dips are located in the range $3.8 \cdot 10^{+0} \leq \langle \delta r^2(t) \rangle \leq 6.4 \cdot 10^{+0}$, which is less than the corresponding value at $\rho = 0.15$. This continues the trend, that the bigger clusters, present at higher densities, restrict the cluster movement more than the smaller clusters at lower densities.

Diffusion Coefficient

The diffusion coefficient D can be computed from the mean square displacement $\langle \delta r^2(t) \rangle$ at a sufficiently large time t via the Einstein relation for two-dimensional systems [30] given by

$$2tD = \frac{1}{2} \langle |\mathbf{r}(t) - \mathbf{r}(0)|^2 \rangle = \frac{1}{2} \langle \delta r^2(t) \rangle, \quad (5.9)$$

assuming a purely diffusive behavior ($z(t) = 1$).

Figure 5.42 shows the particle diffusion coefficient D^{pt} computed via equation (5.9) as a function of the inverse temperature $1/T$ for the three investigated densities ($\rho = 0.10$, $\rho = 0.15$ and $\rho = 0.20$). The inset of this figure shows the diffusion constant on a logarithmic scale.

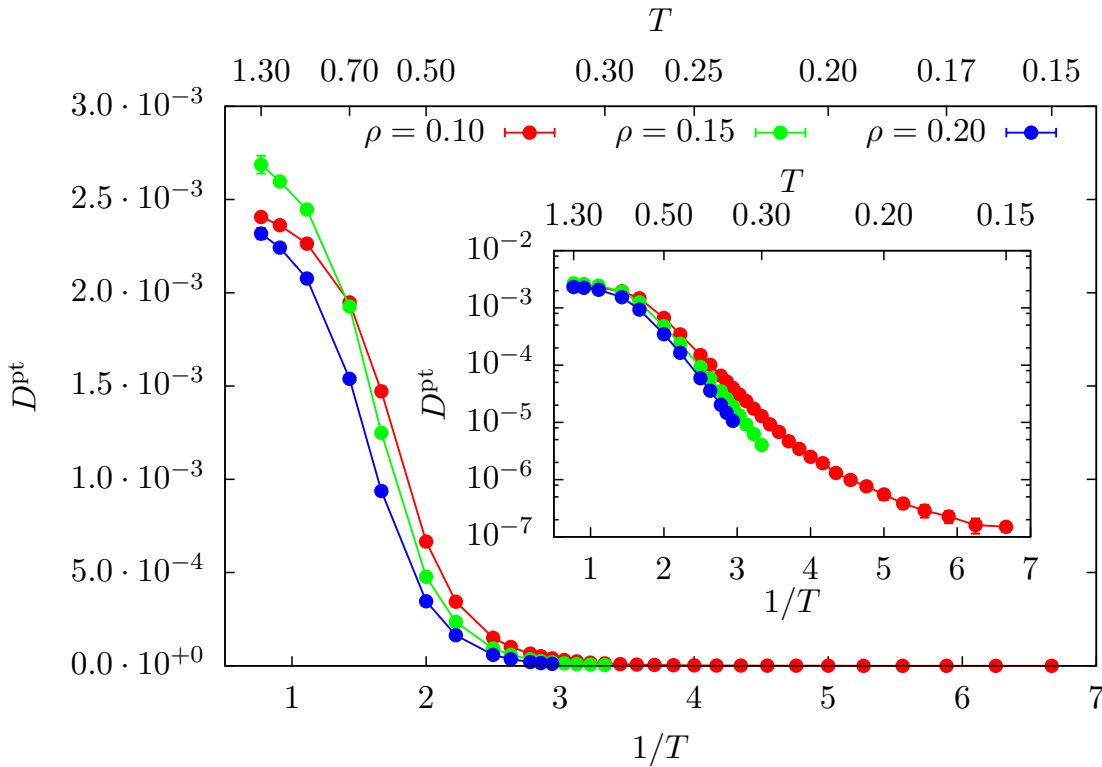


Figure 5.42: Particle diffusion coefficient D^{pt} as a function of inverse temperature $1/T$.

From figure 5.42 one can see, that the diffusion coefficient for the particles shows for all three investigated densities a similar qualitative behavior, with a steep drop of the particle diffusion coefficient D^{pt} in the temperature region $0.70 \geq T \geq 0.50$. It can also be seen from figure 5.42, that this steep drop of D^{pt} takes place at higher temperatures for systems with higher densities.

Figure 5.43 shows the cluster diffusion coefficient D^{cl} as a function of the inverse temperature $1/T$ for the three investigated densities ($\rho = 0.10$, $\rho = 0.15$ and $\rho = 0.20$).

As in the previous figure, the inset of figure 5.43 shows the diffusion coefficient on a logarithmic scale.

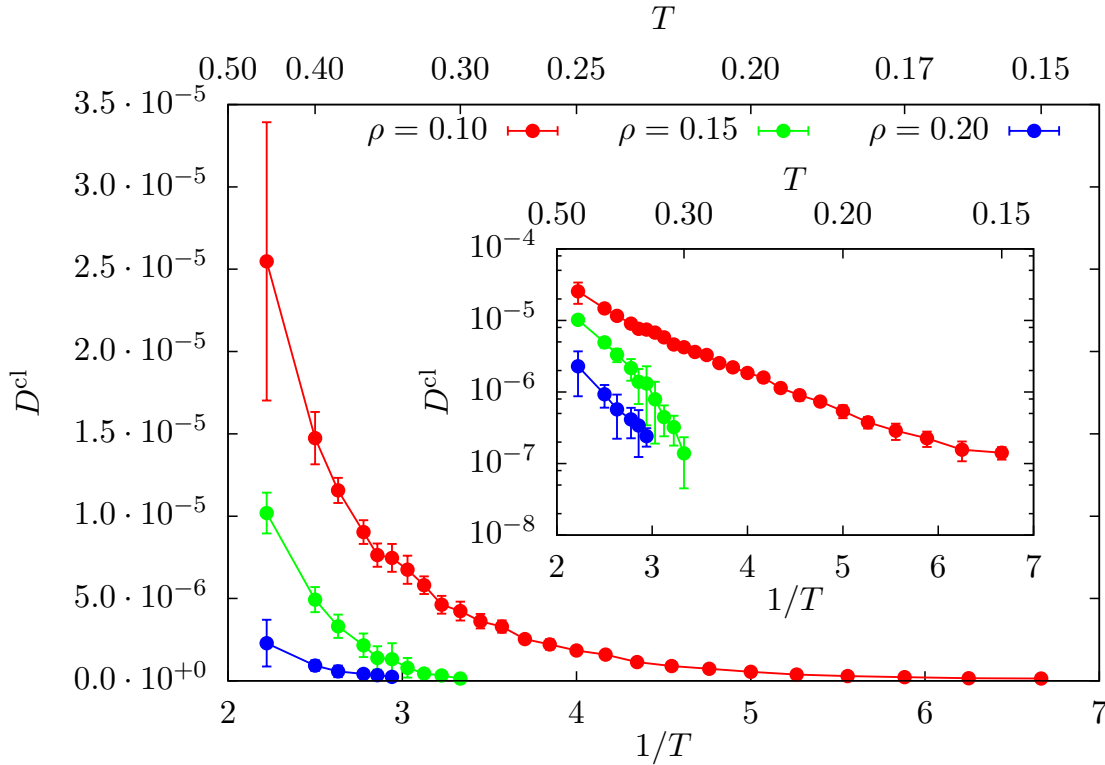


Figure 5.43: Cluster diffusion coefficient of the clusters D^{cl} as a function of inverse temperature $1/T$.

In contrast to the particle diffusion coefficient, the cluster diffusion coefficient is significantly smaller for systems with higher density, comparing at equal temperature. At $T = 0.45$ the cluster diffusion coefficient for systems with $\rho = 0.10$ differs from the cluster diffusion coefficient for systems with $\rho = 0.20$ by an entire order of magnitude. The inset of figure 5.43 shows a steep drop of $\log D^{\text{cl}}$ as a function of $1/T$ down to a value of $D^{\text{cl}} = 10^{-7}$ for $\rho = 0.15$ and $\rho = 0.20$, with decreasing temperature. Systems with a density of $\rho = 0.10$, on the other hand, show a notably slower decrease in the cluster diffusion coefficient (see inset of figure 5.43), approaching the value of $D^{\text{cl}} = 10^{-7}$ only for the lowest investigated temperatures ($T < 0.20$). This different behavior between systems with $\rho = 0.15$ and $\rho = 0.20$ on one hand, and systems with $\rho = 0.10$ on the other hand, suggests, that the clusters in the latter systems are more mobile over a much wider temperature range compared to clusters of the former systems. The qualitative difference of the cluster diffusion coefficient between systems with $\rho \geq 0.15$ and systems with $\rho = 0.10$ even supports the assumption that the clusters in the former systems freeze, while they keep liquid in the latter systems.

Figure 5.44 shows a comparison of the particle and cluster diffusion coefficient (on a logarithmic scale) as a function of inverse temperature $1/T$, for all three investigated

densities.

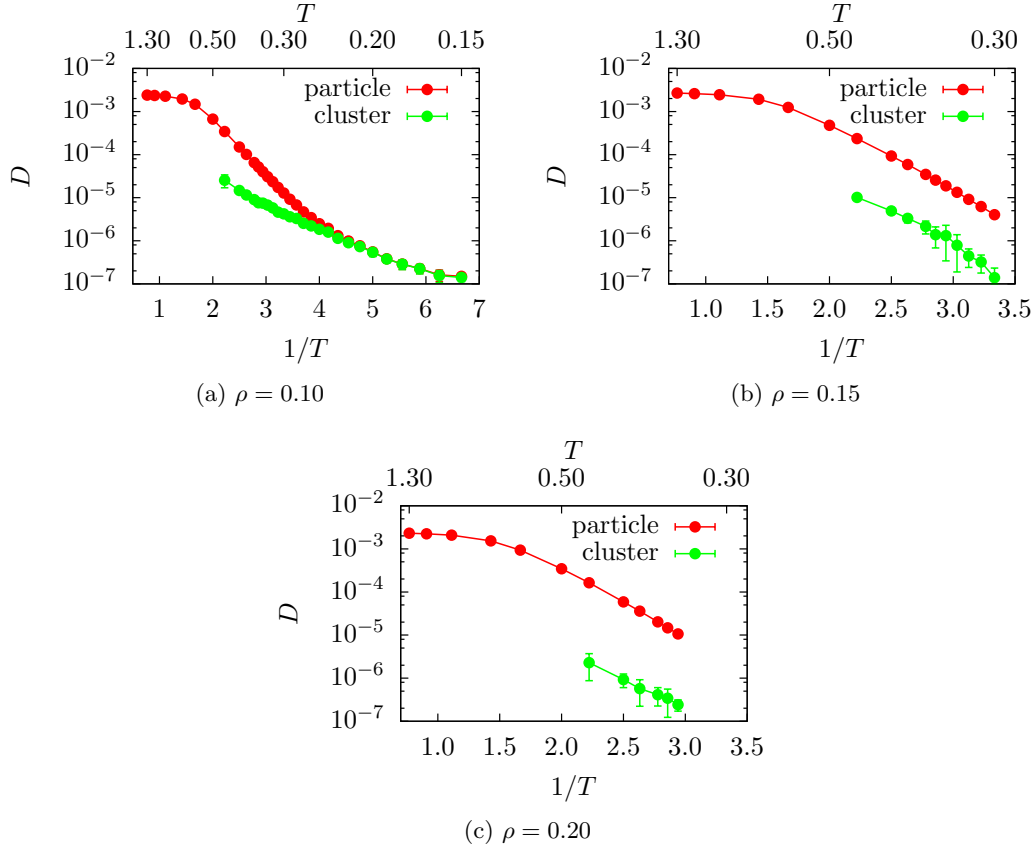


Figure 5.44: Comparison of the diffusion coefficient D of particles and clusters as a function of inverse temperature $1/T$ at the three investigated densities $\rho = 0.10$, $\rho = 0.15$ and $\rho = 0.20$.

As in figure 5.43, a qualitative different behavior is visible for the diffusion coefficient at a density of $\rho = 0.10$ compared with the other two investigated densities (see top left panel of figure 5.43). For $\rho = 0.15$ and $\rho = 0.20$ the particle diffusion coefficient as a function of $1/T$ is always about 1.5 orders of magnitude larger than the cluster diffusion coefficient as a function of $1/T$, independent of T . In case of $\rho = 0.10$ however, the gap between the particle diffusion coefficient curve and the cluster diffusion coefficient curve shrinks with decreasing temperature, and becomes zero at $T \approx 0.20$. For lower temperatures the particle diffusion D^{pt} coefficient and the cluster diffusion coefficient D^{cl} are basically identical. This means that at low enough temperature the particles do not leave the cluster anymore and particle diffusion only occurs as part of the cluster parallel to the cluster center of mass.

Intermediate Scattering Function

The total- and the self intermediate scattering function $f_{\text{total}}(\mathbf{k}, t)$ and $f_{\text{self}}(\mathbf{k}, t)$ are commonly used to assess the slowing dynamics in particle simulations [27, 65, 24]. The total intermediate scattering function $f_{\text{total}}(\mathbf{k}, t)$ can be calculated via

$$f_{\text{total}}(\mathbf{k}, t) = \frac{\overline{\langle \rho_{\mathbf{k}}(t) \rho_{-\mathbf{k}}(0) \rangle}}{\langle \rho_{\mathbf{k}}(0) \rho_{-\mathbf{k}}(0) \rangle} \quad (5.10)$$

with the Fourier transform of the particle density $\rho_{\mathbf{k}}(t)$ given by

$$\rho_{\mathbf{k}}(t) = \sum_{j=1}^N \exp[-i\mathbf{k} \cdot \mathbf{r}_j(t)]. \quad (5.11)$$

The overbar $\overline{\dots}$ in equation (5.10) represents the additional average over the independent Monte-Carlo simulations (quenches), and should be only strictly necessary in the case of quenched-annealed systems (see section 5.3), while $\langle \dots \rangle$ denotes the ensemble average.

From equation (5.10), it is obvious that for $t = 0$ the total intermediate scattering function is equal to one.

Using the static structure factor (see equation (3.94)) the total intermediate scattering function can be written as

$$f_{\text{total}}(\mathbf{k}, t) = \frac{\overline{\langle \rho_{\mathbf{k}}(t) \rho_{-\mathbf{k}}(0) \rangle}}{\langle \rho_{\mathbf{k}}(0) \rho_{-\mathbf{k}}(0) \rangle} = \frac{\overline{\langle \rho_{\mathbf{k}}(t) \rho_{-\mathbf{k}}(0) \rangle}}{N S(\mathbf{k})} \quad (5.12)$$

(see [65, 24, 27]).

The self intermediate scattering function $f_{\text{self}}(\mathbf{k}, t)$ given by

$$f_{\text{self}}(\mathbf{k}, t) = \frac{\overline{\langle \rho_{\mathbf{k}}^{[1]}(t) \rho_{-\mathbf{k}}^{[1]}(0) \rangle}}{\langle \rho_{\mathbf{k}}^{[1]}(0) \rho_{-\mathbf{k}}^{[1]}(0) \rangle}, \quad (5.13)$$

with $\rho_{\mathbf{k}}^{[1]}(t)$ defined as

$$\rho_{\mathbf{k}}^{[1]}(t) = \exp[-i\mathbf{k} \cdot \mathbf{r}_j(t)], \quad (5.14)$$

represents the part of the total intermediate scattering function $f_{\text{total}}(\mathbf{k}, t)$, only correlating single particle densities $\rho_{\mathbf{k}}^{[1]}(t)$ [65, 27, 24].

The common representation of intermediate scattering functions (ISFs) is to set k to a fixed value and plotting $f(k, t)$ as a function of the time t is adopted here [65]. The length of the k -vector was chosen to be at the characteristic wavevector for the microphase formation $k = k_c = 0.573$ (see equation (5.5)), in order to expose the decay of the density correlations associated with the cluster formation. A number of other k -vectors in the vicinity of $k_c = 0.573$, where also used to compute the intermediate scattering functions for testing reasons, they were found to yield qualitatively similar results.

In figures 5.45 to 5.50, the center of mass positions of the clusters were used for the calculation of the intermediate scattering functions $f_{\text{total/self}}(k, t)$, as well as the positions of the individual particles. Intermediate scattering functions derived from the positions of the clusters, centers of mass are labeled *cluster* or *cl*, while the ISFs computed from the individual particle positions are labeled *particle* or *pt*.

$\rho = 0.10$:

Figure 5.45 shows the total-ISFs (top panels) as well as the self-ISFs (bottom panels) computed from the particle positions (left panels) and the positions of the cluster centers of mass (right panels) at various temperatures (as labeled) for systems with a density of $\rho = 0.10$.

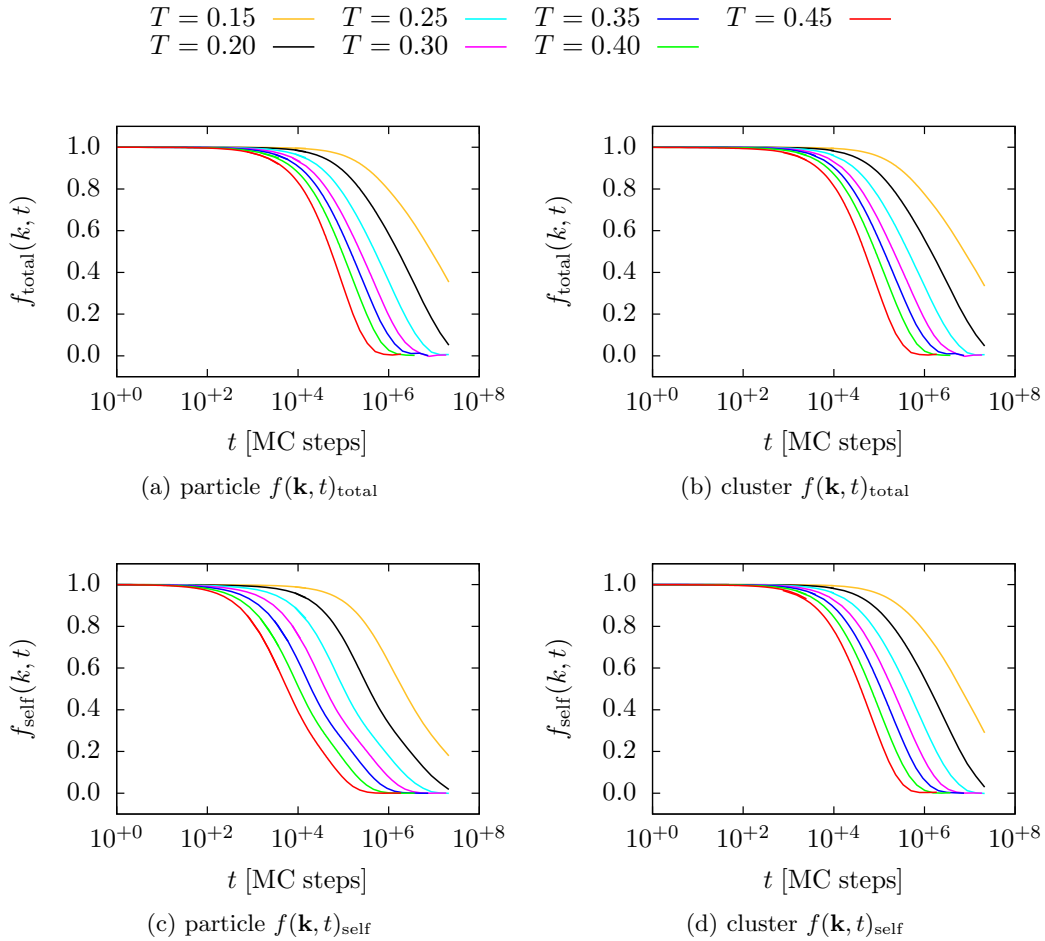


Figure 5.45: Intermediate scattering functions $f_{\text{total}}(k = 0.573, t)$ (top panels) and $f_{\text{self}}(k = 0.573, t)$ (bottom panels), using particles positions (left panels) and clusters positions (right panels) for the calculation. The ISFs are presented for a density of $\rho = 0.10$ at various temperatures (as labeled).

The total-ISFs computed from the particle positions (top left panel of figure 5.45), show

a single step relaxation (α -relaxation [65]) from one to zero. However the relaxation is not complete (i.e. does not reach zero until the end of the simulation) for $T = 0.15$. As expected the relaxation in $f_{\text{total}}(k, t)$ sets in at a later time for lower temperatures.

The self-ISFs determined from the particle positions (bottom left panel of figure 5.45) also show a single step relaxation to zero. Compared to the total-ISFs, the relaxations in the self-ISF set in earlier but, due to a flatter slope the particle self-ISF reaches zero approximately at the same time as $f_{\text{total}}(k, t)$, when comparing at the same temperature. Again the relaxation to zero in the self-ISF computed from particle positions, is not complete for $T = 0.15$.

The total- and self-ISF computed from the cluster positions (right panels of figure 5.45), both look similar to the total-ISF computed from the particle positions (top left panel of figure 5.45), when comparing at the same temperature. As already mentioned for the total-ISF computed from the particle positions the relaxation in the total and self cluster $f(k, t)$ takes place in a single step.

Direct comparisons of the total- and self-ISFs computed from the particle positions as well as the positions of the cluster centers of mass are shown in figure 5.46 at various temperatures, for systems with $\rho = 0.10$.

The different panels in figure 5.46 show that the total-ISF computed from the particle positions at $k = 0.573$ behaves qualitatively and quantitatively similar to the total-ISF computed from the cluster centers of mass and to a lesser degree also similar to the self-ISF computed from the cluster centers of mass at equal temperatures. This similarity occurs at all temperatures, within the investigated temperature region ($0.15 \leq T \leq 0.45$). The self-ISF calculated from the particle positions, on the other hand, is markedly different from the self-ISF calculated from the cluster position as well as the total-ISFs shown in the panels of figure 5.46. The curve of the particle- $f_{\text{self}}(k, t)$ lies significantly below all other intermediate scattering functions, for all investigated temperatures. The relaxation of the particle- $f_{\text{self}}(k, t)$, sets in earlier than the relaxation in the other intermediate scattering functions, but it is not as steep. The difference of the particle- $f_{\text{self}}(k, t)$ increases with rising T , when comparing to the other ISFs at the same temperature.

$\rho = 0.15$:

The top panels in figure 5.47 show the total-ISF computed from particle positions (top left panel) and cluster positions (top right panel) respectively, while the bottom panels show the self-ISF, also computed from particle positions (bottom left panel) and cluster positions (bottom right panel), at various temperatures (as labeled), for a density of $\rho = 0.15$.

From figure 5.47 the total-ISF ($k = 0.573$) computed from the cluster positions and the total-ISF computed from particle positions looks similar to the self-ISF computed from cluster positions when comparing at the same temperature (see figure 5.47). As for $\rho = 0.10$, the self-ISF computed from the particle positions shows a significant different behavior from the others ISFs at $\rho = 0.15$. The total-ISFs, as well as the self-ISF computed from the cluster positions, show only a single step relaxation of the correlations at $k = 0.573$ towards zero. This relaxation sets in at later times (i.e. more MC-steps), when decreasing the temperature. In addition, the relaxations of

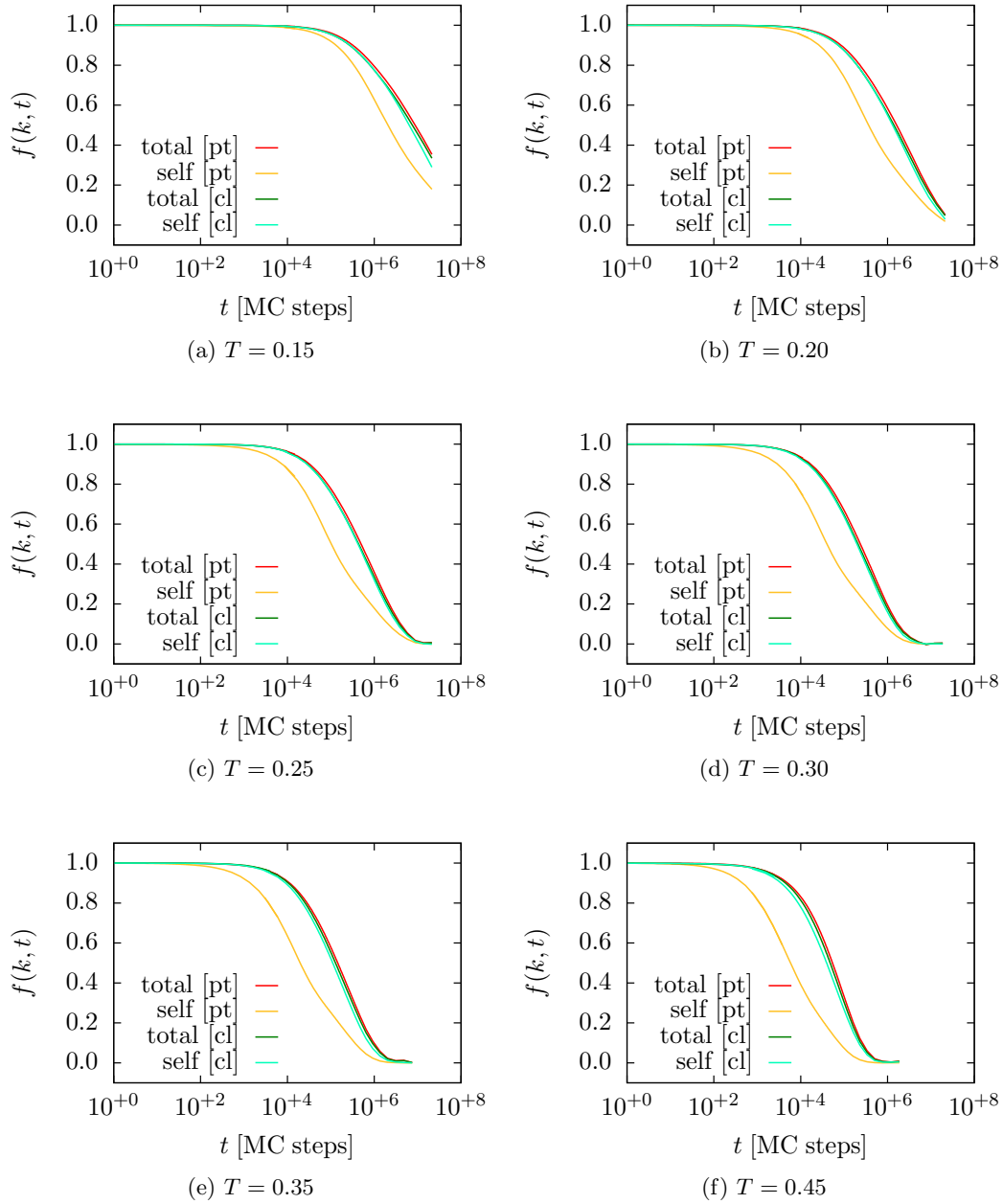


Figure 5.46: Comparison of the self and total intermediate scattering functions $f(k = 0.573, t)$ computed from particle- and cluster-coordinates, respectively, at a density of $\rho = 0.10$ and at different temperatures (as labeled).

the total-ISFs as well as the self-ISFs computed from cluster positions is less steep at $T = 0.35$ and $T = 0.30$ when compared to the respective ISFs at higher temperature. For $T \leq 0.35$ the total-ISFs and the self-ISFs computed from cluster positions do not

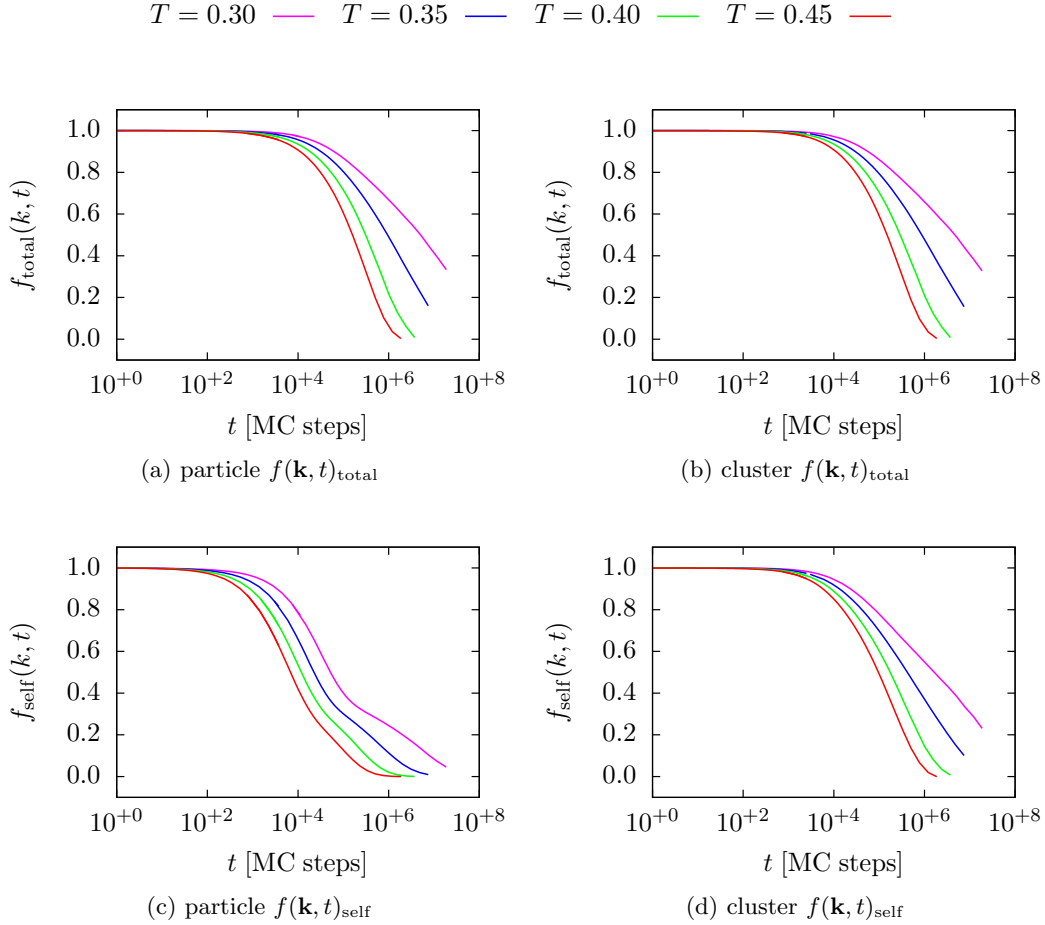


Figure 5.47: Intermediate scattering functions $f_{\text{total}}(k = 0.573, t)$ (top panels) and $f_{\text{self}}(k = 0.573, t)$ (bottom panels), using particles positions (left panels) and clusters positions (right panels) for the calculation. The ISFs are presented for a density of $\rho = 0.15$ at various temperatures (as labeled).

relax to zero within the duration of the simulation.

The relaxation of the self intermediate scattering function computed from the particle positions, on the other hand, set in earlier than those of the total intermediate scattering functions and the cluster- $f_{\text{self}}(k, t)$. Moreover for $T = 0.30$ and $T = 0.35$ the relaxation in the particle- $f_{\text{self}}(k, t)$ clearly takes place in two separate steps, with a plateau between them at a height of $\sim 30\%$. In contrast to the other ISFs, all self-ISFs computed from the particle positions at $k = 0.573$ do relax to zero, within the duration of the simulation.

Figure 5.48 shows a direct comparison of the total- and self-ISFs computed from the particle and cluster positions, respectively, at a density of $\rho = 0.15$.

Figure 5.48 shows, that the total-ISFs computed from the particle and the cluster positions are nearly identical for all investigated temperatures. The self-ISF computed

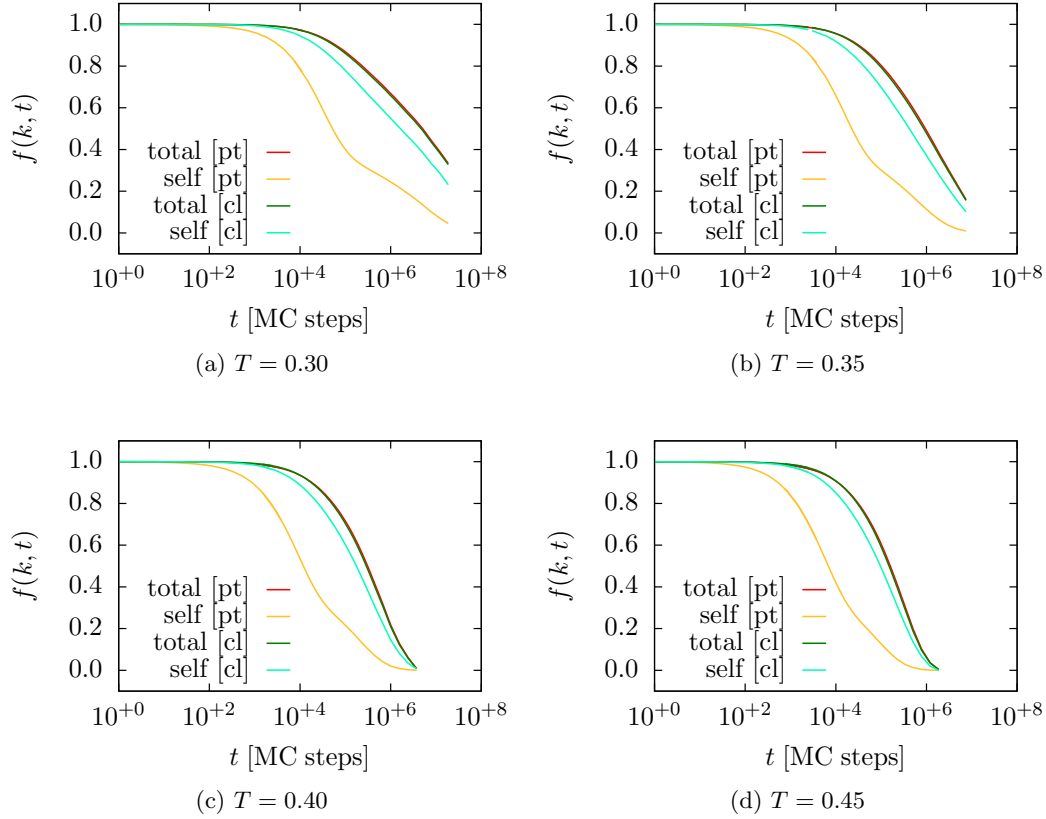


Figure 5.48: Comparison of the self and total intermediate scattering functions $f(k = 0.573, t)$ computed from particle- and cluster-coordinates, respectively, at a density of $\rho = 0.15$ and at different temperatures (as labeled).

from the cluster positions is qualitatively similar to the total-ISFs at the same T , however during the relaxation towards zero the value of the self-ISF computed from the cluster positions is noticeably ($< 20\%$) smaller than the value of the total-ISFs at the same temperature and time. The difference between the cluster- $f_{\text{self}}(k, t)$ and the total intermediate scattering functions becomes smaller with increasing temperatures. The significantly different behavior (faster, two step relaxation) of the self-ISF computed from the particle positions was already mentioned before.

$\rho = 0.20$:

Figure 5.49 shows the total-ISFs computed from the particle positions (top left panel) and cluster positions (top right panel), as well as the self-ISFs computed from the particle positions (bottom left panel) and cluster positions (bottom right panel) for a density of $\rho = 0.20$, at various temperatures.

As for $\rho = 0.10$ and $\rho = 0.15$, the self-ISF computed from the particle positions (bottom left panel) differs significantly from the other three ISFs shown in figure 5.49.

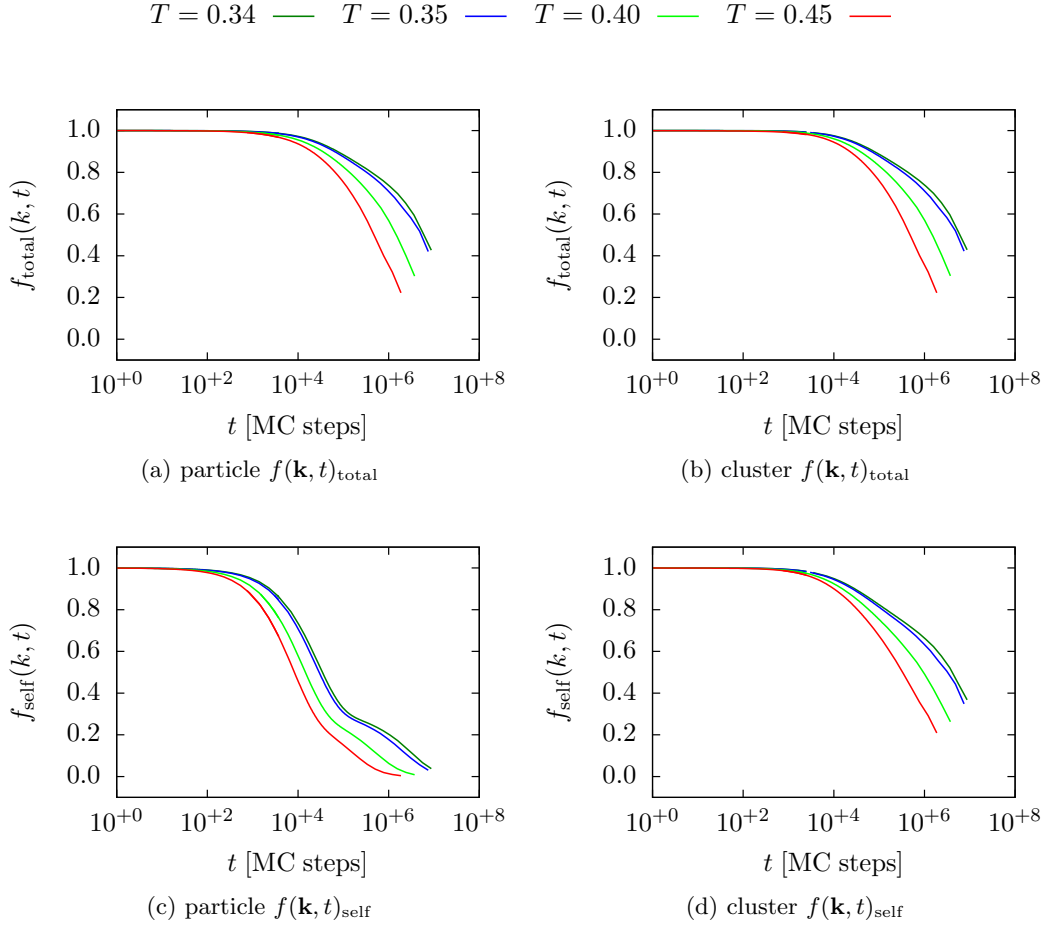


Figure 5.49: Intermediate scattering functions $f_{\text{total}}(k = 0.573, t)$ (top panels) and $f_{\text{self}}(k = 0.573, t)$ (bottom panels), using particles positions (left panels) and clusters positions (right panels) for the calculation. The ISFs are presented for a density of $\rho = 0.20$ at various temperatures (as labeled).

Compared to these other intermediate scattering functions, the particle self-ISF for $k = 0.573$, shows a two step relaxation with a plateau between these steps at $\sim 20\text{--}30\%$ height for all temperatures.

The total-ISFs (from particle and cluster positions), as well as the self-ISFs computed from the cluster positions on the other hand show a single step relaxation starting at a latter time than the one of the particle- $f_{\text{self}}(k, t)$, that do not reach zero during the simulations duration for any of the investigated temperatures.

Figure 5.50 shows a direct comparison of the total and self intermediate scattering functions computed from the particle and cluster positions, respectively, at a particle density of $\rho = 0.20$ and at various temperatures.

The total-ISFs computed from the particle and cluster positions, are nearly identical in figure 5.50. The self-ISF computed from the cluster positions is also quite similar

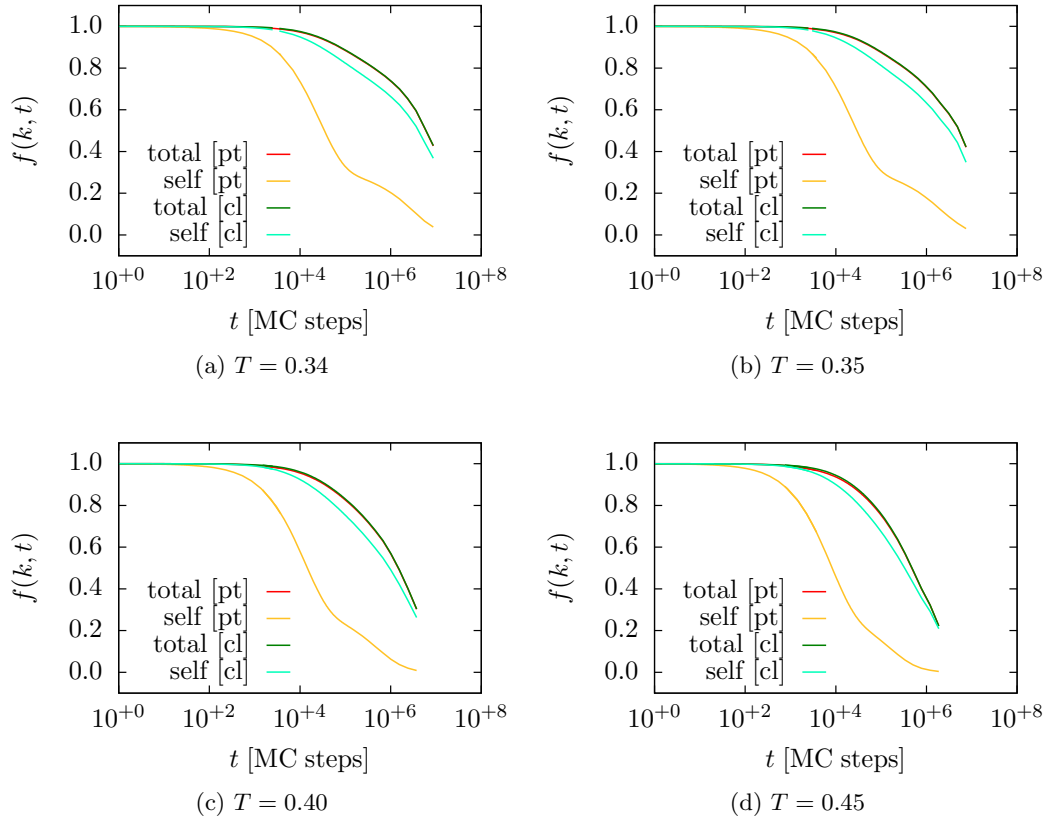


Figure 5.50: Comparison of the self and total intermediate scattering functions $f(k = 0.573, t)$ computed from particle- and cluster-coordinates, respectively, at a density of $\rho = 0.20$ and at different temperatures (as labeled).

to the total intermediate scattering functions. However, the cluster- $f_{\text{self}}(k, t)$ shows a faster relaxation than the total-ISFs at $\rho = 0.20$, with the difference between the cluster- $f_{\text{self}}(k, t)$ and the total intermediate scattering functions slightly decreasing with increasing temperature. The significantly different behavior of the self intermediate scattering function computed from the particle positions has already been mentioned before.

5.3 Quenched Annealed Systems

In this section, the influence of a disordered, porous matrix on a fluid with competing interactions is discussed. Some of the results presented here have been published already in [66].

5.3.1 Overview of investigated systems

In the present investigations, the matrix is represented by a quenched equilibrium configuration of the matrix particles (quenched component). The fluid particles (annealed component) are immersed into the matrix, after fixing the matrix particles. For additional information on the quenched-annealed concept, see [23, 24] and references therein.

In order to distinguish between excluded volume effects, and energetic effects of the matrix on the fluid particles, we investigate different combinations of matrix-matrix as well as fluid-matrix interactions. The interaction potentials, used in this case, where the hard sphere potential $\Phi_{\text{hc}}(r)$ and the Imperio-Reatto potential $\Phi_{\text{IR}}(r)$, which has been used as fluid-fluid interaction throughout the previous sections of this thesis. The three combinations ('cases') of matrix-matrix and fluid-matrix interactions used here, are listed in table 5.5 [66].

name	matrix-matrix interaction	fluid-matrix interaction	fluid-fluid interaction
case 1	Φ_{hc}	Φ_{hc}	Φ_{IR}
case 2	Φ_{hc}	Φ_{IR}	Φ_{IR}
case 3	Φ_{IR}	Φ_{IR}	Φ_{IR}

Table 5.5: The three different cases of interaction combinations, $\Phi_{\text{hc}}(r)$ represents the hard sphere interaction (see equation (2.1)), while $\Phi_{\text{IR}}(r)$ represents the Imperio-Reatto potential, given in equation (2.5).

In this section, the parameters of the Imperio-Reatto potential are the same as in [12, 17, 18, 19], namely $\epsilon_{\text{r}} = \epsilon_{\text{a}} = 4e/(4 - \sqrt{e})$, $R_{\text{a}} = \sigma$, $R_{\text{r}} = 2\sigma$, while the diameter of the hard sphere potential, mentioned above, is the same as the diameter of the hard core of the Imperio-Reatto potential (i.e. $\sigma_{\text{hc}} = \sigma_{\text{IR}} = \sigma$).

To keep the investigated systems in the cluster forming region of phase space, a temperature of $T = 0.50$ was used for all investigations of the current section. In case 3 the temperature of $T = 0.50$ was also used for the creation of the matrix configurations.

For each of the three interaction combinations in table 5.5, Monte Carlo simulations have been run along two paths in the $(\rho_{\text{m}}, \rho_{\text{f}})$ -plane, shown in figure 5.51 [66].

Along **path A**, the fluid density has been kept fixed at $\rho_{\text{f}} = 0.2$, while the matrix density was varied within the range $0.0 \leq \rho_{\text{m}} \leq 0.1$ (green line in figure 5.51). Along **path B**, the total density has been kept fixed at $\rho_{\text{m}} + \rho_{\text{f}} = 0.2$, with the matrix density varying within the range $0.0 \leq \rho_{\text{m}} \leq 0.1$ and thus resulting in a fluid density within $0.2 \geq \rho_{\text{f}} \geq 0.1$ (blue line in figure 5.51). The maximum total density of $\rho_{\text{m}} + \rho_{\text{f}} = 0.3$

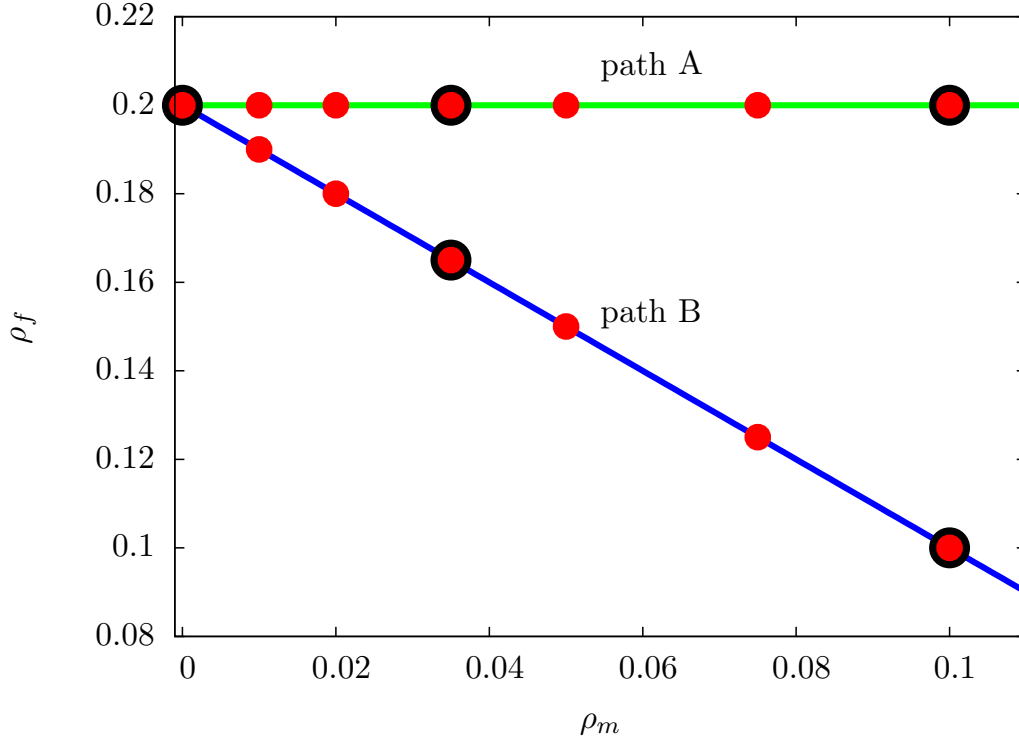


Figure 5.51: The red dots in the (ρ_f, ρ_m) -plane show the density combinations investigated in this thesis. Along **path A** (green line) the fluid density is fixed at $\rho_f = 0.2$, while along **path B** (blue line) the total density is fixed at $\rho_m + \rho_f = 0.2$. Along both paths the matrix density ρ_m is increased from 0.0 to 0.1.

(**path A**, $\rho_m = 0.1$) is still within the cluster forming region of phase space.

The Monte Carlo simulations of this sections were performed in the NVT -ensemble, using the lattice Monte Carlo method described in section 4.1.3, in addition to several other implementation details described in section 4.1.3. Supplemental parameters used in the Monte Carlo simulations of this section can be found in table 5.6.

parameter	symbol	value (range)
simulation box length	L	141.42σ
potential cutoff radius	r_c	17.2σ
particle displacement	Δ	0.6σ
number of matrix particles	N_m	0 – 2000
number of fluid particles	N_f	2000 – 4000
number of MC-steps	N_{steps}	1 000 000
number of MC-sweeps	N_{sweeps}	10 000

Table 5.6: Parameters for the Monte Carlo simulations used in this section.

For every state-point in the (ρ_m, ρ_f) -plane and every interaction combination, five simulation runs, using independent matrix configurations were performed. The resulting observables were obtained in a two-step averaging process. First each observable is averaged over 10 000 independent configurations of the fluid particles of each simulation run (10 000 MC-sweeps). After that, a second average is performed over the five equivalent, but independent, matrix configurations. Error bars, given in this section, are with respect to the average over the matrix configurations only.

5.3.2 Snapshots and Cluster Properties

Path A:

The discussion of the cluster snapshots will concentrate on **path A** ($\rho_f = 0.2$) first. Selected snapshots of state-points along this path are shown in figure 5.52. The top panel of figure 5.52, shows a snapshot of the pure fluid at $\rho = 0.2$ and $T = 0.50$, below that panel, the left column contains snapshots at low matrix density ($\rho_m = 0.035$), while the right column shows snapshots at the highest investigated matrix density ($\rho_m = 0.1$). The different interaction combinations (case 1, case 2 and case 3) are displayed in the different rows of figure 5.52 [66].

At low matrix density ($\rho_m = 0.035$), only a small effect of the matrix on the clusters is visible. From a visual inspection of the snapshots (left column of figure 5.52), the number of clusters as well as their size seems to be the same as in the pure fluid. This impression is confirmed by the development of the cluster particle number and radius of gyration R_g shown in figure 5.53, as well as the distribution of these properties shown in figure 5.54. These two figures indicate that the number of particles, as well as the radius of gyration is increased by less than 20% from the value of the pure fluid. Additionally, the maximum of the particle number distribution, as well as the maximum of the radius of gyration distribution is shifted by an even smaller amount than that. Keep in mind that the cluster particle number as well as the radius of gyration in this section is computed *including* the matrix particles, that fulfill the distance requirements for being part of the cluster (see section 4.3.1).

In case 1 (see top left panel of figure 5.52), the clusters of fluid particles form exclusively in regions left void by the matrix particles at low matrix density. The reduced height of the cluster particle number distribution (see red line in the top left panel of figure 5.54), originates from the large amount of single matrix particles found outside of the clusters. This height reduction is not present in the radius of gyration (R_g) distribution (top right panel of figure 5.54).

In case 2 however, the clusters form around the matrix particles, or at least include them to a large extent, due to the fluid-matrix interaction being of Imperio-Reatto type. Consequently, the height reduction of the cluster particle number distribution (see red line in the center left panel of figure 5.54), is not as pronounced as in case 1, while the radius of gyration distribution (see red line in the center right panel of figure 5.54), is wider than the one of case 1 and shifted towards larger clusters.

In case 3 (all interactions are of the Imperio-Reatto type), nearly all matrix particles are part of the clusters and it is assumed, that the matrix particles even act as nucleation centers for the fluid particles in this case. Case 3 also shows the least reduction in the peak height of the particle number distribution of all investigated cases (see the bottom left panel of figure 5.54), while the radius of gyration distribution is very similar to that of case 2 (see the bottom right panel of figure 5.54).

At the highest matrix density ($\rho_m = 0.1$) and with matrix-matrix, as well as fluid-matrix interactions being of the hard sphere type (case 1), round clusters form nearly exclusively in the regions left void by the matrix (see figure 5.52), an effect that can be observed at low matrix density already. Yet even at this high matrix density, matrix particles are rarely found inside the clusters formed by the fluid. However matrix

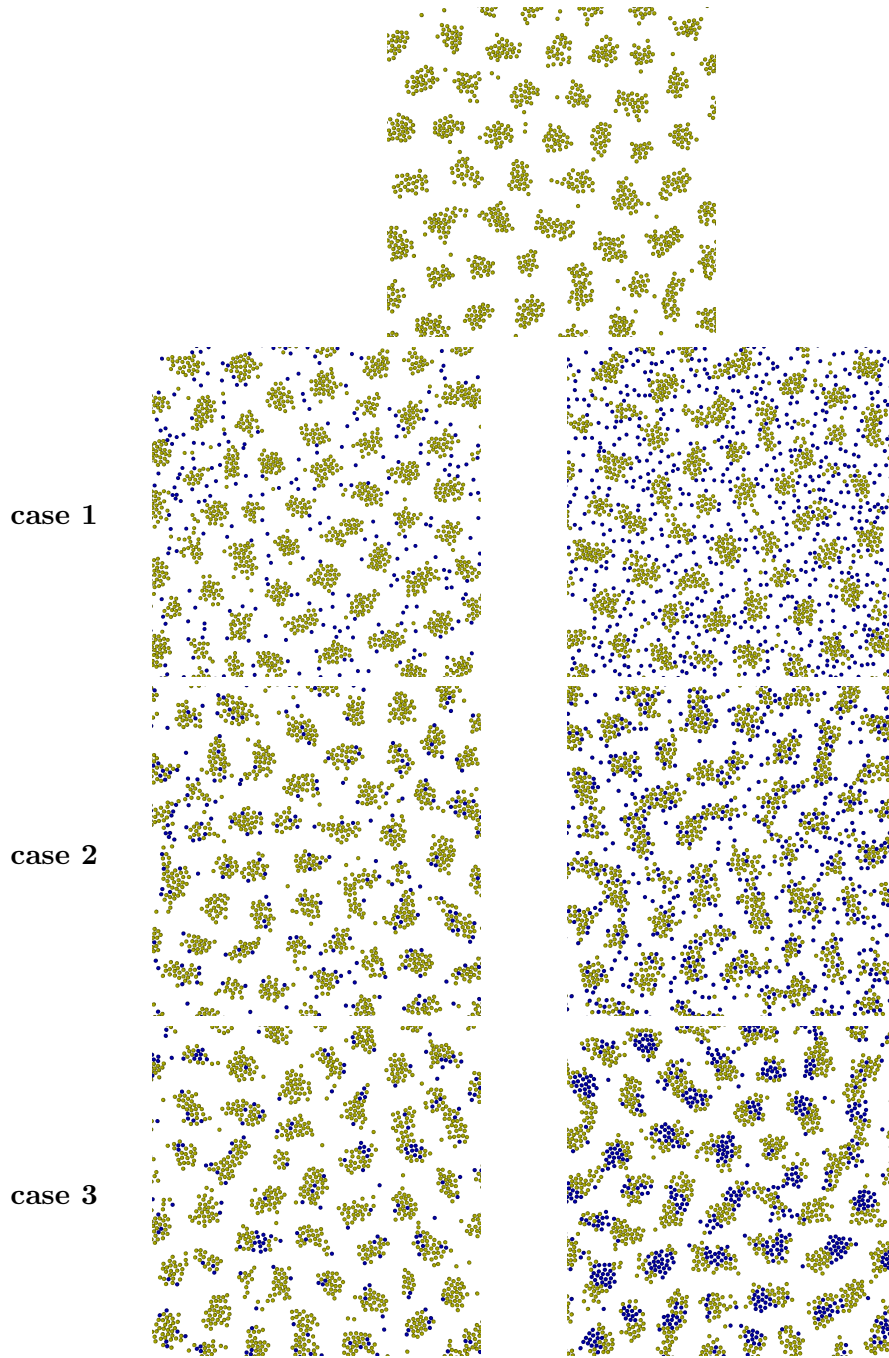


Figure 5.52: Top panel: snapshot of the equilibrated fluid at $\rho_f = 0.200$ and $T = 0.50$. The other panels represent snapshots of systems located in the (ρ_f, ρ_m) -plane along **path A** (see figure 5.51). Matrix particles are colored in blue, while the fluid particles are depicted in yellow. The cases (1-3) in the different rows represent the different combinations of matrix-matrix and fluid-matrix interactions, see table 5.5 for details. The panels on the left side represent systems with $\rho_f = 0.2$, $\rho_m = 0.035$ and $T_f = T_m = 0.50$, whereas the panels on the right side represent systems with $\rho_f = 0.2$, $\rho_m = 0.1$ and $T_f = T_m = 0.50$.

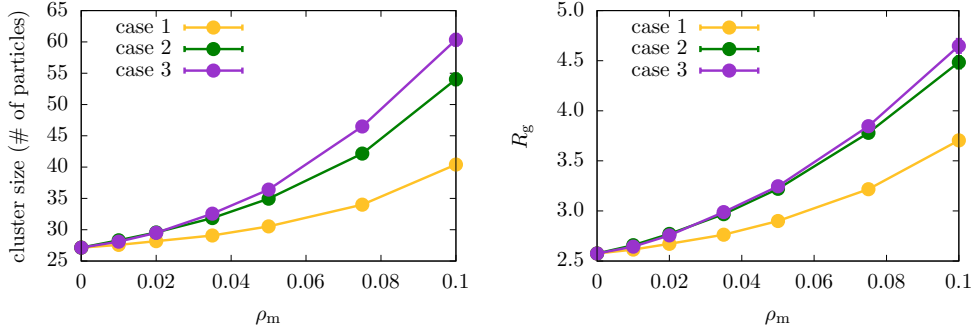


Figure 5.53: Average cluster size in terms of particle number (left), and the radius of gyration (right) versus the matrix density along **path A** for the three investigated combinations of matrix-matrix and fluid-matrix interactions (see table 5.5 for details of the interactions).

particles at the border of the clusters are more common here, than at lower matrix densities. As a consequence, the increase of the average cluster size, as well as the increase in the radius of gyration is smaller than in the two other cases (see figure 5.53). At high matrix density in case 2, the clusters include the matrix particles, just as seen at low matrix density under the same conditions. However, different to the low matrix density scenario, the clusters tend to have slightly elongated shapes. Due to the inclusion of several matrix particles into the clusters, the increase in cluster size and radius of gyration is much higher than in case 1 (see left and right panel of figure 5.53 respectively). The increase in cluster size can already be recognized in the snapshots (see center right panel of figure 5.52).

In case 3, practically all matrix particles are included into the clusters at high matrix density. It is clearly visible from the snapshot in the bottom right panel of figure 5.52, that the size of the clusters has increased. Additionally the elongated shape of the clusters is clearly visible in the snapshot. This behavior is also reflected in by the numerical values for the cluster particle number and the radius of gyration (see figure 5.53). There is also a pronounce tail visible in the cluster particle number distribution of this case at high matrix density (see bottom left panel of figure 5.54).

Path B:

As already stated in section 5.3.1, **path B** consists of states with a fixed total density of $\rho_m + \rho_f = 0.2$. While the matrix density is increased along that path from $\rho_m = 0.0$ to 0.1 the fluid density is decreased from $\rho_f = 0.2$ to 0.1.

Similar as in figure 5.52, the top panel of figure 5.55 shows a snapshot of the pure fluid ($\rho_m = 0.0$) at a temperature of $T = 0.50$, while the left column shows snapshots at low matrix density ($\rho_m = 0.035$, $\rho_f = 0.165$) and the right column shows snapshots at high matrix density ($\rho_m = 0.1$, $\rho_f = 0.1$), for the different combinations of matrix-matrix and fluid-matrix interactions (cases 1-3) [66].

With the matrix-matrix, as well as the fluid-matrix interaction being of the hard sphere

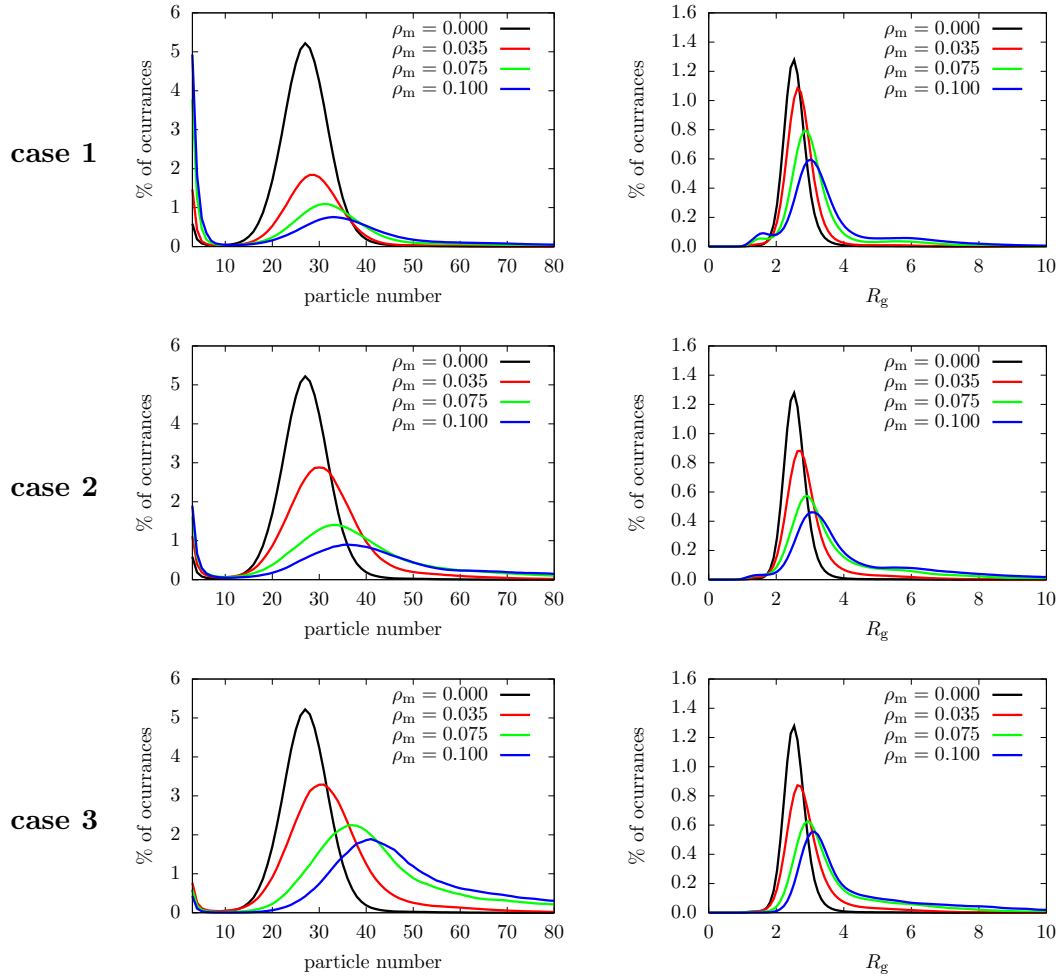


Figure 5.54: Cluster size distribution (right column) and distribution of the radius of gyration (left column) for different matrix densities as labeled for the different cases of matrix-matrix and fluid-matrix interactions (as defined in table 5.5) along **path A**.

type (case 1), the fluid clusters form in the space left void by the matrix particles at low matrix density. The size of the clusters seems to be close to the one of the pure fluid, from visual inspection of snapshots only (see top left panel of figure 5.55). Since this state point is located close to the respective low matrix density point of **path A**, it is not surprising to see similar effects here. The cluster particle number distribution (red curve in the left panel of figure 5.57) shows a pronounced reduction in the height of the peak, due to the large number of matrix particles that are not associated with any cluster, just as in case 1 of **path A**. However in contrast to case 1 of **path A**, the average cluster particle number has decreased by about 12%, while the radius of gyration remained nearly constant (see figure 5.56). Keep in mind that the cluster particle number as well as the radius of gyration in this section is computed *including* the matrix particles, that fulfill the distance requirements for being part of the cluster

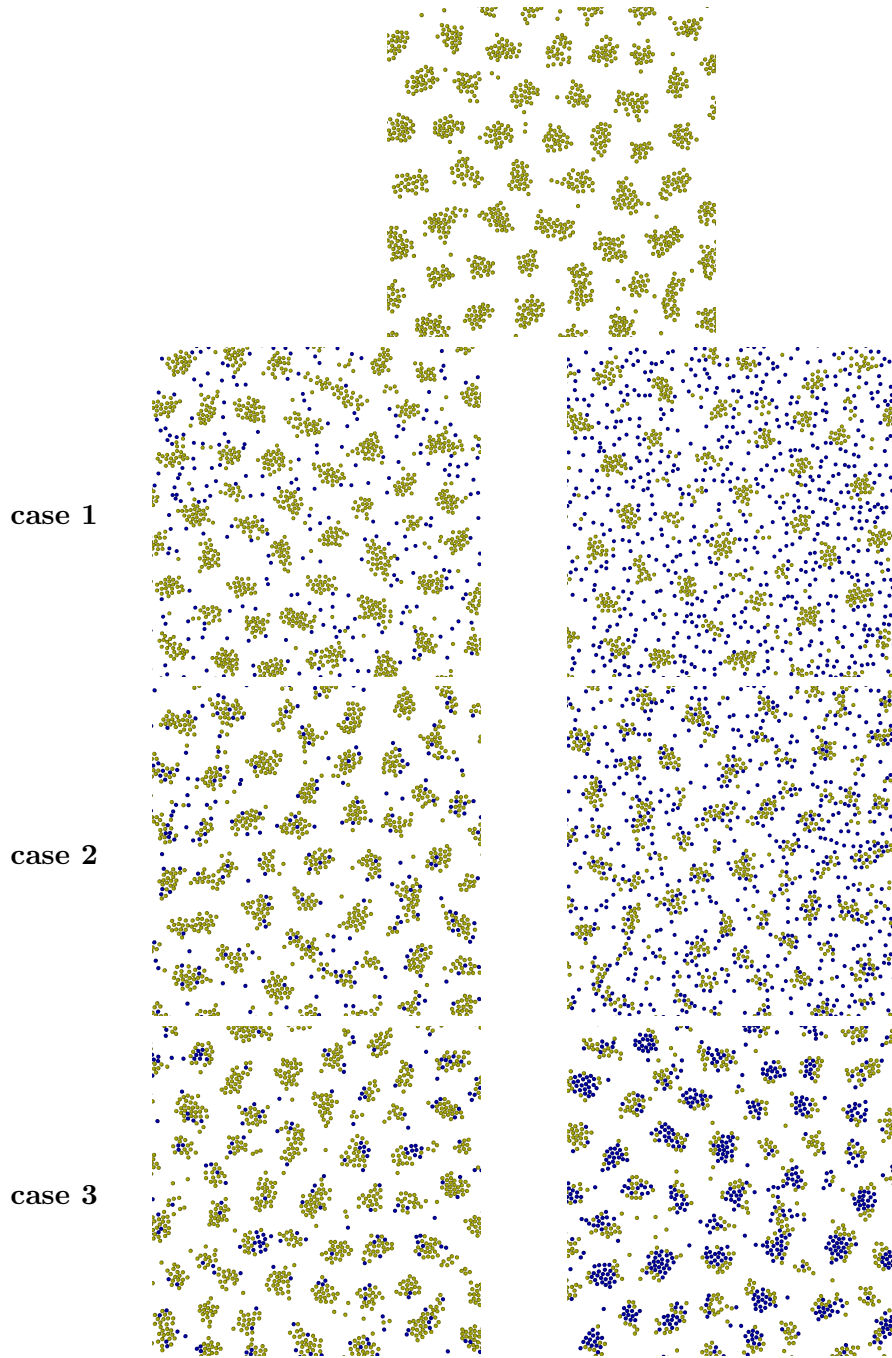


Figure 5.55: Top panel: snapshot of the equilibrated fluid at $\rho_f = 0.2$ and $T = 0.50$. The other panels represent snapshots of systems located in the (ρ_f, ρ_m) -plane along **path B** (see figure 5.51). Matrix particles are colored in blue, while the fluid particles are depicted in yellow. The cases (1-3) in the different rows represent the different combinations of matrix-matrix and fluid-matrix interactions, see table 5.5 for details. The panels on the left side represent systems with $\rho_f = 0.165$, $\rho_m = 0.035$ and $T_f = T_m = 0.50$, whereas the panels on the right side represent systems with $\rho_f = 0.1$, $\rho_m = 0.1$ and $T_f = T_m = 0.50$.

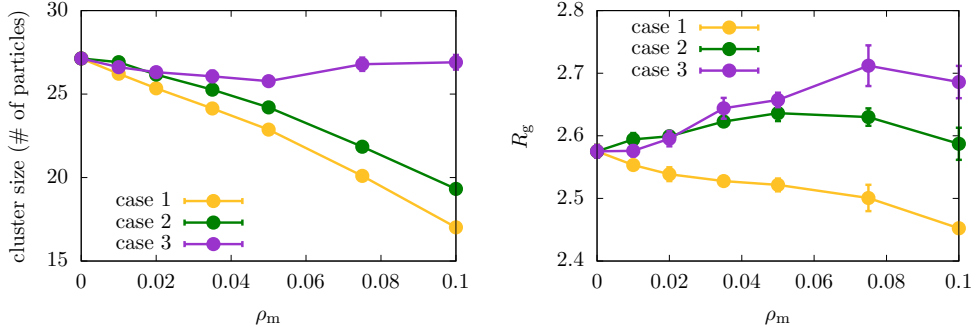


Figure 5.56: Average cluster size in terms of particle number (left), and the radius of gyration (right) versus the matrix density along **path B** for the three investigated combinations of matrix-matrix and fluid-matrix interactions (see table 5.5 for details of the interactions).

(see section 4.3.1).

The snapshot of case 2 (center left panel of figure 5.56) shows that several matrix particles have become part of the clusters at low density, similar as the corresponding case along **path A**. Apart from that, the clusters themselves look quite like the clusters in case 1 of **path B** or the clusters of the pure fluid. Figure 5.56 shows that the number of cluster particles decreased, compared to the pure fluid however, due to the inclusion of the matrix particles into the clusters, to a lesser extent than in case 1 of **path B**. As in the previous case the radius of gyration is essentially constant (case 1 of **path B**: $\sim 2\%$ decrease; case 2 of **path B**: $\sim 2\%$ increase). Similar to case 2 of **path A** the reduction of the peak in the cluster particle distribution is not as pronounced as in case 1 due to the inclusion of the matrix particles into the clusters.

The snapshot of case 3 at low matrix density (bottom left panel of figure 5.56) looks similar to the snapshot of case 2, however the matrix particles are included into the clusters to a larger extent. In fact, nearly all of the matrix particles are part of the clusters, just as in case 3 of **path A** at low matrix density. Because of the virtually complete inclusion of the matrix particles into the clusters, the cluster particle number is nearly the same as in the pure fluid, while the radius of gyration has slightly increased (see left panel of figure 5.56). The distribution of the cluster particle number as well as the distribution of the radius of gyration at low ρ_m look quite similar than in case 2, as can be seen in the bottom panels of figure 5.57.

At high matrix density $\rho_m = 0.1$ ($\rho_f = 0.1$), the difference in cluster size compared to the pure fluid is clearly visible in case 1. The much smaller clusters still populate the void space between the matrix particles (see top right panel of figure 5.55). The development of the cluster particle number as function of the matrix density, shown in the left panel of figure 5.56, confirms that impression, the size of the clusters is reduced by as much as $\sim 40\%$ compared to the value of the pure fluid. Additionally the peak of the cluster particle distribution, shown as the blue curve in the top left panel of figure 5.57, is shifted towards lower particle numbers. The radius of gyration is also

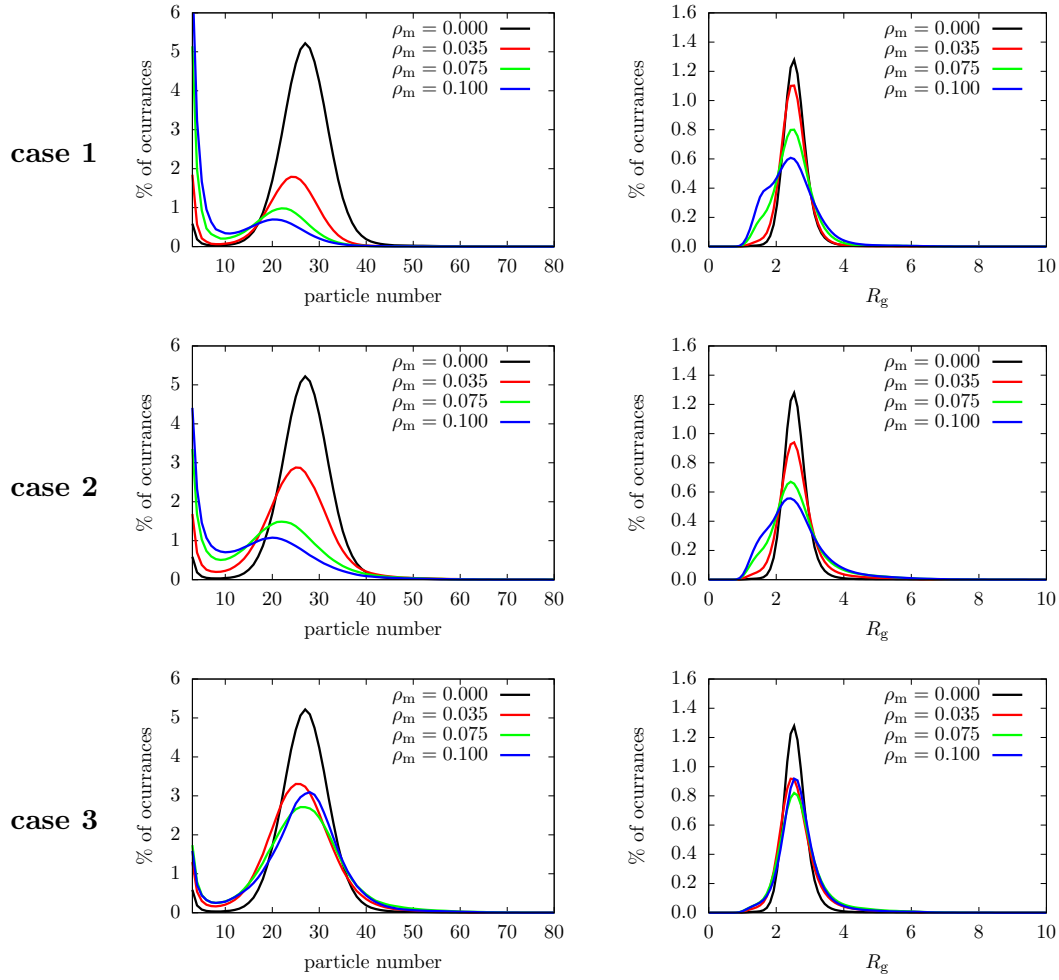


Figure 5.57: Cluster size distribution (right column) and distribution of the radius of gyration (left column) for different matrix densities as labeled for the different cases of matrix-matrix and fluid-matrix interactions (as defined in table 5.5) along **path B**.

reduced, as can be seen from the right panel of figure 5.56, however to a lesser extent than the cluster particle number. The radius of gyration distribution, displayed as the blue curve in the top right panel of figure 5.57, shows a shoulder of the peak towards smaller values of R_g for high matrix densities ($\rho_m \geq 0.075$).

In case 2, the clusters, built by the fluid particles, incorporate the matrix particles at high matrix densities; however, due to the unfavorable numerical ratio between fluid and matrix entities, particles of the matrix are absorbed into the clusters to a much lesser extent when compared to low matrix densities in **path B** or all matrix density in **path A**. The resulting clusters are therefore visibly smaller than the ones in the pure fluid. The left panel of figure 5.56 shows that the average cluster particle number is reduced to an extent similar to case 1, when increasing the matrix density. On the other hand, the radius of gyration is essentially constant in case 2 along **path B**, when

increasing the matrix density. The peak in the radius of gyration distribution (blue curve in the center right panel of figure 5.57), shows a similar shoulder as in case 1, while the peak in the cluster particle number is rather small (blue curve in the center left panel of figure 5.57), giving rise to the impression, that the clustering of the fluid particles is suppressed in this case at high matrix densities.

The snapshot of the high matrix density in case 3 (bottom right panel of figure 5.55), shows clusters that incorporate nearly all the available matrix particles in contrast to case 2. This is only possible, because the matrix particles already form small clusters themselves, due to the short-range attractive long-range repulsive type of the matrix-matrix interaction. In contrast to case 3 of **path A** the clusters do not show elongated shapes and in fact look quite similar as the ones of the pure fluid. This impression is confirmed by the fact, that the cluster particle number remains nearly constant over the entire range of matrix densities, as can be seen from the left panel of figure 5.56. The radius of gyration depicted in the right panel of figure 5.56 shows also only a slight increase compared to the value of R_g of the pure fluid. Surprisingly, the cluster particle number distribution as well as the radius of gyration distribution, shown in figure 5.57, seem to be nearly independent of the matrix density, but do not match the height of the respective distribution of the pure fluid.

5.3.3 Structure functions

In order to investigate the structure of the fluid on a more quantitative level, several structure functions of the system were calculated: the static structure factors and the radial distribution functions. These structure functions are depicted and discussed in this section.

Fluid-fluid structure factor

Our discussion starts with the fluid-fluid structure factor, which can be computed via

$$S_{\text{ff}}(k) = \frac{1}{N_{\text{f}}} \overline{\langle \rho_{\text{f}}(\mathbf{k}) \rho_{\text{f}}(-\mathbf{k}) \rangle}, \quad (5.15)$$

where the Fourier transform of the fluid density $\rho_{\text{f}}(\mathbf{k})$ is given by

$$\rho_{\text{f}}(\mathbf{k}) = \sum_{j=1}^{N_{\text{f}}} \exp(i\mathbf{k} \cdot \mathbf{r}_j). \quad (5.16)$$

In equation (5.15) N_{f} denotes the number of fluid particles, while $\langle \dots \rangle$ stands for the thermal average over the degrees of freedom of the fluid and $\overline{\dots}$ expresses the average over different matrix realizations. The positions of the fluid particles are given by the \mathbf{r}_j in equation (5.16). Note the average over the different matrix realizations in equation (5.16) is missing in equation (3.94) of chapter 3.

The fluid-fluid structure factors $S_{\text{ff}}(k)$ of cases 1-3 of **paths A** and **B** are given in figure 5.58, with the structure factors of **path A** (constant ρ_{f}) shown in the left column and the structure factors of **path B** (constant $\rho_{\text{f}} + \rho_{\text{m}}$) presented in the right column. The structure factor of the pure fluid ($\rho = 0.2$) is also displayed for reference as a black line in all panels.

All fluid-fluid structure factors $S_{\text{ff}}(k)$ discussed in this section have two features in common, which are also observed in the structure factors of the pure fluid (see figure 5.9):

- The presence of a pronounced and narrow main peak at $k \approx k_{\text{c}} = 0.573$, the wave-number correlated to the average cluster-cluster distance.
- The appearance of a short, but wide peak at $k \approx 6.2$, which can be attributed to the hard core contact distance of the fluid particles.

From these two peaks it can be deduced, that the average inter-cluster distance in these systems is a factor of ~ 11 larger, than the inter-particle distance at hard core contact. Figure 5.58 shows, that the height of the main peak of the fluid-fluid structure factor at $k \approx 0.573$ decreases with increasing matrix density ρ_{m} , while the ρ_{m} -dependence of the height of the second peak at $k \approx 6.2$ is rather weak. To determine this tendency more clearly the main peak is also shown in the inset in all panels of figure 5.58, using an enlarged horizontal axis. Note that the poor k -resolution here and in the subsequent figures, originates from the fact, that the accessible k -vectors for the calculation have to be compatible with the periodic boundary conditions of the finite simulation box.

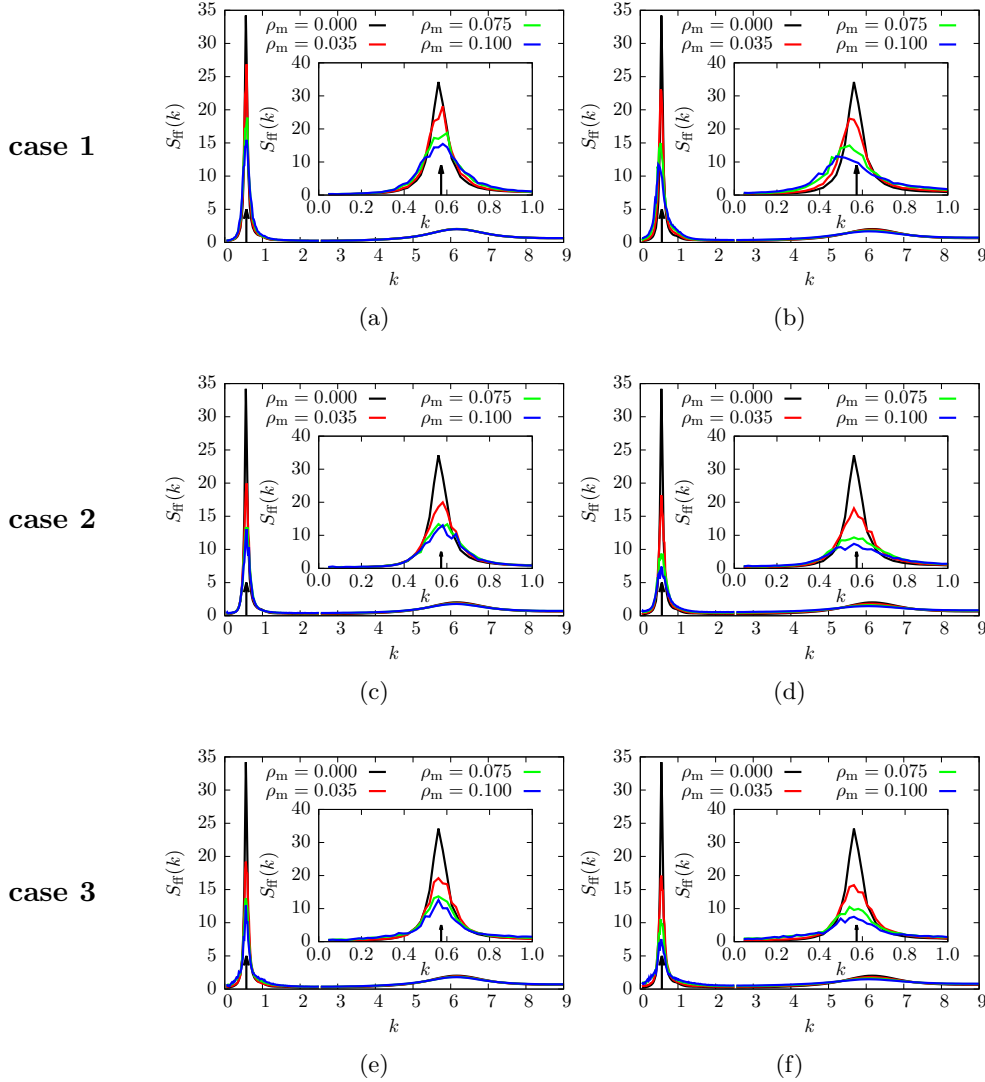


Figure 5.58: Static structure factors for the fluid-fluid correlations $S_{\text{FF}}(k)$ as function of k , of systems along **path A** (left column) and **path B** (right column) in the (ρ_f, ρ_m) -plane [66]. Different rows correspond to different combinations of matrix-matrix and fluid-matrix interactions (see table 5.5 for details). Different lines in the graphs represent different values of the matrix density ρ_m (as labeled), while the insets show an enlarged view of the low- k range.

The details of the development of the two peaks, featured by the fluid-fluid structure factor, as a function of the matrix density, will be discussed in more detail, starting with systems along **path A** in the (ρ_f, ρ_m) -plane.

Along **path A**, the static correlations at $k \approx 0.573$ are very pronounced at the highest matrix density in case 1; they decay faster in case 2 and case 3 with increasing matrix density, due to the different interaction of the fluid with the matrix in these cases. The

correlations at $k \approx 6.2$ in case 1, do not show any dependence on the matrix density along **path A**, while there is a slight decrease of these correlations in case 2 and case 3, when increasing the matrix density (see left panels of figure 5.58).

Along **path B**, there is a marked shift of the small- k peak in case 1 towards smaller wave-numbers, when increasing the matrix density ρ_m . Translated into real space coordinates this means an increase in distance between the clusters, which can be observed in the snapshot in the top left panel of figure 5.55. The shift of the cluster-cluster correlation peak at $k \approx 0.573$ towards smaller wave-numbers is *not* present in cases 2 and 3. The snapshots at the two bottom rows of figure 5.55 show indeed clusters with approximately the same spacing as the ones of the pure fluid, depicted in the top panel of the same figure. Similar to the fluid-fluid structure factors along **path A**, the height of the low- k peak decreases in cases 2 and 3 faster than in case 1. A possible explanation for these effects is that due to the inert matrix (case 1), the fluid is able to form well defined clusters, leading to a slower decrease of the low- k peak in $S_{ff}(k)$. However, because of the spatial constraints present at higher matrix density, the distance between these clusters increases. In cases 2 and 3, on the other hand, the inclusion of matrix particles into the clusters leads to a faster decrease of the low- k peak in $S_{ff}(k)$, but also results in a (nearly) constant cluster spacing when increasing the matrix density.

Connected structure factor

The connected structure factors $S_c(k)$, presenting information about the correlation between the fluid particles exclusively mediated by other fluid particles, is computed via

$$S_c(k) = \frac{1}{N_f} \overline{\langle \delta\rho_f(\mathbf{k}) \delta\rho_f(-\mathbf{k}) \rangle}, \quad (5.17)$$

where

$$\delta\rho_f(\mathbf{k}) = \rho_f(\mathbf{k}) - \langle \rho_f(\mathbf{k}) \rangle. \quad (5.18)$$

As before the thermal average over the degrees of freedom of the fluid is represented by $\langle \dots \rangle$ in equations (5.17) and (5.18), while the average over the different matrix configurations is represented by $\overline{\dots}$. Further, N_f denotes the number of fluid particles and $\rho_f(\mathbf{k})$ stands for the Fourier transform of the fluid density given by equation (5.16). The resulting connected structure factors $S_c(k)$ are shown in figure 5.59, where the left panels represent states along **path A** (of figure 5.51), while the right panels represent states along **path B**. As in the case of $S_{ff}(k)$ the structure factor of the pure fluid is shown for reference. Note that in the case of a pure fluid, the fluid-fluid structure factor and the connected structure factor are identical.

The development of the second peak of $S_c(k)$ at $k \approx 6.2$ is essentially the same as in the fluid-fluid structure factors, thus it will not be discussed here.

The first peak of the connected static structure factor $S_c(k)$ at $k \approx 0.573$ on the other hand, shows a more pronounced reduction of its height for $\rho_m > 0$ when compared to

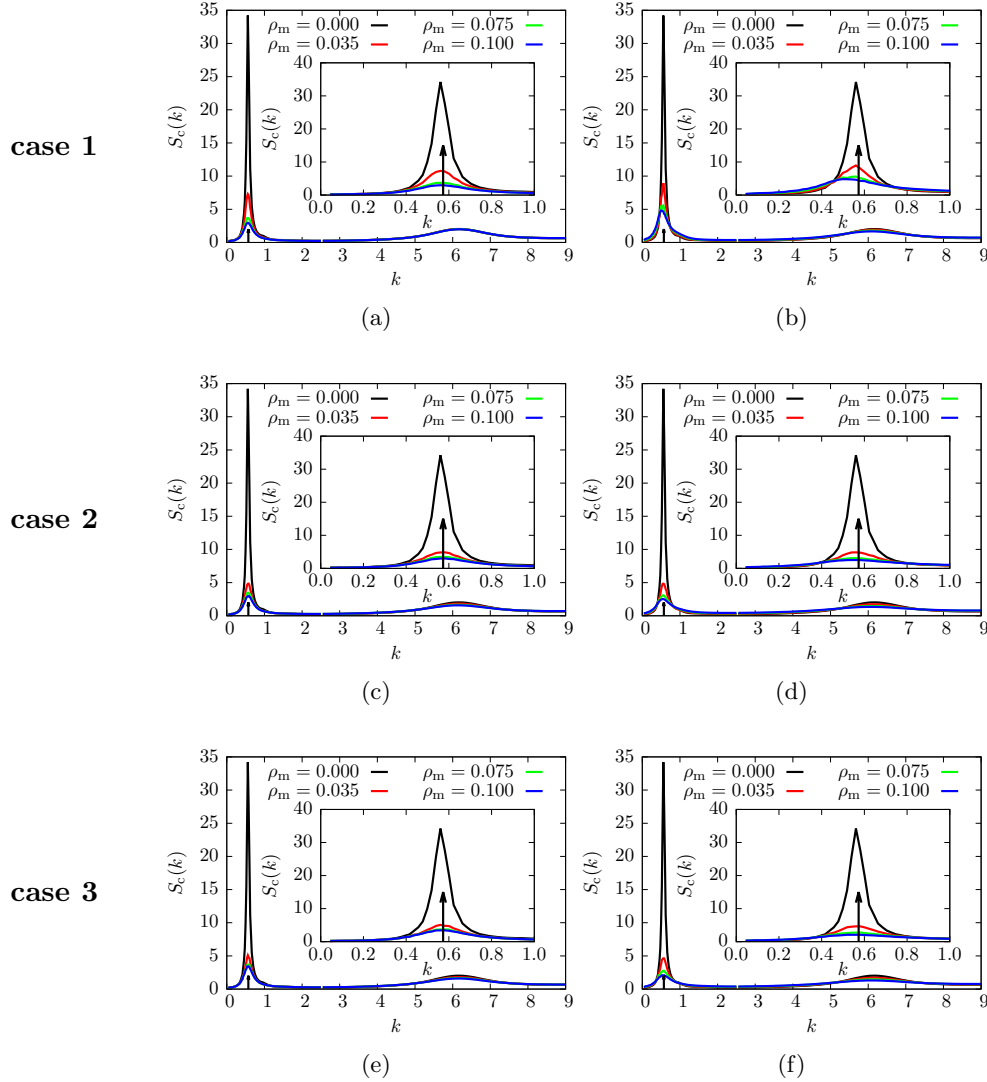


Figure 5.59: Connected static structure factors $S_c(k)$ as function of k , of systems along **path A** (left column) and **path B** (right column) in the (ρ_f, ρ_m) -plane [66]. Different rows correspond to different combinations of matrix-matrix and fluid-matrix interactions (see table 5.5 for details). Different lines in the graphs represent different values of the matrix density ρ_m (as labeled), while the insets show an enlarged view of the low- k range.

the first peak of $S_{ff}(k)$ of the same path and case. Since $S_c(k)$ only exhibits correlations mediated by fluid particles, the effect of increasing matrix density on the peak height is much stronger than for the fluid-fluid static structure factor at all interaction combinations (cases).

As for the fluid-fluid static structure factor $S_{ff}(k)$, the reduction in the height of the first peak of $S_c(k)$ is more pronounced in cases 2 and 3 (fluid-matrix interaction of Imperio-

Reatto type), when comparing to case 1 (fluid-matrix interaction of hard sphere type).

Fluid-matrix structure factor

The fluid-matrix structure factor, $S_{\text{fm}}(k)$ is computed via

$$S_{\text{fm}}(k) = \frac{1}{\sqrt{N_{\text{f}} N_{\text{m}}}} \overline{\langle \rho_{\text{f}}(\mathbf{k}) \rho_{\text{m}}(-\mathbf{k}) \rangle}, \quad (5.19)$$

with N_{f} and N_{m} being the number of fluid and matrix particles, respectively, and the Fourier transform of the matrix density given by

$$\rho_{\text{m}}(\mathbf{k}) = \sum_{j=1}^{N_{\text{m}}} \exp(i\mathbf{k} \cdot \mathbf{r}_j); \quad (5.20)$$

$\rho_{\text{f}}(k)$ has already been defined in equation (5.16).

As in equation (5.15), $\langle \dots \rangle$ denotes thermal average over the degrees of freedom of the fluid and $\overline{\dots}$ represents the average over different matrix realizations. Obviously \mathbf{r}_j stands for the positions of the matrix particles in equation (5.20).

The features of the fluid-matrix structure factor are qualitatively similar along **paths A** and **B** and even do agree quite well on a quantitative level. Thus the structure factors obtained along both paths will be discussed together, differences will be mentioned only when required.

The most prominent feature of the fluid-matrix structure factor in case of the non interacting matrix (case 1, see top row of figure 5.60), is the negative correlation at $k \approx k_{\text{c}} = 0.573$. This negative correlation is attributed to the fact, that the clusters only form in spaces left void by the matrix. Moreover the positive correlations at $k \approx 6.2$, are considerably less pronounced in case 1 of **path A** and nearly absent in **path B**, when compared to the other two cases. This can be traced back to the combination of matrix-matrix and fluid-matrix interactions; while the hard-sphere matrix-matrix interaction leads to a homogeneous distribution of the matrix particles, the hard-sphere fluid-matrix interaction in combination with the Imperio-Reatto fluid-fluid interaction impedes the adsorption of fluid particles to the matrix.

In contrast to case 1, we observe a positive correlation for case 2 at $k \approx k_{\text{c}} = 0.573$, which can be explained by the inclusion of the matrix particles into the clusters due to the attraction of the fluid-matrix interaction at small distances. There is also a pronounced positive correlation at $k \approx 6.2$ in this case (see second row of figure 5.60), which can be attributed to the fluid-matrix interactions attraction at small particle separations.

Case 3, shows a distinct positive correlation at $k \approx k_{\text{c}} = 0.573$ as well as a positive correlation at $k \approx 6.2$ (see bottom row of figure 5.60). Note that the vertical axis of the panels of case 3 in figure 5.60 covers twice the range compared to the vertical axis of the panels of cases 1 and 2 of the same figure. The peak at $k \approx k_{\text{c}} = 0.573$ is much higher in case 3 compared to case 2, which can be attributed to the higher localization of the cluster due to the IR-type of the matrix-matrix interaction.

Moreover the peak at $k \approx k_{\text{c}} = 0.573$ shows distinct, negative side peaks for wavenumbers larger and smaller than k_{c} . These side-peaks are probably induced by the matrix

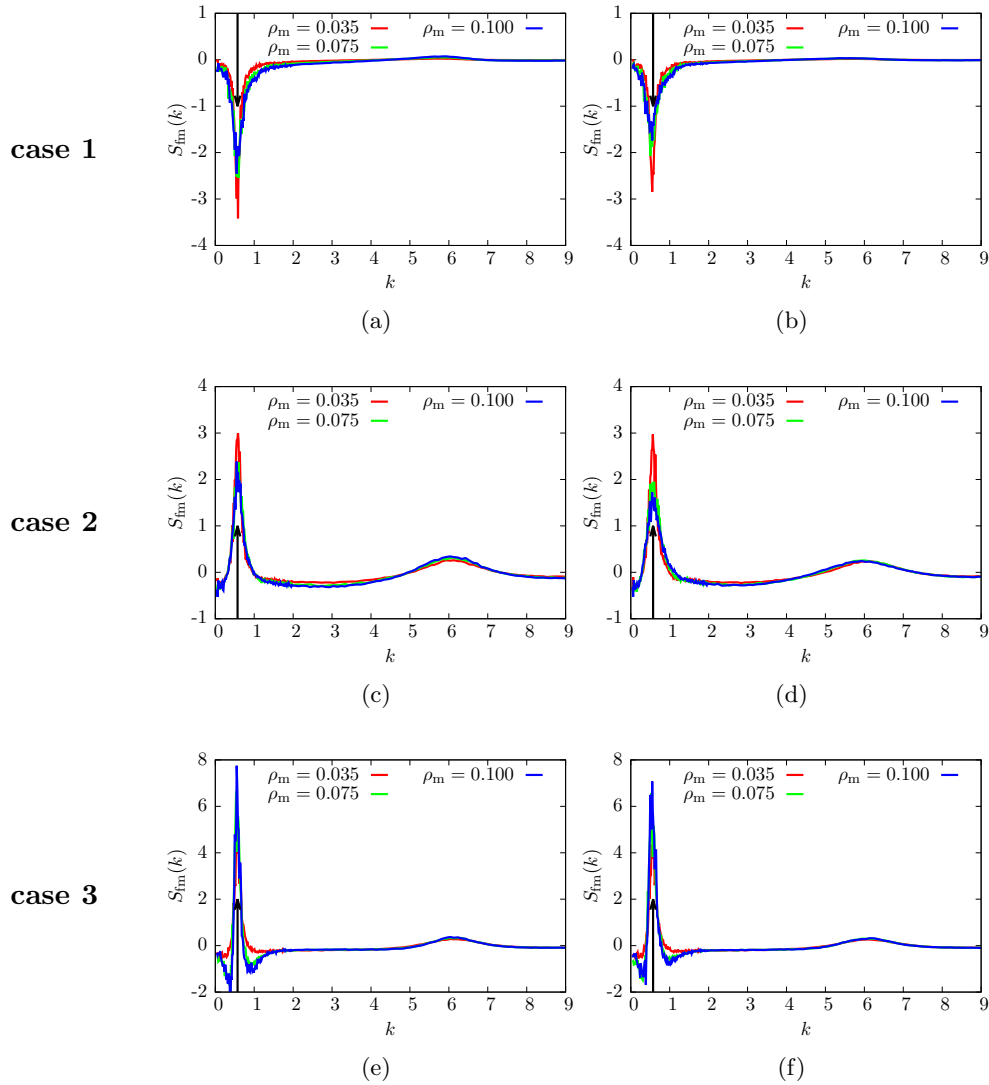


Figure 5.60: Static structure factors for the fluid-matrix correlations $S_{\text{fm}}(k)$ as function of k , of systems along **path A** (left column) and **path B** (right column) in the (ρ_f, ρ_m) -plane. Different rows correspond to different combinations of matrix-matrix and fluid-matrix interactions (see table 5.5 for details). Different lines in the graphs represent different values of the matrix density ρ_m (as labeled).

occupying the ideal clustering spots forcing the fluid to attach to the nucleation sites formed by the matrix at not that ideal positions.

The correlation at $k \approx 6.2$ on the other hand is as pronounced as in case 2 (mind the different vertical ranges of the panels).

Fluid-fluid radial distribution function

The fluid-fluid radial distribution function can be computed via

$$g_{\text{ff}}(r) = \frac{A}{N_{\text{f}}(N_{\text{f}} - 1)} \left\langle \overline{\sum_{i=1}^{N_{\text{f}}} \sum_{\substack{j=1 \\ i \neq j}}^{N_{\text{f}}} \delta(\mathbf{r} - \mathbf{r}_j + \mathbf{r}_i)} \right\rangle, \quad (5.21)$$

with A denoting the area as the 2-dimensional equivalent to the volume, N_{f} representing the number of fluid particles, while \mathbf{r}_i and \mathbf{r}_j are the position of the fluid particles. Note the average over the different matrix realizations in equation (5.21) is missing in equation (3.91) of chapter 3.

As in the figures for the structure factor, the left panels of figure 5.61 show the radial distribution functions of systems along **path A** (c.f. figure 5.51), while the panels in the right column show the radial distribution functions of systems along **path B**.

From a qualitative point of view, the six panels of figure 5.61 look very similar. Features common to all fluid-fluid radial distribution functions of the investigated quenched-annealed systems are:

- The existence of a pronounced peak at $r = 1.0$ with a sudden drop to zero at the hard sphere diameter and at least two identifiable side peaks at $r \approx 2$ and $r \approx 3$. This series of peaks is associated to the structure factor peak at $k \approx 6.2$.
- The presence of a long range peak at $r \approx 12$, which shows the clustering of the fluid particles and which is related to the peak in $S_{\text{ff}}(k)$ at $k_{\text{c}} = 0.573$.

The peak in $S_{\text{ff}}(k)$ at $r \approx 12$ slightly decreases in height for all combinations of matrix-matrix and fluid-matrix interactions investigated with increasing matrix density, irrespective of the path (A or B). In contrast, the short range correlations (low- r peaks) are independent of the matrix density in case 1 along **path A** (ρ_{f} constant, matrix-matrix and fluid-matrix interactions of hard sphere type), while the height of these peaks increases in case 1 along **path B** ($\rho_{\text{f}} + \rho_{\text{m}}$ constant) with increasing matrix density. For all other combinations of matrix-matrix and fluid-matrix interactions the peak height of the low- r peaks decreases with increasing the matrix density ρ_{m} regardless of the path.

A direct comparison of $g_{\text{ff}}(r)$ between the different types of interactions (case 1-3) at the same matrix density ρ_{m} shows that the decrease in height of the peak of the radial distribution at $r \approx 12$ is similar for all three interaction combinations along **path A**. Along **path B**, however, the peak of $g_{\text{ff}}(r)$ at $r \approx 12$ in case 1 resembles the peak of the pure fluid at the same fluid density, while the peaks of the two other cases are similar to each other but different from the pure fluid at the same fluid density. Naturally for a sufficiently low matrix density, $\rho_{\text{m}} \leq 0.01$, the fluid-fluid radial distribution functions become, for all three cases indistinguishable from that of the pure fluid.

Other than the peak at $r \approx 12$, the low- r correlations ($0.0 \leq r \leq 5.0$) of the fluid-fluid radial distribution function are similar along **path A**, for cases 2 and 3 at the same matrix density. The correlations of $g_{\text{ff}}(r)$ in case 1, within that range, closely resemble

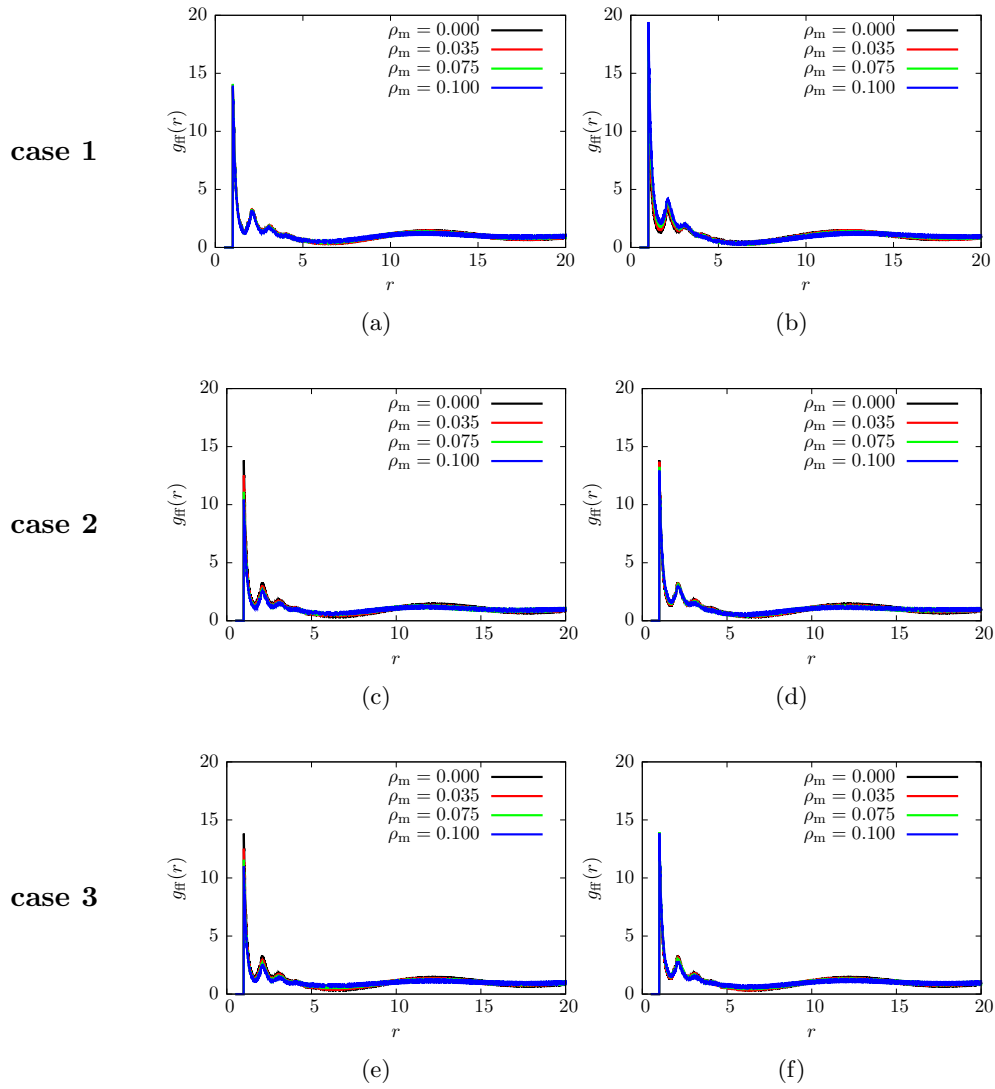


Figure 5.61: Radial distribution function for the fluid-fluid correlations $g_{\text{ff}}(r)$ as function of r , of systems along **path A** (left column) and **path B** (right column) in the (ρ_f, ρ_m) -plane. Different rows correspond to different combinations of matrix-matrix and fluid-matrix interactions (see table 5.5 for details). Different lines in the graphs represent different values of the matrix density ρ_m (as labeled).

those of the pure fluid at $\rho = 0.2$ for all investigated matrix densities. Along **path B**, on the other hand, $g_{\text{ff}}(r)$ closely resembles at low- r ($0.0 \leq r \leq 5.0$) $g(r)$ of the pure fluid with a density equal to the fluid density ρ_f of the quenched-annealed system in case 1. In cases 2 and 3 along path B the fluid-fluid radial distribution functions are nearly equal and resemble the $g(r)$ of a pure fluid with a density equal to the total density $\rho_f + \rho_m = 0.2$ to a good degree. At low enough matrix densities $\rho_m \leq 0.02$ the radial distribution functions become indistinguishable from those of the pure fluid

again.

Fluid-matrix radial distribution function

The fluid-matrix radial distribution function is defined by

$$g_{\text{fm}}(r) = \frac{A}{N_{\text{f}} N_{\text{m}}} \left\langle \sum_{i=1}^{N_{\text{f}}} \sum_{j=1}^{N_{\text{m}}} \delta(\mathbf{r} - \mathbf{r}_j + \mathbf{r}_i) \right\rangle, \quad (5.22)$$

with N_{f} and N_{m} being the number of fluid and matrix particles respectively, A being the two-dimensional volume (area) and \mathbf{r}_i denoting the position of the fluid particles while \mathbf{r}_j denotes the position of the matrix particles.

The fluid-matrix radial distribution functions along **path A** are shown in the panels on the left column of figure 5.62, while those along **path B** are shown in the right panels of this figure. The different cases of interaction combinations (see table 5.5) are shown in the rows of figure 5.62.

A first look at figure 5.62 reveals that the $g_{\text{fm}}(r)$ is qualitatively similar along **paths A** and **B**. However, there is a huge qualitative difference between the fluid-matrix radial distribution functions of case 1, compared to the other two cases (also keep in mind the different vertical scale for these cases).

It is quite obvious, that the peak at hard core contact ($r = 1.0$) is significantly reduced in height in case 1, when compared to the contact peak in the other cases. For a matrix density $\rho_{\text{m}} \geq 0.035$ the height of the peak at contact in case 1 is even lower than unity. The limited height of the contact peak in case 1 is an result of the cluster formation which preferentially takes place in regions left void by the matrix, as has already been discussed in section 5.3.2. At high enough matrix density, $\rho_{\text{m}} \geq 0.075$ side peaks can be identified for $r > 1$.

At larger particle separation, a maximum in $g_{\text{fm}}(r)$ at $r \approx 6$ and a minimum at $r \approx 12$ can be identified. Interestingly the maximum in $g_{\text{fm}}(r)$ at $r \approx 6$ occurs at a particle separation, which shows a minimum in $g_{\text{ff}}(r)$, while the minimum of $g_{\text{fm}}(r)$ at $r \approx 12$ is found at a separation featuring a maximum in $g_{\text{ff}}(r)$ of the same system. The fact that $g_{\text{fm}}(r)$ has a minimum where $g_{\text{ff}}(r)$ has a maximum and vice versa in case 1, can be attributed to the fact, that in this particular case fluid clusters form preferentially in the places void of any matrix particles. The small peak $g_{\text{fm}}(r = 1.0) < 1.0$ originates from the rare cases of hard core contact between matrix and fluid.

The fluid-matrix radial distributions of cases 2 and 3, on the other hand, shows the same general features as the respective fluid-fluid radial distribution functions; there is a pronounced main peak at $r = 1$ with the sudden drop towards smaller r , due to the hard core part of the interaction potential. This main peak is accompanied by up to three side peaks at $r \approx 2$, $r \approx 3$, ($r \approx 4$). As for $g_{\text{ff}}(r)$ there is a minimum at $r \approx 6$ and a maximum at $r \approx 12$, exactly at the same positions as in the fluid-fluid radial distribution function. The maximum as well as the minimum in $g_{\text{fm}}(r)$ are more pronounced in case 3 than in case 2. The identical positions of minima and maxima when comparing $g_{\text{fm}}(r)$ to $g_{\text{ff}}(r)$ in cases 2 and 3 can be explained by the preferential formation of the fluid clusters around the matrix particles, due to the attractive part of

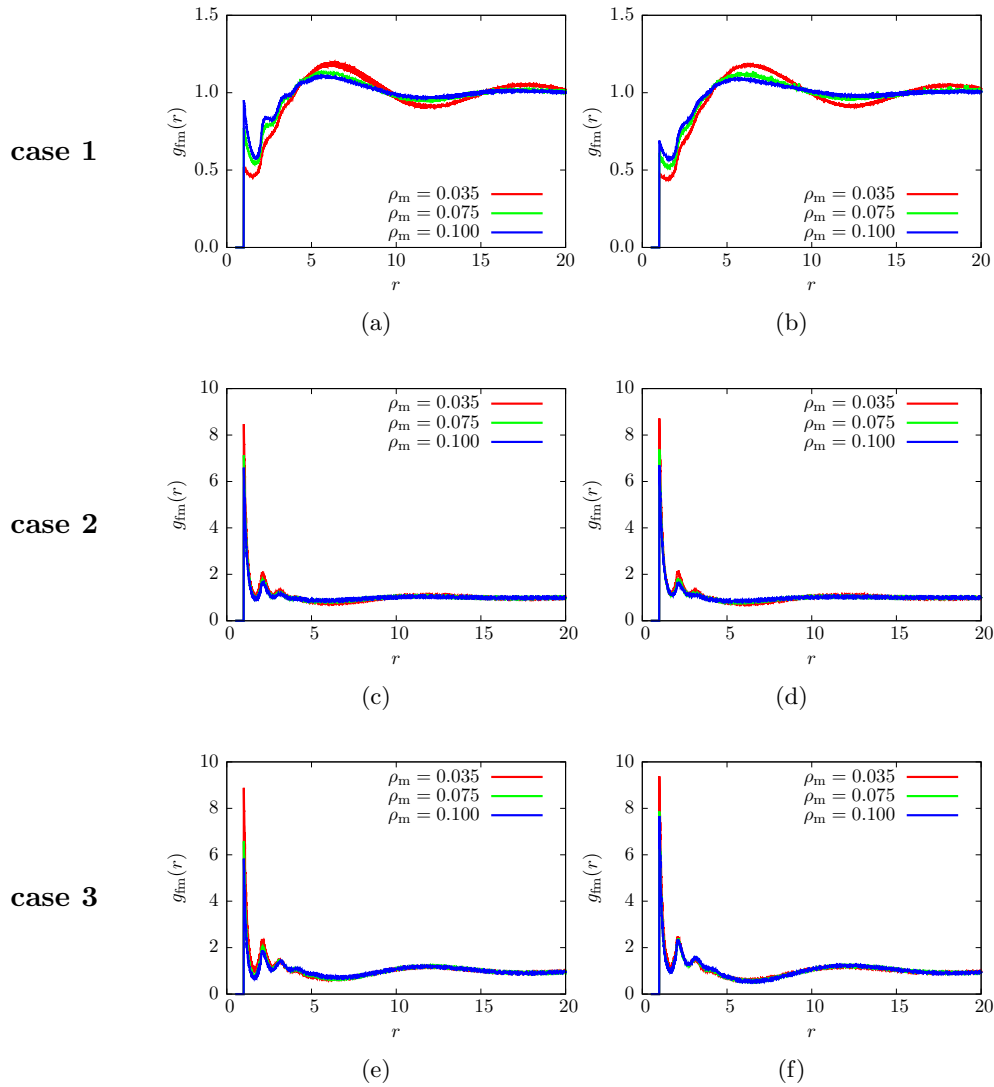


Figure 5.62: Radial distribution function for the fluid-matrix correlations $g_{fm}(r)$ as function of r , of systems along **path A** (left column) and **path B** (right column) in the (ρ_f, ρ_m) -plane. Different rows correspond to different combinations of matrix-matrix and fluid-matrix interactions (see table 5.5 for details). Different lines in the graphs represent different values of the matrix density ρ_m (as labeled).

the fluid-matrix interaction, in contrast to the hard core only fluid-matrix interaction of case 1. The minima and maxima in $g_{fm}(r)$ of case 3 are more pronounced than those in $g_{fm}(r)$ of case 2, because of the small clusters of matrix particles the fluid is adsorbed to in case 3 compared to the rather distributed matrix particles in case 2.

5.3.4 Mean Square Displacement

The particle mean square displacement $\langle \delta r^2(t) \rangle$ at any given time t can be computed via

$$\langle \delta r^2(t) \rangle = \overline{\langle |\mathbf{r}(t) - \mathbf{r}(0)|^2 \rangle}, \quad (5.23)$$

with $\langle \dots \rangle$ denoting the ensemble average over the degrees of freedom of the fluid at a fixed matrix configuration and $\overline{\dots}$ denoting the average over the matrix realizations, while $\mathbf{r}(t)$ and $\mathbf{r}(0)$ stand for the particle positions at time t and $t = 0$ respectively. Note that the average over the different matrix realizations present in equation (5.23) is missing in equation (5.7) of section 5.2. Figure 5.63 shows the mean square displacement as a function of time (MC-steps) for **paths A** and **B** and cases 1-3 at several matrix densities. The diffusion constant D is given by the slope of mean square displacement as function of the time t via equation (5.9). Plots of the diffusion constant against the matrix density are shown in figure 5.64.

The dependence of the mean square displacement on the matrix density ρ_m of systems along **path A** (constant ρ_f), given in the left hand side panels of figure 5.63, shall be discussed first. As in the sections before, the different combinations of matrix-matrix and fluid-matrix interactions are arranged in the rows of figure 5.63 (case 1 to case 3). Along **path A**, an increase in matrix density always leads to both a decrease of the mean square displacement as well as to a decrease of the diffusion constant D (see left panel of figure 5.64). This behavior is not unexpected since more fixed matrix particles correspond to a larger number of obstacles for the movement of the fluid particles. Naturally the extent of the decrease of the mean square displacement is different in the three investigated cases.

From figure 5.63 it becomes obvious that in case 3 the matrix density has the least effect on the diffusion of the fluid particles. This can be explained by the high localization of the matrix in this case: As can be seen from the bottom panels of figure 5.52, the matrix consists of small, cluster-like structures, hindering the movement of the fluid to a smaller extent than the more distributed matrix particles in case 1 and case 2.

The value of the diffusion constant D in case 2 is close to the one of case 3 for low matrix densities. However an increase of the matrix density above $\rho_m = 0.050$ leads to a dramatic drop in D . At a matrix density of $\rho = 0.1$ the diffusion constant in case 2 has nearly dropped to the level of D in case 1.

The initially high diffusion constant of case 2 at low matrix density can be explained by the fact, that in this case the fluid clusters form around the matrix particles, covering nearly all of the matrix particles (see center left panel of figure 5.52), therefore leaving much space for the free (non clustered) fluid particles to move. At higher matrix density however, not all of the more distributed matrix particles can be included into the fluid clusters. The matrix particles not included into the clusters therefore limit the free space for the moving fluid particles (see the similarity of the top right and center right panels of figure 5.52 compared to the bottom right panel of that figure).

Along **path B** (constant $\rho_f + \rho_m$) a distinct non-monotonic behavior in the development of the diffusion constant D , with respect to the matrix density, can be observed for all combinations of matrix-matrix and fluid-matrix interactions (see right panel of

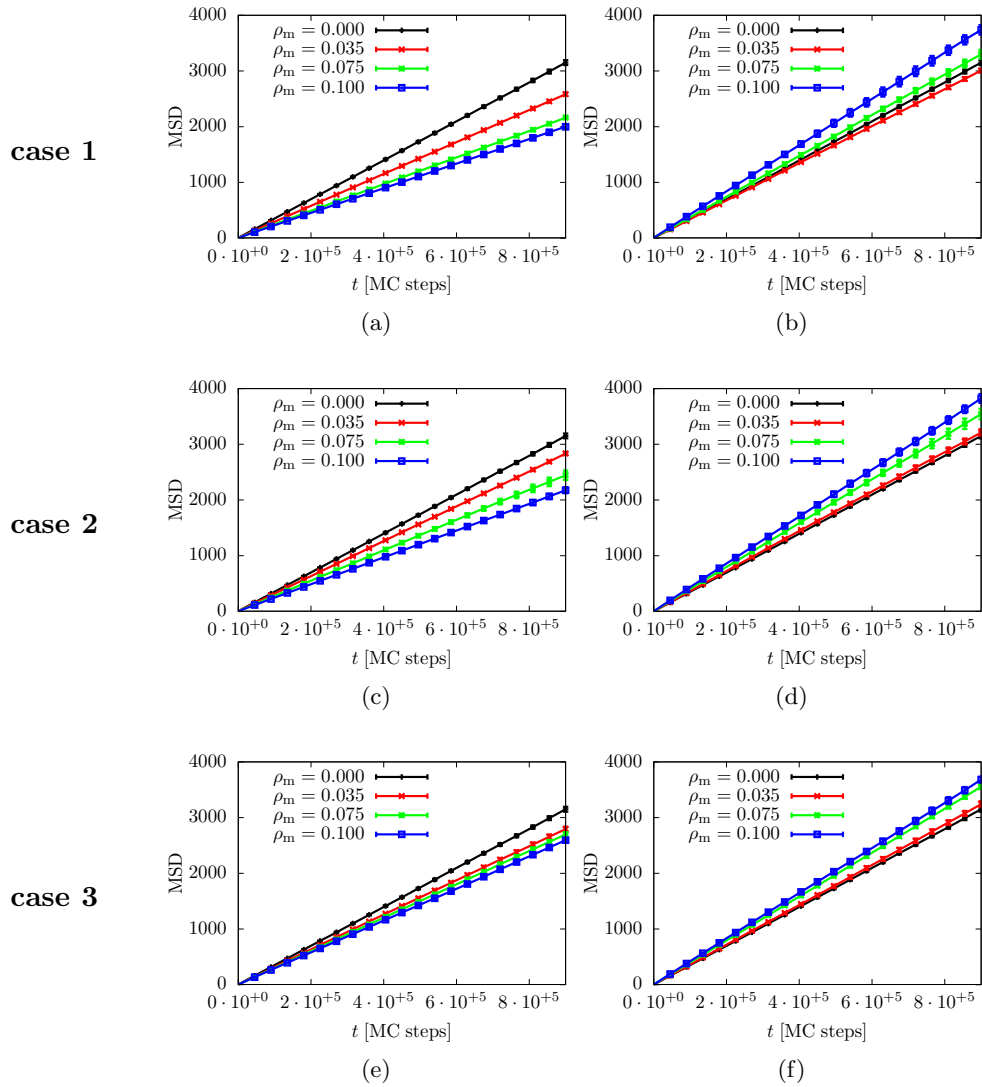


Figure 5.63: Mean square displacement (MSD) as a function of time (MC steps) of the fluid particles for systems along **path A** (left column) and **path B** (right column) in the (ρ_f, ρ_m) -plane [66]. Different rows correspond to different combinations of matrix-matrix and fluid-matrix interactions (see table 5.5 for details). The lines in the graphs represent different values of the matrix density ρ_m (as labeled).

figure 5.64, especially the inset). This non-monotonous behavior becomes apparent in a suppression of the diffusion at low matrix densities and a later increase in D for higher matrix densities, increasing above the level of D of the pure fluid (at $\rho = 0.2$). However in figure 5.63 this non-monotonous behavior is only visible for case 1, because it is only present for the smallest values of the matrix density in the other two cases ($\rho_m \leq 0.035$).

As already stated above, case 1 shows the most pronounced non-monotonic behavior

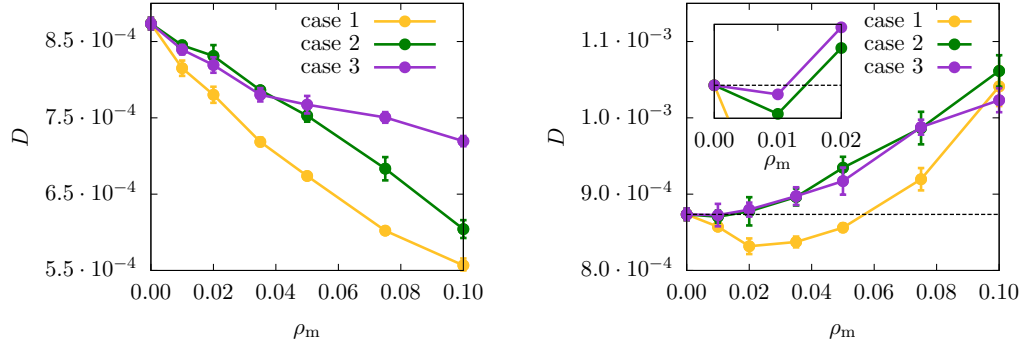


Figure 5.64: Average diffusion constant D as a function of matrix density ρ_m for **path A** (left panel) and **path B** (right panel). See table 5.5 for details of the interactions. The dashed horizontal line in the right panel marks the value of the diffusion constant of the pure fluid. The inset in this panel shows an enlarged view of the diffusion constant as a function of the matrix density in cases 2 and 3.

with regards to D along **path B**. In this case the minimum of the diffusion constant lies between $0.020 < \rho_m < 0.035$. The diffusion constant increases steeply after that minimum to become bigger than D of the pure $\rho = 0.200$ fluid, for matrix densities $\rho_m \geq 0.060$.

In case 2 the minimum of the diffusion constant is located at $\rho_m \sim 0.010$, while D of the quenched annealed system with $\rho_m = 0.020$ is already larger than that of the pure fluid (at $\rho = 0.200$).

Case 3 shows the smallest non-monotonic behavior of D with respect to the matrix density along **path B**. In this case the diffusion constant of the quenched annealed system at $\rho_m = 0.010$ is only slightly smaller than the diffusion constant of the pure fluid at $\rho = 0.200$ (see inset of figure 5.64).

Chapter 6

Conclusions

This thesis presents the author's investigations on systems with competing interactions in two dimensions, using the interaction potential given in equations (2.1) to (2.4), introduced by Sear *et al.* in [9]. The main emphasis of this work is put on the microphase formation, that is typical for these systems. Particular focus was put on the formation of clusters and the investigation of the properties of these clusters.

Previous studies on such systems have been conducted by Imperio and Reatto [12, 17, 18, 19] as well as by Archer [20].

Section 5.1 of this work is dedicated to the identification of those potential parameter sets that lead to microphase formation or that induce a liquid-vapor phase separation. This is achieved by calculating the phase diagrams of systems for different sets of potential parameters ($0.5 \leq R_r \leq 3.0$, $0.0 \leq \epsilon_r \leq 1.0$), using the Ornstein-Zernike equation in combination with the PY-closure relation.

From the results we conclude, that microphase separation only takes place, if the repulsion range R_r or the repulsion strength ϵ_r is large enough. A height of the resulting repulsive potential hump of $\Phi_{\text{IR}}(r_{\text{max}}) \geq 0.02$ seems to guarantee microphase formation at suitable densities and temperatures.

Structure functions, such as the radial distribution function $g(r)$ or the structure factor $S(k)$, obtained by the Ornstein-Zernike equation and Monte-Carlo simulations respectively are also summarized in section 5.1, for state points close to the phase separation or the microphase region.

Comparison of the data sets show a good agreement between the two approaches and therefor confirm the applicability of the Ornstein-Zernike equation to compute the phase diagrams.

Investigations on the structure factor $S(k)$, presented in section 5.1.3, confirm that the wavevector k_c that characterizes microphase formation, is independent of and temperature, as already suggested by a relation given by A. Archer in [20].

The phase diagrams of those systems that show liquid-vapor phase separation, are summarized in section 5.1.4. The critical density, estimated for these systems, approaches zero for potential parameters close to the micro phase forming region.

In section 5.2 of this work, investigations focus on the properties of the clusters such as

the number of contained particles and radius of gyration R_g . Additionally static and dynamic observables computed from cluster positions such as the static structure factor $S(k)$, the mean square displacement and the intermediate scattering function $f(k, t)$ are studied and compared to the same observables computed from particle positions. Since the related simulations are time-consuming our investigations focus on the potential parameters used by Imperio *et al.* in [12, 17, 18, 19].

Clusters are identified by an algorithm presented in section 4.3.1, while the emergence of a relative maximum in the cluster size distribution (percentage of clusters as a function of the cluster size in number of particles) at a particle number bigger than one is defined as a criterion for the clustering of the systems. This *cluster size distribution criterion* is confirmed as a valid measure for the transition of the system from a homogeneous phase to a cluster-forming one by the development of a maximum in the radius of gyration of the clusters and an equal percentage of free particles ($\sim 12\%$) in these systems at the transition temperature.

Form the cluster centers of mass, cluster structure functions like the radial distribution function $g(r)$ and the hexagonal order parameter Φ_6 , as well as the mean square displacement and the intermediate scattering functions (ISF) can be computed for the clusters.

The double peak structure emerging in the second peak of the radial distribution function at temperatures below $T \sim 0.35$ indicates freezing (exact values depend on the density, see table 5.3) which is in good agreement with results from [12, 17]. Similarly the radial distribution function of the clusters indicates a freezing transition for densities $\rho = 0.15$ and $\rho = 0.20$ at $T \sim 0.30$ and $T \sim 0.40$ respectively. However at the lowest investigated density $\rho = 0.10$ no indication of cluster freezing is observed in the entire temperature range investigated. Related results, based on investigations of the static structure factor instead of the pair distribution function, have been reported in [17]. The transition temperatures reported in [17] agree with those of the present work in most cases except for the highest investigated density ($\rho = 0.20$). According to the above criterion, the freezing of the particles within the clusters takes place for all investigated densities at similar temperatures (as already reported in [12]), whereas the freezing temperature of the clusters increases with density. It shall also be noted, that the freezing of the clusters at $\rho = 0.15$ and $\rho = 0.20$ does not lead to the development of a double peak structure at $r \approx 24$ and $r \approx 36$ in the radial distribution function computed from the particle positions.

Our predictions about the freezing of the clusters is confirmed by the development of the hexagonal bond order parameter Φ_6 of the clusters as a function of temperature, which increases much less at low densities as the temperature is decreased. Analyzing simulation snapshots, showing the positions of the clusters as well as their individual bond order parameters (by color code, see figures 5.34 to 5.36) suggests, that the overall bond order parameter of the system does not rise by increasing the individual bond order parameters of the clusters simultaneously, when decreasing T , but by enlarging groups of clusters with an already high individual bond order parameter.

Computations of dynamic parameters are conducted on the particles, as well as on the clusters. The logarithmic derivative of the mean square displacement of the particles $z(t)$, shows two regions of slow dynamics. The reason for the first slowdown is caging

by neighboring particles, while the second one observed at long t is caused by the attraction of neighboring cluster particles. For the clusters, the logarithmic derivative of the mean square displacement $z(t)$, also shows two dips: while the first dip is located at $t < 10$ MC-steps in most instances and is not considered an important feature due to the influence of the MC-simulation method imposed on the dynamics of the system, the dip at large t values is caused by the surrounding clusters, acting as obstacles to the motion of the tagged cluster. It shall be noted, that although the location of the second dip in $z(t)$ usually varies by more than one order of magnitude (e.g. $5.9 \cdot 10^4 \leq t \leq 1.3 \cdot 10^5$ for $\rho = 0.15$) for the different investigated temperatures, the associated mean square displacement value is roughly the same in all the cases (e.g. $5.8 \leq \langle \delta r^2(t) \rangle \leq 7.6$ for $\rho = 0.15$).

Intermediate scattering functions (ISFs) are computed from the particle and cluster positions for all systems at a wavevector $k = 0.573$, in order to analyze the relaxation of the cluster-cluster correlations. For all investigated densities and temperatures, the total ISF computed from particle positions is in good agreement with the total ISF computed from cluster positions. The self ISF calculated from the cluster positions also agrees with the total ISFs at all densities and temperatures, however to a much lesser degree. All of the above mentioned ISFs show a single step relaxation towards zero, at all investigated densities and temperatures. The self ISF computed from the particle positions on the other hand, starts to decay at lower t than the other ISFs and even shows a two step decay to zero at $\rho = 0.15$ and $\rho = 0.20$ at low enough temperatures.

In addition two dimensional QA-systems are also investigated in this work (section 5.3). These systems consist of a porous matrix of immobile particles and fluid particles that are embedded in this matrix. The configurations of the matrix are generated in a separate simulation run without the fluid, with the matrix particles interacting via the matrix-matrix (mm) potential $\Phi_{\text{mm}}(r)$. During the subsequent simulation of the entire QA-system, the fluid interacts with the now immobile matrix via the fluid-matrix (fm) potential $\Phi_{\text{fm}}(r)$, while the fluid particles interact via the fluid-fluid (ff) potential $\Phi_{\text{ff}}(r)$. The Imperio-Reatto (IR) potential $\Phi_{\text{IR}}(r)$ given by equations (2.1) to (2.4), was used as fluid-fluid interaction for all investigations of QA-systems in this work. In order to separate energetic from excluded volume effects while investigating the microphase formation of the QA-systems, three different combinations (case 1-3) of the hard core (hc) potential $\Phi_{\text{hc}}(r)$ and the Imperio-Reatto (IR) potential $\Phi_{\text{IR}}(r)$ are considered as matrix-matrix and fluid-matrix interaction. While $\Phi_{\text{IR}}(r)$ is used as fluid-matrix interaction in cases 2 and 3 and as matrix-matrix interaction in case 3, the had core potential $\Phi_{\text{hc}}(r)$ is used as matrix-matrix interaction in cases 1 and 2 and as fluid-matrix interaction in case 1. As in section 5.2 the parameters $R_r = 2.0$ and $\epsilon_r = 1.0$ are used for the Imperio-Reatto potential.

Investigations are carried out via Monte Carlo simulations for the three interaction cases along two paths. Along **path A** the fluid density is kept constant at $\rho_f = 0.20$ and along **path B** the total density is kept constant at $\rho_{\text{tot}} = \rho_m + \rho_f = 0.20$, while increasing the matrix density from $\rho_m = 0.0$ to $\rho_m = 0.1$.

Snapshots of the simulations show, that the fluid particles are adsorbed to the matrix

particles, if the fluid-matrix interaction is given by Φ_{IR} (case 2 and 3), while the fluid clusters do prefer the spaces left void by the matrix, when the fluid-matrix interaction is of the hard core type (case 1) [66]. Due to the relatively high total density the beginning of the transition to the stripe phase is visible in cases 2 and 3 along **path A**, however case 1 shows no such change in morphology, because of the different interaction between the fluid and the matrix. Along **path B** on the other hand, the clusters clearly shrink in case 1, due to the smaller fluid density compared to the pure fluid at $\rho = 0.2$ and because the fluid is not adsorbed to the matrix in this case. The shrinking of the clusters can also be observed in case 2, however to a lesser extent, while in case 3 the cluster size remains roughly constant (when also counting matrix particles as cluster particles), due to the fluid sticking to clusters of matrix particles. These effects are also seen in the cluster size as a function of the matrix density.

Structure factors computed for these systems show, that the cluster-cluster distance remains constant under the influence of the matrix, except for systems in case 1 along **path B**. For these systems a slight shift of the first peak in the fluid-fluid structure factor $S_{\text{ff}}(k)$ at $k \sim k_c = 0.573$ to lower values of k , with increasing matrix density, suggests an increasing cluster-cluster distance. The reason of this increase most likely is the fitting of the fluid clusters to the spaces left void by the matrix and the bigger influence of the matrix along **path B**, due to the larger matrix ratio.

The significant qualitative differences of the matrix-fluid (fm) structure functions ($S_{\text{fm}}(k)$, $g_{\text{fm}}(r)$) of case 1 systems, when compared to systems with interaction combinations of case 2 and 3, found in this investigation shall also be mentioned here. Most notable is the negative correlation of $S_{\text{fm}}(k)$ at $k \sim k_c = 0.573$ in case 1 (**path A** and **path B**). The observed differences can be attributed to the different interactions between fluid and matrix in this case.

Investigating the dynamics of quenched-annealed systems, the diffusion constant D of the fluid particles is found to decrease monotonically, with increasing matrix density along **path A**. While the decrease of D is the smallest in case 3 systems, due to the high localization of the matrix, case 1 systems are most effected by the matrix particles. In systems along **path B**, on the other hand the diffusion constant behaves non-monotonically with increasing density. This non-monotonic behavior is most pronounced in case 1 systems [66].

Finally a few topics to continue this research shall be mentioned here. First it would be of interest to study the influence of the potential parameters on the dynamics. Since only systems with a particular potential parameter set have been investigated here, a more comprehensive range of potential parameter might be considered for future investigations. However, the use of a well optimized simulation code is recommended for such a research, due to the high required computational costs. Consideration of different potential parameters could also be extended to the QA systems presented in section 5.3, or to fluid-fluid mixtures, which have not been addressed in this work at all.

Additionally the phase diagrams presented in section 5.1 could be verified by performing Gibbs ensemble simulations on the respective systems, this would result in a better validation of the method of using the Ornstein-Zernike equation presented here.

Appendix A

Approximation in the computation of the 2D Fourier Transform

In section 4.2.4, the function $M(t)$ is given by (see equation (4.129))

$$M(t) = \frac{1}{2\pi} 2^{-it} \frac{\Gamma\left(\frac{1}{2} - \frac{it}{2}\right)}{\Gamma\left(\frac{1}{2} + \frac{it}{2}\right)}. \quad (\text{A.1})$$

The absolute value of the Γ -functions in equation (A.1) can be found in [67] (equation 8.332-2) as

$$\left| \Gamma\left(\frac{1}{2} + iy\right) \right|^2 = \frac{\pi}{\cosh(\pi y)} \quad \forall y \in \mathbb{R}. \quad (\text{A.2})$$

Since the hyperbolic cosine is an even function ($\cosh(-\pi y) = \cosh(\pi y)$) the absolute value of the fraction of the two Γ -functions in equation (A.1) is given by

$$\left| \frac{\Gamma\left(\frac{1}{2} - \frac{it}{2}\right)}{\Gamma\left(\frac{1}{2} + \frac{it}{2}\right)} \right| = 1. \quad (\text{A.3})$$

Therefor the function $M(t)$ can be rewritten as

$$M(t) = \frac{1}{2i\pi} 2^{-it} \exp(i\psi(t)) \quad (\text{A.4})$$

using the phase $\psi(t)$ given by

$$\psi(t) = \Im \left[\ln \left(\frac{\Gamma\left(\frac{1}{2} - \frac{it}{2}\right)}{\Gamma\left(\frac{1}{2} + \frac{it}{2}\right)} \right) \right], \quad (\text{A.5})$$

with $\Im[x]$ denoting the imaginary part of x . In order to simplify the Γ -functions in equation (A.5) the relation

$$\Gamma(x+1) = x\Gamma(x) \quad (\text{A.6})$$

(see [67] equation 8.331-1) is used. Applying equation (A.6) n -times recursively starting with $x = n + \frac{1}{2} + \frac{it}{2}$ results in

$$\Gamma\left(n + \frac{1}{2} + \frac{it}{2}\right) = \prod_{k=1}^n \left(k - \frac{1}{2} + \frac{it}{2}\right) \Gamma\left(\frac{1}{2} + \frac{it}{2}\right). \quad (\text{A.7})$$

The logarithm of equation (A.7) is given by

$$\ln \Gamma\left(\frac{1}{2} + \frac{it}{2}\right) = \ln \Gamma\left(n + \frac{1}{2} + \frac{it}{2}\right) - \sum_{k=1}^n \ln\left(k - \frac{1}{2} + \frac{it}{2}\right). \quad (\text{A.8})$$

Using the same procedure described above starting from $x = n + \frac{1}{2} - \frac{it}{2}$ results in

$$\ln \Gamma\left(\frac{1}{2} - \frac{it}{2}\right) = \ln \Gamma\left(n + \frac{1}{2} - \frac{it}{2}\right) - \sum_{k=1}^n \ln\left(k - \frac{1}{2} - \frac{it}{2}\right) \quad (\text{A.9})$$

Inserting equations (A.8) and (A.9) into the term $\ln \left[\Gamma\left(\frac{1}{2} - \frac{it}{2}\right) / \Gamma\left(\frac{1}{2} + \frac{it}{2}\right) \right]$ leads to

$$\begin{aligned} \ln \left(\frac{\Gamma\left(\frac{1}{2} - \frac{it}{2}\right)}{\Gamma\left(\frac{1}{2} + \frac{it}{2}\right)} \right) &= \ln \Gamma\left(\frac{1}{2} - \frac{it}{2}\right) - \ln \Gamma\left(\frac{1}{2} + \frac{it}{2}\right) \\ &= \ln \Gamma\left(n + \frac{1}{2} - \frac{it}{2}\right) - \sum_{k=1}^n \ln\left(k - \frac{1}{2} - \frac{it}{2}\right) \\ &\quad - \ln \Gamma\left(n + \frac{1}{2} + \frac{it}{2}\right) + \sum_{k=1}^n \ln\left(k - \frac{1}{2} + \frac{it}{2}\right) \\ &= \ln \Gamma\left(n + \frac{1}{2} - \frac{it}{2}\right) - \ln \Gamma\left(n + \frac{1}{2} + \frac{it}{2}\right) + \sum_{k=1}^n \ln\left(\frac{k - \frac{1}{2} + \frac{it}{2}}{k - \frac{1}{2} - \frac{it}{2}}\right). \end{aligned} \quad (\text{A.10})$$

Using the expression

$$\arctan(x) = \frac{i}{2} (\ln(1 - ix) - \ln(1 + ix)) \quad (\text{A.11})$$

with $x = \frac{t}{2k-1}$ results in

$$\begin{aligned} \arctan\left(\frac{t}{2k-1}\right) &= \frac{i}{2} \ln\left(1 - \frac{it}{2k-1}\right) - \frac{i}{2} \ln\left(1 + \frac{it}{2k-1}\right) \\ &= \frac{i}{2} \ln\left(\frac{1 - \frac{it}{2k-1}}{1 + \frac{it}{2k-1}}\right) \\ &= \frac{i}{2} \ln\left(\frac{2k-1-it}{2k-1+it}\right) \\ &= \frac{i}{2} \ln\left(\frac{k - \frac{1}{2} - \frac{it}{2}}{k - \frac{1}{2} + \frac{it}{2}}\right). \end{aligned} \quad (\text{A.12})$$

(using [64])

Using equation (A.12), equation (A.10) can be written as

$$\ln \left(\frac{\Gamma \left(\frac{1}{2} - \frac{it}{2} \right)}{\Gamma \left(\frac{1}{2} + \frac{it}{2} \right)} \right) = 2i \sum_{k=1}^n \arctan \left(\frac{t}{2k-1} \right) + \ln \Gamma \left(n + \frac{1}{2} - \frac{it}{2} \right) - \ln \Gamma \left(n + \frac{1}{2} + \frac{it}{2} \right). \quad (\text{A.13})$$

For large values of n the $\ln \Gamma$ -terms in equation (A.13) can be expressed by the asymptotic form

$$\ln \Gamma(z) = \left(z - \frac{1}{2} \right) \ln(z) - z + \frac{1}{2} \ln(2\pi) + \sum_{k=1}^{\infty} \frac{B_{2k}}{2k(2k-1)z^{2k-1}}, \quad (\text{A.14})$$

valid for large values of $|z|$ (see [67] equation 8.344), with B_m being the first Bernoulli number of order m , ($B_0 = 1$, $B_1 = -\frac{1}{2}$, $B_2 = \frac{1}{6}$, $B_3 = 0$, $B_4 = -\frac{1}{30}$, $B_5 = 0$, $B_6 = \frac{1}{42}$, $B_7 = 0$, $B_8 = -\frac{1}{30}$).

A recursive expression for the first Bernoulli numbers is given by

$$B_m = - \sum_{k=0}^{m-1} \frac{m!}{k!(m-k)!} \frac{B_k}{m-k+1} \quad (\text{A.15})$$

with the starting point of the recursion defined as $B_0 = 1$.

Using equation (A.14), while omitting the limit of $n \rightarrow \infty$ to simplify the notation, the last two terms of equation (A.13) can be written as

$$\begin{aligned}
& \ln \Gamma \left(n + \frac{1}{2} - \frac{it}{2} \right) - \ln \Gamma \left(n + \frac{1}{2} + \frac{it}{2} \right) = \\
& = \left(n - \frac{it}{2} \right) \ln \left(n + \frac{1}{2} - \frac{it}{2} \right) - \left(n + \frac{1}{2} - \frac{it}{2} \right) + \frac{1}{2} \ln(2\pi) \\
& \quad - \left(n + \frac{it}{2} \right) \ln \left(n + \frac{1}{2} + \frac{it}{2} \right) + \left(n + \frac{1}{2} + \frac{it}{2} \right) - \frac{1}{2} \ln(2\pi) \\
& \quad + \sum_{m=1}^{\infty} \left(\frac{B_{2m}}{2m(2m-1) \left(n + \frac{1}{2} - \frac{it}{2} \right)^{2m-1}} - \frac{B_{2m}}{2m(2m-1) \left(n + \frac{1}{2} + \frac{it}{2} \right)^{2m-1}} \right) = \\
& = it + n \ln \left(\frac{n + \frac{1}{2} - \frac{it}{2}}{n + \frac{1}{2} + \frac{it}{2}} \right) - \frac{it}{2} \ln \left(\left(n + \frac{1}{2} - \frac{it}{2} \right) \left(n + \frac{1}{2} - \frac{it}{2} \right) \right) \\
& \quad + \sum_{m=1}^{\infty} \left(\frac{B_{2m} \left(\left(n + \frac{1}{2} + \frac{it}{2} \right)^{2m-1} - \left(n + \frac{1}{2} - \frac{it}{2} \right)^{2m-1} \right)}{2m(2m-1) \left(\left(n + \frac{1}{2} - \frac{it}{2} \right) \left(n + \frac{1}{2} - \frac{it}{2} \right) \right)^{2m-1}} \right) = \\
& = it - i 2n \arctan \left(\frac{t}{2n+1} \right) - \frac{it}{2} \ln \left(\left(n + \frac{1}{2} - \frac{it}{2} \right) \left(n + \frac{1}{2} - \frac{it}{2} \right) \right) \\
& \quad + \sum_{m=1}^{\infty} \left(\frac{B_{2m} \left(\left(n + \frac{1}{2} + \frac{it}{2} \right)^{2m-1} - \left(n + \frac{1}{2} - \frac{it}{2} \right)^{2m-1} \right)}{(4m^2 - 2m) \left(\left(n + \frac{1}{2} \right)^2 + \frac{t^2}{4} \right)^{2m-1}} \right), \tag{A.16}
\end{aligned}$$

while also making use of equation (A.12). The sum in the last line of equation (A.16) can be further rewritten as

$$\begin{aligned}
& \sum_{m=1}^{\infty} \left(\frac{B_{2m} \left(\left(n + \frac{1}{2} + \frac{it}{2} \right)^{2m-1} - \left(n + \frac{1}{2} - \frac{it}{2} \right)^{2m-1} \right)}{(4m^2 - 2m) \left(\left(n + \frac{1}{2} \right)^2 + \frac{t^2}{4} \right)^{2m-1}} \right) = \\
& = \sum_{m=1}^{\infty} \frac{B_{2m}}{4m^2 - 2m} \frac{1}{\left(\left(n + \frac{1}{2} \right)^2 + \frac{t^2}{4} \right)^{\frac{2m-1}{2}}} \times \\
& \quad \times \left[\frac{\left(n + \frac{1}{2} + \frac{it}{2} \right)^{2m-1}}{\left(\left(n + \frac{1}{2} - \frac{it}{2} \right) \left(n + \frac{1}{2} + \frac{it}{2} \right) \right)^{\frac{2m-1}{2}}} - \frac{\left(n + \frac{1}{2} - \frac{it}{2} \right)^{2m-1}}{\left(\left(n + \frac{1}{2} - \frac{it}{2} \right) \left(n + \frac{1}{2} + \frac{it}{2} \right) \right)^{\frac{2m-1}{2}}} \right] = \\
& = \sum_{m=1}^{\infty} \frac{B_{2m}}{4m^2 - 2m} \frac{1}{\left(\left(n + \frac{1}{2} \right)^2 + \frac{t^2}{4} \right)^{\frac{2m-1}{2}}} \left[\left(\frac{n + \frac{1}{2} + \frac{it}{2}}{n + \frac{1}{2} - \frac{it}{2}} \right)^{\frac{2m-1}{2}} - \left(\frac{n + \frac{1}{2} - \frac{it}{2}}{n + \frac{1}{2} + \frac{it}{2}} \right)^{\frac{2m-1}{2}} \right] = \\
& = \sum_{m=1}^{\infty} \frac{B_{2m}}{4m^2 - 2m} \frac{1}{\left(\left(n + \frac{1}{2} \right)^2 + \frac{t^2}{4} \right)^{\frac{2m-1}{2}}} \times \\
& \quad \times \left[\exp \left(\frac{2m-1}{2} \ln \left(\frac{n + \frac{1}{2} + \frac{it}{2}}{n + \frac{1}{2} - \frac{it}{2}} \right) \right) - \exp \left(\frac{2m-1}{2} \ln \left(\frac{n + \frac{1}{2} - \frac{it}{2}}{n + \frac{1}{2} + \frac{it}{2}} \right) \right) \right] = \\
& = \sum_{m=1}^{\infty} \frac{B_{2m}}{4m^2 - 2m} \frac{1}{\left(\left(n + \frac{1}{2} \right)^2 + \frac{t^2}{4} \right)^{\frac{2m-1}{2}}} \times \\
& \quad \times \left[\exp \left(+i(2m-1) \arctan \left(\frac{t}{2n+1} \right) \right) - \exp \left(-i(2m-1) \arctan \left(\frac{t}{2n+1} \right) \right) \right] = \\
& = i \sum_{m=1}^{\infty} \frac{B_{2m}}{2m^2 - m} \frac{\sin \left((2m-1) \arctan \left(\frac{t}{2n+1} \right) \right)}{\left(\left(n + \frac{1}{2} \right)^2 + \frac{t^2}{4} \right)^{\frac{2m-1}{2}}}, \tag{A.17}
\end{aligned}$$

using equation (A.12) as well as the expression $\sin(x) = \frac{i}{2} (\exp(-ix) - \exp(+ix))$. Inserting equations (A.16) and (A.17) into equation (A.13), and including the limit $n \rightarrow \infty$ again, finally results in

$$\begin{aligned}
\ln \left(\frac{\Gamma \left(\frac{1}{2} - \frac{it}{2} \right)}{\Gamma \left(\frac{1}{2} + \frac{it}{2} \right)} \right) & = \lim_{n \rightarrow \infty} \left[2i \sum_{k=1}^n \arctan \left(\frac{t}{2k-1} \right) + it - i2n \arctan \left(\frac{t}{2n+1} \right) \right. \\
& \quad \left. - \frac{it}{2} \ln \left(\left(n + \frac{1}{2} \right)^2 + \frac{t^2}{4} \right) + i \sum_{m=1}^{\infty} \frac{B_{2m}}{2m^2 - m} \frac{\sin \left((2m-1) \arctan \left(\frac{t}{2n+1} \right) \right)}{\left(\left(n + \frac{1}{2} \right)^2 + \frac{t^2}{4} \right)^{\frac{2m-1}{2}}} \right]. \tag{A.18}
\end{aligned}$$

Therefore the function $\psi(t)$ can be written as

$$\begin{aligned}
\psi(t) &= \Im \left[\ln \left(\frac{\Gamma\left(\frac{1}{2} - \frac{it}{2}\right)}{\Gamma\left(\frac{1}{2} + \frac{it}{2}\right)} \right) \right] \\
&= \lim_{n \rightarrow \infty} \left[2 \sum_{k=1}^n \arctan \left(\frac{t}{2k-1} \right) + t - 2n \arctan \left(\frac{t}{2n+1} \right) \right. \\
&\quad \left. - \frac{t}{2} \ln \left(\left(n + \frac{1}{2} \right)^2 + \frac{t^2}{4} \right) + \sum_{m=1}^{\infty} \frac{B_{2m}}{2m^2 - m} \frac{\sin \left((2m-1) \arctan \left(\frac{t}{2n+1} \right) \right)}{\left(\left(n + \frac{1}{2} \right)^2 + \frac{t^2}{4} \right)^{\frac{2m-1}{2}}} \right] \\
&= \lim_{n \rightarrow \infty} \left[2 \sum_{k=1}^n \arctan \left(\frac{t}{2k-1} \right) + t - 2n\alpha - t \ln(x) \right. \\
&\quad \left. + \sum_{m=1}^{\infty} \frac{B_{2m}}{2m^2 - m} \frac{\sin((2m-1)\alpha)}{x^{2m-1}} \right] \\
&\approx \lim_{n \rightarrow \infty} \left[2 \sum_{k=1}^n \arctan \left(\frac{t}{2k-1} \right) + t - 2n\alpha - t \ln(x) \right. \\
&\quad \left. + \frac{\sin(\alpha)}{6x} - \frac{\sin(3\alpha)}{180x^3} + \frac{\sin(5\alpha)}{630x^5} - \frac{\sin(7\alpha)}{840x^7} \right], \tag{A.19}
\end{aligned}$$

with

$$x = \sqrt{\left(n + \frac{1}{2} \right)^2 + \frac{t^2}{4}} \tag{A.20}$$

and

$$\alpha = \arctan \left(\frac{t}{2n+1} \right), \tag{A.21}$$

while using only the first four terms of the sum on the last line of equation (A.19). The last equality (or rather approximation) in equation (A.19) together with equations (A.20) and (A.21) exactly represents equations (4.131) to (4.133) in section 4.2.4.

A.1 remarks

- The large value of n (or the limit $n \rightarrow \infty$) is necessary to be able to use the approximation given by equation (A.14)
- The limit

$$\lim_{n \rightarrow \infty} \left[-2n \arctan \left(\frac{t}{2n+1} \right) \right] = -t \tag{A.22}$$

which cancels with the $+t$ term in equation (A.19) (computed using [64])

- By replacing \arctan in the term $2 \sum_{k=1}^n \arctan\left(\frac{t}{2k-1}\right)$ by the first non-zero term of its Taylor series around $\frac{t}{2k-1} = 0$, $\frac{t}{2k-1}$, the limit

$$\lim_{n \rightarrow \infty} \left[2 \sum_{k=1}^n \left(\frac{t}{2k-1} \right) - \frac{t}{2} \ln \left(\left(n + \frac{1}{2} \right)^2 + \frac{t^2}{4} \right) \right] = C_{\text{Euler}} + \ln(4), \quad (\text{A.23})$$

with the Euler-Gamma constant $C_{\text{Euler}} = 0.577215\dots$ (computed using [64])

Bibliography

- [1] C. N. Likos; Effective interactions in soft condensed matter physics, *Phys. Rep.*, **348** 267, (2001).
- [2] R. J. Hunter; *Foundations of Colloid Science, Vol I*, Clarendon Press, Oxford, (1986).
- [3] W. B. Russel, D. A. Saville, and W. R. Schowalter; *Colloidal Dispersions*, Cambridge University Press, Cambridge, (1990).
- [4] M. Kalab; The beauty of milk at high magnification, *Royal Microscopy Society: Infocus Magazine*, **18** 4, (2010).
- [5] W. Hu; *Polymer Physics: A Molecular Approach*, Springer, (2012).
- [6] C. A. Murray and D. G. Grier; Video microscopy of monodisperse colloidal systems, *Annu. Rev. Phys. Chem.*, **47** 421, (1996).
- [7] P. Habdas and E. R. Weeks; Video microscopy of colloidal suspensions and colloidal crystals, *Curr. Opin. Colloid In.*, **7** 196, (2002).
- [8] C. N. Likos; Soft matter with soft particles, *Soft Matter*, **2** 478, (2006).
- [9] R. P. Sear, S. W. Chung, G. Markovich, W. M. Gelbart, and J. R. Heath; Spontaneous patterning of quantum dots at the air-water interface, *Phys. Rev. E*, **59**(6) R6255, (1999).
- [10] M. Seul and D. Andelman; Domain Shapes and Patterns: The Phenomenology of Modulated Phases, *Science*, **267**(5197) 476, (1995).
- [11] D. Roux, W. M. Gelbart, A. Ben-Shaul, editor; *Micelles Membranes, Microemulsions and Monolayers*, Springer, (1994).
- [12] A. Imperio and L. Reatto; A bidimensional fluid system with competing interactions: spontaneous and induced pattern formation, *J. Phys: Cond. Mat.*, **16** S3769, (2004).
- [13] L. D. Gelb, K. E. Gubbins, R. Radhakrishnan, and M. Sliwinska-Bartkowiak; Phase separation in confined systems, *Rep. Prog. Phys.*, **62** 1573, (1999).

- [14] R. P. Sear and W. M. Gelbart; Microphase separation versus the vapor-liquid transition in systems of spherical particles, *J. Chem. Phys.*, **110(9)** 4582, (1999).
- [15] J. R. Heath, P. J. Kuekes, G. S. Snider, and R. Stanley Williams; A defect-tolerant computer architecture: Opportunities for nanotechnology, *Science*, **280(5370)** 1716, (1998).
- [16] S. H. Choi, K. L. Wang, M. S. Leung, G. W. Stupian, N. Presser, S. W. Chung, G. Markovich, S. H. Kim, and J. R. Heath; Fabrication of nanometer size photoresist wire patterns with a silver nanocrystal shadowmask, *Journal of Vacuum Science & Technology A*, **17(4)** 1425, (1999).
- [17] A. Imperio and L. Reatto; Microphase separation in two-dimensional systems with competing interactions, *J. Chem. Phys.*, **124(16)** 164712, (2006).
- [18] A. Imperio and L. Reatto; Microphase morphology in two-dimensional fluids under lateral confinement, *Phys. Rev. E.*, **76(4)** 040402, (2007).
- [19] A. Imperio, L. Reatto, and S. Zapperi; Rheology of colloidal microphases in a model with competing interactions, *Phys. Rev. E.*, **78(2)** 021402, (2008).
- [20] A. J. Archer; Two-dimensional fluid with competing interactions exhibiting microphase separation: Theory for bulk and interfacial properties, *Phys. Rev. E*, **78(3)** 031402, (2008).
- [21] M. Chan, N. Mulders, and J. Reppy; Helium in aerogel. *Physics Today*, **49** 30, (1996).
- [22] M. L. Rosinberg; Liquid state methods for disordered systems, C. Caccamo, J. P. Hansen, and G. Stell, editors, in: *New Approaches to problems in liquid state theory*. Kluwer Academic, Dordrecht, MA, (1999).
- [23] J. Kurzidim, D. Coslovich, and G. Kahl; Single-particle and collective slow dynamics of colloids in porous confinement, *Phys. Rev. Lett.*, **103** 138303, (2009).
- [24] J. Kurzidim, D. Coslovich, and G. Kahl; Impact of random obstacles on the dynamics of a dense colloidal fluid. *Phys. Rev. E*, **82** 041505, (2010).
- [25] C. N. Likos; Introduction to soft matter (lecture). (2008) [Vienna].
- [26] A. P. Lyubartsev and A. Laaksonen; Calculation of effective interaction potentials from radial distribution functions: A reverse monte carlo approach, *Phys. Rev. E*, **52** 3730, (1995).
- [27] J. P. Hansen and I. R. McDonald; *Theory of Simple Liquids, Third Edition*, Academic Press, 3rd edition, (2006).
- [28] A. J. Archer and N. B. Wilding; Phase behavior of a fluid with competing attractive and repulsive interactions, *Phys. Rev. E*, **76(3)** 031501, (2007).

- [29] D. Frenkel and B. Smit. *Understanding Molecular Simulation*. Academic Press, London, 2nd edition, (2002).
- [30] M. P. Allen and D. J. Tildesley; *Computer Simulation of Liquids*, Clarendon Press, Oxford, (1990).
- [31] T. Gleim, W. Kob, and K. Binder; How does the relaxation of a supercooled liquid depend on its microscopic dynamics?, *Phys. Rev. Lett.*, **81** 4404, (1998).
- [32] N. Metropolis, A. W. Rosenbluth, M. N. Rosenbluth, A. H. Teller, and E. Teller; Equation of state calculations by fast computing machines, *J. Chem. Phys.*, **21** 1087, (1953).
- [33] H. E. A. Huitema and J. P. van der Eerden; Can monte carlo simulation describe dynamics? a test on lennard-jones systems, *J. Chem. Phys.*, **110(7)** 3267, (1999).
- [34] A. Z. Panagiotopoulos and S. K. Kumar; Large lattice discretization effects on the phase coexistence of ionic fluids, *Phys. Rev. Lett.*, **83** 2981, (1999).
- [35] A. Z. Panagiotopoulos; On the equivalence of continuum and lattice models for fluids, *J. Chem. Phys.*, **112(16)** 7132, (2000).
- [36] K. Kikuchi, M. Yoshida, T. Maekawa, and H. Watanabe; *Metropolis Monte Carlo method as a numerical technique to solve the FokkerPlanck equation*, **185**, (1991)
- [37] L. Berthier and W. Kob; The monte carlo dynamics of a binary lennard-jones glass-forming mixture, *Journal of Physics: Condensed Matter*, **19(20)** 205130, (2007).
- [38] L. Berthier; Revisiting the slow dynamics of a silica melt using monte carlo simulations, *Phys. Rev. E*, **76** 011507, (2007).
- [39] J. K. Percus; Approximation methods in classical statistical mechanics. *Phys. Rev. Lett.*, **8** 462, (1962).
- [40] J. F. Springer, M. A. Pokrant, and Jr. F. A. Stevens; Integral equation solutions for the classical electron gas, *J. Chem. Phys.*, **58(11)** 4863, (1973).
- [41] J. M. Ortega and W. C. Rheinboldt; *Iterative Solutions of Nonlinear Equations in Several Variables*, Academic Press, (1970).
- [42] E. Lomba; An efficient procedure for solving the reference hypernetted chain equation (rhnc) for simple fluids. *Mol. Phys.*, **68(1)** 87, (1989).
- [43] A. A. Broyles; Radial distribution functions from the Born-Green integral equation, *J. Chem. Phys.*, **33** 456, (1960).
- [44] K. C. Ng; Hypernetted chain solutions for the classical one-component plasma up to $\gamma = 7000$, *J. Chem. Phys.*, **61(7)** 2680, (1974).

- [45] F. Lado; Numerical fourier transforms in one, two, and three dimensions for liquid state calculations, *Journal of Computational Physics*, **8** 417, (1971).
- [46] J. D. Talman; Numerical Fourier and Bessel transforms in logarithmic variables, *Journal of Computational Physics*, **29(1)** 35, (1978).
- [47] J. J. Weis, J. M. Caillol and D. Levesque; Theoretical determination of the dielectric constant of a two dimensional dipolar fluid. *Mol. Phys.*, **44(3)** 733, (1981).
- [48] N. Hoffmann, C. N. Likos, and H. Löwen; Microphase structuring in two-dimensional magnetic colloid mixtures. *J. Phys. - Condens. Mat.*, **18** 10193, (2006).
- [49] T. Morita; Theory of classical fluids: Hyper-netted chain approximation, *Progress of Theoretical Physics*, **23(5)** 829, (1960).
- [50] L. L. Lee; Correlation functions of classical fluids. iii. the method of partition function variation applied to the chemical potential: Cases of py and hnc2, *J. Chem. Phys.*, **60(4)** 1197, (1974).
- [51] L. L. Lee; Chemical potentials based on the molecular distribution functions. an exact diagrammatical representation and the star function, *J. Chem. Phys.*, **97(11)** 8606, (1992).
- [52] M. J. Feraud, E. Lomba, and L. L. Lee; Chemical potential distributions of inclusion gas in quenched-annealed random porous media, *J. Chem. Phys.*, **111** 10275, (1999).
- [53] B. M. Mladek, D. Gottwald, G. Kahl, M. Neumann, and C. N. Likos; Formation of polymorphic cluster phases for a class of models of purely repulsive soft spheres, *Phys. Rev. Lett.*, **96** 045701, (2006).
- [54] B. M. Mladek, D. Gottwald, G. Kahl, M. Neumann, and C. N. Likos; Erratum: Formation of polymorphic cluster phases for a class of models of purely repulsive soft spheres, [Phys. Rev. Lett. **96**, 045701 (2006)], *Phys. Rev. Lett.*, **97** 019901, (2006).
- [55] A. Okabe, B. Boots, K. Sugihara, and S. N. Chiu; *Spatial tessellations: Concepts and applications of Voronoi diagrams*, Probability and Statistics. Wiley, NYC, 2nd edition, (2000).
- [56] G. Lejeune Dirichlet; über die reduction der positiven quadratischen formen mit drei unbestimmten ganzen zahlen, *Journal für die reine und angewandte Mathematik*, **40** 209, (1850).
- [57] G. Voronoi; Nouvelles applications des paramtres continus la thorie des formes quadratiques. premier mmoire. sur quelques proprits des formes quadratiques positives parfaites, *Journal für die reine und angewandte Mathematik*, **133** 97, (1908).

- [58] F. Aurenhammer; Voronoi diagrams a survey of a fundamental geometric data structure, *ACM Comput. Surv.*, **23(3)** 345, (1991).
- [59] B. I. Halperin and D. R. Nelson; Theory of two-dimensional melting, *Phys. Rev. Lett.*, **41** 121, (1978).
- [60] H. Weber, D. Marx, and K. Binder; Melting transition in two dimensions: A finite-size scaling analysis of bond-orientational order in hard disks, *Phys. Rev. B*, **51** 14636, (1995).
- [61] P. M. Reis, R. A. Ingale, and M. D. Shattuck; Crystallization of a quasi-two-dimensional granular fluid, *Phys. Rev. Lett.*, **96** 258001, (2006).
- [62] N. Gribova, A. Arnold, T. Schilling, and C. Holm; How close to two dimensions does a lennard-jones system need to be to produce a hexatic phase? *J. Chem. Phys.*, **135(5)** 054514, (2011).
- [63] D. F. Schwanzer and G. Kahl; Two-dimensional systems with competing interactions: microphase formation versus liquidvapour phase separation, *Journal of Physics: Condensed Matter*, **22(41)** 415103, (2010).
- [64] Wolfram Research, Inc.; Mathematica, Version 8.0, Champaign, IL (2010).
- [65] J. Kurzidim; *Glass Formation of Colloids in Porous Media*. PhD thesis, Vienna University of Technology, (2013).
- [66] D.F. Schwanzer and G. Kahl; Two-dimensional systems with competing interactions: microphase formation under the effect of a disordered porous matrix, *Condensed Matter Physics*, **14(3)** 33801, (2011).
- [67] I. S. Gradshteyn and I. M. Ryzhik; *Table of integrals, series, and products*. Elsevier/Academic Press, Amsterdam, 7th edition, (2007).

The thesis presented here resulted in the following original publications:

- D.F. Schwanzer, D. Coslovich, J. Kurzidim and G. Kahl; Effects of porous confinement on the structural properties of the Gaussian core model *Molecular Physics*, **107(4)** 433 (2009).
- D. F. Schwanzer and G. Kahl; Two-dimensional systems with competing interactions: microphase formation versus liquidvapour phase separation, *Journal of Physics: Condensed Matter*, **22(41)** 415103, (2010).
- D.F. Schwanzer and G. Kahl; Two-dimensional systems with competing interactions: microphase formation under the effect of a disordered porous matrix, *Condensed Matter Physics*, **14(3)** 33801, (2011).
- D.F. Schwanzer, D. Coslovich and G. Kahl; Two-dimensional systems with competing interactions: static and dynamic properties of the clusters *in preparation*, (2015).

Financial support by the Austrian Research Fund (FWF) under Proj. Nos. P19890N16 and W004 is gratefully acknowledged.

Acknowledgments

At this point I would like to express my gratitude to all the people that were a part of my life in general and especially during the years I worked on this thesis:

My supervisor **Prof. Gerhard Kahl** for accepting me to his group, his advice and support and most importantly for his patience with me.

The many people that were part of the Soft Matter Theory group during my time here (in order of appearance): **Maria Feraud**, **Bianca Mladek**, **Gernot Pauschenwein**, **Julia Fornleitner**, **Jan Kurzidim**, **Daniele Coslovich**, **Emanuela Bianchi**, **Lukas Strauss**, **Camille Jouvie**, **Arash Nikoubashman**, **Giannis Georgiou**, **Moritz Antlanger**, **Martina Lechner**, **Ulf Pedersen**, **Andreas Tröster**, **Ismene Kolovos**, **Marta Montes Saralegui**, **Cecillia Bores Quijano** and **Clara Abaurrea Velasco** for creating a pleasant working atmosphere, our talks at the lunch breaks about quite obscure topics sometimes and the help on to many occasions to count. Special tanks to **Maria Feraud** for introducing me to the concept of the integral equations, **Bianca Mladek** for teaching me about Monte Carlo simulations and **Daniele Coslovich** for providing me with his great post processing tool and for his quick and straightforward help even long after he left Vienna.

The administrative staff of the institute **Elfriede Mösmer**, **Franz Hochfellner**, **Heike Höller** and **Silvia Riedler** for the help in all bureaucratic matters.

Prof. Martin Neumann for agreeing to be the opponent in my PhD exam on short notice.

Prof. Christos Likos the originally planned opponent in my PhD exam, for always cheering us up on his visits to the group. Get well soon!

Prof. Enrique Lomba for providing me with the Fast Fourier Transform code needed for my work.

My friends **Florian Libisch**, **Barbara Kovacs**, **Viktoria Appolona**, **Sarah Wantoch**, **Lukas Klausner**, **Stefan Wibihal** and **Wilhelm Lubenik** for their moral support and the long evenings of much needed distraction from my work. Special thanks to **Florian Libisch** for the honor of choosing me as best man for his wedding.

My family, especially my grandparents **Franziska** and **Josef Schwanzer** as well as **Adele** and **Anton Klimpfinger**, my parents **Leopold** and **Anna Schwanzer** and my sisters **Cornelia Schwanzer** and **Astrid Schneiber** for their support in everything and for making me the person I am now and also my little niece **Viktoria Schneiber** for being an enormous source of joy for all of us.

My thesis is written in



WWW.PHDCOMICS.COM

Figure A.1: "Piled Higher and Deeper" by Jorge Cham www.phdcomics.com

Dieter Schwanzer - Curriculum Vitae

Personal Information

Full Name: Dipl.-Ing. Dieter Franz Schwanzer
 Contacts: Email: schwanzer@cmt.tuwien.ac.at
 Institut für theoretische Physik (E136)
 Wiedner Hauptstrasse 8–10, A-1040 Vienna
 Date of Birth: February 6th, 1978
 Place of Birth: Tulln, Austria
 Nationality: Austrian



Basic Education

1992–1997 HBLVA für Chemische Industrie,
 Rosensteingasse 79
 A-1170 Vienna

Higher Education

1997–2005 Studies in Technical Physics at the Vienna University of Technology,
 Wiedner Hauptstrasse 8–10
 A-1040 Vienna, Austria
 17.11.2005 Diploma Exam passed with distinction
 thesis topic: *Construction of a pulsed field system*
 01.2007–now PhD Student at the Institute for Theoretical Physics,
 Soft Matter Theory and Center for Computational Material Science
 thesis topic: *Static and Dynamic Properties of two-dimensional
 systems with competing interactions*

Work Experience

02.2006–10.2006 Civil service in a shelter for homeless people,
 Caritas Betreuungszentrum Gruft,
 A-1060 Vienna, Austria
 01.2007–02.2010 Project Assistant at the Institute for Theoretical Physics,
 Vienna University of Technology
 Wiedner Hauptstrasse 8–10
 A-1040 Vienna, Austria
 04.2010–now Caregiver in a shelter for homeless people,
 Caritas Betreuungszentrum Gruft,
 A-1060 Vienna, Austria
